UNIVERSITY OF OKLAHOMA

GRADUATE COLLEGE

MEASUREMENTS AND MODELING OF THE GREAT PLAINS LOW-LEVEL JET

A Dissertation

SUBMITTED TO THE GRADUATE FACULTY

in partial fulfillment of the requirements for the

degree of

Doctor of Philosophy

By

WILLIAM JOHN MARTIN
Norman, Oklahoma
2003

UMI Number: 3082922

UMI®

UMI Microform 3082922

ProQuest Information and Learning Company
300 North Zeeb Road
P.O. Box 1346
Ann Arbor, MI 48106-1346

MEASUREMENTS AND MODELING OF THE
GREAT PLAINS LOW-LEVEL JET

A Dissertation APPROVED FOR THE
SCHOOL OF METEOROLOGY

BY

Acknowledgments

Many people and institutions have been of assistance in various parts of this project. First and foremost is my adviser, Alan Shapiro with whom I have had a great many fruitful discussions. A half hour with Al has many times saved a week's worth of work. His criticism, creative contributions, and careful consideration of the work have been invaluable and his patience essential (especially as the project was delayed a year by a need to work). I would also like to acknowledge John Lewis and Doug Lilly and the other members of my doctoral committee for important ideas, discussions and direction. Of paramount importance as well were Dusan Zrnić, Josh Wurman and Andy Pazmany who made available to me their radars, helped me to acquire data with them, and helped me to understand their engineering details.

Acknowledgments and appreciation are also due to Mike Schmidt for help in the use of the Cimarron radar; for Dusan Zrnić and Dick Doviak for discussing and criticizing some of the work; for Mark Askelson for sharing his experience and work with the Cimarron radar; and Jeanette Bider and Gary Schnell for valuable discussions and information on the habits of birds. I would also like to thank CAPS and CMRP and their directors, Kelvin Droegemeier and Brian Fiedler for supporting this work.

Archived data were acquired from the NCAR mass store and from NCDC. Recent advancements in accessing archived data through the international data network has been a great help for this research.

This research was supported by the Coastal Meteorological Research Program (CMRP) under Grant N00014-96-1-1112 from the United States Department of Defense (Navy), by the Center for the Analysis and Prediction of Storms (CAPS) under grant ATM91-20009 from the National Science Foundation, by the NSF IHOP program under NSF grant ATM01-29892 and by the University of Oklahoma.

The help and support of my friends and peers in Norman has made my life pleasant. While this has made it easier to work long hours as a graduate student, their friendship is a wonderful accomplishment in and of itself.

In numerical modeling, one can create the weather for a particular date in a computer

multiple times, while changing a variable to see how much that variable mattered. In real life, this is never possible. The weather is the way it is and it is sometimes simply not knowable if it would have come out differently had some variable been altered. Similarly, in our personal lives, we are stuck with being on the particular path we find ourselves. We can not be certain how this path would have been different had some detail of our history been altered. Sometimes, though, you just know how much certain things matter. In November of 2001 I met the love of my life. And while she may fret that her distracting me has delayed completing this document by many months, in reality it might never have been completed had I not met her. I am quite sure I would have run off to a care-free life of sleeping under bridges and dining from dumpsters had not Sharon provided a spark and an inspiration to my life. I owe more to her than to anyone else I have ever met.

Contents

SYMBOLS

a	ωt or a constant
A	Area
b	Constant depending on radar beam shape, or a general constant
B_I,B_T,B_R	Incident, transmitted, and reflected magnetic field vector amplitude
β	Radar tilt angle
C_n^2	Refractivity structure constant
c	Speed of electromagnetic waves
c(t)	Viscous damping coefficient
D_a	Antenna diameter
D_n	Structure function
E_I,E_T,E_R	Incident, transmitted, and reflected electric field vector amplitude
ϵ	Turbulent eddy dissipation rate
ϵ_0	Permitivity constant
f	Coriolis parameter; $f=2\Omega\sin\phi$
Φ	Spectral density function
ϕ	Latitude, or radar beam width angle, or radar azimuth angle
G	Antenna gain
g	Gravitational acceleration at sea level
h	Radar pulse length
J	Cost function or electric current

K	Turbulent kinematic viscosity or wave number or spatial wave number
$\lvert K\rvert^2$	An Optical material property
k	Absorption coefficient
$\widehat{k}$	Unit vector in z-direction
l, L	Lengths or length scales
L	Loss factor
λ	Radar wavelength
μ	Molecular viscosity
μ_0	Permeability constant
n	Index of refraction or an integer
N	Index of refraction in N-units = $(n-1)*10^6$
ν	Molecular kinematic viscosity
ω	electromagnetic wave frequency
Ω	Earth's rotation rate = $7.292X10^{-5}$rad/s
ψ	(-Wind shear angle) or a phase angle
φ	90-ϕ (for ϕ=azimuth)
$\rho_0, \rho, \overline{\rho}, \rho$	Respectively: background density, density, mean density, and perturbation density
P_0,P,p,p'	Respectively: hydrostatic pressure, pressure, mean pressure, and perturbation pressure
P	Radar power
R,r	Range to radar probe volume center

R	Ratio of incident to reflected electromagnetic energy, "reflectivity" in electrodynamics
R	Rainfall rate
Ri	Richardson number
S	Amplitude of the Poynting vector (energy flux vector)
$\triangle S$	A layer thickness
σ	Standard deviation or backscatter cross-section
σ^2	Variance
t	time or a time scale
T	Absolute temperature
θ	Potential temperature or an angle
τ	Viscous stress or a characteristic time
τ_{xy}	Stress tensor component (stress in direction y on plane normal to x)
U,V,W	Total x,y,z wind components. V is also used for speed, V=$\lvert\vec{u}\rvert$
u,v,w	Mean x,y,z wind components
u′,v′,w′	Perturbation wind components
$\vec{u}$	Wind vector
u_a,v_a	Ageostrophic wind components
u_g,v_g	Geostrophic wind components
V	Volume
v_r	Radial velocity measured with radar
x,y,z or X,Y,Z	Cartesian coordinates (x is East-West, y is North-South, Z is up-down)

Z	Reflectivity factor
η	Radar reflectivity
dBZ	Z measured in decibels

ABSTRACT

This dissertation describes a project to elucidate the turbulent and momentum structure of the Great Plains Low-Level Jet (LLJ), primarily by the use of Doppler radar. Simple theoretical and numerical models of the LLJ are developed which are extensions of the Blackadar inertial oscillation theory. The results of this research are generally consistent with this theory. Turbulence is central to this theory and the core of this research is measurements of turbulence and wind speeds in actual LLJs, in addition to simple models.

The use of clear-air Doppler radar data appropriate for LLJ study, requires an understanding of the nature of the clear-air echo. It is important to avoid migrating birds as targets as they are a large potential source of velocity bias. For this reason, considerable attention is given to the source of clear-air echo, and a couple cases are analyzed with high-resolution radars. This work strongly implies that the clear-air echo for the cases considered was primarily insects. This contrasts with much recent work (reviewed here) supporting the theory that migrating birds are a major source of clear-air echo.

Using radar data believed to be mostly free from migrating bird contamination, this works describes and develops data reduction and quality control techniques so that high-quality profiles and time-height cross-sections can be routinely obtained. These techniques include dealiasing, minimizing the impact of ground clutter bias, obtaining a measure of large scale turbulence from a VAD, and using spectral width information to extract both a measure of small-scale turbulence as well as wind shear.

The principle original components of this research are:

1. Simple theoretical analysis and modeling of LLJ dynamics. This includes the extension of Blackadar's 0-dimensional LLJ model to include turbulence; the development of a detailed conceptual description of the LLJ oscillation; and the development of the concept of resonance of the LLJ, with modeling studies showing a resonance effect.

2. Analysis of the source of clear-air radar echo using high-resolution radars. Data from high-resolution radars in two cases of nocturnal clear-air radar echo implied that the

source of echo was insects for both cases.

3. Development of a technique for extracting wind shear and turbulence information from radar spectrum width data with VAD analysis. This technique is successfully demonstrated.

4. Obtaining high vertical and temporal resolution profiles and time-height cross-sections of velocity, turbulence, and wind shear of the LLJ using Doppler radar. Time-height cross-sections of momentum and turbulence were obtained from NEXRAD radars in the Great Plains for 4 cases which span the warm season. The results tend to confirm the Blackadar theory.

5. Analyzing VAD-derived wind profiles for ground clutter contamination. Ground clutter was found to be a problem at both low and high tilts. This work revealed an optimum tilt angle for VAD work of 1.5° when using NEXRAD radars.

Chapter 1

Introduction

1.1 Project History

I began this study as an investigation of turbulence in the LLJ (low-level jet). One night I was flying a small airplane from Ada to Norman, Oklahoma. While descending to land at Max Westheimer Field in Norman, I noticed that the plane's ground speed was much higher than expected and that I was off course to the North. I quickly realized I was in the LLJ and corrected the plane's course. I also noticed that the air I was flying in was very smooth; it had not a trace of aerodynamic turbulence and the only clue that I was in the jet was the rapid and unexpected movement past objects on the ground. I was curious more than anything about what made the flow so smooth, rather than turbulent as one might have expected from a free, fluid jet. Upon embarking on this research project, the Cimarron Doppler radar was made available to me so that I could make measurements on the LLJ with the radar collecting clear-air data. The question as to what causes the radiation to be back-scattered in clear air gained in importance throughout the project, and understanding and analyzing radar data became a large component of this dissertation. This is because the temporal and spatial patterns of clear-air return are difficult to explain. One explanation involves the presence of migratory birds. If migratory birds were the main cause of my data, then the data would be far less useful then if the cause of the data was insects or refractive index gradients. A lot of data was acquired with various radars in an attempt to determine the cause of the nocturnal clear-air return. This issue should not be regarded as firmly settled by this research, but I hope I have shed some light on it.

The Appendix to this dissertation began as a subsection of Ch. 3 covering a simple derivation to determine the best tilt angle to use for VAD work. It gradually grew in size as anomalies and errors in the data were tracked down and explained. It eventually became a substantial piece of work by itself. It is presented as a self-contained document, though the concepts explored are closely related to other issues in clear-air radar work explored in Ch. 3.

1.2 Motivation for this Work

The possibility that the LLJ might be laminar is an interesting one. This is because free fluid jets are ordinarily turbulent, even for small Reynold's numbers (see, for example, Tennekes and Lumley, 1972, pp. 127-133). With the very large length scales (and, therefore Reynold's numbers) in atmospheric flows, turbulence is the most common state. Stratification provides one mechanism for suppressing turbulence; however, the LLJ generates considerable wind shear, so it is not clear if static stability is sufficient to account for a possible reduction or elimination of turbulence in the LLJ. For the LLJ, the extent of turbulence has important implications for theories about it. With the Blackadar (1957) theory, a large reduction or elimination of turbulence in the nocturnal phase is necessary while other theories do not requiring a specific turbulent behavior. Only scattered and inconsistent observations of turbulence in the LLJ have been reported in the literature. To verify or refute the Blackadar theory, much better measurements are necessary than have been heretofore reported. This research is an attempt to find out the extent to which turbulence is suppressed in the LLJ and the basic cause of this suppression. Essentially, it is an attempt to verify the Blackadar theory. This will help to clarify the relative importance of different physical mechanisms proposed to account for the LLJ. This is being addressed by using Doppler radar to obtain high-resolution (in both time and space) velocity and turbulence measurements combined with some numerical and theoretical modeling. Radar measurements can provide a detailed picture of the actual momentum and turbulent structure and time-history of the jet, while modeling provides a means of guiding the acquisition, reduction and analysis of data.

Numerical and analytic modeling inevitably has limitations due to the truncation of physics, numerical approximations, or possible coding errors. However, modeling provides the means to explore and test the implications of theories. The physical parameters and boundary and initial conditions can be varied to test theoretical predictions untestable by other means. Nearly complete fields of physical variables are also available, something not attainable with measurements. Measurements have limitations due to the limited temporal and spatial extent they are available, the limited number of variables that can be measured, and possible instrument failures. However, measurements, properly criticized, provide the ultimate ground truth for any models, numerical or theoretical.

Chapter 2

Theory and Modeling of the LLJ

I think that the Root of the Wind is Water-
It would not sound so deep
Were it a Firmamental Product-
Airs no Oceans keep-
Mediterranean intonations-
To a Current's Ear-
There is a maritime conviction
In the atmosphere-
-Dickinson, c. 1874

2.1 Literature Review of the Great Plains LLJ

2.1.1 The Low-Level Jet

The broadest definition of a low-level jet (LLJ) is simply any lower-tropospheric maximum in the vertical profile of the horizontal winds. A LLJ can occur under favorable synoptic conditions anywhere in the world. Of practical interest is their impact on the transport of moisture. Of theoretical interest is the large amount of vertical wind shear associated with them and the observation that they are typically supergeostrophic by a large (>50%) amount. A large number of specific geographic locations all over the world have been identified as especially favorable for LLJ development (Stensrud, 1996). Among these locations is the Great Plains region of the United States, in which one of the most significant LLJs, in terms of its impact on precipitation and severe weather, occurs. The

Great Plains LLJ has consequently been studied more than any other and it is the principal focus of this research as well.

In the climatology study of Bonner (1968), both southerly and northerly LLJs were cataloged; but there were far more cases of southerly jets than northerly jets. For the southerly jets in Bonner's study, it was found that they tended to have a wind maximum near 800 meters above ground level; that strong jets were primarily a nighttime feature; that they occurred with greatest frequency during the spring and summer; that the states of greatest activity include: Texas, Oklahoma, Kansas, Nebraska, Iowa, Missouri, and Arkansas; and that favorable synoptic conditions for LLJ formation are those which have a strong west to east pressure gradient across the Great Plains and an uninterrupted flow of air from the Gulf of Mexico. A more recent study by Whiteman (1997) has shown that 50% of LLJ maxima actually occur below 500m. Whiteman also found that the temporal wind maximum typically occurs around 0200 LST (local standard time). The low altitude and timing of the jet maximum means that routine observing systems such as wind profilers and rawinsondes will poorly sample LLJs in the Great Plains, since the first gate above the ground for the operational wind profiler network is at 500 meters and routine rawinsondes are taken near 0600 and 1800 LST. In the climatological analysis of Bluestein and Banacos (2002), a mean LLJ was found in the northwest quadrant of surface cyclones, but not in other quadrants of cyclones and anticyclones.

The low altitude and southerly flow of the LLJ make it a key element in the return-flow cycle of air from the Gulf of Mexico (a typically event for the November through April season). In this cycle, northerly flow advects dry, typically cool continental air out over the Gulf of Mexico where it is modified by surface processes and gains moisture. To complete the return-flow cycle, this modified air then advects northward back onto the continent by way of low-level winds. The LLJ is a principal mechanism by which this moist and unstable air from the Gulf is advected northward into the United States where it ultimately becomes precipitation. Higgins et al. (1997) in an analysis based on the assimilated data sets of NCEP/NCAR and NASA/DAO found that low-level flow of moisture from the Gulf of Mexico at night is increased by 48% from mean values when a LLJ is present. Indeed, Arritt et al. (1997) showed that the widespread Great Plains flooding event of 1993 was associated with a prolonged period of strong LLJs.

In addition to being a powerful means of moisture transport, the LLJ can also promote convection by inducing uplifting from convergence along the nose of the jet (Zhong et al., 1996) which can combine with divergence aloft from an upper-level jet (Beebe and Bates, 1955). The strong nocturnal phase of the jet is widely believed to be particularly important in promoting nighttime convection. The LLJ has been linked to the occurrence and intensity of mesoscale convective systems and appears to be an essential ingredient in the environment that produces mesoscale convective complexes. This is due presumably to the enhancement of both warm advection and the advection of moist, unstable air (Maddox, 1983). Such complexes produce a large portion of the warm season rainfall over the United States.

Further, the presence of a LLJ, especially when combined with an upper-level jet, provides a veering of winds with height that is favorable for the development of severe weather and tornadoes (Uccellini, 1979). Helicity values from operational models are strongly enhanced by nocturnal LLJs, which leads to the issuance of tornado watches instead of thunderstorm watches. Research hasn't been reported which backs-up the association between nocturnal enhancement of helicity by a LLJ and the occurrence of tornadoes, but at least some forecasters believe it to be reasonable.

2.1.2 The Blackadar Theory

A number of theories have been proposed to account for LLJ dynamics. Probably the most important theory is due to Blackadar (1957). This theory accounts for both the daily oscillation in jet intensity and for the significantly supergeostrophic velocities observed during the nocturnal phase. Even when another theoretical mechanism is believed to be important in a particular case, the Blackadar idea is still often invoked to fully account for the observations. Numerous modeling studies (e.g., Djurić, 1981; Beyrich and Klose, 1988; Fast and McCorcle, 1990; Savijarvi, 1991; and Zhong et al., 1996) have supported the importance of the Blackadar mechanism. The observations of Parish et al. (1988)

also strongly support the Blackadar mechanism. Blackadar explains the cycle of the LLJ as an inertial oscillation that relies on the retardation to subgeostrophic speeds of lower tropospheric air due to vertical, turbulent mixing with the heated surface during the day. Once surface heating ceases near nightfall, the layer of air in contact with the ground undergoes radiative cooling, becomes statically stable, and decouples from the layer of air above which becomes nearly frictionless and turbulence free and accelerates due to the synoptic pressure gradient. The effect of the Coriolis force on this accelerating, frictionless air stream is to cause an inertial oscillation with supergeostrophic speeds being reached after several hours. Some of the analysis and results of the Blackadar are repeated in Secs. 2.2.2 and 2.3.

The inertial oscillation caused by the Coriolis force has long been known to oceanographers (e.g., Sverdrup, 1942, pp. 431-442) who observe rotating ocean currents and who use the same mathematically used later by Blackadar to analyze it.

2.1.3 Other Theories and Modeling of the LLJ

Theories other than the Blackadar theory have been proposed to account in whole or part for the LLJ. One mechanism analyzed by Holton (1967) describes the nature of the LLJ as a response to the diurnal heating and cooling of sloping terrain, which results in a periodic variation in thermal wind and a consequent surface geostrophic wind oscillation. This mechanism makes no appeal to variations in turbulent mixing and has the advantage of explaining why the LLJ tends to be located over the (gently sloped) Great Plains, which the Blackadar theory does not address. However, Holton realized there were discrepancies between his results and observations which he thought were likely due to time and height variation in turbulence as in the Blackadar mechanism. Holton's analysis also includes the Coriolis force as an essential ingredient which rotates the fluctuating east-west wind component into the north-south direction, creating a southerly LLJ. In a two-dimensional modeling study, McNider and Pielke (1981) supported the view that both the Blackadar mechanism and the impact of differential heating of sloping terrain are of importance to LLJ dynamics, though they found that the terrain effect was actually dominant. This study is important in that it is the only one which found effects of terrain to be dominant. In direct contrast, Savijarvi (1991), who also used a two-dimensional model, found that terrain had very little impact. In a sensitivity study, Savijarvi removed the terrain in the model and found only a 15% decrease in maximum jet amplitude.

Wexler (1961) applied the boundary current concept that accounts for the Gulf Stream in the Atlantic Ocean as an explanation for the preponderance of LLJs east of the Rocky Mountains. Holton (1967), however, suggested that scale analysis does not support a close analogy between ocean boundary currents and the LLJ. Anderson (1976), on the other hand, showed that a model based on the boundary current idea worked well in simulating an African LLJ.

Finally, Uccellini and Johnson (1979) presented a theory for the dynamical coupling of upper-level and low-level jets, with the LLJ forming in response to mass adjustment and isallobaric forcing. Their analysis covered the interaction of upper jet streaks and lower-level jets in general, though they specifically looked at a case study for a developing ageostrophic LLJ over the Ohio to Kentucky area during the day (May 10-11, 1973, a severe weather outbreak case). Their analysis indicated that this jet became supergeostrophic in response to the upper jet streak by about 20%.

Terrain, horizontal variation in surface heating, the general synoptic situation, the Coriolis force and temporal and vertical variations in turbulence all are potential contributors to LLJ dynamics. It is likely that the proposed mechanisms vary in importance with different cases and with different geographic regions in which LLJs occur. It is also likely that several mechanisms, if not all of them, make simultaneous contributions to what ultimately results as a supergeostrophic, nocturnal jet, and this is indeed what most of the modeling studies cited above have found.

2.1.4 Turbulence and the LLJ

In the Blackadar theory of the LLJ, boundary layer turbulence is crucial to the formation of supergeostrophic winds and to the diurnal cycle in general. During the daytime, the vertical mixing in the convective planetary boundary layer prevents the jet from developing as momentum is mixed down to the surface and lost. Without this daytime frictional force, there can be no nocturnal oscillation since, theoretically, the amplitude of the oscillation is related to the amount the jet is retarded during the day. The stronger the daytime mixing, the greater the jet exceeds geostrophic speeds at night. However, the extent of turbulence at night is important in the Blackadar theory too. As recognized by Blackadar (1957), his model is only valid where there is insignificant nocturnal mixing. He hypothesized that the LLJ rides above a layer of statically stable, but still somewhat turbulent air (due to vertical wind shear). In the Blackadar theory, the LLJ itself must quickly become turbulence-free after nightfall, otherwise turbulent dissipation will rob the jet of inertia and diffuse away the wind shear. Since the core of the LLJ has only marginal static stability, the spread of turbulence from the vertically sheared winds above and below is a significant possibility which, if it occurred, would weaken the importance of the Blackadar model. Fluids with free shear layers in general and free jets in particular are almost always highly turbulent (e.g., Tennekes and Lumley, 1972), so it is not all obvious that the LLJ ought to be laminar.

Free jets tend to be turbulent due to the lack of nearby boundaries to stabilize the flow. Atmospheric flows have vertical stratifications of buoyancy which can enhance or suppress hydrodynamic instability (and consequent turbulence) by affecting vertical motions. A non-dimensional parameter called the "gradient Richardson number" or Ri, balances the effect of shear and stratification. It can be defined as (Turner, 1973, p. 12):

$$Ri = \frac{-g\frac{\partial \rho}{\partial Z}}{\rho\left(\frac{\partial u}{\partial Z}\right)^2}$$

where ρ is the air density and $\partial u/\partial Z$ is the magnitude of the vertical wind shear. Ri thus represents the ratio of buoyant to shear forces. As defined, small values of Ri are more likely to be turbulent. Theoretical considerations and experiments imply a critical Ri of 0.25, below which turbulence is expected (i.e., flow is hydrodynamically unstable for Ri$<$.25). Mahrt et al. (1979) reported measurements from the Wangara experiment and from experiments in Colorado and Nebraska of the nocturnal atmospheric boundary layer. They produced averaged profiles of wind speed and Ri for cases with weak LLJs and found strong maxima in Ri (of the order of 1 to 2) in the jet cores while being less than .25 below the jet core in the shear layer. This is reasonable because the center of the jet itself has little wind shear and is typically located in an inversion.

Some data have been published about nocturnal turbulence in the LLJ. Kaimal and Izumi (1965) obtained turbulence measurements for a nocturnal LLJ from an instrumented tall tower in Texas. Their data shows turbulence developing at the level of maximum shear just above the inversion and below the jet maximum. This turbulence then spread throughout the jet and lasted for several hours. During this time, the jet continued to develop and did not appear to be altered by the turbulence, even though, according to the Blackadar theory, it should have been. Since only one jet was reported in this study, it is not clear how typical this behavior is. Parish et al. (1988) reported turbulence measurements from an airborne sensor in another LLJ case. They also found a substantial increase in turbulence at about 0230 LST which involved most of the jet below the jet peak and which did not appear to hinder the development of the jet. These researchers attributed this increase in turbulence to vertical shear. It is particularly interesting that while Parish et al. documented a several orders of magnitude decrease in turbulence from daytime values in the region above the jet, the half of the jet below 940 mb became almost as turbulent at 0230 LT as it was during during the day. Their measurements are also curious in that while the amount of vertical shear was about the same in the upper jet half as the lower, the upper jet half had insignificant turbulence even though the static stability was less there. In contrast, Lenschow et al. (1988), reported aircraft measurements for two LLJs which showed very little turbulence in the jet core. In addition, Frisch et al. (1992) reported turbulence measurements in an LLJ obtained with Doppler radar. They found that turbulence (measured as the variance in the vertical velocity) diminished by an order of magnitude at all levels at night relative to daytime values, with some increase in turbulence late at night in the shear layer below the jet core. However, recent preliminary measurements using aircraft penetrations on two jets reported by Clark and McDermott (1997) indicated that the level of turbulence in the two jets differed by an order of magnitude, with the more highly sheared jet having more turbulence; and that, for the more intense case, the turbulence could be as important to dynamical forcing as other terms in the momentum equation. It appears from these measurements that turbulence may be more important in some LLJs than others. If a threshold of vertical shear (or some other parameter) exists above which turbulence is triggered, then the impact would be highly non-linear. In any case, not enough measurements or analyses are available to clearly define the role of turbulence in the LLJ.

2.2 Development of Governing Equations and Turbulence Parameters

2.2.1 Basic Equations

Using the Boussinesq approximations (namely $\nabla \cdot \vec{u} \approx 0$ and $1+\frac{\rho}{\rho_0} \approx 1$, with ρ a deviation density from a constant background density, ρ_0) and ignoring molecular viscosity, the general equations of motion are (e.g. Arya, 1988, p. 123) for wind vector $\vec{u}$ =(U,V,W):

$$\nabla \cdot \vec{u} = 0 \tag{2.1}$$

Which expresses mass conservation, and:

$$\begin{aligned} \frac{dU}{dt} &= fV - \frac{1}{\rho_0}\frac{\partial P}{\partial x} \\ \frac{dV}{dt} &= -fU - \frac{1}{\rho_0}\frac{\partial P}{\partial y} \\ \frac{dW}{dt} &= -g\frac{\rho}{\rho_0} - \frac{1}{\rho_0}\frac{\partial P}{\partial z} \end{aligned} \tag{2.2}$$

Which express Newton's second law. The parameter f is the Coriolis parameter and g is the gravitational constant. For these equations, P and ρ are deviations from the hydrostatic background values, P_0 and ρ_0. The background states is generally a function of z.

To arrive at equations for mean momentum in the presence of turbulence, we apply Reynolds averaging. We use the decomposition:

$$\begin{aligned} U &= u + u' \\ V &= v + v' \end{aligned}$$

$$
\begin{aligned}
W &= w + w' \\
P &= p + p' \\
\rho &= \overline{\rho} + \rho'
\end{aligned} \tag{2.3}
$$

where $\overline{\rho}$, p, u, v, w are averages and ρ', p$'$, u$'$, v$'$, w$'$ are deviations from the average (which have time averages equal to zero). Strictly speaking, these are ensemble averages over a large number of independent but nominally identical flow realizations. However, if the flow is statistically stationary for some time interval, Δt (i.e., $\frac{dU}{dt}\frac{U}{\Delta t} << 1$), then time averages can be used. The interchangeability of ensemble and dynamical averages is known as the ergodic hypothesis.

Using the decomposition (2.3) in (2.2), averaging the equations, applying rules for averages, and using $\nabla \cdot \overrightarrow{u'} = 0$, gives the following for $\overline{\frac{dU}{dt}}$:

$$
\begin{aligned}
\overline{\frac{dU}{dt}} = \overline{\frac{du}{dt}} + \overline{\frac{du'}{dt}} &= \overline{\frac{\partial u}{\partial t}} + \overline{(u+u')\frac{\partial u}{\partial x}} + \overline{(v+v')\frac{\partial u}{\partial y}} + \overline{(w+w')\frac{\partial u}{\partial z}} \\
&\quad + \overline{\frac{\partial u'}{\partial t}} + \overline{(u+u')\frac{\partial u'}{\partial x}} + \overline{(v+v')\frac{\partial u'}{\partial y}} + \overline{(w+w')\frac{\partial u'}{\partial z}} \\
&= \frac{\partial u}{\partial t} + \overline{u\frac{\partial u}{\partial x}} + \overline{v\frac{\partial u}{\partial y}} + \overline{w\frac{\partial u}{\partial z}} + \overline{u'\frac{\partial u}{\partial x}} + \overline{v'\frac{\partial u}{\partial y}} + \overline{w'\frac{\partial u}{\partial z}} \\
&\quad + \overline{u\frac{\partial u'}{\partial x}} + \overline{v\frac{\partial u'}{\partial y}} + \overline{w\frac{\partial u'}{\partial z}} + \overline{u'\frac{\partial u'}{\partial x}} + \overline{v'\frac{\partial u'}{\partial y}} + \overline{w'\frac{\partial u'}{\partial z}} \\
&= \frac{du}{dt} + \overline{u'\frac{\partial u'}{\partial x}} + \overline{v'\frac{\partial u'}{\partial y}} + \overline{w'\frac{\partial u'}{\partial z}} \\
&= \frac{du}{dt} + \overline{\frac{\partial(u'u')}{\partial x}} + \overline{\frac{\partial(u'v')}{\partial y}} + \overline{\frac{\partial(w'u')}{\partial z}} - \left[\overline{u'\frac{\partial w'}{\partial z}} + \overline{u'\frac{\partial v'}{\partial y}} + \overline{u'\frac{\partial u'}{\partial x}}\right] \\
&= \frac{du}{dt} + \frac{\partial}{\partial x}\overline{u'u'} + \frac{\partial}{\partial y}\overline{u'v'} + \frac{\partial}{\partial z}\overline{w'u'} - \left[u'\nabla \cdot \overrightarrow{u'} = 0\right]
\end{aligned}
$$

with similar expressions for $\overline{\frac{dV}{dt}}$ and $\overline{\frac{dW}{dt}}$. Equating with the average of (2.2) gives equations for the average wind acceleration components:

$$
\frac{du}{dt} = fv - \frac{1}{\rho_0}\frac{\partial p}{\partial x} - \frac{\partial}{\partial x}\overline{u'u'} - \frac{\partial}{\partial y}\overline{u'v'} - \frac{\partial}{\partial z}\overline{u'w'}
$$

$$
\begin{aligned}
\frac{dv}{dt} &= -fu - \frac{1}{\rho_0}\frac{\partial p}{\partial y} - \frac{\partial}{\partial x}\overline{u'v'} - \frac{\partial}{\partial y}\overline{v'v'} - \frac{\partial}{\partial z}\overline{v'w'} \\
\frac{dw}{dt} &= -g\frac{\overline{\rho}}{\rho_0} - \frac{1}{\rho_0}\frac{\partial p}{\partial z} - \frac{\partial}{\partial x}\overline{w'u'} - \frac{\partial}{\partial y}\overline{w'v'} - \frac{\partial}{\partial z}\overline{w'w'} \qquad (2.4)
\end{aligned}
$$

The correlation terms ($\overline{u'u'}$, $\overline{u'v'}$, $\overline{u'w'}$, $\overline{v'v'}$, $\overline{v'w'}$, $\overline{w'w'}$) have the physical effect of shear stress, similar mathematically to molecular viscous stress, τ . Shear stress due to viscosity, from the constitutive relation for a Newtonian fluid with constant kinematic viscosity, ν, is:

$$
\frac{\tau_{xy}}{\rho} = \nu\left(\frac{\partial u}{\partial y} + \frac{\partial v}{\partial x}\right)
$$

We can hypothesize a constant turbulent kinematic viscosity (or eddy viscosity), K, as first done by Boussinesq in 1877, and model:

$$
\begin{aligned}
-\overline{u'v'} &= K\left(\frac{\partial u}{\partial y} + \frac{\partial v}{\partial x}\right) \\
-\overline{u'w'} &= K\left(\frac{\partial u}{\partial z} + \frac{\partial w}{\partial x}\right) \\
-\overline{v'w'} &= K\left(\frac{\partial v}{\partial z} + \frac{\partial w}{\partial y}\right) \\
-\overline{w'w'} &= 2K\left(\frac{\partial w}{\partial z}\right) \\
-\overline{u'u'} &= 2K\left(\frac{\partial u}{\partial x}\right) \\
-\overline{v'v'} &= 2K\left(\frac{\partial v}{\partial y}\right)
\end{aligned}
$$

Physically, the correlation terms, for example $\frac{\partial}{\partial z}(\overline{u'w'})$, are expected to be non-zero and to transport momentum in a manner somewhat analogous to molecular perturbations (Tennekes and Lumley, 1972, pp 34-50). A fluid perturbation moving at w$'$ up or down will acquire u$'$ if $\frac{\partial u}{\partial z}$ is non-zero, as w$'$ transports x-momentum upward or downward. This transported x-momentum creates some u$'$. If a mixing parcel is being moved by w$'$ for a characteristic time, t, then an estimate of the parcel's change in u is:

$$
\Delta u' = -w't\frac{\partial u}{\partial z} \qquad (2.5)
$$

which suggests a correlation will exist in observed u$'$ and w$'$ for a flow with shear. Equivalently, $w't$ can be replaced by a characteristic length scale, l, analogous to the mean-free-path of molecular motions. This also, once again, suggests modeling turbulence by analogy with molecular viscosity which transports momentum by the same correlation mechanism. If (2.5) were exactly true, with $u' \sim \Delta u'$:

$$\begin{aligned}\frac{\partial}{\partial z}(\overline{u'w'}) &= -\frac{\partial}{\partial z}(\overline{w'^2 t \frac{\partial u}{\partial z}}) \\ &= -\frac{\partial}{\partial z}(\overline{w'^2 t}\frac{\partial u}{\partial z}) = -\frac{\partial}{\partial z}(\overline{w'l}\frac{\partial u}{\partial z})\end{aligned}$$

Which suggests modeling K in terms of characteristic velocity, time, and length scales as:

$$K \propto w'^2 t = w'l = \frac{l^2}{t}$$

Expressing K in terms of any two of the three characteristic scales w', l, and t; is again analogous to requiring any two of the three physical properties of pressure, temperature, and density in order to determine molecular viscosity. From the standpoint of making measurements of turbulence (as in Ch. 4), the velocity scale, w', is the easiest to measure directly and may be the only one available (by way of measurements of the turbulent kinetic energy). Since K is what matters in the equations of motion, w' is not by itself sufficient to characterize the effect of the turbulence. Either a length or time scale are additionally needed. However, in the mixing layer theory of Prandtl (1925), it is assumed that the velocity scale can be related to the length scale and the mean shear:

$$w' = l\,|\nabla \vec{u}| \tag{2.6}$$

Where $\vec{u}$ =(u,v,w) and l is known as the mixing length. This assumption does not follow by analogy with molecular viscosity where it would be invalid because the characteristic velocity perturbation of molecules is related to the temperature and is completely unrelated to the bulk shear. If this assumption is made for turbulence where one can argue that turbulent velocities are related to the shear, then K can be estimated in terms of a single characteristic scale as:

$$K \propto \frac{w'^2}{|\nabla \vec{u}|} \tag{2.7}$$

which is entirely in terms of quantities that can be directly measured with a Doppler radar. This equation will be used for deducing K from radar data in Sec. 4.7.4.

The assumption of (2.6) is probably reasonably good during nighttime conditions when the turbulence is generated mostly by shear. In this case, $w' \sim l\frac{du}{dz}$. However, during daytime conditions, turbulence is generated largely by buoyancy. In this case, velocity perturbations are caused in large part by buoyancy and not shear, so that (2.6) and (2.7) would not be expected to be valid as w' would be due to both buoyancy and the existing shear that was being mixed . Even during nighttime conditions, regions of stable stratification could make (2.6) invalid due to suppression of vertical motion from positive static stability. However, the error is certainly less than an order of magnitude, and possibly within a factor of 2. Nonetheless, K values calculated by applying (2.7) should be viewed with some skepticism.

There are many theoretical short comings of the turbulent viscosity and mixing length concepts due to differences between molecular and eddy dynamics. For example, in simple plane Poiseuille flow, the laminar solution is a parabolic profile. The solution using a uniform turbulent viscosity is also a parabolic profile using a constant K, while the problem is unsolvable using (2.7); but observations of turbulent and laminar Poiseuille flow reveal that while the laminar solution is correct, actual turbulent profiles are quite different, having a much flatter profile in the core of the flow. Mixing length theory can be made to work in the case of Poiseuille only if the mixing length can be empirically related to distance from the solid boundary (for example, White, 1974, p. 469-70). The concepts of eddy viscosity and mixing length are at least dimensionally correct and are prevalent due to the lack of superior alternatives.

2.2.2 f-Plane Analysis of LLJ Dynamics

The purpose of this section is primarily to provide a description of how energy can build-up in the LLJ due to the action of turbulence, a phenomena suggested by the Blackadar

(1957) theory. This is at first glance paradoxical as turbulence ordinarily subtracts energy from systems.

For a non-convective (w=0) and approximately horizontally homogeneous boundary layer of air: (2.4) reduce to f-plane equations (which assumes f has no latitudinal variation):

$$\begin{aligned}
\frac{du}{dt} &= fv - \frac{1}{\rho_0}\frac{\partial p}{\partial x} - \frac{\partial}{\partial z}\overline{u'w'} && (2.8)\\
\frac{dv}{dt} &= -fu - \frac{1}{\rho_0}\frac{\partial p}{\partial y} - \frac{\partial}{\partial z}\overline{v'w'} && (2.9)\\
0 &= -\frac{\overline{\rho}}{\rho_0}g - \frac{1}{\rho_0}\frac{\partial p}{\partial z} - \frac{\partial}{\partial z}\overline{w'w'}
\end{aligned}$$

With the turbulent viscosity model, these become:

$$\begin{aligned}
\frac{du}{dt} &= fv - \frac{1}{\rho_0}\frac{\partial p}{\partial x} - \frac{\partial}{\partial z}K\frac{\partial u}{\partial z}\\
\frac{dv}{dt} &= -fv - \frac{1}{\rho_0}\frac{\partial p}{\partial y} - \frac{\partial}{\partial z}K\frac{\partial v}{\partial z}\\
0 &= -\frac{\overline{\rho}}{\rho_0}g - \frac{1}{\rho_0}\frac{\partial p}{\partial z} - [\frac{\partial}{\partial z}K\frac{\partial w}{\partial z} = 0]
\end{aligned} \qquad (2.10)$$

We note that the vertical equation reduces to the hydrostatic relation. Also:

$$K = K(z,t) = \frac{\overline{-u'w'}}{\frac{\partial u}{\partial z}} = \frac{\overline{-v'w'}}{\frac{\partial v}{\partial z}}$$

For geostrophic balance with no turbulence, $\frac{du}{dt} = \frac{dv}{dt}$ =0 and the geostrophic wind is:

$$v_g = \frac{1}{\rho_0 f}\frac{\partial p}{\partial x} \qquad u_g = -\frac{1}{\rho_0 f}\frac{\partial p}{\partial y} \qquad (2.11)$$

For analyzing the LLJ, it is convenient to restate (2.8) and (2.9) in terms of the geostrophic and ageostrophic wind components:

$$u = u_a + u_g \qquad v = v_a + v_g$$

With an approximately constant pressure gradient, $\frac{du_g}{dt} = \frac{dv_g}{dt} = 0$ and (2.8) and (2.9) $\Rightarrow$

$$\begin{aligned}\frac{du_a}{dt} &= fv_a - \frac{\partial}{\partial z}(\overline{u'w'}) \\ \frac{dv_a}{dt} &= -fu_a - \frac{\partial}{\partial z}(\overline{v'w'})\end{aligned} \tag{2.12}$$

Ignoring any variation in the geostrophic wind, allows these equations to only represent the Blackadar inertial oscillation theory of the LLJ and, in particular, can not capture the Holton theory involving heating and cooling of terrain (which impact the geostrophic wind through the hydrostatic pressure gradient fluctuation). A constant geostrophic wind essentially implies a balance between the ageostrophic wind and the acceleration of the ageostrophic wind. Blackadar (1957) originally solved these for no turbulence, getting:

$$\begin{aligned}u_a &= u_{a0}cos(ft) + v_{a0}sin(ft) \\ v_a &= -u_{a0}sin(ft) + v_{a0}cos(ft)\end{aligned} \tag{2.13}$$

Where u_{a0} and v_{a0} are initial values. The amplitude of the solution wind is:

$$\sqrt{u_a^2 + v_a^2} = \sqrt{u_{a0}^2 + v_{a0}^2} = const.$$

The angle of the ageostrophic wind, θ, can be found from $tan(\theta) = v_a/u_a$ and is found using (2.13) and trigonometric reduction to be $\theta = \theta_0 - ft$ (where $tan(\theta_0) = v_{a0}/u_{a0}$) implying clockwise rotation. (2.13) describes the classic inertial oscillation from the Coriolis force in which the ageostrophic wind vector perpetually rotates around a circle with a constant amplitude. See Fig. 2.1 for a hodograph of this oscillation.

The total kinetic energy per unit mass, KE is:

$$KE = \frac{1}{2}(\vec{u_a} + \vec{u_g}) \cdot (\vec{u_a} + \vec{u_g}) = \frac{1}{2}(u^2 + v^2)$$

To get an equation for KE, we multiply (2.8) by u and (2.9) by v and add:

$$\frac{1}{2}\frac{du^2}{dt^2} = fuv - \frac{u}{\rho_0}\frac{\partial p}{\partial x} - u\frac{\partial}{\partial z}\overline{u'w'}$$

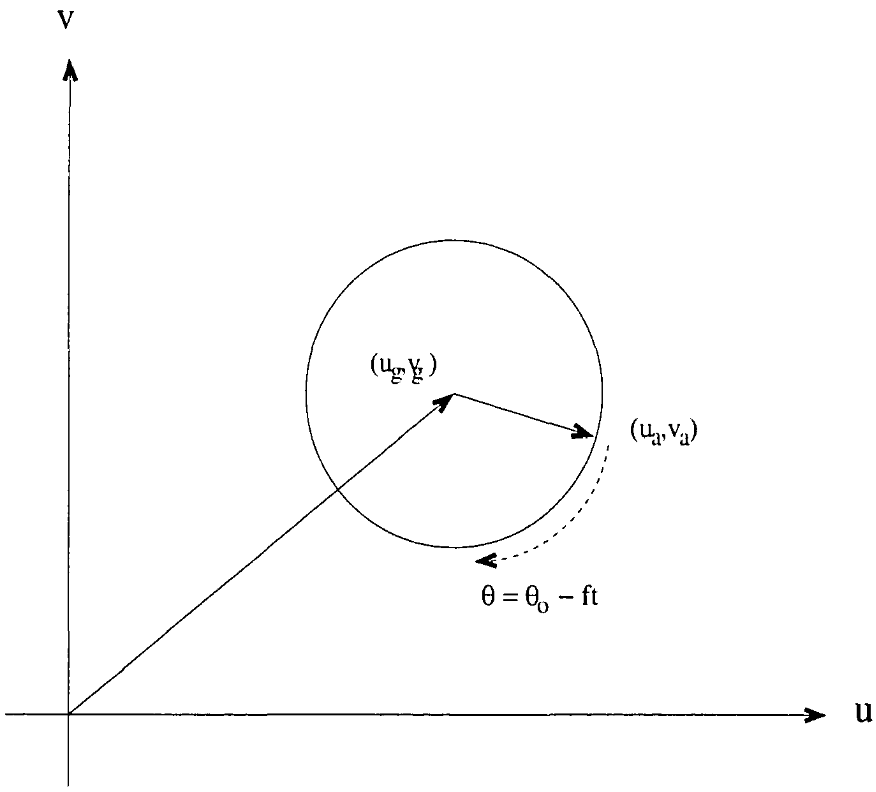

Figure 2.1: Diagram of hodograph of inertial oscillation. Figure shows fixed geostrophic wind vector (u_g,v_g) and ageostrophic wind vector (u_a,v_a) which rotates clockwise.

$$\frac{1}{2}\frac{dv^2}{dt^2} = -fuv - \frac{v}{\rho_0}\frac{\partial p}{\partial y} - v\frac{\partial}{\partial z}\overline{v'w'}$$

$$\Rightarrow \frac{d}{dt}(KE) = -\frac{u}{\rho_0}\frac{\partial p}{\partial x} - \frac{v}{\rho_0}\frac{\partial p}{\partial y} - u\frac{\partial}{\partial z}\overline{u'w'} - v\frac{\partial}{\partial z}\overline{v'w'} \tag{2.14}$$

The Coriolis terms drop out, as they should since the Coriolis force acts perpendicular to motion and, hence, does no work. However, the Coriolis force does ultimately affect KE as it affects u and v, which are involved in (2.14). Neglecting the turbulence terms (as might be appropriate under nocturnal conditions), and expressing the pressure gradient in terms of the geostrophic wind, (2.14) $\Rightarrow$

$$\frac{d}{dt}(KE) = -\frac{u}{\rho_0}\frac{\partial p}{\partial x} - \frac{v}{\rho_0}\frac{\partial p}{\partial y} = f(vu_g - uv_g) \tag{2.15}$$

$$= -\frac{1}{\rho_0}\vec{u} \cdot \vec{\nabla p} \tag{2.16}$$

If the flow is geostrophic, $u=u_g$ and $v=v_g$ and $\frac{d(KE)}{dt}=0$.

In terms of geostrophic and ageostrophic winds:

$$KE = \frac{1}{2}(\vec{u_a} + \vec{u_g}) \cdot (\vec{u_a} + \vec{u_g}) = \frac{1}{2}\vec{u_a} \cdot \vec{u_a} + \frac{1}{2}\vec{u_g} \cdot \vec{u_g} + \vec{u_a} \cdot \vec{u_g} \neq KE_a + KE_g \tag{2.17}$$

where $KE_a = \frac{1}{2}\vec{u_a} \cdot \vec{u_a}$ and $KE_g = \frac{1}{2}\vec{u_g} \cdot \vec{u_g}$. In the case of a constant geostrophic wind and no turbulence, we know that only the term $\vec{u_a} \cdot \vec{u_g}$ oscillates (e.g., Fig. 2.1), so:

$$KE = KE_a + KE_g + oscillation \tag{2.18}$$

Since the time average of the oscillating term is 0:

$$\overline{KE} = \overline{KE_a} + \overline{KE_g} \tag{2.19}$$

As we wish to consider the situation of a constant geostrophic wind, changes in $\overline{KE}$ will be related only to changes in $\overline{KE_a}$. It is therefore useful to examine the equation for KE_a, from (2.12):

$$\frac{d}{dt}(KE_a) = -u_a\frac{\partial}{\partial z}(\overline{u'w'}) - v_a\frac{\partial}{\partial z}(\overline{v'w'}) \tag{2.20}$$

It is clear that only turbulence can alter KE_a. KE_a is the KE that would be measured in a reference frame moving at $\vec{u_g}$. For $\vec{u_g}$ = const., this inertial frame of reference is as valid as any for describing energetics and is simpler for this situation as the constant energy from the geostrophic wind does not appear. (2.20) is valid even if $\vec{u_g} \neq$ const, though the geostrophic reference frame is no longer inertial, and interpretation of KE_a would be more complicated.

To facilitate further analysis, an attempt will be made to model the turbulent transport/diffusion terms by viscous damping terms:

$$\begin{aligned} \frac{\partial}{\partial z}\overline{u'w'} = c(t)u &= -\frac{\partial}{\partial z}K\frac{\partial u}{\partial z} \\ \frac{\partial}{\partial z}\overline{v'w'} = c(t)v &= -\frac{\partial}{\partial z}K\frac{\partial v}{\partial z} \end{aligned} \tag{2.21}$$

Where c(t) is some positive definite function of time. Doing this makes the 1-D equations (2.8) and (2.9) 0-D, by eliminating the z-dependence. This is justifiable physically as one way to model turbulent stress in a bulk expression is as a damping coefficient proportional to speed (i.e., viscous damping). Damping proportional to speed is a crude, but potentially effective, way to model turbulent dissipation. In numerical fluid dynamical methods, viscous damping is used (where it is known as "Rayleigh damping") in some areas of the model domain to dampen unwanted flow. Mathematically, this can be partially justified by considering the turbulent viscosity term:

$$\frac{\partial}{\partial z}\left[K(z,t)\frac{\partial u(z,t)}{\partial z}\right] \tag{2.22}$$

If K is replaced by a layer average, (2.22) =

$$\overline{K}(t)\frac{\partial^2 u(z,t)}{\partial z^2} \tag{2.23}$$

If u can be expanded in z approximately as a cosine function of wave number l with an arbitrary, but separable, temporal dependence function, f(t), as:

$$\begin{aligned} u(z,t) &= cos(lz)f(t) \\ &\quad then \\ \frac{\partial u}{\partial z} &= -lsin(lz)f(t) \\ \frac{\partial^2 u}{\partial z^2} &= -l^2cos(lz)f(t) = -l^2u(z,t) \end{aligned}$$

and

$$\frac{\partial}{\partial z}\overline{u'w'} = -\frac{\partial}{\partial z}K\frac{\partial u}{\partial z} = l^2\overline{K}(t)u(z,t) = c(t)u$$

The use of a frictional term proportional to wind speed and in the opposite direction was first done by Guldberg and Mohn in 1876 (reviewed by Kutzbach, 1979, p. 101-110). Viscous damping of the surface layer is sometimes referred to as the "Guldberg-Mohn hypothesis" (Lewis, 1997).

The question arises as to the usage of the ground-relative $\vec{u}$ in (2.21), since $\overline{u'w'}$ is independent of the choice of inertial reference frame while $\vec{u}$ is reference frame dependent. $\vec{u}$ is appropriate here, instead of, say, $\vec{u_a}$ or $\vec{u_g}$, because it is the velocity relative to the ground that gives rise to turbulence. In other words, when $\vec{u}$ is zero, there will be no turbulence, which (2.21) correctly models.

With (2.21), (2.20) becomes:

$$\begin{aligned} \frac{d}{dt}(KE_a) &= -u_a cu - v_a cv = -c(\vec{u_a} \cdot \vec{u}) \\ &= -c(\vec{u_a} \cdot (\vec{u_a} + \vec{u_g})) = -c(2KE_a + \vec{u_a} \cdot \vec{u_g}) \\ &= -2cKE_a - c\vec{u_a} \cdot \vec{u_g} \end{aligned} \tag{2.24}$$

In (2.24), the term -2cKE$_a$ is always negative and the term c $\vec{u_a} \cdot \vec{u_g}$ can be positive or negative. (2.12) becomes:

$$\frac{du_a}{dt} = fv_a - cu \tag{2.25}$$

$$\frac{dv_a}{dt} = -fu_a - cv \tag{2.26}$$

(2.25) and (2.26) are zero-dimensional and describe the behavior of an air parcel subject to the Coriolis force, a constant pressure gradient (which does not appear, having been removed with the geostrophic wind), and turbulent damping. There are no spatial gradients to the velocity components. Pressure, of course, has a spatial gradient, but this gradient is a constant in the equations, and since pressure is not solved for, there are no relevant spatial gradients.

To understand how the inertial oscillation arises as the result of friction, we consider a situation initially in geostrophic balance, $\vec{u_a} = 0$. By (2.24), $\frac{d}{dt}(\mathrm{KE}_a)$ =0. However, by (2.25) and (2.26):

$$\begin{aligned}\frac{du_a}{dt} &= -cu_g \\ \frac{dv_a}{dt} &= -cv_g\end{aligned} \tag{2.27}$$

(2.27) show the transport of momentum from the ground to the air parcel due to friction at the ground. This occurs since, in this reference frame, the ground is moving by an amount of -$\vec{u_g}$.

After a short time, Δt,

$$u_a = -cu_g\Delta t \qquad v_a = -cv_g\Delta t \tag{2.28}$$

$$but\ \vec{u} \approx \vec{u_g} \tag{2.29}$$

so from (2.24), KE$_a$ then develops according to:

$$\begin{aligned}\frac{d}{dt}KE_a &= c^2u_gu_g\Delta t + c^2v_gv_g\Delta t \\ &= c^2(\vec{u_g}\cdot\vec{u_g})\Delta t\end{aligned}$$

And KE$_a$ will be created initially due to the action of turbulence making the flow ageostrophic.

The second term in (2.24), -c$\vec{u_a} \cdot \vec{u_g}$, can be positive or negative depending on the orientation of $\vec{u_a}$ relative to $\vec{u_g}$, while the first term, -2cKE$_a$ is always negative, and, therefore, always subtracts energy. It is clearly only the second term that can add energy to the system. For this to happen, we need:

$$\vec{u_a} \cdot \vec{u_g} < 0 \qquad with\ \vec{u_a} \cdot \vec{u_g} = |\vec{u_a}|\,|\vec{u_g}|\,cos\theta$$

which occurs when the angle between $\vec{u_a}$ and $\vec{u_g}$, θ, is:

$$90^\circ < \theta < 270^\circ \tag{2.30}$$

For KE_a to grow, we also must have, from (2.24):

$$(2KE_a + \vec{u_a} \cdot \vec{u_g}) < 0$$

or

$$-\vec{u_a} \cdot \vec{u_g} > \vec{u_a} \cdot \vec{u_a} \tag{2.31}$$

or

$$-\,|\vec{u_a}|\,|\vec{u_g}|\,cos\theta > |\vec{u_a}|^2 \quad or \quad |\vec{u_a}| < -\,|\vec{u_g}|\,cos\theta$$

This gives a maximum possible amplitude to the ageostrophic wind. In order for (2.31) to be satisfied, we must have $|\vec{u_a}| < |\vec{u_g}|$ or $|\vec{u_a}|_{max} = |\vec{u_g}|$, and $|\vec{u}|_{max} = 2|\vec{u_g}|$.

According to the inertial oscillation theory, c(t) is large during the day giving rise to $\vec{u_a}$. After sunset, c(t) is much smaller. If it is zero at night, then from (2.24):

$$\frac{d}{dt}(KE_a) = 0$$

and from (2.25) and (2.26):

$$\frac{du_a}{dt} = fv_a \qquad \frac{dv_a}{dt} = -fu_a$$

And the ageostrophic wind vector rotates according to (2.13), and total KE will increase by way of the oscillating term in (2.18). KE_a will increase during the day only if $\vec{u_a} \cdot \vec{u_g} < 0$

and $|\vec{u_a}| < -|\vec{u_g}|\,cos\theta$.

If the turbulent damping, c, is large, then one might suspect a steady-state solution might exist despite that fact that (2.8) and (2.9) are known to have oscillating solutions (such as the inertial oscillation). This is because, with sufficient damping, the Coriolis force should be overwhelmed and $\vec{u_a}$ ought to approach -$\vec{u_g}$ (which is constant) according to (2.25) and (2.26) with c/f large. Seeking a steady-state solution to (2.25) and (2.26), we start with:

$$\begin{aligned} c(u_a + u_g) &= f v_a \\ c(v_a + v_g) &= -f u_a \end{aligned}$$

Solving these for u_a and v_a gives:

$$\begin{aligned} u_a &= \frac{\frac{-c^2}{f^2} u_g - \frac{c}{f} v_g}{1 + \frac{c^2}{f^2}} \\ v_a &= \frac{\frac{c}{f} u_g - \frac{c^2}{f^2} v_g}{1 + \frac{c^2}{f^2}} \end{aligned}$$

The squared amplitude and direction, θ, of the ageostrophic wind are then:

$$u_a^2 + v_a^2 = \frac{u_g^2 + v_g^2}{1 + \frac{f^2}{c^2}}$$

and

$$tan(\theta) = \frac{v_a}{u_a} = \frac{u_g - \frac{c}{f} v_g}{-\frac{c}{f} u_g - v_g} \qquad (2.32)$$

For c/f large, these equations imply that $\vec{u_a} = -\vec{u_g}$. For c=f, $|\vec{u_a}| = \frac{1}{\sqrt{2}} |\vec{u_g}|$ with $\vec{u_a}$ at a 135° angle from $\vec{u_g}$. However, these results would only be reasonable for large c/f. During daytime conditions of intense surface heating, they might have some validity, but their value here is mostly conceptual, allowing the understanding of what happens during daytime conditions in a zeroth order sense.

The developments in this section lead to the following conceptual picture of the LLJ oscillation and how energy can build-up in it due to the action of turbulence:

1. If you begin at point A of the hodograph of Figure 2.2 with an air parcel in geostrophic balance ($\vec{u_a} = 0$) at some time during the day, this parcel will initially acquire ageostrophic wind $\Delta\vec{u_a} = -c\Delta t\vec{u_g}$ due to turbulent transport with the ground, according to (2.27). The Coriolis force and the pressure gradient do not act initially, as the flow is in approximate geostrophic balance. KE_a increases while KE_g is constant. However, Total KE decreases due to the negative sign of the oscillating term in (2.18). This obviously must be the case as damping subtracts energy from the system, and it is the only force active initially. In the reference frame of the geostrophic wind, KE (=KE_a) increases due to the action of turbulence as the ground is moving at -$\vec{u_g}$ and some of this momentum is transferred to the air. In the ground-relative reference frame, KE decreases due to turbulence.

2. After some time, significant ageostrophic wind develops and the ageostrophic wind vector will tend to rotate clockwise due to the constant pressure gradient. Turbulence will continue to increase KE_a only if the amplitude of the ageostrophic wind is less than the geostrophic wind and if the angle, θ, between the geostrophic wind and the ageostrophic wind is between 90° and 270° (visually, if $\vec{u_a}$ points to the left of the 90° - 270° line indicated in Fig. 2.2). Total KE is decreased by the action of turbulence and can oscillate due to the pressure gradient, following (2.14). Following (2.20), KE_a can increase or decrease from turbulence, depending on the direction and amplitude of $\vec{u_a}$. $\vec{u_a}$ rotates clockwise due to the Coriolis force, but this does not affect KE_a.

3. At sunset, $\vec{u_a}$ is possibly at point B in Fig. 2.2. The angle between $\vec{u_a}$ and $\vec{u_g}$ at B depends to some extent on the ratio c/f (possibly similar to [2.32]). The greater the turbulence during the day, the closer $\vec{u_a}$ would be to -$\vec{u_g}$ and the more rapidly it would get there.

4. After sunset, c, the measure of turbulence, is conceived to be nearly eliminated as the boundary layer stabilizes from radiative cooling at the Earth's surface. Consequently, $\vec{u_a}$ only rotates at night, according to (2.13), by an amount that depends on f (and consequently on latitude), ending at point C at sunrise. KE_a is constant while KE

oscillates due to the action of the prevailing pressure gradient (and indirectly the Coriolis force). When θ=0, the peak in KE is reached and equals (from (2.17)) KE_g $+3\mathrm{KE}_a$.

5. After sunrise, the cycle repeats with turbulence again affecting the wind, in addition to the Coriolis force. How $\vec{u_a}$ develops on the second day depends on where point C in Fig. 2.2 is. If C is to the right of the 90°-270° line, then KE_a will initially decrease due to turbulent damping. However, if $\vec{u_a}$ begins at point C′ instead, then turbulence could immediately increase KE_a. This means that certain combinations of c(t) and f can be more effective in creating inertial oscillations and LLJs. The possibility of resonance, in which the periodicity of c(t) and the value of f are matched so that the amplitude of KE_a increases on subsequent days is explored in the following section.

When turbulence is creating KE_a, it is reducing total KE, as would be expected from a source of diffusion. Total KE eventually increases, however, because of the action of the Coriolis force which, when turbulence is weak, rotates the ageostrophic wind vector. The rotation of this wind vector towards the direction of the geostrophic wind cause the geostrophic and ageostrophic wind vectors to add constructively, and results in an increase in KE.

More precise solutions with varying functions for c(t) are explored in the next section.

2.3 Zero-Dimensional Modeling

In Blackadar's 1957 paper, he formulated a simple 0-D model of the LLJ which illustrated the basic physics of the inertial oscillation. The equations of motion for a Lagrangian parcel subject only to horizontal motion, the Coriolis force, a pressure gradient, and friction reduce to [2.10]:

$$\frac{du}{dt} = fv - \frac{1}{\rho_0}\frac{\partial p}{\partial x} - \frac{\partial}{\partial z}K\frac{\partial u}{\partial z} \tag{2.33}$$

$$\frac{du}{dt} = -fu - \frac{1}{\rho_0}\frac{\partial p}{\partial y} - \frac{\partial}{\partial z}K\frac{\partial v}{\partial z} \tag{2.34}$$

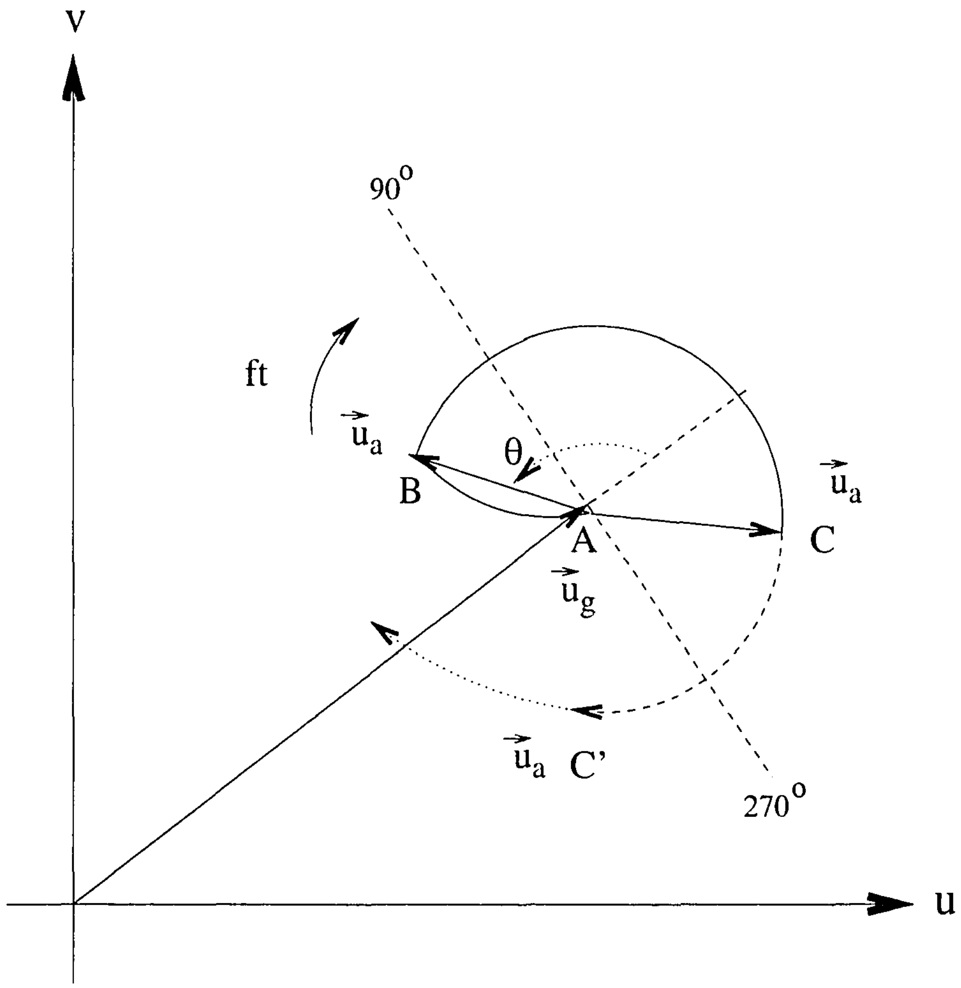

Figure 2.2: Hodograph diagram of history of ageostrophic wind under f-plane conditions with a constant pressure gradient and daytime turbulence, beginning during the day at geostrophic conditions (point A), passing through daytime subgeostrophic conditions (point B), and rotating during the night through supergeostrophic conditions to point C or C′, which may or may not be supergeostrophic.

If the turbulence term is dropped from these equations, then they describe the motion of a particle subject only to a pressure gradient and the Coriolis force. If the pressure gradient is constant in space and time, then this is a 0-dimensional system (that is, v and v vary temporally, but not in space). The solution is straight forward and was shown by Blackadar (1957) to be:

$$u_a = u_{a0} cos(ft) + v_{a0} sin(ft), \qquad v_a = v_{a0} cos(ft) - u_{a0} sin(ft)$$

Where u_a and v_a are the ageostrophic components of the wind and u_{a0} and v_{a0} are the initial ageostrophic values. This describes a circular oscillation of the motion vector in hodograph space which goes on indefinitely in the absence of friction. The amplitude of the ageostrophic amplitude is exactly equal to the magnitude of the initial ageostrophic wind. If the flow is initially in geostrophic balance, then there is no oscillation. This ageostrophic oscillation with a frequency equal to the Coriolis parameter, f, neatly shows the inertial oscillation of the Blackadar theory with the supergeostrophic amplitude at night equal to the (initial) subgeostrophic amplitude during the day.

We also obtain this solution using a Runge-Kutta integration of (2.33) and (2.34), shown in Fig. 2.3 for a latitude of 30° and in Fig. 2.4 for a latitude of 50°, both for an initial ageostrophic wind of u=0 and v=0 m/s and for a pressure gradient corresponding to a geostrophic wind of u_g= 0 and v_g=10 m/s (i.e., the winds are initially subgeostrophic by 10 m/s). Runge-Kutta integration is used later for alterations of these equations which are more difficult to integrate, here it merely provides a check that the code is working correctly. These figures illustrate that the frequency of the oscillation depends on the latitude.

Integration of (2.33) and (2.34) becomes nontrivial when turbulence (K) is included (Martin and Shapiro, 1999). In order to keep the equations 0-dimensional, it is necessary to replace the Laplacian with a viscous damping term (that is, damping which is proportional to wind speed). Here, we will take a proportionality coefficient $c(t)=r(1+\cos\omega t)$, where r is a constant:

$$\frac{dv}{dt} = -fu - \frac{1}{\rho_0}\frac{\partial p}{\partial x} - c(t)v \qquad (2.35)$$

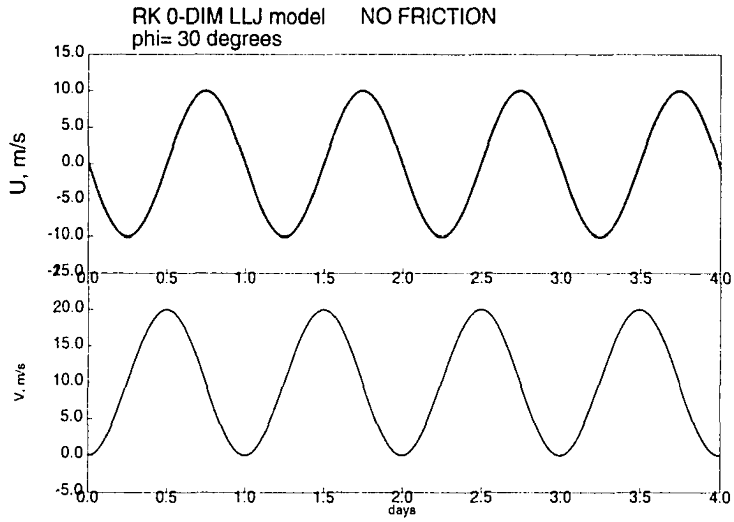

Figure 2.3: Inertial oscillation at 30°N latitude for no friction.

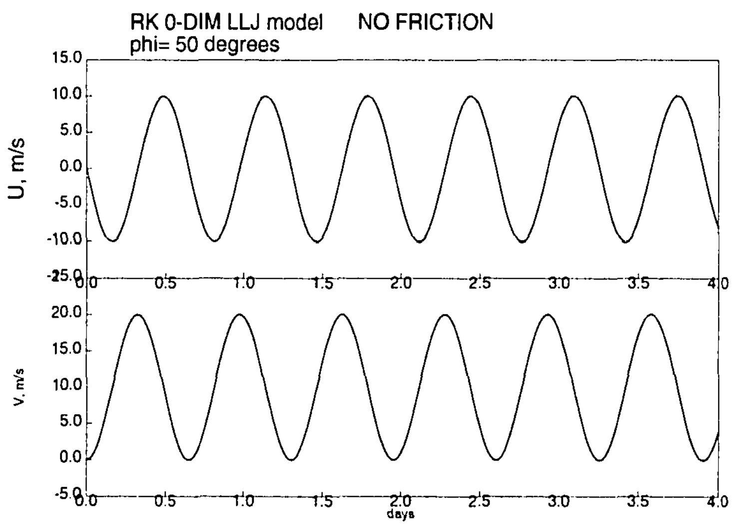

Figure 2.4: As Fig. 2.3 at 50°N latitude.

$$\frac{du}{dt} = fv - \frac{1}{\rho_0}\frac{\partial p}{\partial y} - c(t)u \tag{2.36}$$

The coefficient r in the viscous damping is unknown, but could in principle be found by comparison with multi-dimensional models. This depends on surface physics and turbulence in the PBL. Damping plays a complex role in these equations. If the flow is initially geostrophic, then with no damping, the flow will remain geostrophic; while very large damping will damp-out the inertial oscillation and any possibility of resonance. An intermediate level of damping is necessary for resonance of the inertial oscillation to manifest itself. A value of r is chosen here such that a LLJ forms with a supergeostrophic amplitude similar to that typically observed (i.e., a wind speed 40% above the geostrophic value).

An exact solution of (2.33) and (2.34) is available due to Shapiro (personal communication):

$$\begin{aligned}
v &= (v_0 cosft - u_0 sinft)e^{-\int_0^t c(\tau)d\tau} + A\int_0^t sinf(t-t')e^{\int_{t'}^t c(\tau)d\tau}dt' \\
u &= (v_0 sinft + u_0 cosft)e^{-\int_0^t c(\tau)d\tau} - A\int_0^t cosf(t-t')e^{-\int_{t'}^t c(\tau)d\tau}dt' \\
where\,A &= the\,constant\,pressure\,gradient\,force = -\frac{1}{\rho}\frac{\partial p}{\partial y},\ and\,\frac{\partial p}{\partial x} = 0
\end{aligned}$$

Using the exact solution produced results identical to the Runge-Kutta integration to within round-off error.

Equations (2.35) and (2.36) are integrated for a constant geostrophic pressure gradient corresponding to winds of u_g=0 and v_g=10 m/s as in Figs. 2.3 and 2.4. However, now we start from geostrophic balance and let the model friction generate the subgeostrophic flow. The results at 30 and 50 degrees latitude are shown in Figs. 2.5 and 2.6.

While the amplitude in Fig. 2.5 at 30°N latitude grows with each day reaching a supergeostrophic amplitude 40% above the geostrophic in 3 days, the amplitude at 50°N latitude shown in Fig. 2.6 doesn't grow and remains very close to the geostrophic value. This shows a very clear resonance effect. Since the Coriolis parameter (and the frequency of natural oscillation, f, is: $2\Omega\sin(\phi)$ where ϕ is latitude, and the frequency of diurnal forcing is Ω (i.e., 2π radians per day), resonance is expected when these two frequencies

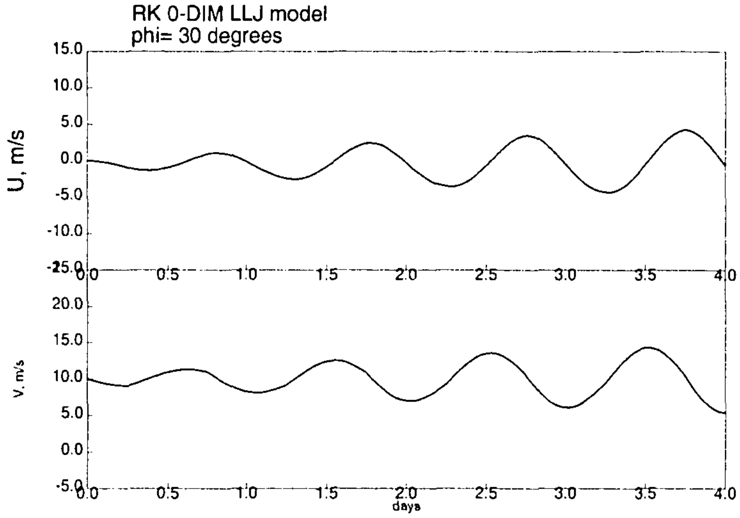

Figure 2.5: Inertial oscillation from 0-D model with friction at latitude 30°N.

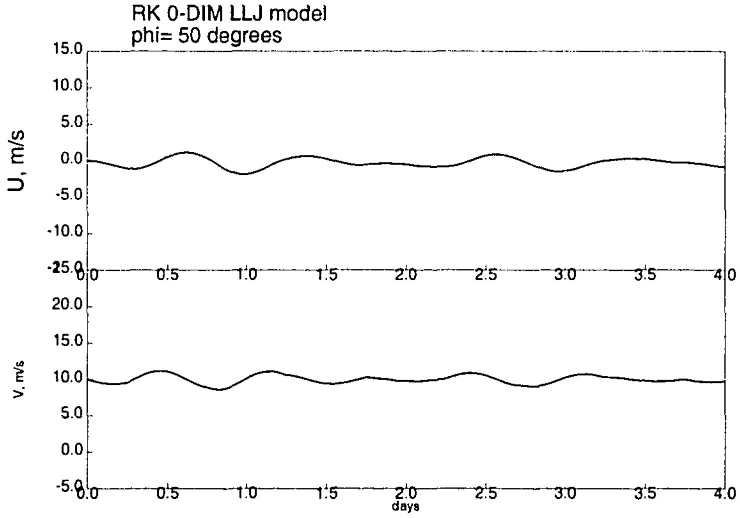

Figure 2.6: As Fig. 2.5 at 50°N latitude.

are the same, which occurs when:

$$\Omega = 2\Omega sin(\phi) \quad or \quad \phi = 30^\circ$$

With initial conditions that are ageostrophic, the evolution would be different, depending on whether the ageostrophic amplitude was in phase or out of phase with the forcing, though it is expected that the final amplitude of the oscillation, after a sufficient number of days, would be the same.

2.3.1 Resonance in 0-D model

The possibility of resonance was first suggested by Buajitti and Blackadar (1957), but has not been analyzed since and Buajitti and Blackadar did not believe it would be significant due to viscous damping. Actually, viscous damping is essential to the creation of the inertial oscillation and to resonance. If the Blackadar theory of the LLJ as an inertial oscillation is correct, the jet decouples from the boundary layer at night and damping at night will be minimal, while damping during the day is necessary to drive the oscillation.

By running the 0-D model over a range of latitudes, a resonance plot can be created, Fig. 2.7, in which the amplitude of the oscillation after a period of time (in this case 11 days) is plotted as a function of latitude. The damping coefficient is the same as Fig. 2.5, but the solution is integrated out to 11 days and the peak-to-peak amplitude of the last cycle is analyzed at each latitude. Fig. 2.8 was generated in the same way as Fig. 2.7 except the damping function was chosen to be a square wave instead of cosine wave. This more abrupt transition in forcing appears to lead to a stronger resonance peak, which is at 30 degrees in both cases, as expected theoretically. These plots suggest that resonance will be a possibly significant factor at latitudes of 25 to 40 degrees north or south. By reducing the damping, the resonance peak becomes more sharply defined, as shown in Fig. 2.9 where the damping coefficient was selected to be 1/3 that of Fig. 2.8. As damping is reduced, the oscillation takes longer to establish itself due to weaker forcing of the inertial oscillation, but the amplitude of the oscillation after a long time is more sharply defined near the theoretical maximum as the reduced damping allows more energy to accumulate in the oscillator.

2.4 One-Dimensional Modeling

As a next step towards modeling the LLJ, we now take an advanced 3-D mesoscale model (the Advanced Regional Prediction System, ARPS) with a complete suite of surface physical, radiative, and turbulent parameterizations and run it in a 1-D mode that retains all variables as a function of height (but does not allow horizontal variations). Fig. 2.10 shows the winds at 300m when all sources of friction and mixing in the model have been

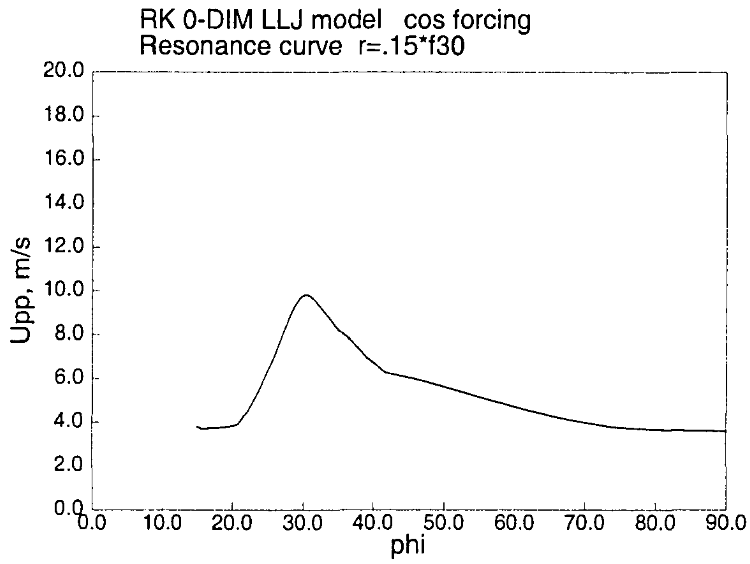

Figure 2.7: Resonance curve with cosine damping.

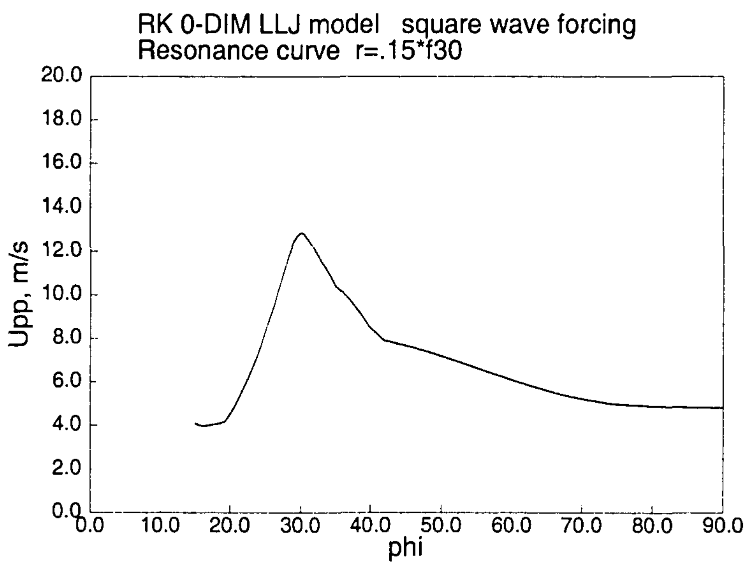

Figure 2.8: Resonance curve with square-wave damping.

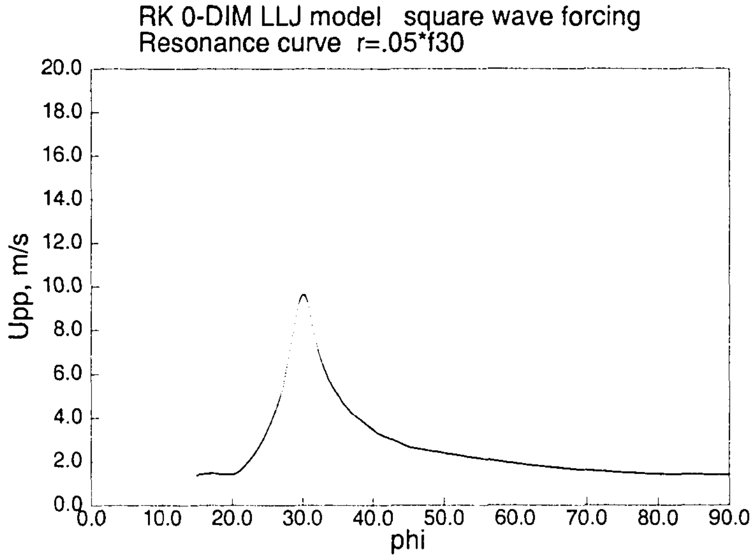

Figure 2.9: As Fig. 2.8, but with 1/3 of the damping.

turned-off, and run from the same initial conditions as Fig. 2.3. Here, with no sources of friction, the model behaves just as the 0-D model did in Fig. 2.3. This generally confirms that the model is functioning correctly.

All the appropriate physical parameterizations are then turned-on and started from the same initial condition of geostrophic balance as in Figs. 2.5 and 2.6. Figs. 2.11 and 2.12 show the results at 30 and 50 degrees latitude respectively. The 1-D model runs are quite similar to the 0-D model runs. The difference between Figs. 2.5 and 2.6 (0-D) and Figs. 2.11 and 2.12 is that the oscillation in the 0-D model depends on an assumed damping function while the oscillation for the 1-D runs depends on complex radiative, surface, and turbulent transfer parameterizations.

2.4.1 1-D Model Sensitivities

Mesoscale models inevitably come with a wide selection of different physical parameterizations that can be selected by the user for each physical process. By experimenting with some of these selections, we have found, not too surprisingly, that the LLJ is strongly dependent on which parameterization is chosen. Figs. 2.13 and 2.14 show results with model conditions identical to those of Fig. 2.11 (1-D at 30°N latitude) except for the selection of turbulence model. In Fig. 2.11, a turbulent kinetic energy formulation of

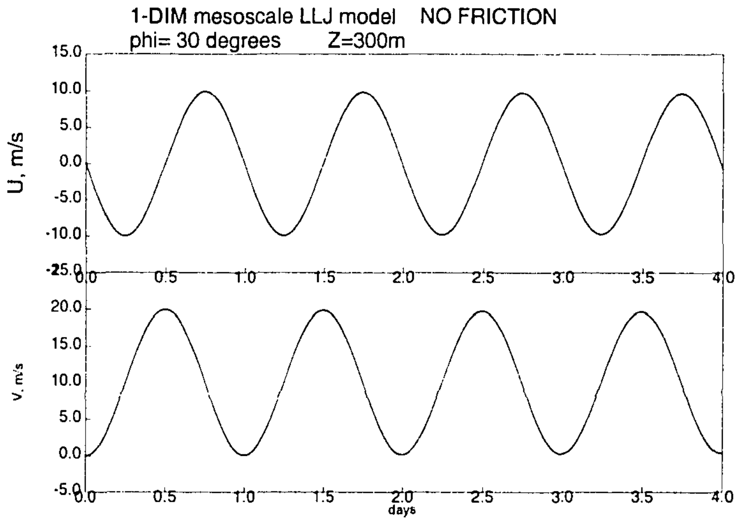

Figure 2.10: 1-D mesoscale model with no friction at 30°N latitude.

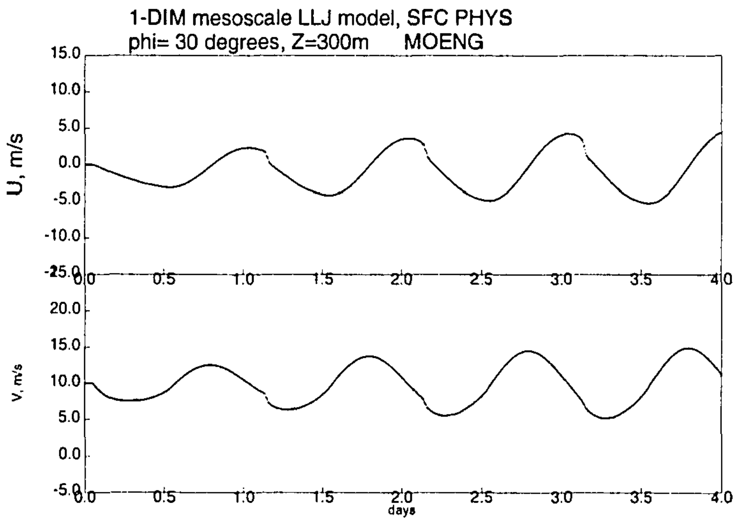

Figure 2.11: 1-D mesoscale model at 30°N latitude using Moeng and Wyngaard (1986) turbulence.

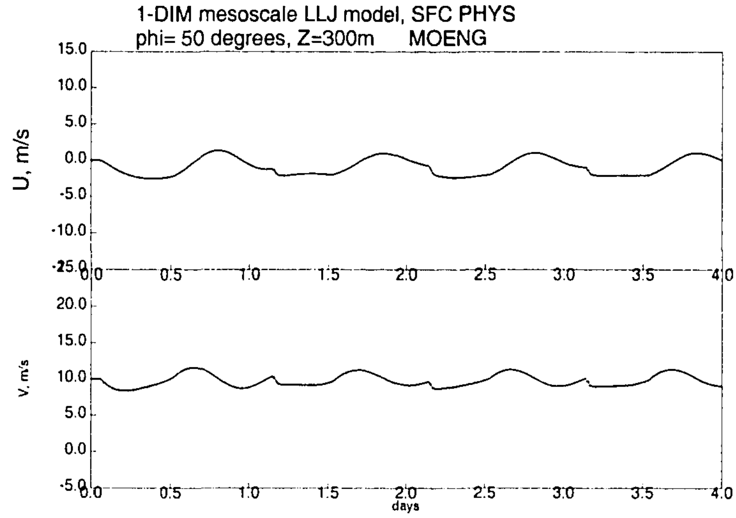

Figure 2.12: Same as Fig. 2.11 at 50°N latitude.

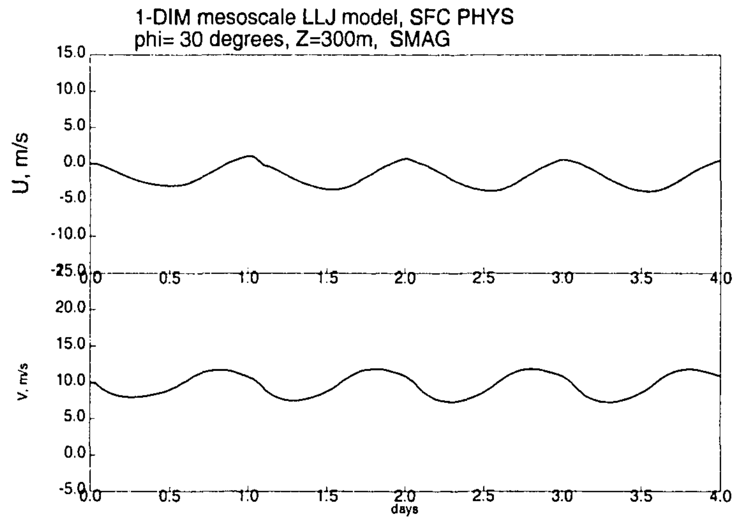

Figure 2.13: As Fig. 2.11 but with Smagorinsky turbulence.

turbulence following a scheme of Moeng and Wyngaard (1986) is used, while for Fig. 2.13, a Smagorinsky (1963) parameterization is used, and in Fig. 2.14, a turbulent kinetic energy formulation of Sun and Chang (1986) is used. The Sun and Chang and Smagorinsky turbulence models produced a much weaker jet than the Moeng and Wyngaard, showing very little evidence of a resonance effect. The Smagorinsky turbulence model (the simplest parameterization of turbulence used here) produced a particular weak jet with only slightly supergeostrophic winds.

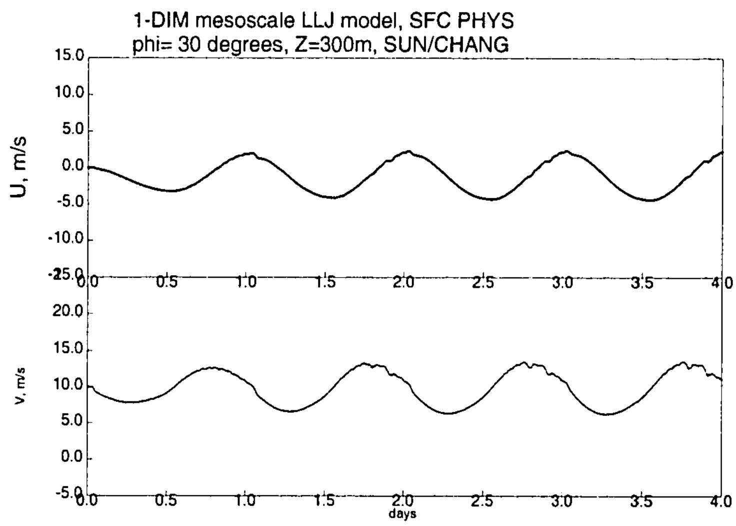

Figure 2.14: As Fig. 2.11 but with Sun & Chang turbulence.

Chapter 3

Clear-Air Radar Data

What I can not create, I do not understand — Richard Feynman

3.1 Scope of Clear-Air Work

It is the purpose of this chapter to provide a general review and discussion of radars and of clear-air radar data, and to analyze and come to some conclusions about the nature of clear-air radar signals. In later chapters, clear-air radar data will be used to deduce momentum and turbulence profiles of LLJs. A basic initial goal of this project was to acquire and analyze data of the LLJ using Doppler radar. The most relevant conditions from a standpoint of both LLJ dynamics and radar data analysis are conditions free of rain, which will generally be clear-air conditions for the radar. For NEXRAD and Cimarron radars, clouds that do not have precipitation usually have very low reflectivity, often too low to measure, so clear-air conditions can be cloudy, but not rainy. It is, thus, necessary to understand from basic principles what the nature of the clear-air signal is. This topic has been the subject of some controversy and confusion over the years. It is a large and complex subject, with hundreds of references extending back to the beginnings of radar. Knowledge from numerous diverse fields is drawn upon in studying clear-air return, including the fields of electromagnetics, fluid mechanics, meteorology, ornithology, and entomology.

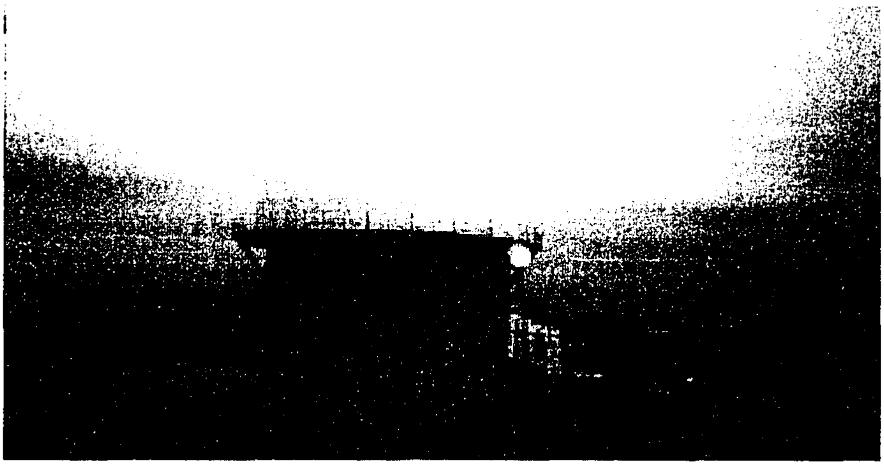

Figure 3.1: NSSL's Cimarron Radar, looking NNW.

3.2 Radars Used for This Study

Altogether, data from 6 radars in 5 different raw data formats are included in this dissertation. The most important of these is the Cimarron Doppler Radar (Figure 3.1) maintained by the National Severe Storms Laboratory as a research radar. It is located just south of Page airport, about 15 miles west of Oklahoma City with an elevation of 413 meters.

Table 3.1 shows the parameters for the Cimarron Doppler Radar and some of the same information for NEXRAD radars (Zahrai and Zrnić 1993; and Crum and Alberty, 1993), the Doppler on Wheels radar (DOW3, Wurman, 1997, 2001), and the University of Massachusetts 3 mm mobile radar (UMASS, Bluestein and Pazmany, 2000); all radars which were used as part of this work. Cimarron has better spatial resolution than the NEXRAD radars, due to the larger antenna. However, it is less sensitive (due to lower power) and suffers more from noise. Its advantages are its higher spatial resolution, its dual-polarization capabilities, and the fact that it can be used by researchers in any desired mode (i.e., the user can specify the scan strategy, single or dual-polarization, number of samples, etc.). It's disadvantages are its non-standard data format, frequent maintenance problems, and a lack of a display console to monitor data collection (now fixed). On balance, the Cimarron Doppler radar has been invaluable for this study.

Data are collected remotely at the NSSL offices in Norman onto 8 mm tapes, which are then read using software which has been recently translated by NSSL to run on a Sun workstation (Cimarron and another similar radar [now decommissioned] in Norman were developed in the 1970's). The software supplied by NSSL reads and decodes the raw data one radial at a time (a radial is the data received from one set of sent and received pulses with the radar at a certain azimuth and elevation angle) into speed, reflectivity, spectrum width, and polarization fields. All subsequent analysis and display software for these data used for this study were developed as part of this study. One radial of data contains 768 gates 150m apart in radial direction. Each gate contains one byte of data for speed, reflectivity, and spectrum width. When in dual-polarization mode, 3 more fields are stored: differential reflectivity, differential phase, and correlation coefficient. In dual-polarization mode, twice as many radar pulses are needed to produce one radial of data, with pulses alternating between horizontal and vertical polarization. With 32 bytes of housekeeping information, this means each radial has 2336 bytes of information in single-polarization mode and 4640 bytes in dual-polarization mode. The number of samples (transmitted pulses in single-polarization mode and half the number of pulses in dual-polarization mode) used to determined values for a radial is selectable by the operator. If a small number of samples is chosen, radials are output more frequently, but they are noisier. 128 samples was generally used here. With a PRT (pulse repetition time, Table 4.1) of 768 μs, this will give a radial every .098 seconds in single polarization mode and data will accumulate at the rate of 86 Mbytes per hour (for either mode) and a standard 5 Gbyte 8 mm tape will hold about 58 hours of data.

The data digitization resolution is 1 m/s in speed, .25 m/s in spectrum width, and approximately 1 dBZ in reflectivity. Reflectivity values are obtained from a look-up table of calibration values based on raw-returned power corrected for range. Values for azimuth and elevation are directly measured at the radar and stored with the housekeeping information for each radial with a resolution of .1 degree. The Zulu time of each radial is also stored in the housekeeping information to a resolution of 1 second.

Table 3.1: Cimarron, DOW3, NEXRAD, and UMASS Parameters

Parameter	Cimarron	DOW3	UMASS	NEXRAD
Frequency	2735 MHz	9380 MHz	95040 MHz	2700-3000 MHz
Wavelength	10.97 cm	3.198 cm	.3157 cm	10.0-11.1 cm
Beam Width	0.9°	.95°	.18°	.95°(3dB)
Peak Power	500 kW	250 kW	1.2 kW	750 kW
Antenna gain	46 dB	46 dB	60 dB	46 dB
Antenna diameter	10 m	2.44 m	1.2 m	8.5 m
Pulse Width	1 μs (300m)	.075-2μs(23m-600m)	.2 μs (60m) can be varied	1.57 μs and 4.7 μs (471 m and 1410 m)
Receiver noise level	-110 dBm	-112 dBm	-112 dBm	-112 dBm
Matched filter bandwidth (6 dB)	0.85 MHz	NA	NA	NA
System losses	11.7 dB	NA	NA	NA
Cross-polar isolation	20 dB	NA	NA	NA
Maximum sidelobe level	-22 dB	NA	NA	-27 dB
Gate spacing	150 m	12m-600m	15 m	250 m for velocity 1 km for reflectivity
Velocity resolution	1 m/s	NA	NA	.5 m/s
Nyquist	Varies	Varies	Varies	Varies
Reflectivity resolution	1 dBZ	NA	NA	.5 dBZ

3.2.1 Radar Display Software (RADDISP.F)

For this project, a FORTRAN90/77 program (RADDISP.F) was written to read radar data in raw form from different formats and to display it as gray-scale, half-tone images. It was very useful to have such software available as variants of it were used for analysis of the data in extracting VAD information and velocity profiles. The use of custom-built software also enforces a discipline of knowing the details of the raw format of the data being used, and affords the opportunity to attempt to achieve a display of the best possible resolution and quality.

A gray-scale display, rather than color, was chosen for a couple reasons. First, from a practical standpoint, black and white images on a laser printer are faster, more convenient, and cheaper to obtain. They are also cheaper to reproduce. Second, from a scientific standpoint, the use of a gray-scale with the darkness proportional to magnitude of the variable being displayed gives a more accurate visual impression of the spatial gradient of the variable shown. The selection of a color table is often an arbitrary assignment of colors to specific variable levels.

A color display for the field of velocity, however, is competitive with black and white because color is a positive/negative quantity. If one color is chose for positive velocities and one for negative (red and blue are common, for example), then shades of these two colors (rather than the single grey color) work well for displaying this field. Still, superior contrast interpretation is achieved using a single color. For example, a mesocyclone is identified in color-coded radar velocity data as an area of red in close proximity to an area of blue. This signature stands-out if one is trained to look for it. In a gray-scale image, a mesocyclone would show as an area of white near and area of black. White/black is a sharper contrast than red/blue and stands-out more clearly. With a single color, spatial gradients in velocity are linearly mapped to the display, rather than arbitrarily with a color table mapping. The software used in this research has been carefully optimized so that the best possible resolution hard-copy images result. However, recent experience with human viewers of black and white radar images suggests that the usage of color makes it easier for people to read precise values of the presented variable from images, though gradient information would still be poorly represented.

One problem with displaying velocity on a gray scale is the need to avoid confusing velocity data with missing data. It is most convenient and intuitive to display a region with no valid data as simply white. For velocity displays, the minimum velocity to be shown will be displayed as the lightest shade of gray, not white. This insures that any data to be displayed will show as some level of grey, and will not be confused with no data.

RADDISP.F reads in radar data one radial at a time and maps it to a rectangular array. The rectangular array stores the image to be displayed as pixel values. If radar pixels that are large in size are to be displayed, each datum is mapped to the necessary number of display pixels in range and azimuth. After the image is formed, it is passed to a subroutine which converts it into a halftone Postscript image. To do this, each display pixel is mapped to a 4 by 4 array of dots, which gives a possible 16 different shades of gray to display. For half toning (which works much better than dithering), a single rectangular dot is formed in the 4 by 4 array for a particular pixel value. The size of the rectangular dot scales with the pixel value.

Standard laser printers now are capable of 600 dots per inch (dpi) resolution. With 4 by 4 array pixels, this translates to 150 image pixels per inch. A version of RADDISP.F which uses 8 by 8 dot arrays to achieve 64 different shades of gray was also developed, but is most appropriate for 1200 dpi printers.

The features of RADDISP.F are:

1. Creates Postscript output with 16 shades of gray.

2. Reads Universal Format (DOW3 data converted with the NCAR SOLO program).

3. Reads raw Cimarron format.

4. Reads raw UMASS radar format.

5. Reads NEXRAD level II format.

6. Will display sector scans, RHI, PPI, PPI scaled with height rings, and time-height scans.

7. Has a crude de-aliaser as an option. This de-aliaser works by taking a user specified environmental wind vector, and using it as a reference wind against which the radial velocity datum closest to the radar is compared and checked for aliasing (and potentially dealiased). This de-aliased radial velocity is then used as the reference velocity for checking (and de-aliasing) the radial velocity at the next gate out from the radar. The radial velocity at each subsequent gate is checked using the already processed radial velocity at the previous gate as the reference.

8. Will display fields of velocity, reflectivity, spectral width, raw power, and polarization parameters.

9. Displays range-rings and radial lines speckled so they can be seen through the data.

10. Can display an arbitrary magnification of the data.

11. Annotates each image with 3 lines of identifying text.

3.2.2 Examples of Cimarron Clear-Air data

Figure 3.2 is an example of a clear-air reflectivity PPI scan (plan position indicator scan), in this case with a tilt of 2 degrees obtained on March 17, 1999 at about 730 Z (1:30 am local time). This image displays one complete scan of reflectivity, which took about 1 minute to acquire in this case. Data values in the range of -25 to 20 dBZ are mapped linearly into a gray-scale, half-tone postscript image with 16 shades of gray. Data are plotted in this figure in a non-traditional manner using height above the ground as the radial variable, rather than range from the radar. For analyzing wind profiles, it is much more convenient to plot radar data in terms of height above the ground than in terms of horizontal distance. In Fig. 3.2, range rings are plotted every 250 meters above the ground. The total depth is about 2.5 km. The total horizontal range is then 2.5 km / $\sin(2^\circ) = 72$ km. Data for which the signal strength falls below the noise level are rejected, with the reflectivity being set equal to -999 dBZ (which will appear as white areas in Fig. 3.2).

A few points are worth noting about Fig. 3.2. First of all, the maximum reflectivity is about 25 dBZ, surprisingly high for clear-air. There is also a graininess to the reflectivity

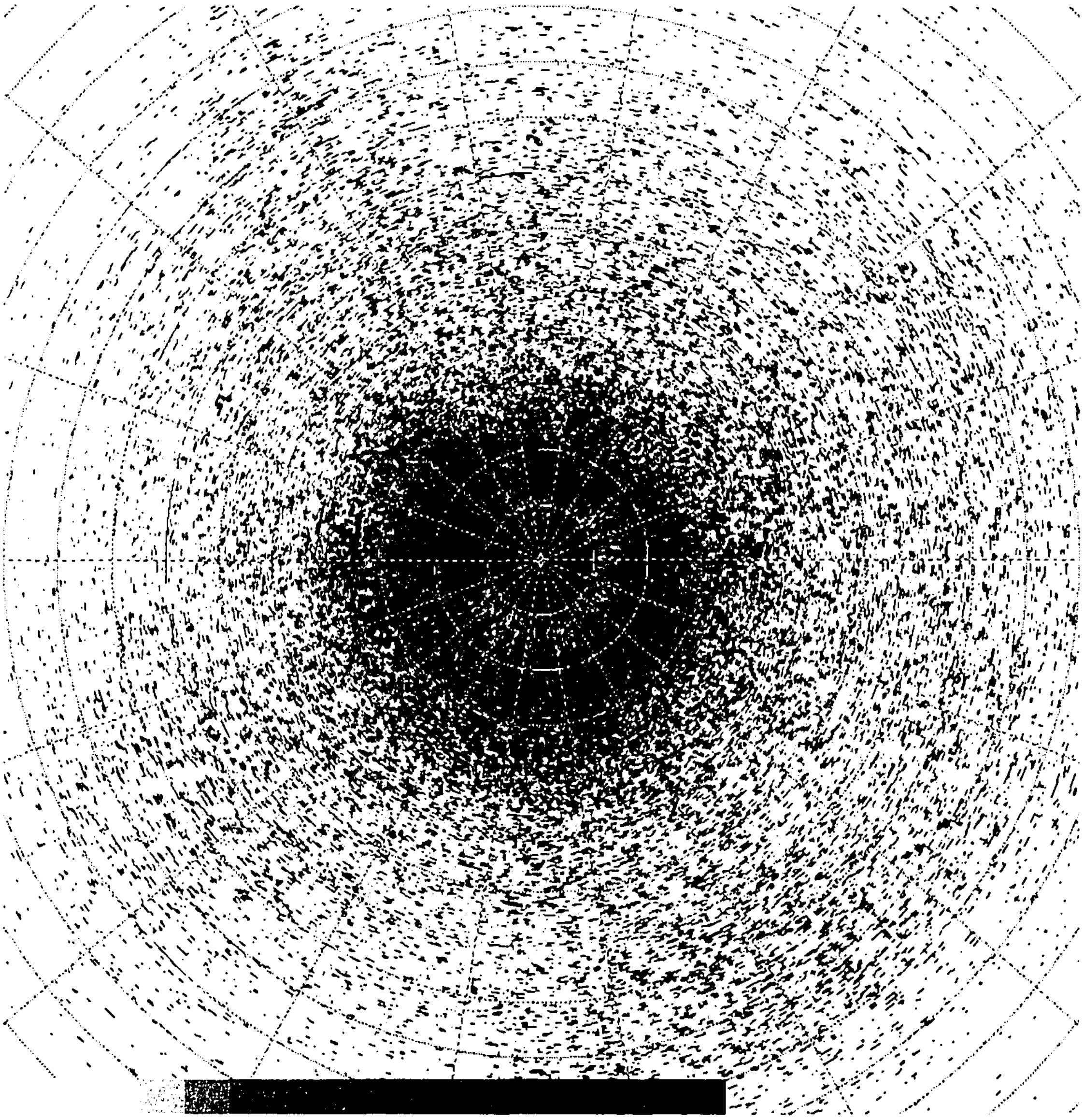

Figure 3.2: Reflectivity PPI scan at 2° of tilt from Cimarron radar, under nocturnal clear-air conditions, 03/17/99 , 730Z. Range rings are drawn every 250 m in height above the ground. Total horizontal range (the 10th range circle) is 72 km. Reflectivity range is from -20 dBZ (white) to 25 dBZ (black).

pattern; a strong variation in reflectivity over very small distances. As will be discussed in Sec. 3.8, this granulation implies that the radar targets are isolated point targets. There is a thick annulus of strong reflectivity within the central third of the image, which has weak reflectivity within it and a rapid drop to much lower reflectivity outside it. There is also a dark central disk of reflectivity which is partly due to ground clutter.

Figure 3.3 shows the velocity determined from the Doppler shift of the reflectivity shown in Fig. 3.2. In this figure, lighter shades are velocities towards the radar and darker shades are velocities away from the radar. This image shows a well defined LLJ from the southwest, with an amplitude over 35 m/s. Some aliasing is apparent as some black areas appear within the white inbound velocity region; and some white within the black. Medium gray shading near the center of the image is caused by ground clutter.

Figure 3.4 shows the spectral variance plot of the velocities of the same radar scan. The modulation of velocity variance with azimuth in a manner similar to the velocity is due to wind shear, as will be discussed in section 4.3.

3.3 Radar Equations and Calibration

Calibration generally involves comparing the output of a measuring instrument (such as a radar) with a known standard input. For Doppler radar, the velocity is determined theoretically from the known physics. As long as the speed of light is known and an accurate time base is available for determining the Doppler shift frequency, radars do not need calibration for velocity. They do, however, need calibration for reflectivity. Reflectivity values are determined from the power detected at the antenna from targets back scattering radar energy. This power depends, among other things, on the precise power output of the transmitter, losses in the wave guides, and the efficiency of the antenna. These losses can not be known accurately enough theoretically and calibration must be done if accurate reflectivity values are to be obtained. For the purposes of this study, precise reflectivity values are needed in order to draw conclusions about the nature of the targets (birds versus insects versus index of refraction gradients).

What is commonly called "the weather radar equation" takes various forms, but gen-

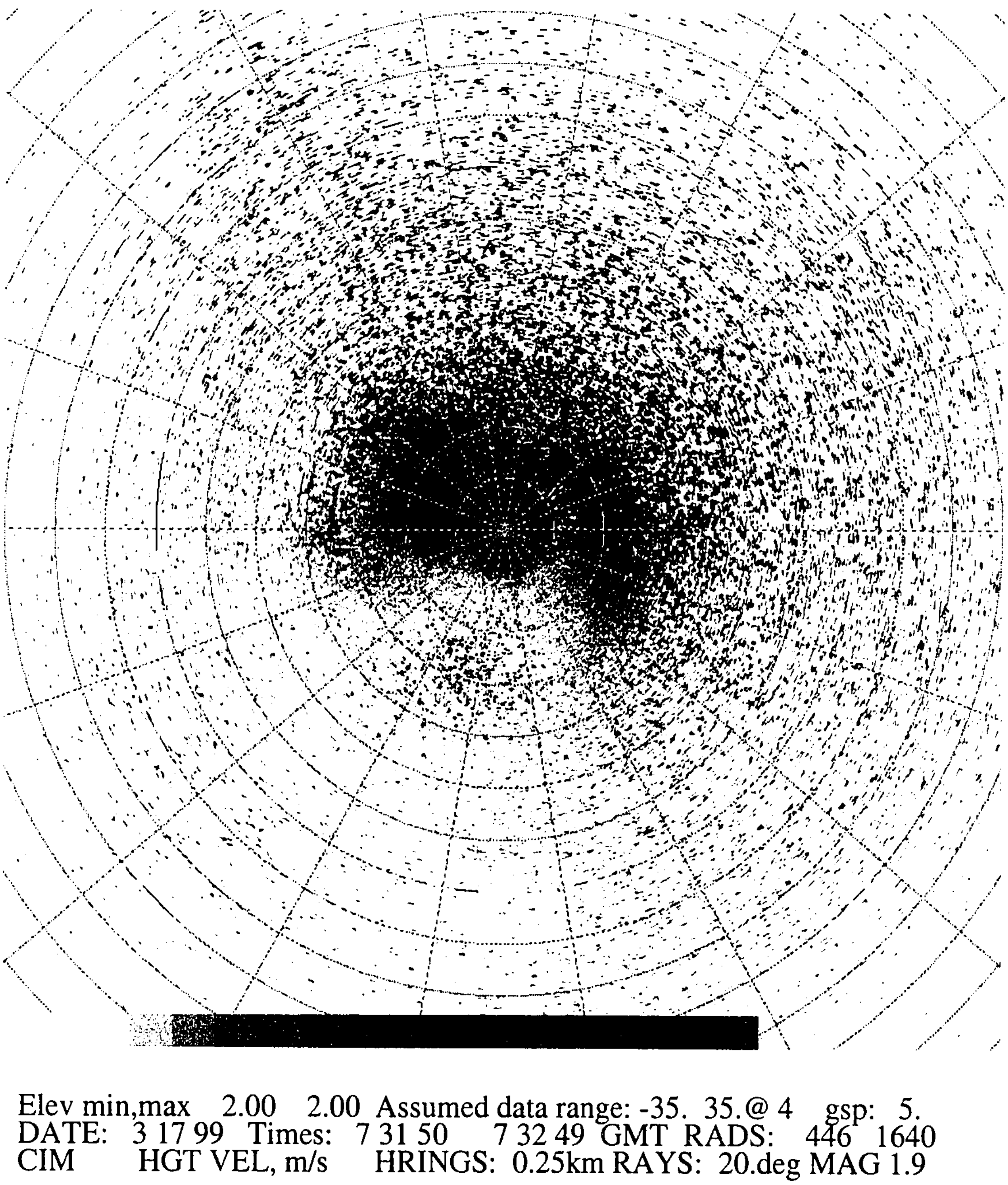

Figure 3.3: Velocity scan of a LLJ from Cimarron radar

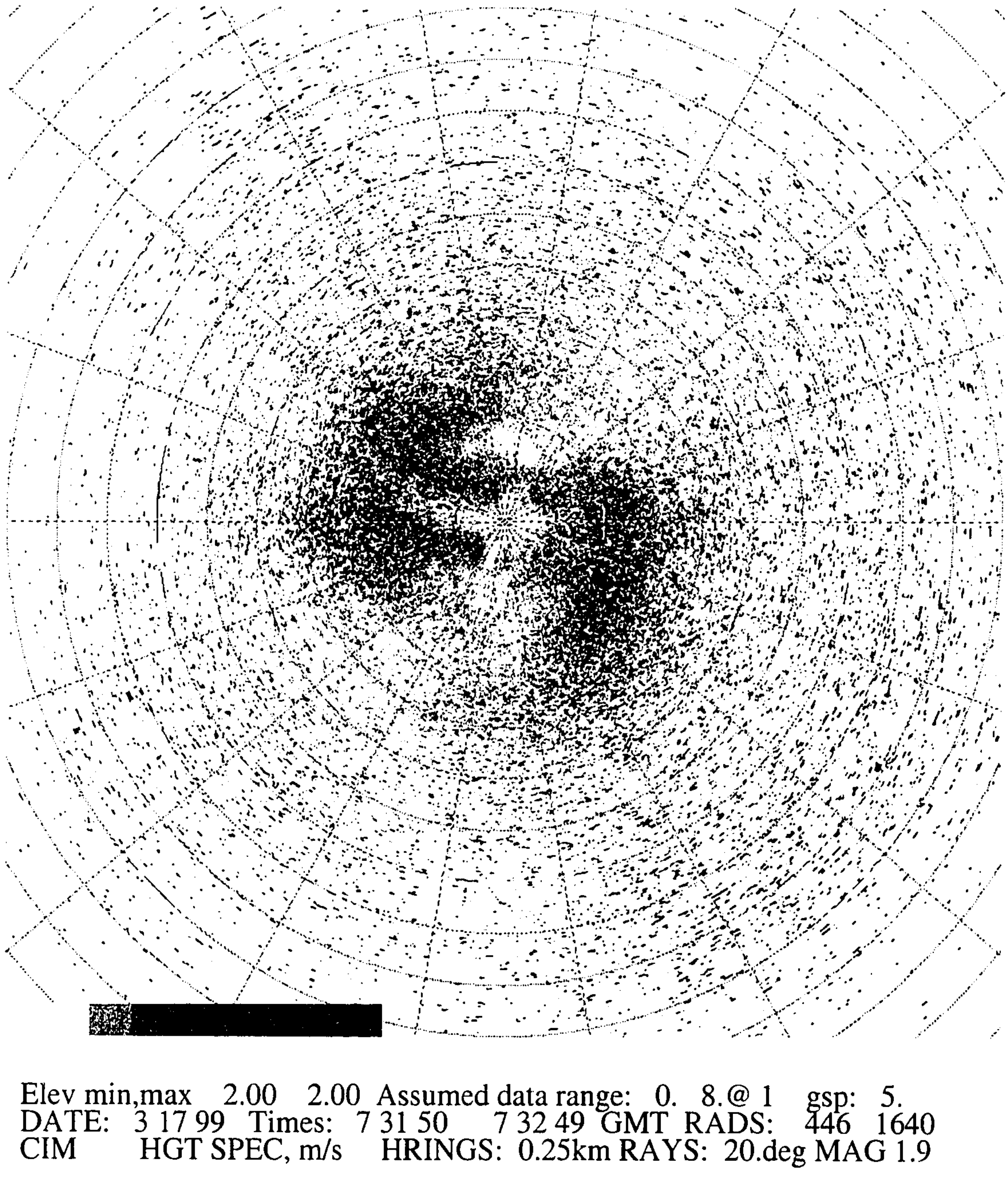

Figure 3.4: Spectral variance data (square of spectral width) for a LLJ from Cimarron radar.

erally relates the received power to numerous radar and target parameters. For a single target near the center of the radar beam for a system using the same antenna for transmitting and receiving, it is (Probert-Jones, 1962; Doviak & Zrnic, 1984, p. 21-58; Battan, 1973, p. 29-33):

$$P_r = \frac{P_t G^2 \lambda^2 L}{(4\pi)^3 r^4}\sigma \tag{3.1}$$

where:

- P_r = average received power
- P_t = transmitted power in pulse
- G = antenna gain
- λ = radar wavelength
- L = loss factor
- r = range to center of probe volume
- σ = backscatter cross section of target

The loss factor, L, includes the effects of wave guide losses, antenna inefficiencies, beam attenuation, receiver bandwith limitations, and any other factors not explicitly included. For an antenna that is a circular paraboloid, the gain, G, is approximately:

$$G = \frac{\pi^2}{\theta^2} \tag{3.2}$$

The beam width, θ, for common meteorological radars is approximately (Doviak and Zrnic, 1984, p. 26):

$$\theta = \frac{1.27\lambda}{D_a}$$

Where D_a is the antenna diameter.

The backscatter cross section, σ, is the cross-sectional area a non-absorbing isotropic scatterer would have which reflects the same amount of energy as the target. σ can be much smaller than the actual physical size of the target if the target is a poor scatterer.

These equations depend upon the targets being in the far-field of the radar beam. The radar beam changes shape with distance away from the antenna, r, due to diffraction effects. The beam exits the radar antenna with a diameter equal to the radar antenna

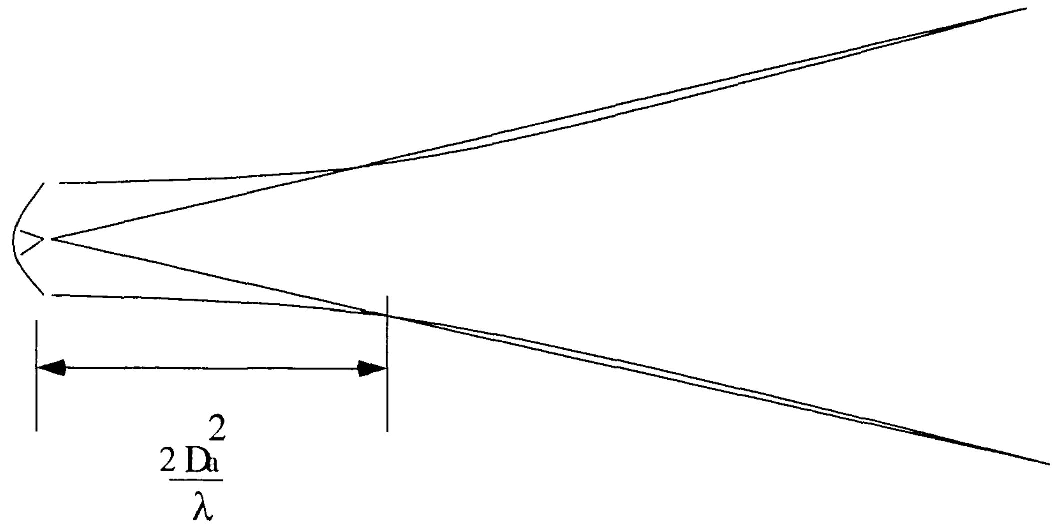

Figure 3.5: Diagram of radar beam.

diameter. At a distance of about $2D_a^2/\lambda$, it becomes the idealized conical shape usually assumed. For a NEXRAD radar or for Cimarron, this distance is about 2 km. At distances less than this, the beam is wider than that assumed by the radar equation and less power is received from such targets than would be expected by (3.1), (see Fig. 3.5). If radar targets need to be considered which are closer than $2D_a^2/\lambda$, then one way to apply the far field equations approximately is by assuming the beam has a width equal to the radar antenna diameter out to a distance of D_a/θ. This allows the replacement of r in radar equations by D_a/θ for $r<D_a/\theta$.

For a population of targets, the contribution from each target to the averaged received power simply add together, after accounting for their phases, (Doviak & Zrnic, 1984, pp. 48-49), and the radar equation is expressed in terms of total back scatter cross section per unit volume times the volume illuminated. The illuminated volume is the volume of space returning echoes to the radar at a particular time, and it depends on the beam width, θ, and the pulse length, h, the two-way transmission characteristics (i.e., the illuminated volume is the intersection of the transmitted and reflected cones of energy), and a factor to account for the Gaussian beam shape. The probe volume is approximately: $\pi(r\theta/2)^2\frac{h}{2}$. The factor h/2 occurs rather than h because at the time that signals arrive at the antenna from a distance r, signals from locations from $r\pm h/4$ are simultaneously arriving, but signals outside $r\pm h/4$ have yet to arrive or have already passed. The probe volume is half of the pulse width. The resulting equation (e.g., Battan, 1973, p. 32) is:

$$P_r = \frac{P_t G^2 \lambda^2 \theta^2 h L}{1024(ln2)\pi^2 r^2} \frac{\sum_i \sigma_i}{Vol} \tag{3.3}$$

where:

θ = round angular beam width

h = pulse length

$\frac{\sum_i \sigma_i}{Vol}$ =summation of backscatter cross section from all i targets in illuminated volume divided by a unit volume

Since radars are designed to see water drops, which are typically small relative to the radar wavelength, it is often assumed that the Rayleigh approximation applies to the scatterers. This approximation is:

$$\sigma_{Ray} = \frac{\pi^5}{\lambda^4} |K|^2 D^6 \tag{3.4}$$

where K is a function of the index of refraction and absorption of water, and D is the drop diameter. For mathematical convenience, the complex index of refraction, m, is defined as: m=n-ik where n is the ordinary index of refraction and k is the absorption coefficient. K is then defined as K=(m^2-1)/(m^2+2) For water at microwave wavelengths, $|K|^2$ is about .93 (see Table 3.2) . The limits of validity of the Rayleigh scattering approximation will be addressed in Sec 3.5. The reflectivity factor, Z, is defined as

$$Z = \frac{\sum_i D_i^6}{Vol} = \frac{\lambda^4}{\pi^5 |K|^2} \frac{\sum_i \sigma_{Ray}}{Vol} \tag{3.5}$$

The reflectivity factor, Z, is distinguished in the literature from the reflectivity, η, which is defined as:

$$\eta = \frac{\sum_i \sigma_i}{Vol}$$

The illumination volume, Vol, for a narrow beam is:

$$Vol = \frac{\pi r^2 \theta^2 h}{8}$$

In common parlance, the reflectivity factor converted to decibels, dBZ, is often referred to as simply "reflectivity". Radar output is typically processed with Rayleigh scattering from spherical water drops (3.4) assumed. Received power is translated through the above equations, into Z values. When the targets are not small spherical drops of water, reported Z values are effective values. A combination of (3.3), (3.4), and (3.5) yields:

$$P_r = \frac{P_t G^2 \theta^2 L h \pi^3 |K|^2}{1024(ln2) r^2 \lambda^2} Z \tag{3.6}$$

When it is believed that the target is a single scatterer in the probe volume, rather than a distribution of Rayleigh scatters, the radar cross-section of the target can be recovered from the reported Z value by equating (3.6) with (3.1), provided the single scatter is near the beam axis, yielding:

$$\sigma = \frac{\pi^6 |K|^2 r^2 \theta^2 h}{16(ln2)\lambda^4} Z = 80.6 \frac{r^2 \theta^2 h}{\lambda^4} Z \tag{3.7}$$

which also yields the total radar cross-section in the illuminated volume.

With (3.2) in (3.6), the radar equation becomes:

$$P_r = \frac{P_t L h \pi^7 |K|^2}{1024(ln2) r^2 \lambda^2 \theta^2} Z \tag{3.8}$$

Converting to conventional units and substituting in constants, (3.8) becomes:

$$P_r = 1.299X10^{-16} \frac{P_t L h}{r^2 \lambda^2 \theta^2} Z \tag{3.9}$$

Where:

P_r and P_t	are in Watts
h	is in meters
r	is in kilometers
λ	is in centimeters
θ	is in degrees
Z	is in $mm^6\ /m^3$
L	is a dimensionless loss factor < 1

Since the power received can span several orders of magnitude, decibels are usually used for recorded power levels. It is standard to used dBm for power measurements, which is decibels of power relative to 1 mW:

$$dBm = 10log\frac{P}{P_0} \quad with\ P_0 = .001\ Watts$$

Converting (3.9) to dBm gives:

$$P_r(dBm) = -128.9 + 10log\frac{P_t h}{\theta^2\lambda^2} + dBZ - 20logr - system\,losses \tag{3.10}$$

Where dBZ is 10logZ, a logarithmic measure of reflectivity. The negative of the first two terms on the RHS of (3.10) is often called the "radar constant", or RC. If the pulse length of the radar can be changed (as in a DOW radar), then the RC changes. In terms of dBZ:

$$dBZ = dBm + RC + 20logr + losses \tag{3.11}$$

Accurate calibration determines the system losses, and can account to some extent for inaccuracies in the assumptions inherent in the radar equation.

3.3.1 Calibration Error Effect on Z-R Relationships

The need for accurate radar calibration is, perhaps, under-appreciated. Because of the logarithmic nature of reflectivity, estimates of rainfall rates made with radar are very sensitive to the precision of the reflectivity measurement. Consider the Z-R relation of Joss and Waldvogel (1970):

$$Z = aR^b \tag{3.12}$$

where Z is reflectivity in mm^6m^{-3} and R is rainfall rate in mm/hr. For Joss and Waldvogel (1970), a=300 and b=1.5; other Z-R relations have this form with a and b taking on different values (Doviak and Zrnic, 1984, p. 201). To find the approximate error in R due to an error in dBZ, we first use the definition dBZ=10logZ and solve 3.12 for R giving:

$$R = a^{\frac{-1}{b}} 10^{\frac{dBZ}{10b}}$$

From basic error analysis, the absolute error in R, δR, is found from:

$$\delta R = \frac{\partial(R)}{\partial dBZ} \delta dBZ = \frac{\partial}{\partial dBZ}(a^{\frac{-1}{b}} 10^{\frac{dBZ}{10b}}) \delta dbZ$$

Where δdBZ is the absolute error in the measurement of dBZ. This gives the fractional error in R of:

$$\frac{\delta R}{R} = \frac{ln 10}{10b} \delta dbZ$$

Or, with the value of b of 1.5:

$$\frac{\delta R}{R} = .15\, \delta dBZ$$

Every 1 dBZ error in calibration leads to a 15% error in rainfall rate. NEXRADs are intended to be calibrated to within 1 dBZ, leading to a significant inherent error in rainfall rate estimation. The inaccuracy of the admittedly crude Z-R relationship and any error in calibration lead to significant reductions in accuracy. Reports of large underestimates in NEXRAD-determined rainfall totals (e.g., Fo and Crawford, 1999, found a 28% underestimate when compared with Oklahoma mesonet rain gauges) could be due partly to simple calibration errors, though large errors in rain gauge estimates of rainfall are also a problem.

3.3.2 Calibration of NEXRAD, DOW3, Cimarron, and UMASS

NEXRAD radars record data in level II format, the rawest format generally available, to a digitization of .5 dBZ. These radars are calibrated to within 1 dBZ by using internal reference signals. This is done by a radio-frequency pulse being injected into the receiver every volume scan. Such calibration checks do not account for some kinds of system degradation (such as antenna gain loss over time), and it is possible that some NEXRADs may not be in accurate calibration. Indeed, those studying radar rainfall estimation point to calibration error as a significant potential source of error (Anagnostou et al., 2001). It is not possible to know the magnitude of possible unaccounted for system losses, but such errors would be losses, not gains, in signal strength. If a NEXRAD were out of calibration, it would likely be underestimating reflectivity values. Absent knowledge of such equipment problems, the precision of NEXRAD reflectivity is assumed to be ± 1 dBZ.

DOW3 has not been calibrated by reference signals or by reference targets. It is possible to calculate what the calibration should be using the formulas above (e.g., 3.10) based on known radar characteristics and then adding a pessimistic 5 dB for system losses (Wurman, personal communication). Such an estimate would then be good to $\pm$ 3 dB, though this would also miss certain equipment problems similar to the problems with NEXRAD calibration. For example, mis-aligned wave-guide connections or a malfunctioning transmitter with fluctuating power levels could lead to grossly erroneous calibration. However, consistency of radar operation (e.g., that radar echoes of certain phenomena are similar to those expected by the radar operator) lead to some confidence that the calibrations are not too far off.

Cimarron radar is similar to NEXRAD in that it is calibrated by reference signals. In recent years (Zrnic, personal communication) the transmitter has had significant power fluctuations as much as 10 dB, leading to inaccurate calibration.

The UMASS radar was calibrated by using a reference target (a corner reflector) after the completion of the 2001 data collection season (Pazmany, personal communication). The calibration was found to quite accurate to within 1 dB and stable at that time.

A theoretical calibration for DOW3 to $\pm$ 3 dB and the system stated calibration for NEXRAD to $\pm$ 1 dB are probably accurate most of the time and most studies using radar reflectivity values simply assume their radars are in calibration, though we should realize the possibility exists for significant calibration error. Ideally, radars should be calibrated by reference target both before and after an experiment. In practice, this is almost never done.

3.4 Review of The Nature and Origin of the Clear-Air Radar Return

The hypothesis that nocturnal clear-air return is due to migrating birds makes this an important topic to cover here, since, if true, it would make radar profiling of LLJs highly inaccurate as birds have air speeds of 10 to 20 m/s. That this might be the case is suggested by the quality control of NOAA's wind profiler network which routinely flags nocturnal LLJ data as being contaminated by birds, and by radar ornithologists (e.g., Eastwood, 1967, Gauthreaux and Belser, 1998) who imply that clear-air 'angel' echoes are almost always birds. Recent studies by meteorologist (e.g., Zrnic and Ryzhkov, 1998; Jungbluth et al., 1995; and O'Bannon, 1995) support the existence of bird contamination of S-band radars; while Wilson et al. (1994) support the more traditional view that angel echoes are mostly insects. Insects are probably acceptable tracers of air motion, except in situations where they are all migrating in the same direction, since their uncorrelated motions would only be expected to add a few meters per seconds to the spectrum width.

Almost all clear-air echos are believed to be caused by either insects, index of refraction gradients (modified by turbulence), or birds. Other things which are known to occasionally cause radar return are particulates in the form of smoke from fires or fireworks and interference from other radio equipment or the sun. In order for particulates as small as dust particles to give a measurable signal, enough needs to be present to give a visible cloud (such as in fireworks). Individual insects, on the other hand, are easily detected by modern meteorological radars. The large body of research available (much of it more than 30 years old) combined with the need to study the habits of birds and insects makes this a daunting subject. Some reviews are available about the topic (e.g., Hardy and Katz, 1969; Battan, 1973, Ch. 12; Gossard and Strauch, 1983; Doviak and Zrnić 1984, Ch. 11; Vaughn, 1985, and Hardy and Gage, 1990).

In the following sections, some of the variety and characteristics of clear-air radar echoes which have been observed (both day and night) are listed and the three possible explanations for nocturnal clear-air return are discussed. Reference is made to some of the data presented later in this report as illustrations of clear-air return.

3.4.1 Characteristics of Clear-Air Radar Echoes

This section lists some characteristics of clear-air return; all of which have been observed as part of this research by either viewing NEXRAD radars from across the country, using the Cimarron radar, or in the literature. However, some of these observations have not been well-documented in the literature, despite the considerable literature on the topic of clear-air return.

Clear-air return can occur as isolated (dot) targets or as layers or volumes filled with reflectivity. Isolated clear-air targets have been referred to as "ghosts", "phantoms", or, most commonly, "angels". The term "angel" is used in the literature to refer to clear-air echoes in general, including volumetric, layer, and point echoes.

Clear-air reflectivity has a very pronounced daily cycle. Typically, it is weak during the day and confined to the lowest kilometer or less. There is a very definite dip in reflectivity and height of return at sunset, followed by a rapid (1 hour) increase in reflectivity and height of return (to 2 or 3 km). At any time of the year, reflectivity values often reach surprisingly strong values. Nocturnal return can reach 25 dBZ in exceptional cases and is commonly 10 dBZ or more, values comparable to those of light rain. Nocturnal return gradually decreases towards the end of the night followed by a rapid dip at sunrise, which is followed by a modest, but rapid increase to the daytime level. This cycle is summarized by the data in Fig. 3.6 which shows average reflectivity below 2 km versus time and height for one night in May. The local minima in reflectivity at sunrise and sunset are quite interesting features which were seen on all nights examined as part of this research in which appreciable clear-air return is received by a radar. Hardy and Glover (1966) suggested that this cycle could be due to insects of one species leaving the atmosphere at sunset while another one enters it at night. Whatever the cause, there is some distinct change from daytime to nighttime scattering mechanism. There are no fixed rules obeyed

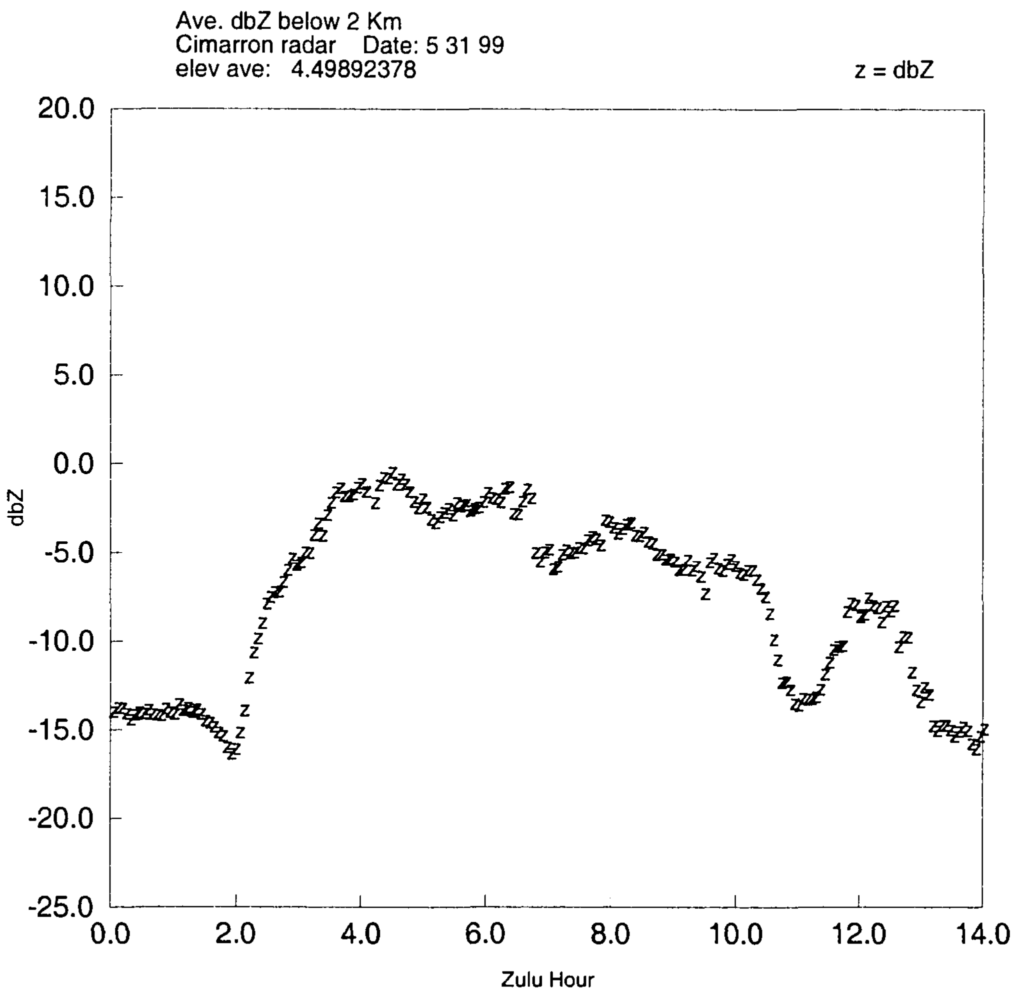

Figure 3.6: Plot of average reflectivity below 2 km versus time for a nocturnal LLJ case. Sunset is near 2Z and sunrise is near 11Z. Data is from the Cimarron radar from May 31, 1999.

by clear-air reflectivity all the time and on some occasions, the clear-air reflectivity is as strong or stronger during the day than at night. Strong clear-air reflectivity during the day does appear to be correlated with strong nocturnal return.

Clear-air reflectivity is usually very weak over large bodies of water. This effect is so marked that often details of a coastline can be discerned by looking at the pattern of the clear-air return. It is common for the Melbourne NEXRAD in Florida to show 10 to 20 dBZ of reflectivity over land at night and none over adjacent coastal waters and Lake Okeechobee. Small islands can sometimes be seen as isolated spots of reflectivity. Sometimes, though, reflectivity is just as strong over water as over land. The frequency of strong reflectivity over water is not known.

There is a pronounced seasonal variation in clear-air return with return generally being stronger in the warm season. In the Great Plains, late spring seems to have the strongest clear-air return at night. Day-to-day values can fluctuate considerably; however with reflectivity magnitudes differing by 20 dBZ from one day to the next.

There are strong day-to-day regional fluctuations. On one night, for example, the clear-air return could be strong over the Gulf Coast states and weak everywhere else while on the next night it might be strong over states in the upper Midwest and weak along the Gulf Coast and everywhere else. Clear-air return tends to be weak at locations west of the rockies year round.

Clear-air return is sensitive to synoptic boundaries. Typically, clear-air return is strong at night in the spring south of a cold front and weak north of it. Boundaries generated from outflow from storms can sometimes be seen to be co-located with gradients in clear-air return for presumably similar reasons (whatever they are); however, clear-air return at night is sometimes strong everywhere, including entirely around an MCS up to the edge of where there is strong reflectivity from water drops. Thin lines of clear-air reflectivity are common in the Great Plains region. For reasons which have never been elucidated, they tend to best defined (thinest and sharpest) in the late afternoon, though they can be present at any time of the day or night. Nocturnal thin lines are most often seen associated with thunderstorm outflow. Daytime thin lines are more common, and so numerous that is not always clear what they are related to. Fronts, drylines, outflow boundaries, and convergence lines are all candidates for the cause of a thin line on NEXRAD radar.

Clear-air reflectivity is often granular in presentation. Fig. 3.2 shows a wide area of reflectivity consisting of a large number of discrete spots. The granularity is different between daytime and nighttime return (Browning & Atlas, 1966), with nighttime return having larger grains. This granulation is strong evidence for large particulates, possibly in the form of insects or birds, being the source. This hypothesis is explored by high-resolution radars in this report in Sec. (3.8).

Rings and lines of clear-air reflectivity are also often seen. Thin lines on radar appear to be associated with a variety of wave phenomena and boundaries including: fronts, drylines, gust fronts, and sea breeze fronts. The source of echos for such lines has been attributed to insects accumulating at meteorological boundaries (Wilson et al., 1994); however, boundaries are also typically locations of potentially large and sharp index of refraction gradients. Apparent convective rolls are commonly seen during the day with the clear-air reflectivity showing a pattern of parallel lines. Expanding rings of clear-air return are also seen at certain times of the year in the morning. Elder (1957) first noticed these and suggested that they might be due to a sort of shear-gravity wave. However, it is now recognized that these expanding rings are almost certainly due to birds leaving nesting sites (Battan, 1973, p. 258-9, Eastwood, 1967, p. 165-181, Gauthreaux and Belser, 1998). These rings occur reliably from the same central geographic point every morning over known nesting sites of birds, and birds can be observed leaving these sites in the early morning hours. In Oklahoma, such rings are seen and have been identified with various species of egrets, a relatively large bird (Bider, personal communication). Personal observations of bird rings in Central Oklahoma have revealed the birds to fly in small isolated groups of 2 to 10 birds. At sunset, expanding rings of reflectivity are also seen in some locations and have been identified with bats leaving roosting sites. Rings of reflectivity 1 to 3 km in diameter which do not expand are also sometimes seen; sometimes numerous such echos are seen covering a considerable horizontal area. These are believed to be the result of convective cells or thermals in the lower atmosphere (Doviak and Zrnić, 1984, p. 417).

Layers of clear-air return are also often seen, especially with the longer wave-length radars. These are often co-located in altitude with inversions (Lane and Meadows, 1963; and Friend, 1940). Sometimes these layers are seen to form Kelvin-Helmholtz rolls which subsequently break into turbulence.

PPI scans (plan-position indicator scans, horizontal displays of data in polar coordinates of range and azimuth) of reflectivity during both day and night (but more often at night) sometimes show quite marked bilateral symmetry in which reflectivity is strongest in two directions 180 degrees apart. An example is given in Fig. 3.30. The bilateral symmetry also extends to polarization variables (Zrnić, 1999). This symmetry was noted by Schaefer (1976) who attributed it to insects being aligned in the same direction. It was noted by Gauthreaux and Belser (1998) who attributed it to migrating birds all being aligned. An insect or bird explanation for this bilateral symmetry stems from the larger radar cross-section from biological targets when viewed broadside, as opposed to head- or tail-on.

3.4.2 Birds as The Cause of Clear-Air Return

Ornithologists began studying birds with radar as early as 1945. Eastwood (1967) gives an excellent review of the early history of radar ornithology. Eastwood accepts that birds are the cause of most point-target angel echoes. He states (p. 88), "Radar studies made by a number of observers both prior and subsequent to this work have left little room for doubt that birds and angels may be substantially equated." In terms of biasing radar wind profiles, it is mostly when birds are all moving in the same direction that they are a problem, which, of course, would be expected to be the case during migration.

Ornithology and the study of bird migration is a fascinating and rich subject (e.g., Berthold, 1993). For meteorological purposes, however, generalizations about bird behavior should probably not be made. Birds exhibit a wide variety of behavior even within a single species, and there are thousands of species. Generally speaking, even though ornithologists are able to make some broad statements about bird behavior, they also cite many exceptions. For example, Lowery and Newman (1966), who studied migration patterns on four specific nights, revealed a great variety of behavior of birds relative to fronts, prevailing winds, and day to day; with birds sometimes flying with the wind, sometimes against it, and sometimes flying in opposite directions in nearby geographic regions. Meteorologists should probably just accept that it is possible for birds to be migrating at anytime of the day or night, on any day of the year, with any relationship to the weather, and in any direction. And any patterns that exist can change from year to year. The *Date Guide to the Occurrences of Birds in Oklahoma* (Grzybowski et al., 1992) lists 441 species of birds which frequent Oklahoma, the majority of which migrate from place to place at varying times throughout the year.

Birds tend to be most active (i.e. flying for whatever purpose) at sunrise and sunset. Migratory birds, which must move long distances, often travel at night, sometimes in flocks, but also individually (Bider and Schnell, personal communication). It may be possible that birds traveling north could deliberately take advantage of the LLJ by flying in it; however, it is not clear by what means they might discern the existence of a jet or what level it is best to fly at. Since the habits of some migratory birds are synchronized with the nocturnal boundary layer, it can be difficult to tell if changes in clear-air reflectivity between night and day are due to differences in bird numbers or differences in boundary layer dynamics. Bird behavior is species-dependent, with many species migrating during day light hours. A great deal of detailed information about birds has been learned by ornithologists; however, reasons for every detail of bird behavior (such as the precise advantage of migrating at night versus day) are not known with any certainty, though speculation is abundant. For example, it is speculated that one of the reasons some species migrate at night is to avoid being spotted by predators. Another reason considered is that during daylight hours, birds are busy feeding, and some fly at night so as to avoid conflicting with this activity. Another theory is the need to use the stars for navigation. There are probably more unproven theories about how birds navigate than any other ornithological topic.

Bird behavior is driven almost entirely by instinct. A remarkable example of this is given by studies of European Blackcaps (Berthold, 1993, p. 146). Blackcaps from the western part of central Europe migrate towards the southwest, while those from eastern Europe migrate towards the southeast. Hybrid Blackcaps that result from cross-breeding western and eastern European birds, exhibit instinctive southerly orientation. The means by which birds determine direction is a subject of debate in ornithology, with some fascinating theories (Able, 1999) that are well beyond the scope of this work.

Birds should certainly be detected by weather radars when present, though it is not obvious if they fly at a high enough altitude and in large enough numbers to really be a serious source of contamination. Most birds spend their lives less than 100 m above the surface. NOAA's Environmental Technology Laboratory (ETL) considers this to be a significant problem and radar wind profiler data at night at low levels during certain months of the year are routinely flagged by them (under certain criteria) as "bad" based on the assumption that the data are due to birds (van de Kamp et al., 1997, Miller, 1997, Wilczak et al., 1995). This is particularly unfortunate since wind profiler measurements of the LLJ in the spring time are almost always rejected by ETL.

The strongest evidence in support of the bird theory are observations from balloon soundings simultaneous with radar derived wind profiles which show radar derived winds significantly different from those derived from balloons. These differences appear to occur only at night and during seasons when birds are expected to migrate. O'Bannon (1995) and Gauthreaux et al. (1998b) report on this discrepancy with NEXRAD VAD wind profiles and Wilczak et al. (1995) report on this problem with long wavelength wind profilers. These differences can be as large as 15 m/s, with the difference wind vector consistent in direction and amplitude with what would be expected if the radar was tracking migrating birds. Jain et al. (1993) examined this problem by comparing Cimarron VADs with CLASS soundings for a LLJ in May. They found radar winds higher than the balloon sounding by about 4 m/s. They considered birds as a possible explanation, but doubted it because of the horizontal uniformity of reflectivity over a wide area. Instead, they blamed the discrepancy on the long sampling time of the CLASS system. The CLASS balloons use sampling times (operator selectable) from 30 seconds to 2 minutes. In 2 minutes a typical balloons will have risen 300 meters. This coarse vertical resolution is significantly poorer than what the radar is capable of and means the balloon may miss recording the actual peak speeds in a jet. Their data indicated that the research-grade CLASS soundings did a very poor job of sampling the LLJ.

Observations of differences between VADs and rawinsondes in a manner consistent with errors due to migrating birds is very strong evidence in favor of birds being the source of nocturnal clear-air return during at least some LLJs. Strong nocturnal clear-air return occurs on almost every night there is an LLJ, and the identification of some bird contamination on some occasions suggests that all radar data for LLJs could be contaminated by birds. However, a number of observations suggest that this is not the case:

- Nocturnal return has a substantial areal coverage and is most often very homogeneous (over length scales larger than the granularity pattern of a few kilometers), with fairly constant reflectivity levels over an area many states in size. Nocturnal return is also commonly strong throughout a depth of 2 to 3 km. The vertical profile of this reflectivity is highly variable, varying from sometimes fairly constant levels up to 2 km, to sometimes thin vertical layers of high reflectivity. In order for birds to be the source of this reflectivity, they must occur in large numbers evenly distributed through the breadth of a wide area and in varying ways in the vertical.

- Bird rings (expanding rings of reflectivity in the morning which are unequivocally due to birds leaving nesting sites) have reflectivities of 5 to 15 dBZ (Gauthreaux and Belser, 1998), comparable to nocturnal reflectivity values. Bird rings are caused by a fairly dense concentration of birds. In order for the strong nocturnal return to be due to birds, this necessary concentration of birds would have to exist over a large volume of space, and would require a very large number of birds. One bird in a radar probe volume can account for 10 dBZ of echo (O'Bannon, 1995). Using a radar probe volume equal to a 100 meter cube, one bird per probe volume over the state of Oklahoma through a depth of 3 km would require a half billion birds. It is not clear, though, how closely spaced the birds would need to be. One bird per 500 meter cube would only require 4 million birds. However, spacing that wide would tend to imply a more intermittent radar signal at short ranges (where the probe volume is smaller) which is not observed. Gossard and Strauch (1983, p. 174) by counting the number of individual echoes with a 1.5 meter resolution FM-CW radar used at night in July in Nebraska, determined there were about 1 echo per 12 meter cube through a depth of about .5 km. They assumed the echoes were caused by insects. This density would imply about 46 billion members over the state the size of Oklahoma, which would certainly preclude birds.

- The observation that nocturnal return is typically extremely weak over water can perhaps be explained by a reluctance on the part of birds to fly over water. However, Gauthreaux and Belser (1998) show images of clear-air reflectivity at night along the gulf coast in southerly flow (their Fig. 2). Typical of nocturnal return, the images show very weak reflectivity over the Gulf and strong reflectivity over land. In order for this reflectivity to be due to birds, the coastal area must be a source of migrating birds all night, as the radar indicates a southerly (rather than parallel to shoreline) direction. This would tend to violate the continuity equation for birds. Observations of NEXRADs along the Gulf of Mexico coast at night often show a more marked boundary in reflectivity over land and water than that shown by Gauthreaux and Belser. Sometimes the reflectivity extends a little ways out over the Gulf, in which case the birds must somehow be materializing over water (or that they fly at low levels over the ocean and gain altitude over land).

- The observation of bilateral symmetry in PPI displays of reflectivity at night has been cited (Gauthreaux, 1998) in support of the bird hypothesis, as it is reasonable to expect the reflectivity of a complex reflector like a bird to differ depending on the azimuth angle. However, this is really rather strong evidence against the bird hypothesis because this bilateral symmetry is rarely seen at night. If the reflectivity is really caused by migrating birds, the bilateral pattern ought to occur all the time.

- The time-height cross sections of the LLJ obtained with radar in Figs. 4.23-4.26 are also inconsistent with a bird explanation because the measured speeds increase too slowly. Sunset is at near 2Z in the figures and the reflectivity rises to strong values within an hour. If this increase in reflectivity was caused by birds taking off for a nights migration, then there ought to be an abrupt increase in speed of 10 to 20 m/s coincident with the reflectivity increase . Instead, the speed gradually increases from 6 to 10 m/s at .5 km within the hour after sunset. It takes 3 hours after sunset for the speed to increase by 10 m/s.

It is difficult to obtain observations of the numbers and altitudes of birds flying at night, and reports of the actual presence of birds during times when radar winds appear to be in error have not been reported. Mueller (1983) is an exception. He had an optical telescope slaved to a tracking radar with a high intensity light. This permitted visual observation of the scattering object if it was a bird. Still, Mueller could only verify the identity of one echo. A standard method of counting birds at night is to observe moon crossings of birds through a telescope, from which traffic rates can be extrapolated. Gauthreaux (1998) has correlated such bird crossings with NEXRAD reflectivity levels. There is, however, a great deal of scatter in this correlation. Also, bird moon crossings do not give any information on the altitude of the birds.

Ornithologists have used meteorological radars extensively in studying birds. Some of the bird behaviors invoked by meteorologists to explain nocturnal clear-air return may have been learned by ornithologists using radar without confirmation by other means. To avoid erroneous reasoning, only facts about bird behavior learned without radar should be used in support of the theory that radar return is caused by birds. For example, if the fact that birds sometimes migrate at 12 000 feet has been learned by ornithologists by studying radar data without confirmation by other observing methods, then this fact should not be used to support the theory that radar echoes at 12 000 feet are caused by birds. The same is true for facts about insect behavior used to support arguments that clear-air return could be due to insects.

3.4.3 Insects as The Cause of Clear-Air Return

Similar to radar ornithology, radar entomology has existed from practically the beginning of radar. As early as 1949, Crawford (1949) identified insects as the cause of most, if not nearly all, angel echoes. He came to this conclusion on the basis of the difficulty of artificially creating refractive index inhomogeneities strong enough to be sensed by radar, and on visual observations of insects coinciding strikingly with radar observations. Riley (1989) provides a review of radar entomology, and Drake and Farrow (1988) and Burt and Pedgley (1997) review issues of insect migration versus meteorology. Most insects stay close to the surface when under self-directed flight, presumably to stay in the layer of air near the surface where ambient winds are weakest (Srygley and Oliveira, 2001). Insects which fly at altitude migrate primarily with the ambient winds, which are typically much faster than insect self-propelled air speeds. As long as insects are not aligned, they pose little threat to radar wind measurement accuracy. However, insect alignment, believed to occur by entomologists, could add an erroneous 5 m/s to radar-determined winds. Alignment of insects was identified by Riley (1975) in which a bilateral pattern of symmetry in the PPI display of radar echoes was believed to be caused by insect alignment and the higher radar cross-section for insects when observed broadside. Comparison of a pilot balloon and radar tracks indicated that the targets were moving against the wind with an air speed of about 5 m/s. The means by which widely separated insects align themselves in the atmosphere are not known with certainty. A target source similar to insects is balloon spiders (Suter, 1999). In the case of balloon spiders, the long threads of silk used by the spiders to suspend themselves in the atmosphere are potentially good reflectors of radar energy.

The LLJ has been cited by several entomologists (Drake, 1984, 1985, Wallin and Loonan, 1971; Berry and Taylor, 1968) as directly assisting insects in migration. Drake (1984, 1985) studied moths migrating in a nocturnal LLJ in Australia. He also observed with a 3.2 cm radar (common among entomologists) bilateral symmetry of PPI reflectivity scans, presumably due to insect alignment. Drake also observed the radar echoes concentrating into thin layers aloft at an inversion. Drake also noted the rapid increase in reflectivity at dusk, which he attributed to a mass take-off of large insects. Aerial trapping with a kite-borne net confirmed the presence of moths up to an altitude of 220 m. Of course, the confirmation of insects does not prove that most of the radar signal was due to insects, since birds may have been present as well. However, Drake reported radar echoes with a radar cross-section of about 1 cm^2 , typical for large insects. This, combined with the large number of echoes and the trapping of some insects, convinced Drake that most of his echoes were insects. The migration of aphids, a very tiny insect, appears to be greatly aided by the LLJ. Wallin and Loonan (1971) found aphids appearing in Iowa after LLJ episodes advecting air from Kansas, Oklahoma, and Texas, where aphid populations were high. They found that LLJs were a predictor of the timing of aphids and infestation from a plant virus they carried. By using airborne traps, Berry and Taylor (1968) confirmed the presence of aphids to an altitude of 610 m at night in Kansas. The concentration of aphids did not depend on the presence of a LLJ for the cases they had data for. They also found that the concentration at night was about one third that during the day.

Influential studies conducted at Wallops Island in the mid 1960's compared the clear-air reflectivity patterns obtained simultaneously with radars of different wavelengths (3 cm, 11 cm, and 71 cm; Hardy and Katz, 1969). These experiments showed a wavelength dependence of the strength of echo for different kinds of clear-air return. These experiments showed that dot echoes in the lower troposphere decreased in reflectivity at longer wavelengths. This is what is expected for scattering from objects smaller than the wavelength of the radar. Such Rayleigh scattering has an inverse dependence on the fourth power of wavelength. This supported the view that the scatters were small objects, probably insects. Thin layer echoes, on the other hand, were stronger at the longer wavelengths. This dependence was shown to be quantitatively consistent with scattering from index of refraction gradients caused by turbulence which has an inverse dependence on the 1/3 power of wavelength. As a result of these experiments, dot echoes are firmly believed to be due to insects or birds, even if they are concentrated into thin layers several thousand meters aloft. More recent work with multiple wavelength radars by Wilson et al. (1994) came to the same conclusion that most daytime clear-air return is due to insects. Gossard (1990) shows high resolution radar images of dot echoes mostly above an inversion, mostly below an inversion, on both sides of an inversion, and in thin layers 50 meters thick; all of which are identified as insects.

Kropfli (1986) using 3.22 and .86 cm radars in the convective boundary layer (CBL) during the day, deduced that the clear-air reflectivity he routinely sensed in Colorado was primarily due to passive scatters such as seeds, insects, and particulates carried aloft by vertical motions. He noted agreement of VAD winds to within .2 m/s with a tall tower anemometer located nearby. He also noted that the typical clear-air reflectivities of -15 to 5 dBZ (for 3.22 cm radar) were much larger than the -50 dBZ that they would expect if the return was due to index of refraction gradients. This, along with the absence of a maximum in reflectivity near the inversion height, ruled out the index of refraction source of reflectivity.

Sometimes strong clear-air reflectivity events are noticed at the same time as unusual numbers of air-borne insects. For example, Hardy and Katz (1969) report on Benard-like cells seen in clear-air during the day with unusually high reflectivity at the same time as an abnormal number of airborne ants were observed.

A problem with the Wallops Island studies and similar ones is that they were conducted on day-time data, while this research is mostly concerned with nighttime data. Daytime and nighttime clear-air return are distinctly different. This was shown by Zrnić and Ryzhkov (1998) in terms of polarimetric parameters. They compared clear-air return in the daytime (which they assumed was due to insects) with that at night (which they assumed was due to birds). The daytime return had higher differential reflectivity (Z_{DR} values) and lower differential phase than the nighttime return. Zrnić and Ryzhkov had no way to confirm positively that the source of the echoes was zoological.

Perhaps the biggest problem with the insect theory for nocturnal return is the difficulty in explaining the daily cycle of reflectivity. In order to explain the time history of reflectivity seen in Fig. 3.6 (which shows a brief dip at sunset and sunrise and a rapid increase after sunset in height and strength of reflectivity), insects (of perhaps a certain species) must fall out of the sky at sunset shortly before some other insects (of perhaps a different species) take flight, some of which propel themselves upward to several kilometers in an hour. These nocturnal flying insects must stay aloft for the entire night. This scenario of different species of insects to account for the transition from daytime to nighttime characteristics of clear-air data was suggested by Hardy and Glover (1966). Schaefer (1976) describes the pattern seen in Fig. 3.6 and interpreted it as an "impressive" evening take-off of insects (locusts and moths). This identical scenario was described by O'Bannon (1995) as an "explosion" of areal coverage and strength of signal at sunset. He believed it to be due to migrating birds.

3.4.4 Index of Refraction Gradients as The Cause of Clear-Air Return

The question of what causes the backscattered radiation that radars receive from apparently clear skies has been around for almost as long as radars themselves and reflections off of index of refraction gradients was the first explanation offered for them. As early as 1939, Friend (1939, based on work begun in 1935), using a vertically pointing radar operating at wavelength of 125 m with an A-scan display, had found that strong reflectivity layers in the lower troposphere (at 1 to 2 km) were related to temperature inversions (deduced from aircraft soundings and, later, radio soundings, Friend, 1940). He attributed the echos to reflections off gradients in the dielectric constant of the propagating medium; more commonly and equivalently referred to in meteorology as gradients in the index of refraction of the air. Friend also found that he could detect turbulence specifically (as verified by aircraft flight) by the fluctuations in the echos.

That refraction of electro-magnetic energy is significant in the atmosphere is obvious to anyone who has ever observed star twinkle. Refraction in air is essentially non-dispersive at radio wavelengths, so the index of refraction is not a significant function of radar frequency. The index of refraction of the air relative to a vacuum at radio wavelengths is a function most strongly of moisture and, to a lesser extent, of temperature, according to the following approximate formula (Doviak and Zrnić, 1984, Eqn. 2.19):

$$N = (77.6/T)(P + 4810e/T) \tag{3.13}$$

Where N is the refractivity in "N-units" (refractivity is the refractive index minus one times 10^6), P is pressure in millibars, T is temperature in Kelvin, and e is the water vapor pressure in millibars. Atlas (1960) gives the following formula for changes in N under average summer conditions:

$$\Delta N = -1.4\Delta T + 4.2\Delta e$$

If clear-air return can be related to index of refraction gradients, then clear-air radar studies have the potential of providing thermodynamic information, as suggested by Gossard et al. (1999).

Calculations of the index of refraction gradients necessary to account for the observed reflectivities indicated that the necessary gradients were on the order of 20 N-units per centimeter–an extremely high value (Battan, 1973, p.255). Doubts about whether such large gradients could actually exist led to the acceptance of the theory of turbulent Bragg scattering (discussed in detail in Sec. 3.7). In this theory, turbulent flow mixes fluid across some gradient in the index of refraction. This mixing creates a field of refractivity perturbations which leads to a much larger reflectivity than a simple gradient. Calculations made with this theory assume homogeneous, isotropic turbulence and make use of Kolmogorov scaling. Despite all the assumptions, very good agreement was obtained by several researchers between predicted reflectivities and those observed with radars of various wavelengths (Kropfli et al., 1968). This success has led to the belief that the problem of accounting for the reflectivity seen in elevated layers has been conclusively solved. Turbulent Bragg scatter is widely accepted as a major source of clear-air return. However, Gage (1990) reviews research with long wavelength radars which suggests that specular (mirror-like) reflections from strong refractivity gradients may be partly responsible for echoes seen with vertically pointing radars.

A couple classic images of layer echoes supposedly caused by turbulent Bragg scatter actually suggests that reflections can sometimes be the mechanism. Figure 3.7 shows a plot from Lane and Meadows (1963) of reflectivity from a vertically pointing radar with a wavelength of 10 cm (on the left) and measurements made with an aircraft-born refractometer of the index of refraction profile (in N-units) made at the same time (on the right). This figure shows a thin line of reflectivity at the exact same altitude (1.4 km) as a sharp gradient in the index of refraction. Lane and Meadows indicate that the maximum gradient was about 10 N-units per meter. It is not clear if this gradient is sufficient to

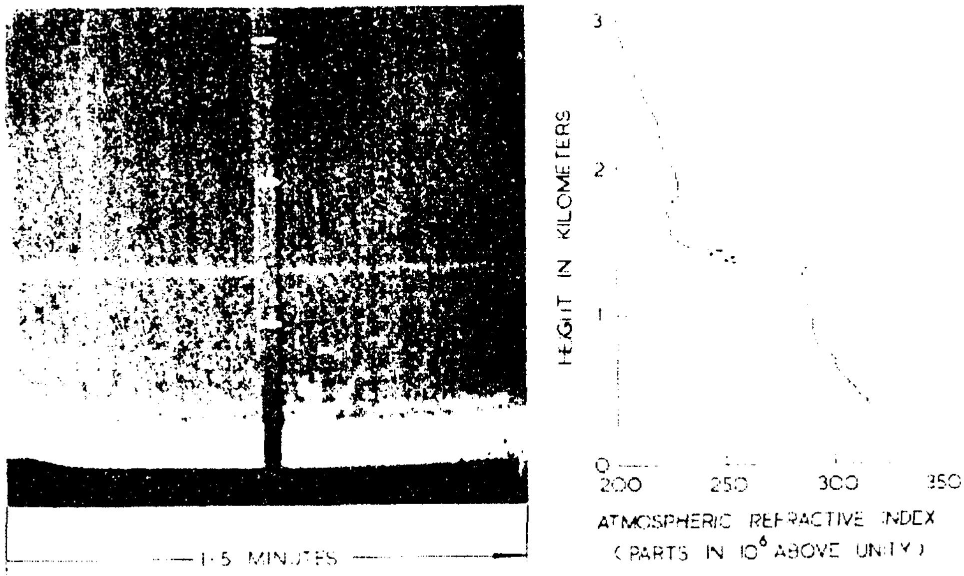

Figure 3.7: Simultaneous radar and refractivity soundings from Lane and Meadows (1963).

account for reflection at a wavelength of 10 cm, but it could still be an underestimate of the actual nearly discontinuous value due to instrumentation limitations. It is very difficult to measure gradients over distances of a few meters with flying aircraft. According to the Bragg scatter theory, this layer of reflectivity must be turbulent in order to generate index of refraction inhomogeneities at half the wavelength of the radar (5 cm in this case). However, the presence of a sharp gradient in thermodynamic properties implies that the flow is definitely not turbulent at this location. The main effect of turbulence is diffusion and smoothing of properties. The existence of a sharp gradient over a distance of a few meters would appear to exclude turbulence at scales greater than a meter. Furthermore, the constant height and thickness of the layer implies that if it was a turbulent layer, the outer scale of eddy size would have to be significantly less than the constant thickness (about 100 meters according to Fig. 3.7). It is much easier to accept that the gradient in index of refraction at this location was much stronger than the instrument was capable of measuring and that what is being seen is actually a specular reflection of radar energy.

Another well-know image reproduced in Figure 3.8 show a layer of reflectivity wrapping-up into Kelvin-Helmholtz (K-H) waves. The radar used was an ultra high resolution FM-CW radar with a range resolution of 1 meter, operating at a wavelength of 10 cm. The use of such a high resolution instrument has revealed a layer of reflectivity as thin as 1 meter.

The radar was pointed vertically and shows structures passing over it. The K-H wave itself is a laminar structure, though it may subsequently break into turbulence. While a pilot flying through a region with K-H waves would experience buffeting of the aircraft and report the experience as "turbulence", it is not turbulence in the more clinical fluid mechanical sense of having a continuous cascade of energy form long to short length scales. In order for the Bragg scatter mechanism to be responsible for the reflectivity in this case, this laminar structure must have a turbulent substructure where there is reflectivity with an outer scale of 1 meter. In addition, the reflectivity of the layer varies as the slope of the layer with vertical segments showing the least reflectivity. This is exactly what would be expected from specular reflections, but not from homogeneous turbulence in which the orientation of the layer shouldn't matter. Finally, broken K-H waves appear at the end of the time-height display, with a greatly diminished reflectivity. This is also exactly what would be expected from the reflection mechanism as turbulent diffusion smooths-out the large index of refraction gradient, but the exact opposite of what would be expected from Bragg scattering since with Bragg scattering, we might expect an increase in scattering with an increase in turbulence. Hardy and Gage (1990) also recognized the problems raised by these measurements for the Bragg scatter mechanism. This reasoning and these figures suggests that measurable reflection of radar energy from index of refraction gradients might occur in the atmosphere. It is not too difficult to accept that, in the absence of turbulence, rather sharp gradients in refractive index can occur and that measurements have simply been too coarse to reveal them.

Pilots also often report very thin layers in the atmosphere which noticeably reflect or scatter light. Such were reported by Friend (1940). Optical scattering seems unlikely to be due to the Bragg mechanism as the wavelengths of visible light are too short (around 1 μm), and are probably below the size of any turbulent eddies.

Using gradients in the index of refraction to explain the nocturnal return over the entire depth of the lower troposphere by either reflection or scattering is problematic, however, because of the granulation of the return. Return is obtained from what appears to be a large number of small reflectors or scatterers through a depth of up to several kilometers.

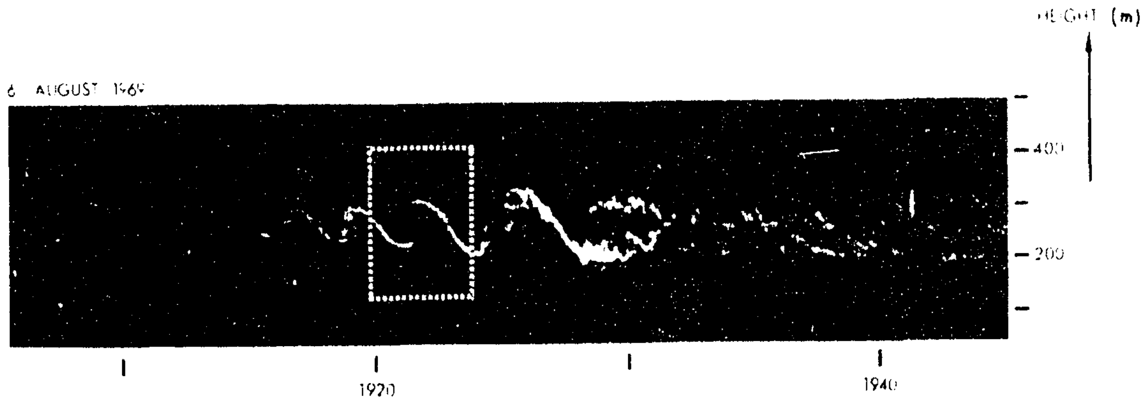

Figure 3.8: Wave features seen with vertically pointing high-resolution FM-CW radar. Horizontal axis is time in minutes. From Gossard and Richter (1970).

To explain this with the reflection mechanism, the existence of areas of sharp gradients distributed throughout space must somehow be explained. It is perhaps possible that sharp vertical gradients form in the stable nocturnal boundary layer which are subsequently gently mixed by flow perturbation, localized convection, or turbulence. However, such a scenario has not been observed in thermodynamic data.

Atlas (1960) directly compared radar echos (from 1.25 cm radar) with sharp gradients in refractivity. Atlas observed sharp gradients in refractivity horizontally along sea breeze fronts and vertically in an inversion, exactly co-located with clear-air return. He specifically was able to exclude birds as a source of echo by having an observer watch the location of the probe volume for birds, and by the fact that the echos were much weaker than birds would have produced. He also ruled out insects as the source of echo due to the lack of a theory explaining how insects could concentrate into thin reflectivity layers aloft, the difficulty in explaining other characteristics of the reflectivity with insect behavior, and due to the excellent agreement between reflectivity and index of refraction gradients. Atlas stated that the evidence in favor of an index of refraction explanation was "overwhelming". This was despite the fact that his observed gradients in refractivity were not large enough to account for measurable echo by reflection. But Atlas accepted that his refractometer would not have been capable of measuring the necessary sharp gradients had they existed. Atlas also applied a theory he devised (Atlas, 1960b) in which curvature of surfaces of refractivity gradient partially focus energy back to the radar, giving echos for much weaker refractivity gradients. This theory has now been abandoned by Atlas and others (Hardy and Gage, 1990).

3.4.5 Summary on the Cause of Nocturnal Clear-Air Return

The general conclusion on the cause of clear-air return as promulgated by various reviews of the topic is that dot echos are due to isolated insects or birds and that diffuse layers or regions of clear-air echo are caused by the turbulent Bragg scatter mechanism, with significant specular reflections rarely if ever happening (except possibly at long wavelengths) due to the excessively large gradients in the index of refraction needed to account for observed reflectivities. Regions of volume-filling, non-granular, clear-air echo could be caused by insects or birds if the density of targets is sufficient to fill every radar volume. Bragg scatter is also expected to be quite weak at the 3 to 11 cm wavelength bands common in surveillance radars, leaving birds or insects to account for strong clear-air return typical at night.

Historically, refractive index gradients were first suspected, but insects were eventually identified as by far the most common source of clear-air dot echoes. More recently, migrating birds have been identified as an important source of nocturnal return which seriously biases wind measurements made with radars. This was first noted in long-wavelength wind profilers, followed the identification of the problem in NEXRAD radars.

Ornithologist and entomologist both use radar to study their creatures. A basic difficulty is the problem of identifying the species being studied. This is a basic problem for meteorologists trying to use clear-air data as well, since they need to know that birds are not biasing velocities. A method to distinguish bird targets from insects is desired, but elusive. Birds can be distinguished if an estimate of the airspeed of the targets can be made. This is often not possible. This leaves ambiguity to many ornithological, entomological, and meteorological studies using clear-air data. It is possible that ornithologists sometimes accidentally study insects while entomologists may sometimes accidentally study birds. It is interesting that Atlas titled his 1960 article "Possible Key to the Dilemma of Meteorological 'Angel' Echoes". 40 years later it remains a dilemma.

This has been and still is a controversial Issue. Atlas (1959) stated, "The evidence indicating that the sea-breeze echoes are due to atmospheric inhomogeneities is overwhelming; the evidence against birds, insects, or other particulate matter being the echo source is similarly impressive." Wilson et al. (1994) stated: "Results...have strongly suggested that the boundary layer clear-air return is generally from insects." Jungbluth (1995) stated "This experiment has revealed conclusively that contamination of the wind profiler data by biological targets does indeed exist". Wilczak et al. (1995) stated, "It has been shown that 915- and 404-MHz wind profiler data are frequently contaminated by migrating birds."

3.5 Mie Scatter Calculations

Eqn. (3.4) above explicitly assumes that rain drops are Rayleigh scatters, i.e., scatters that are much smaller than the wavelength of the radar. For DOW radars, the wavelength is about 3 cm and for the Cimarron and NEXRAD radars, the wavelength is about 10 cm. It will be shown here that the Rayleigh approximation for back scatter cross-section is accurate to 5% for drop radii, r, less than approximately $.02\lambda$. For a NEXRAD and a DOW, this approximation is, then, good for drop radii less than 2 mm and 0.6 mm, respectively. Rain drops vary in size from 100 μ to several millimeters, with a typical size of 1 mm. For insects and birds, which are typically much larger than rain drops, the Rayleigh approximation is not valid at the common meteorological radar wavelengths. In this case, Mie scatter calculations, which can give the correct radar cross section for any object at any radar wavelength should be done.

The equations for scattering from spherical objects were derived first by Mie in 1908 and have been studied in great detail by others since, (e.g., Wiscombe, 1980). The equation for the radar backscatter cross-section from spherical particles in the Mie theory is (Wiscombe, 1979):

$$\sigma_{mie} = \frac{\lambda^2}{4\pi} \left| \sum_{n=1}^{N} (-1)^n (2n+1)(a_n - b_n) \right|^2 \qquad (3.14)$$

Where a_n and b_n are the Mie coefficients which can be expressed as functions of Spherical Bessel and Riccati-Bessel functions of order n. These functions are in turn functions of the

radar wavelength and radar	n	k	$\|K\|^2$
10 cm, NEXRAD, Cimarron	8.88	.63	.928
3.21 cm, DOW	8.14	2.00	.9275
3.19 mm, UMASS	3.41	2.02	.828

Table 3.2: Coefficients for the complex index of refraction of water at 20° from Gunn and East (1954) and Lhermitte (1990); and the resulting values of $|K|^2$ for use in (3.4).

complex index of refraction, the size of the sphere, and the wavelength of the radiation. This equation is generally applicable to the entire electromagnetic spectrum. It is exact for $N \rightarrow \infty$. For practical calculations, N is of the order of the sphere's circumference divided by the wavelength. Computer codes for doing the lengthy and tedious Mie scatter calculations are widely available. This work uses a code obtained from NASA/Goddard and described in Wiscombe (1979, 1980).

The input to the Mie scattering algorithm is the radar wavelength, drop radius, and the complex index of refraction. The complex index of refraction, m=n-ik (which includes the normal index of refraction, n, and the absorption coefficient, k) depends on the radar wavelength and temperature. Values for this study for water were taken from Gunn and East (1954) for 20°C for 10 cm and 3.21 cm wavelengths, and Lhermitte (1990) for 3.2 mm wavelength, as shown in Table 3.2. These wavelengths are very close to those of radars used for this study and the index of refraction is not a strong function of wavelength at microwave wavelengths.

Resulting radar cross sections from the Mie scatter calculations for a range of drop size and for 3 radar wavelengths are shown in Fig. 3.9. On this figure, are plotted for reference the letters 'R', 'I', and 'B' at a location corresponding to the approximate equivalent water sphere sizes for rain drops, insects, and birds (Vaughn, 1985). Also plotted in Fig. 3.9 are three parallel solid lines which are the Rayleigh scatter value, and another solid line crossing the three parallel lines with is the so-called "optical limit" line. This line is the line for which the radar cross-section equals the drop cross-section. For large drop radii, the radar cross-section from Mie calculations are a little below the optical limit due to absorption of energy.

The percent error in the Rayleigh assumption is shown in Fig. 3.10. From this figure, it

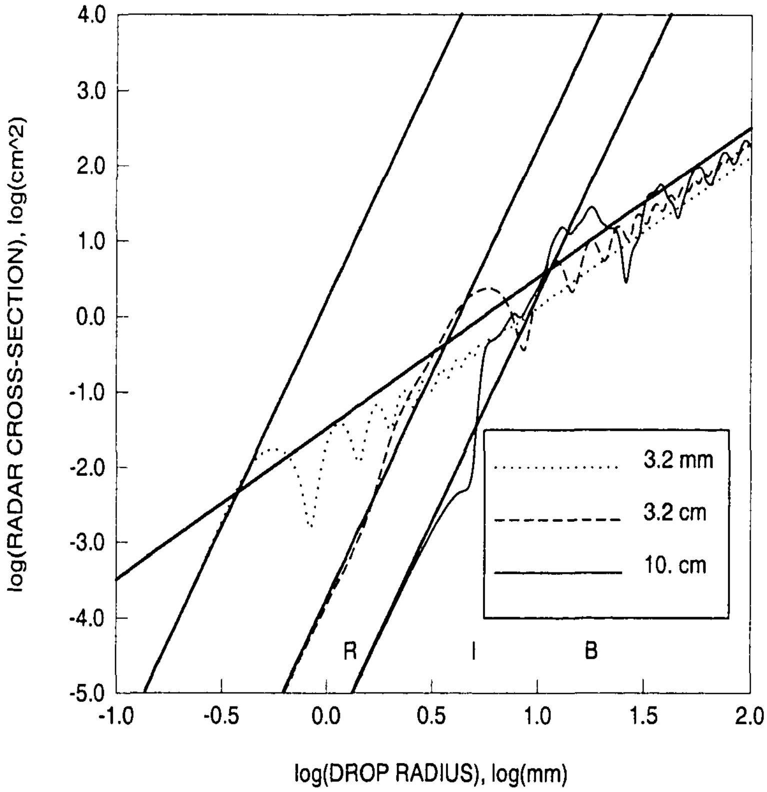

Figure 3.9: Radar cross-section in cm^2 as a function of water sphere radius at 20° C. for 3 mm, 3 cm, and 10 cm radars; from Mie scatter calculations. Three parallel solid lines are the Rayleigh scatter approximation. Solid line crossing the three parallel lines is the line for which the radar cross-section equals the actual spherical cross-section. The letters 'R', 'I', and 'B' are plotted at the approximate equivalent water sphere sizes for rain drops, insects, and birds, respectively.

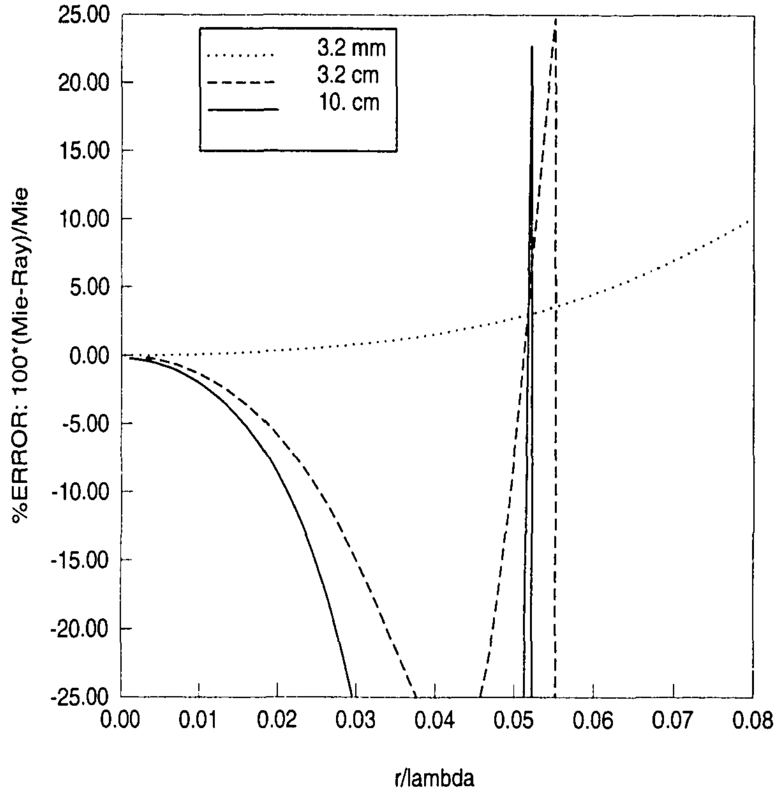

Figure 3.10: Error in Rayleigh approximation of back scatter cross-section, σ, as a function of water sphere radius for three radar wavelengths. Error is calculated as $100^*(\sigma_{Mie} - \sigma_{Rayleigh})/\sigma_{Mie}$.

is clear that the error in calculated cross-sections are less than 5% for approximately r<.02 λ for 3 to 10 centimeter wavelengths and r<.06 λ for a wavelength of 3 mm. Backscatters are good to 25% for r<.04 λ at centimeter wavelengths and for r<.15 λ at the 3 mm wavelength. These limits are consistent with Gunn and East (1954), who did similar calculations.

Radars are configured to give dBZ values for a distribution of Rayleigh scatters, whether the actual targets are such scatters or not. Fig. 3.11 indicates the equivalent reflectivity that a radar would report if a single Mie-scattering water sphere were in the radar beam at a distance of 2 km. This was calculated by solving for Z in (3.7). For the more common case of a distribution of targets, Fig. 3.12 shows the equivalent reflectivity that the three radars would report if there were 5 targets per 20 m cube, all of the same radius. This would constitute a very light shower for small drops. The curves for Fig. 3.12 were calculated from (3.5). For this figure, the curves for all three radars overlap for small radii, as they

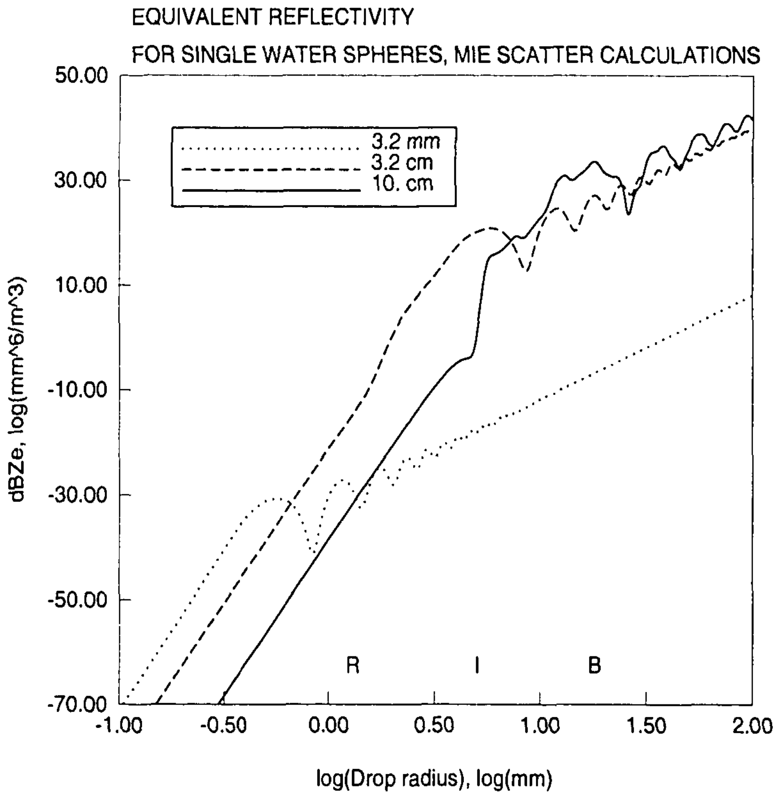

Figure 3.11: Equivalent reflectivity, dBZ_e, for single water spheres at 3 radar wavelengths. Radar parameters from Table 3.1 were used for NEXRAD, DOW, and UMASS radars, with a range of 2 km and $|K|^2 = .93$. A pulse width of 24 meters was used for DOW3, and 1410 m for NEXRAD.

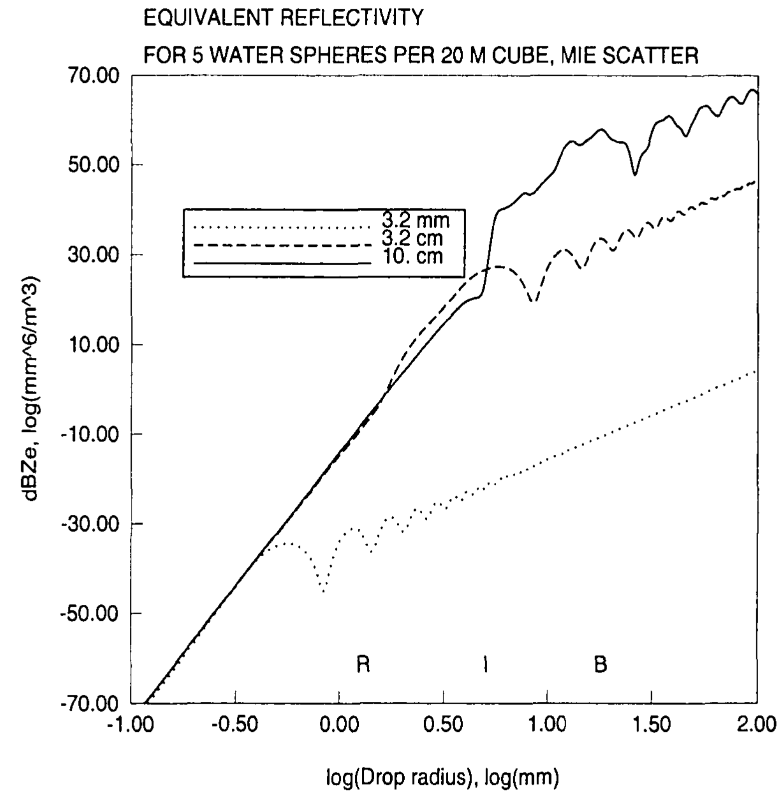

Figure 3.12: Equivalent reflectivity, dBZ_e for a distribution of 5 water spheres per 20 m cube.

should since the Rayleigh approximation and dBZ estimates are accurate for small radii drops.

From these calculations, it is clear that birds and insects may be difficult to distinguish on the basis of back-scatter cross-section or reflectivity alone. While birds are almost always larger than insects, reported values for radar cross-section (Vaughn, 1985; Riley, 1985) of birds and insects show considerable overlap, with insects ranging from 10^{-3} cm^2 to 10 cm^2 and birds ranging from 10^{-1} cm^2 to 10^3 cm^2.

3.6 Theory of Radar Reflections from Refractivity Gradients and Discontinuities (Fresnel Reflection)

In this section, a theoretical development from first principles is given for predicting the amount of energy reflected from changes in the index of refraction of the propagating medium. This section covers mirror-like or specular reflections from planar discontinuities

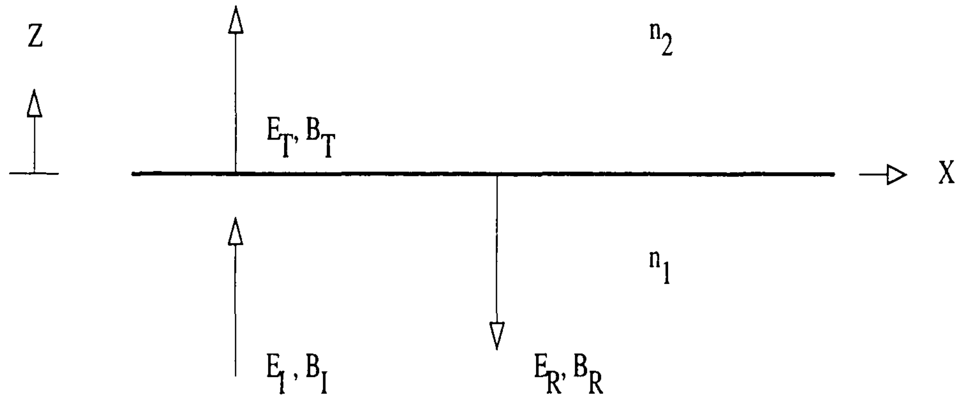

Figure 3.13: Conceptual diagram for electromagnetic planar wave reflection/transmission, at the interface between two media of different refractive indicies.

and gradients in the index of refraction. From electro-magnetics theory, the first principles are Maxwell's equations, which include Faraday's and Ampere's Laws.

For a single reflection of a plane wave propagating from a medium with refractive index n_1 across a discontinuity in n into a medium of index of refraction n_2, we refer to Fig. 3.13. With a propagation speed of c, wavelength of λ and a frequency of ω, $\overrightarrow{E_I}$ and $\overrightarrow{B_I}$ are the incident electric and magnetic fields, respectively, oscillating in the x-y plane (i.e., pointing in a direction transverse to the direction of propagation) and propagating in the z-direction:

$$\overrightarrow{E_I} = \overrightarrow{E_I}(z,t)\ with\, amplitude\, E_I cos(kz - \omega t)$$

$$and$$

$$\overrightarrow{B_I} = \overrightarrow{B_I}(z,t)\ with\, amplitude\ B_I cos(kz - \omega t) \qquad (3.15)$$

$$where\ k = \frac{2\pi}{\lambda}$$

$\overrightarrow{E_R}$ and $\overrightarrow{B_R}$ are the reflected electric and magnetic fields and $\overrightarrow{E_T}$ and $\overrightarrow{B_T}$ are the transmitted fields. $\overrightarrow{E_I}$, $\overrightarrow{E_T}$, $\overrightarrow{E_R}$, and $\overrightarrow{B_I}$, $\overrightarrow{B_T}$, $\overrightarrow{B_R}$ are all in phase at the interface. The direction of the electric and magnetic field vectors is perpendicular to the direction of propagation, z.

By Faraday's Law:

$$\nabla X \vec{E} = -\frac{\partial \vec{B}}{\partial t} \qquad (3.16)$$

and from [3.15], $\frac{\partial \vec{B}}{\partial t} = -\omega \vec{B}\tan(\text{kz-}\omega\text{t})$ and $\nabla X \vec{E} = k\hat{k}X\vec{E}\tan(\text{kz-}\omega\text{t})$ with $\hat{k}$ the unit vector in the z-direction.

$$\Rightarrow \vec{B} = \frac{k\hat{k}}{\omega}X\vec{E}$$

By definition, the index of refraction is

$$n \equiv \frac{c_{vacuo}}{c_{dielectric}} = \frac{kc}{\omega}$$

$$\Rightarrow \vec{B} = \frac{n}{c}\hat{k}X\vec{E} \tag{3.17}$$

[3.17] requires that $\vec{E_I}$ and $\vec{B_I}$ are in phase, which was assumed in [3.15].

By Ampere's Law:

$$\oint \vec{B} \cdot d\vec{l} = \int_s \mu_0\epsilon_0 \frac{\partial \vec{E}}{\partial t} \cdot d\vec{A} + \int_s \mu_0 \vec{J} \cdot d\vec{A} \tag{3.18}$$

For no currents present, $\vec{J} = 0$ and using a rectangular prism with faces parallel to the interface, $\frac{\partial \vec{E}}{\partial t} \cdot d\vec{A} = 0$ on the faces of the prism parallel to the interface as $\vec{E}$ is $\perp$ to d$\vec{A}$. By symmetry, $\int \frac{\partial \vec{E}}{\partial t} \cdot d\vec{A}$ over the faces perpendicular to the interface vanishes.

$$\Rightarrow \oint \vec{B} \cdot d\vec{l} = 0 \tag{3.19}$$

Taking this integral around a rectangular circuit surrounding the interface with two sides parallel to the interface gives:

$$B_I + B_R = B_T \tag{3.20}$$

Similarly, Faraday's law in integral form gives

$$\oint \vec{E} \cdot d\vec{l} = -\int_s \frac{d\vec{B}}{dt} \cdot d\vec{A} \tag{3.21}$$

with $\overrightarrow{B}$ parallel to the interface, $\int_s \frac{d\overrightarrow{B}}{dt} \cdot d\overrightarrow{A} = 0$ and $\oint \overrightarrow{E} \cdot d\overrightarrow{l} = 0$ implies:

$$E_I + E_R = E_T \tag{3.22}$$

By [3.17]:

$$\begin{aligned} B_I &= \frac{n_1}{c} E_I \\ B_R &= -\frac{n_1}{c} E_R \, (E_R \, in \, opposite \, direction \, of \, E_I) \\ B_T &= \frac{n_2}{c} E_T \end{aligned}$$

and [3.20] becomes:

$$n_1 E_I - n_1 E_R = n_2 E_T \tag{3.23}$$

Eliminating E_T from [3.22] and [3.23] gives:

$$\frac{E_R}{E_I} = \frac{n_1 - n_2}{n_1 + n_2} \tag{3.24}$$

[3.24] is know as "the Fresnel equation for normal incidence".

The energy flux vector is the Poynting vector, $\overrightarrow{S}$:

$$\overrightarrow{S} = \frac{1}{\mu_0} \overrightarrow{E} X \overrightarrow{B} \tag{3.25}$$

With $\overrightarrow{E}$ and $\overrightarrow{B}$ mutually perpendicular:

$$\overrightarrow{S} = \frac{1}{\mu_0} EB\hat{k}$$

and by [3.17]

$$S = \frac{n}{c\mu_0} E^2$$

The ratio of incident to reflected energy, R, is the square of [3.24], called the "reflectivity" in electrodynamics (not to be confused with reflectivity in radar meteorology, which is the

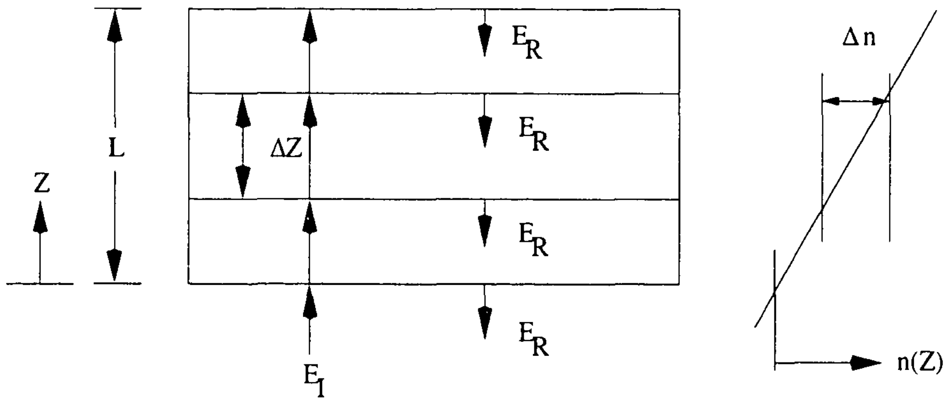

Figure 3.14: Conceptual diagram for electromagnetic energy reflection from an index of refraction gradient

back scatter cross-section per unit volume):

$$R = \left(\frac{E_R}{E_I}\right)^2 = \left(\frac{n_1 - n_2}{n_1 + n_2}\right)^2 \tag{3.26}$$

In air, n≈ 1 (typically 1.0002 in the lower troposphere) so for a discontinuous change in n of Δn , [3.26] is:

$$R = \left(\frac{\Delta n}{2}\right)^2 \tag{3.27}$$

So far, this development has followed that found in standard texts on classical electrodynamics (e.g., Jackson, 1962). We now use these results to calculate the energy reflected from a gradient. Similar derivations have appeared in technical reports by Swingle (1950) and Bauer (1956). The book by Brekovskikh (1960) also covers this topic in some detail for various forms of layered media for the reflection of acoustic and electro-magnetic waves (the former being of interest to seismologists). We divide the gradient into a series of differential steps of spatial size Δz and diffraction change Δn. Fig. 3.14 illustrates the situation, where L is the radar pulse width. The electric field received at the antenna, $\overrightarrow{E_M}$, will be the sum of all the differential wave reflections that reach the receiver at one time. These waves will generally have different phases depending on z, the point at which the reflection occurred. With $\left|\overrightarrow{E_I}\right| = E_I cos(\omega t)$ and using [3.27]:

$$\left|\overrightarrow{E_m}(t)\right| = \Sigma_{z=0}^{L/2} \frac{\Delta n}{2} E_I cos(\omega t + \phi) \tag{3.28}$$

ϕ is the phase of the differential reflection relative to $\overrightarrow{E_I}$ at z=0. [3.28] neglects secondary reflections and attenuation, which are good approximations if Δn is small (it is typically $\sim 10^{-4}$) and R in [3.27] and [3.26] is small. The summation is over L/2 instead of L because reflected energy from only 1/2 the pulse width is received by the antenna at one time. To see this, consider that if the receiver is gated to measure energy reflected from the back of the pulse at z=0 at t=t_0. All energy reflected at later times as the pulse propagates in the z-direction will arrive after t_0 and will not add to $\overrightarrow{E_M}$. However, some energy reflected from the pulse at earlier times and at distances z>0 will arrive at the same time. Since the outbound pulse travels at the same speed as inbound reflections, reflections from locations z$\leq \frac{L}{2}$ will arrive at the same time as those from z=0.

With $\Delta n = \frac{dn}{dz}\Delta z$ for a constant refractive index gradient, and $\phi = \frac{4\pi z}{\lambda}$ [3.28] becomes

$$\left|\overrightarrow{E_M}(t)\right| = \Sigma_{z=0}^{\frac{L}{2}} \frac{dn}{dz}\frac{\Delta z}{2} E_I cos(\omega t + \frac{4\pi z}{\lambda})$$

as $\Delta z \to 0$

$$\left|\overrightarrow{E_M}(t)\right| = \frac{dn}{dz}\frac{E_I}{2}\int_0^{\frac{L}{2}} cos(\omega t + \frac{4\pi z}{\lambda})\, dz \tag{3.29}$$

With some manipulations:

$$\begin{aligned}\left|\overrightarrow{E_M}(t)\right| &= \frac{dn}{dz}\frac{E_I}{2}\frac{\lambda}{4\pi}\left[\Big|_0^{\frac{L}{2}} sin(\omega t + \frac{4\pi z}{\lambda})\right] \\ &= \frac{dn}{dz}\frac{\lambda}{8\pi}E_I\left[sin(\omega t + \frac{2\pi L}{\lambda}) - sin(\omega t)\right]\end{aligned}$$

or

$$\left|\overrightarrow{E_M}(t)\right| = \frac{dn}{dz}\frac{\lambda}{8\pi}E_I(sin(\omega t)cos(\frac{2\pi L}{\lambda}) + cos(\omega t)sin(\frac{2\pi L}{\lambda}) - sin(\omega t))$$

This is equivalent to:

$$\left|\overrightarrow{E_M}(t)\right| = \frac{dn}{dz}\frac{\lambda}{8\pi}E_I\left[\sqrt{2 - 2cos(\frac{2\pi L}{\lambda})}\right] sin(\omega t + \psi)$$

where ψ is a phase angle:

$$tan(\psi) = \frac{sin(\frac{2\pi L}{\lambda})}{cos(\frac{2\pi L}{\lambda}) - 1}$$

$\left|\overrightarrow{E_M(t)}\right|$ is then sinusoidal in time with an amplitude, E_M:

$$E_M = \frac{dn}{dz}\frac{\lambda}{8\pi}E_I\sqrt{2 - 2cos(\frac{2\pi L}{\lambda})}$$

The reflectivity is then:

$$R = \left(\frac{E_M}{E_I}\right)^2 = \left(\frac{dn}{dz}\frac{\lambda}{8\pi}\right)^2 (2 - 2cos(\frac{2\pi L}{\lambda})) \tag{3.30}$$

[3.30] contains a cosine term, the value of which depends on the gate width L. Radars determine received power by averaging typically around 100 pulses. Typical pulses are about 300 m in length and typical wavelengths are about 10 cm, or 1/3000 of a pulse length. It is therefore not expected that L of the transmitted radiation will be exactly the same (to within a fraction of λ) in each pulse (variation in L laterally across the pulse would have the same effect), so $\frac{2\pi L}{\lambda}$ will be an essentially random phase and the radar will detect the average of [3.30] over L which is:

$$R = 2\left(\frac{dn}{dz}\frac{\lambda}{8\pi}\right)^2 = \left(\frac{1}{2}\frac{dn}{dz}\frac{\lambda}{2\sqrt{2}\pi}\right)^2 \tag{3.31}$$

A similar result was derived by Swingle (1950) and Bauer (1956). A form of the Swingle equation, equivalent to one half of (3.31), was used by many researchers in the 1950's (e.g., Atlas, 1960b), which leads to a factor of 2 underestimation in the reflectivity of refractive index gradients.

If L was exactly the same in each pulse used to obtain the average power, then R could vary by a factor of 0 to 2 from (3.31). Comparing [3.31] and [3.27], we note that a radar will effectively see a refractive index gradient as if all the n-change through a distance $\frac{\lambda}{2\sqrt{2}\pi}$ was concentrated into a discontinuity. The actual size of the pulse width, L, does not matter. For this reason, longer wavelength radars are expected to more easily detect refractive index gradients.

If the entire refractive index gradient occurs in a thin layer with a thickness, $\triangle s$, less than L/2, then the integration of [3.29] is carried out over $\triangle s$ instead of L/2, and [3.30] becomes:

$$R = \left(\frac{dn}{dz}\frac{\lambda}{8\pi}\right)^2 (2 - 2cos(\frac{4\pi\Delta s}{\lambda}))\ for\ \Delta s \le \frac{L}{2} \tag{3.32}$$

In this case, we need to keep the cosine term as the actual layer thickness will approach λ. The total change in n across this thin gradient is $\Delta n = \frac{dn}{dz}\Delta s$ or $\frac{dn}{dz} = \frac{\Delta n}{\Delta s}$. For a given Δn, we can examine what happens as $\Delta s \to 0$ and the gradient becomes a discontinuity. For small Δs :

$$1 - cos\frac{4\pi\Delta s}{\lambda} \approx \frac{1}{2}\left(\frac{4\pi\Delta s}{\lambda}\right)^2$$

and [3.32] $\Rightarrow$

$$R = \left(\frac{\Delta n}{\Delta s}\frac{\lambda}{8\pi}\right)^2 \left(\frac{4\pi\Delta s}{\lambda}\right)^2 = \left(\frac{\Delta n}{2}\right)^2$$

which recovers the discontinuity formula [3.27].

If the entire n-gradient within the probe volume of length L/2 had been concentrated into a single discontinuity, then, by (3.27) the reflectivity would be:

$$R = \left(\frac{\frac{dn}{dz}\frac{L}{2}}{2}\right)^2$$

This is $\left(\frac{L\pi}{2\lambda}\right)^2$ times the value of R for a constant gradient from (3.31). For a NEXRAD L of 250 m and λ of 10 cm, the gradient reflectivity is one fifteen millionth of that from the same n change in a discontinuity (or 70 dB weaker). This enormous decline in reflectivity is due to the destructive interference of the energy reflected across the gradient, energy which is mostly not in phase. Clearly, if refractivity gradients can be sharp, with significant changes occurring over a distance of a radar wavelength, then the reflectivity can be orders of magnitude stronger then for gradual gradients. Because of instrumentation limitations, it is difficult to measure gradients of refractivity in the atmosphere at scales much less than a meter, consequently it is not known precisely how sharp gradients typically are. It is commonly assumed that discontinuities sufficient for strong reflections do not normally occur.

To determine the effective reflectivity factor, Z_e, a radar would detect if it was observing a discontinuity or gradient in n, we first find the reflectivity, η, the backscatter cross section per unit volume. For a single discontinuity, the backscatter cross section for a reflection is RA_r, where A_r is the cross sectional area at the probe volume. This implies $\eta = \frac{RA_r}{A_r L/2} = \frac{2R}{L}$. Using (3.5) we then find Z_e for a gradient in n:

$$Z_e = \frac{\lambda^4}{\pi^5 |K|^2} \frac{2}{L} (2(\frac{dn}{dz} \frac{\lambda}{8\pi})^2 \approx 2.2X10^{-5} \frac{\lambda^6}{L} \left(\frac{dn}{dz}\right)^2 \tag{3.33}$$

and for a discontinuity in n of Δn:

$$Z_e = \frac{\lambda^4}{\pi^5 |K|^2} (\frac{\Delta n}{2})^2 \tag{3.34}$$

Strictly speaking, this derivation is for radiation reflected from planes perpendicular to the radar beam. Layers of refractive index perturbations occurring at other angles would reflect energy specularly at this angle and not be seen by the radar. However, undulations in the surface might be expected to give back-scattering through a wide range of incidence angle.

Using these equations, we can revisit the thin reflectivity layer of Lane and Meadows (1963) shown in Fig. 3.7. The radar display is an analog representation of signal power. The refractivity sounding shows a near discontinuity in n of 30 N-units, or .00003. By (3.34) this would give a reflectivity of 19 dBZ for the 10 cm Lane and Meadows radar. Other parameters of the radar are: P_t=500,000 W; L=30 m; beam width=3.6° (antenna gain of 34 dB); a noise level of -91 dBm (for a signal to noise ratio of 1); a detection threshold of -104 dBm; and a range to the layer echo of 1.3 km. Using these values and assuming system losses of about 5 dB, we can apply (3.10) to calculate the expected signal strength:

$$dBm = dBZ - 94.4$$

This discontinuity would therefore give a signal of -75.4 dBm, which is 29 dB above the detection threshold for a signal-to-noise ratio of 16 dB. If the observed refractivity change was concentrated into a discontinuity, then it would have been easily detected by the Lane and Meadows radar. If instead of a discontinuity, the refractivity change occurred gradually across a gradient, then we apply (3.33) with (3.10) yielding:

$$dBm = 20log(\frac{dn}{dz}) - 36$$

With a detection threshold of -104 dBm, this would mean that the gradient would have to be at least 30 N-units in 8 cm, or that the refractivity change would need to be concentrated into a layer at most 8 cm deep.

3.7 Bragg Scatter

The scattering of radar energy from inhomogeneities in the index of refraction of air generated by the action of turbulence on a mean gradient in refractivity, is currently commonly referred to as "Bragg scatter". It is referred to in the meteorological literature by various other terms, including: Refractive index turbulence (RIT) and turbulence scatter. The term "Bragg scatter" was borrowed from the physics of X-ray diffraction from crystals, wherein the Bragg condition must be met. As will be discussed later in this section, the selection of the term "Bragg" to describe this kind of scattering is confusing as the phenomenon has little in common with X-ray diffraction. However, the term has become fairly common in recent years and an attempt to change it will not be made here.

Fairly complete reviews of Bragg scatter (each from different perspectives and with differing notation) are available from Tatarski (1961), Gossard and Strauch (1983), and Doviak and Zrnic (1984). Tatarski gives the best discussion in terms of the underlying physical arguments, though it is necessary to read most of the book in order to follow the notation. Many aspects of Tatarski (1961) are closely followed by Doviak and Zrnic (1984) and Gossard and Strauch (1983)

The Bragg scatter theory has its origin in high energy physics where Bragg's law (or the Bragg condition) is used to predict the conditions under which diffracted X-ray beams from a crystal are possible. The term "Bragg scatter" does not appear in high energy physics, with the term "diffraction" being selected instead for the phenomenon of interest.

3.7.1 The Bragg Condition and X-Ray Diffraction

Readable discussions of this topic can be found in most second year general physics texts (e.g., Tipler, 1978).

X-rays were discovered in 1895 by Wilhelm Roentgen (for which he won the first Nobel Prize granted in physics in 1901). By 1899, H. Haga and C. H. Wind had estimated the wavelength of X-rays to be of the order of 1 Angstrom by observing a slight broadening (presumably diffraction) of X-rays after passing through slits a few thousandths of a millimeter wide. Precise measurement of the wavelength of X-rays were elusive because of the difficulty in constructing diffraction gratings with a spacing small enough for significant diffraction to occur. In 1912, Max von Laue realized that the estimated spacing of the atoms in a regular crystal lattice was about the same as the estimated wavelength of X-rays, and therefore, that crystals could act as a three-dimensional diffraction grating for X-rays. Experiments by Laue demonstrated X-ray diffraction from crystals and confirmed theories of both the wave nature of X-rays and the regular structure of crystals. Laue received the Nobel prize for discovering X-ray diffraction in 1914. Methods to quantitatively analyze X-ray diffraction were devised by W. H. Bragg and W. L. Bragg (father and son), work for which they received the Nobel prize in 1915 (W. L. Bragg was the youngest recipient of a Physics Nobel). X-ray diffraction is still a principle tool used by crystallographers.

In X-ray diffraction studies, a collimated beam of X-rays are passed through a crystalline material (in modern work, this is usually a fine powder, but classically, it was a single crystal), and a pattern of diffraction spots will be exposed on a photographic plate behind the crystal. By classical diffraction, each atom in the crystal can be thought of as acting as a spherical radiation source. The diffracted energy pattern is the sum of the radiation from each atomic source. When all these waves interfere constructively, a spot (or image of the radiation source) appears. Constructive interference occurs because there are certain characteristic spacings of the atoms in the crystal. If the atoms were randomly arranged, only a diffuse and weak pattern of radiation would result. The Braggs realized that the characteristic beam diffraction angles of X-rays were related to the spacing between planes in which the atoms in the crystal lie. Fig. 3.15 is a simple diagram of an

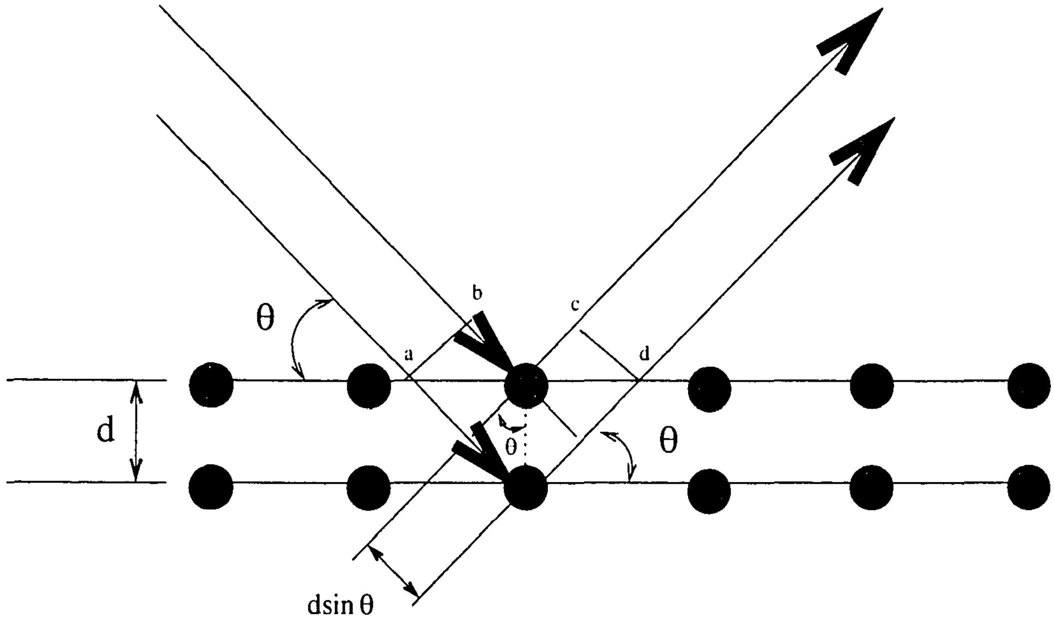

Figure 3.15: X-ray wave front a-b reflecting from a family of planes in a crystal with reflected wave front c-d.

incoming wave front being reflected from a family of planes in a crystal. The incoming wave front is at a-b and the reflected front is at c-d. The reflected wave front energy will be the result of constructive interference only if the path difference between the two fronts is an integral number of wavelengths. This leads to the Bragg condition:

$$2dsin\theta = m\lambda \tag{3.35}$$

Where d is an interplanar spacing, θ is the angle the beam makes with the plane (and the diffracted beam angle), and m is an integer. For even simple crystals, numerous planes exist and deducing the crystal structure from diffraction information is a complex problem. Early X-ray experiments also had "unclean" radiation with multiple wavelengths. The Braggs first had to measure the wavelengths of their radiation by using crystals of known geometry (NaCl); they could then measure interplanar spacings (d) of other crystals using the then known wavelengths of their radiation, and finally they could deduce the previously unknown crystal structure.

It is instructive that modern X-ray crystallography uses fine powders rather than single crystals. Since planes of atoms only reflect energy specularly, only planes which have certain orientations with respect to the incoming radiation (values of θ which satisfy (3.35)) will give rise to constructive interference and diffraction spots. By using a powder of crystals, all possible angles are present simultaneously, and all the possible diffraction angles are obtained without having to rotate a crystal.

3.7.2 The Bragg Condition in Radiation Scatter from Turbulent Air

In the Bragg scatter theory, turbulent mixing of a mean refractive index gradient leads to local perturbations in the refractive index. By applying the Bragg condition, only turbulent eddies about the size of half the radar wavelength ultimately contribute to the received signal. This results in an expression for the backscatter energy from such eddies as a function of the amount of turbulence, the mean refractive index gradient, and the radar wavelength.

The development of this theory was driven in significant part by the need to explain beyond the horizon propagation of radio waves (e.g., the exceptional long range of short wave radios). For such long range propagation, it was eventually deduced that radio waves were scattered in the forward direction from the ionosphere by turbulence-induced fluctuations in the electron density. The same theory was applied to scattering in forward and backward directions of radio waves in the troposphere, with fluctuations in refractive index replacing fluctuations in electron density. Booker and Gordon (1950), Gallet (1955) and Villars and Weisskopf (1955) identified turbulent mixing as the primary mechanism for such scattering, however, the quantitative theories they proposed were later replaced by a statistical theory using Obukov/Kolmogorov scaling. This application was accomplished by Silverman (1956), who derived equivalent forms for the equations still used today. Silverman points to Krasilnikoff (1949) and Batchelor (1955) as earlier, similar work which he discovered after finishing his 1956 paper. While Silverman (in 1956) arrived at the form of the theory still used today, the book by Tatarski (1961, translated by Silverman) is often cited as a basic reference.

There are three main steps of physical/mathematical reasoning which lead to a simple expression for radar back scatter: Obukov/Kolmogorov scaling to give an expression for the spectral density function of index of refraction gradients, the solution of Maxwell's equations so as to obtain energy emission from radar targets in terms of perturbations in index of refraction, and the derivation of an integral to give the total scattered energy as a function of this spectral density function. The Bragg condition does not need to be explicitly invoked. The purpose of the rest of this section is not to redevelop the theory stated in Tatarski (1961), but to provide the basic physical and mathematical reasoning behind the resulting expression for reflectivity. The complete derivation is lengthy and involves various subtle mathematical manipulations and has been reviewed by Tatarski (1961) and Doviak and Zrnic (1984).

The development in Tatarski (1961) follows the scaling arguments of Obukov (1949) and Yaglom (1949), treating refractive index as a passive additive scaler. Obukov and Yaglom base their development on the classic scaling arguments of Kolmogorov. It is generally assumed that the turbulence is homogeneous, isotropic and statistically steady in some local region, and that the fluid is incompressible. These scaling arguments lead to the following expression for the spectral density function of refractive index inhomogeneities (Tatarski, p. 48):

$$\Phi_n(K) = \frac{\Gamma(8/3) * sin(\pi/3)}{4\pi^2} C_n^2 K^{-11/3} \approx .03301 C_n^2 K^{-11/3} \approx .033 C_n^2 K^{-11/3} \tag{3.36}$$

where:

Φ_n(K) = spectral density function of the refractive index perturbations

K= spatial wave number in any spherical direction $=4\pi/\lambda_s$, for a spatial wave length λ_s

C_n^2 = the refractivity structure parameter

C_n^2 is defined in connection with the structure function for refractive index, n, D_n :

$$D_n(r) = \overline{[n(r_1) - n(r + r_1)]^2}$$

Where r is a spherical distance relative to the location of r_1. D_n, the autocorrelation of refractive index inhomogeneities, is a representation of the intensity of the turbulent fluctuations in n. Kolmogorov scaling arguments lead to:

$$D_n(r) = C_n^2 r^{\frac{2}{3}}$$

Where C_n^2 is:

$$C_n^2 = L_o^{\frac{4}{3}} (\overrightarrow{\nabla} n)^2 \tag{3.37}$$

With L_o being an outer scale of the turbulence. Doviak and Zrnic (1984, Ch. 11) derive a more complex formula for C_n^2 as a function of thermodynamic variables, wind shear, and eddy dissipation. The spectral density function, Φ_n(K), is the Fourier transform of D_n(r), leading to (3.36). D_n(r) is therefore the inverse Fourier transform of Φ_n(K). (3.36) is, of course, only valid for wave numbers in the inertial sub-range of turbulence.

The expression for backscatter cross-section per unit volume, η, in terms of a field of refractivity perturbations, derived by a perturbation analysis of Maxwell's equations is, after integrating over the probe volume, V, Tatarski (1961, p. 65-66):

$$\eta = \frac{64\pi^2}{\lambda^4 V} \int\int \overline{n(r_1)n(r_2)} e^{-ik2|\overrightarrow{r_1} - \overrightarrow{r_2}| sin(\theta_s)} dV_1 dV_2 \tag{3.38}$$

Where:

θ_s =half the angle between transmitting and receiving directions.

k = radar wavelength $=4\pi/\lambda$

For backscatter, θ_s=$\pi/2$.

Since $\overline{\Delta n(r_1)\Delta n(r_2)}$ is just the structure function, D_n, this is recast with D_n replaced by its Fourier integral, and with $\rho = |\overrightarrow{r_1} - \overrightarrow{r_2}|$:

$$\eta = \frac{64\pi^2}{\lambda^4 V} \int\int\int \Phi_n(K) e^{-iK\rho} dK e^{-ik2\rho sin(\theta_s)} dV_1 dV_2 \tag{3.39}$$

This integral can be rearranged to contain the term $e^{-ip(K-2ksin(\theta_s))}$. This integral will tend towards zero except for K=2ksin(θ_s); since, similar to the analysis for Fourier coefficients, for K$\neq$2ksin(θ_s), the integrated function has positive and negative regions which tend to cancel. This implies:

$$\lambda_s = \frac{\lambda}{2sin(\theta_s)} \; or \; \lambda_s = \frac{\lambda}{2} \; for \; backscatter$$

(3.39) can be interpreted as a Fourier integral in which the Fourier component of the structure function at K=2ksin(θ_s) results. This can also be seen as being equivalent to the Bragg condition (3.35) for m=1. Tatarski (1961) appears to have been the first to identify the condition as the same as the Bragg condition. Earlier workers simply carried-out the integrations without such a physical interpretation. Despite the fact that the integration does select that part of the refractive index inhomogeneities with a length scale of half the radar wavelength, there is a significant difference between this situation and X-ray diffraction from crystals. In the latter case, interference spots occur because of certain characteristic spacings in crystal, while in the former, no such spots occur as there is no uniform organization to the turbulent eddy structure. If the refractivity perturbations occurred randomly, the spectral component of this random field would still have a component near $\lambda/2$ that would be responsible for the scattered energy. Indeed, this result is similar to the integration producing a formula for reflections from index of refraction gradients, which also has a dependence on radar wavelength (Sec. 3.6). While the Bragg condition in relation to radar scatter from turbulent air was first identified by Tatarski (1961), the generalization to the term "Bragg scatter" appeared first in print (apparently) in Gossard et al. (1982).

After substituting (3.36) into (3.39) and executing the integrations, the resulting expression for η in backscatter is (Tatarski, 1961):

$$\eta = \frac{\pi^2}{2} k^4 \Phi_n(k)$$

substituting (3.36) into this $\Rightarrow$

$$\eta = 0.38C_n^2\lambda^{-1/3} \tag{3.40}$$

To convert this to effective reflectivity factor, Z_e, from (3.5):

$$Z_e = \frac{\lambda^4}{\pi^5 |K|^2}\eta$$

$$\Rightarrow \; Z_e = .0013C_n^2\lambda^{11/3} \tag{3.41}$$

Direct experimental verification of (3.40) was carried out by Kropfli et al. (1968). They towed a refractometer of the Birnbaum type suspended from a helicopter on an inbound radial. Simultaneously, a 10 cm radar tracked the helicopter and measured the reflectivity ahead of it. By this means, simultaneous measurements were made of η and C_n^2. They effectively found that (3.40) fit the data, with considerable scatter, to within a factor of 2 on two clear-air days. This has been considered exceptionally good agreement, considering all the assumptions that went into the theory. Indeed, on one of these two days, organized convective cells were seen in the radar imagery. Flows of this nature are dominated by buoyancy and the assumption of isotropic turbulence is probably a poor one, yet the theory of Bragg scattered seemed to work reasonably well anyway.

We again revisit the layer echo seen by Lane and Meadows (1963) shown in Fig. 3.7 in order to calculate the expected signal strength that might occur due to Bragg scatter. The level of turbulence is not known directly, nor is the wind shear or buoyancy profile. However, the thin layer implies a discontinuity in fluid properties over a vertical distance of at most a few meters. This implies that the outer turbulence scale is on the order of a few meters. If turbulence is present, as we are assuming for Bragg scatter, then there is mixing of the two fluid regions across this distance, and the mean gradient in refractivity is then approximately $\left|\vec{\nabla} n\right| = \frac{\Delta n}{L_o}$. Combining (3.37) and (3.41):

$$Z_e = .0013L_o^{-2/3}(\Delta n)^2\lambda^{11/3}$$

With Δn=.00003, L_o=3 m, and λ=.1 m, this gives a reflectivity of 21 dBZ_e, some 31 dB above the detection threshold at a range of 1.3 km for this particular radar. This result is very close to that found for a reflection from a discontinuity (19 dBZ_e) in Sec. (3.6), with a discontinuity in the refractivity assumed rather than turbulence. This is not too surprising since the turbulence acts on the existing refractivity gradient and mixes the perturbations throughout the mixing zone, rather than having them in one place as in a lamina. The magnitude of the perturbations in refractivity is similar for both cases. The advantages of the turbulence theory are that energy is reflected in all directions rather than as mirror reflections, and that large changes in refractivity over distances of only a few centimeters are not required. However, the advantage of the reflection theory is that thin layers of turbulence need not exist.

3.7.3 The Bragg Condition in RASS

An application of the Bragg scatter idea which, unlike turbulent-related scattering, is analogous to the scattering of X-rays from crystals is RASS. RASS (Radio Acoustic Sounding Systems) are acoustic systems for determining temperature profiles which are used in conjunction with a radar wind profiler. In RASS, a radio diffraction grating is created in the atmosphere by using sound waves (Kropfli, 1990). Vertically propagating (and audible) acoustic waves are generated at a frequency such that the strongest radar return scattered from the density anomalies of the evenly-spaced, longitudinal acoustic waves is received. This occurs at the Bragg condition for backscatter, $2d=m\lambda$ with $m=1$ selected. The wavelength of the sound waves, d here, is then known. With the known generated sound frequency, the speed of the sound can then be found. From the speed of sound, the temperature is easily determined. By range gating, a temperature profile can be obtained.

3.7.4 Discussion and Criticism of Bragg Scatter Theory

Bragg scatter theory has been widely used and verified in the last 40 years in such diverse areas as astronomic seeing conditions, short-wave radio propagation, star twinkle, and clear-air returns in meteorology. However, despite the success of its application, there are many sometimes questionable assumptions that go into the theory which we should be aware of.

The assumption of locally homogeneous turbulence is particularly suspect in atmospheric flows, which are often dominated by buoyancy.

The expression for the scattered electric field in terms of perturbations in the refractive index (3.38) is not always physically realistic. Strictly speaking, this equation is only true for an isolated, infinitesimal perturbation. In the absence of small-scale turbulence, this expression could be incorrect. For example, if a region of air of the size of the radar probe volume happened to be of uniform n, different by some perturbed amount from the regional average, then Bragg scatter would predict significant scatter while in reality there would be none. For Bragg scatter equations to be accurate, the region around each infinitesimal perturbation must be representative of the average, and this situation may not always be the case.

It should be recognized in Bragg scatter that some process is needed in order to maintain the refractivity gradient; otherwise, the action of turbulence would diffuse away any gradients. These processes for thin layers are presumably subsidence and radiation. An increase in turbulence would not necessarily give an increase in Bragg scatter, since increasing turbulence could reduce the mean gradients in refractivity.

It should also be realized that, while the Bragg scatter result derived here is only valid for cases where half the radar wavelength lies within the inertial subrange of the turbulence, scattering at some level should still occur even when that condition is not met. Indeed, scattering could be significantly stronger for cases of gentle turbulence as the reduction of small scale mixing would lead to less diffusion and stronger refractivity perturbations. Equations for Bragg scatter for turbulence of large inner scale have never been developed.

Usage of the term "Bragg" is unfortunate as it can lead to a mis-interpretation of the physics. Diffraction spots as in X-ray diffraction do not occur in Bragg scatter (with the exception of RASS). Instead, for turbulent applications, the integral leading to the total energy scattered depends inherently on the radar wavelength. This is true regardless of the spectral structure of the refractivity inhomogeneities and is related to the destructive interference of most of the wave energy emitted over a spatial volume. The mathematics is similar to radar reflections from simple gradients in refractivity (Sec. 3.6) which have no eddy structure. Turbulent eddies do not act like a diffraction grating.

With regard to scatter from thin layers such as those seen in Figs. 3.7 and 3.8, the application of Bragg scatter theory seems questionable. Bragg scatter for these cases would require exceptionally thin layers of turbulence (less than a few meters) which seem unrealizable physically. Of these thin-layer echoes, Atlas (1969) stated, "It would therefore appear that we have the first striking evidence of the existence of an unusual refractivity spectrum in which all the perturbations are in sub-meter scale eddies." I would instead suggest the possibility that these data imply that thin layers such as these are not turbulent at all, but that reflections are adequate to explain them. If the existence of very sharp gradients can be accepted, it is easier to hypothesize such gradients than the unusual combination of physical circumstances that would give rise to thin layers of persistent turbulence in the atmosphere, which have never been explained nor definitively observed. Since such layers tend to be stable layers, they will not be turbulent unless sufficient vertical shear exists. If sufficient shear exists, it would be expected that large scale turbulence would result, as is usually observed (for example lock-exchange flows, or the breaking of K-H waves into turbulence seen in Fig. 3.8). It is not sensible to claim that the scattered energy from such thin layers results from turbulence. This reluctance to accept the existence of layers of turbulence with an outer scale less than a meter was also expressed by Hardy and Gage (1990, p. 137). Nonetheless, scattering from deeper layers probably is adequately explained by Bragg scatter.

3.8 Clear-Air Radar Studies

This section analyzes and discusses data acquired on two nights and one day with different radars specifically to study the nature of the nocturnal clear-air radar echo. Because all the different scattering mechanisms have different dependencies on radar wavelength (see Table 3.3), important information can be obtained about the nature of the scatterers

Mechanism	Z_e, m^3	η, m^{-1}
Reflections from grads.	$2.2\mathrm{X}10^{-5}\left(\frac{dn}{dz}\right)^2\frac{\lambda^6}{h}$	$\frac{4}{h}\left(\frac{dn}{dz}\frac{\lambda}{8\pi}\right)^2$
Reflections from discons.	$\frac{\lambda^4}{2\pi^5\|K\|^2 h}(\Delta n)^2$	$\frac{1}{2h}(\Delta n)^2$
Bragg scatter	$.0013\mathrm{C}_n^2\lambda^{11/3}$	$0.38\mathrm{C}_n^2\lambda^{-1/3}$
Rayleigh scatter	const.$=\frac{\sum D_i^6}{V}$	$\frac{\pi^5\|K\|^2}{\lambda^4}\sum D_i^6/V$
Mie scatter	Fig. 3.12, from Ray. to $\frac{\lambda^4}{\pi^5\|K\|^2}\frac{\sum \pi r_i^2}{V}$	Fig. 3.9 from Ray. to $\frac{\sum \pi r_i^2}{V}$
Ray. with one target	$\mathrm{D}^6/V=\frac{8D^6}{\pi R^2\theta^2 h}$	$\frac{\pi^5\|K\|^2}{\lambda^4}D^6/V=\frac{8\pi^4\|K\|^2}{\lambda^4}\frac{D^6}{R^2\theta^2 h}$
Mie with one target	$\frac{const}{V}$ to $\frac{\lambda^4}{\pi^5\|K\|^2}\frac{\pi r^2}{V}=\frac{\lambda^4}{\pi^5\|K\|^2}\frac{8r^2}{R^2\theta^2 h}$	to $\pi r^2/V=\frac{8r^2}{R^2\theta^2 h}$

Table 3.3: Collection of reflectivity formulas. R is radar range, r and D are radius and diameter of targets, V is resolution volume.

if different wavelength radars happen to be available to probe the same air at the same time. Two such studies were done as described in this section.

The known mechanisms include: Bragg scatter, reflections, Rayleigh scattering, and Mie scattering. Table 3.3 collects some of the equations together for effective reflectivity factor, Z_e and reflectivity, η, gathered from the developments in this chapter. For isolated point targets, there is a volumetric effect. Since a point target has a fixed backscatter cross-section, the backscatter cross-section per unit volume (η) will decline as the radar resolution volume increases. For determining Mie cross-sections, Fig. 3.9 needs to be consulted to get σ, reflectivity or Z_e values depend on specific radar parameters and can be found by applying (3.5). It is important to pay careful attention to unit conversion factors when doing such calculations.

It is important to note the wavelength dependence indicated in this table. In terms of Z_e values, if the radar targets are tiny Rayleigh scatters, then the reflectivity is independent of the radar used. If the targets are refractivity inhomogeneities causing Bragg scatter, then there is a $\lambda^{11/3}$ dependence. For large Mie scatters, the dependence varies, but approaches λ^4 for very large objects. From a practical standpoint, a λ^4 dependence will be difficult to discern from a $\lambda^{11/3}$ dependence, so it will probably not be useful to try to discriminate bird scatter from Bragg scatter by using multiple wavelengths, since birds tend to be very large Mie scatters for most meteorological radars (Fig. 3.9).

There is also a volumetric effect. Since Z_e is only meaningful for a volumetric distribution of targets, if a single point target is being sensed, the reported reflectivity of it will depend on the resolution volume.

3.8.1 Analysis of a Clear-Air Density Current Measured by DOW3

Some light is thrown on clear-air signals by some data acquired using DOW3 of a density current (thunderstorm outflow). Fig. 3.16 is a reflectivity scan in RHI mode (Range-Height Indicator) of a density current obtained on June 1, 2000 in a wheat field in southwest Kansas. The spatial resolution was high for these data, with a gate spacing of 49 m. This was a clear-air situation with active convection some distance away. Figs. 3.17 and 3.18 are the velocity and spectral width data for the same RHI. The data are contaminated by some ground clutter and by second trip echo. This second trip echo is from the distant thunderstorm and is indicated quite well in the spectral width RHI of Fig. 3.18, showing as a horizontal band of high spectral width. The velocity data also show significant aliasing in Fig. 3.17, with a Nyquist of only 17 m/s. The data could be easily dealiased and filtered to remove ground clutter and second trip data; however, that is not necessary for the purpose of this section which simple aims to analyze the reflectivity in some sections of the current.

Of interest in Fig. 3.16 are the two point echoes at a range of about 4 km and an elevation of 20°, which are probably birds. A box has been drawn around these echoes in the data. Similar point echoes are seen in a layer about 3 km above the ground. These echoes have higher reflectivity than surrounding reflectors and by examining Fig. 3.17, it is seen that they have a significantly different Doppler shift than surrounding material. By examining the data closely it is found that the two strong echoes are both 15 dBZ in reflectivity, and the surrounding air is -17 dBZ. The radial velocity of one of the two echoes is -13 m/s and the other is -8 m/s, which compares with +6 m/s for the surrounding air. This is a difference of 16 m/s, a reasonable air speed for a bird. This difference cannot be accounted for by aliasing since aliasing causes errors of twice the Nyquist, or 34 m/s in this case. The most reasonable explanation for these echoes are that they are birds flying against the wind. By Fig. 3.9, a typical bird would have a radar cross-section at 3 cm of

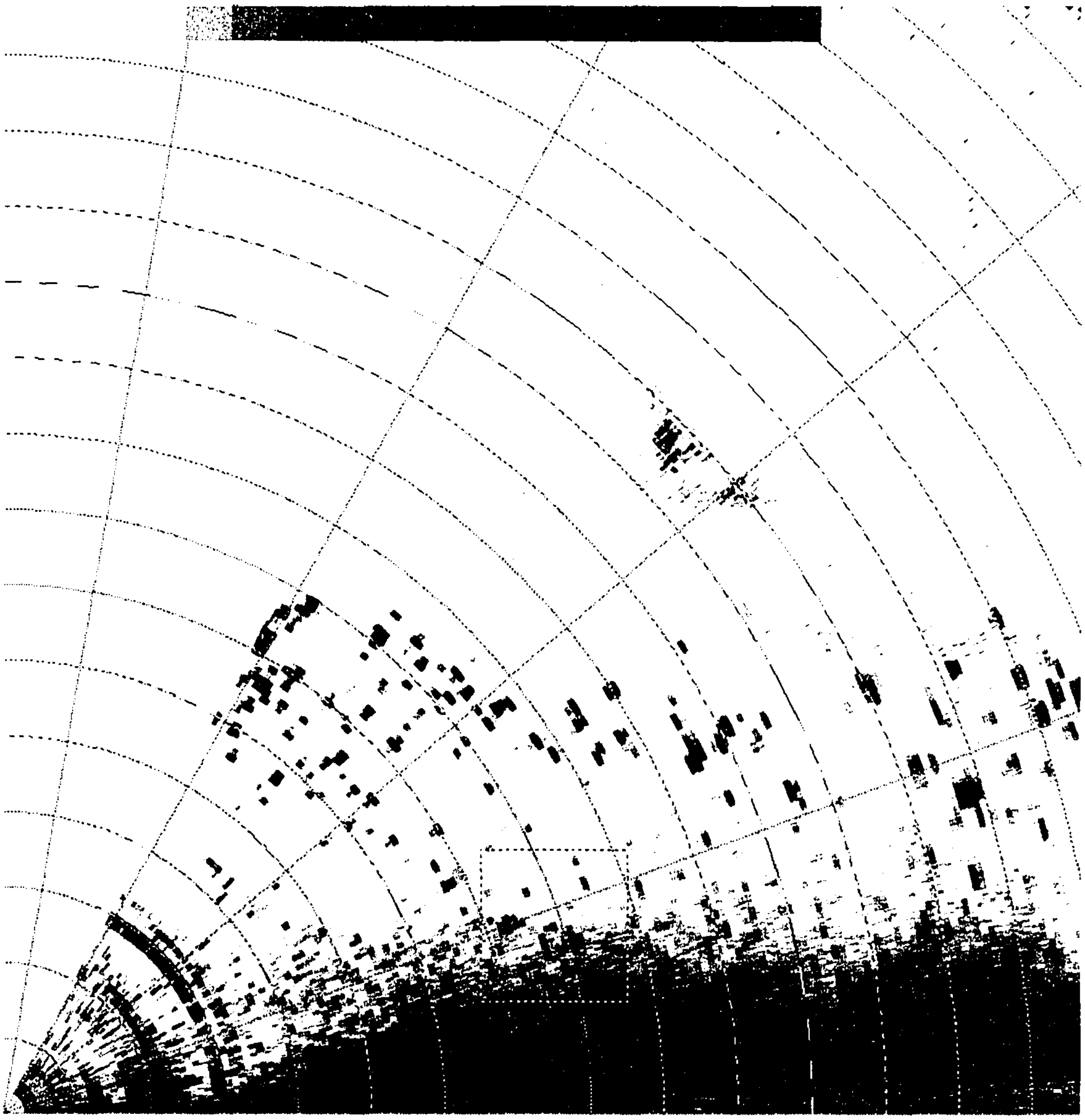

AZM min,max 220.84 221.14 Assumed data range: -25. 10.@ 2 gspace 49.
DATE: 6 1100 Times: 23 4 37 23 4 43 GMT RADS: 24689 25200
DOW3 RHI dbZ RINGS : 0.50km RAYS: 20.deg MAG 2.0

Figure 3.16: DOW3 RHI for reflectivity of a thunderstorm outflow. DBZ_e values range from -25 dBZ (white) to 10 dBZ (black). Range rings are drawn every 500 m and radials are drawn every 20°. Box is drawn around two high reflectivity point targets of interest.

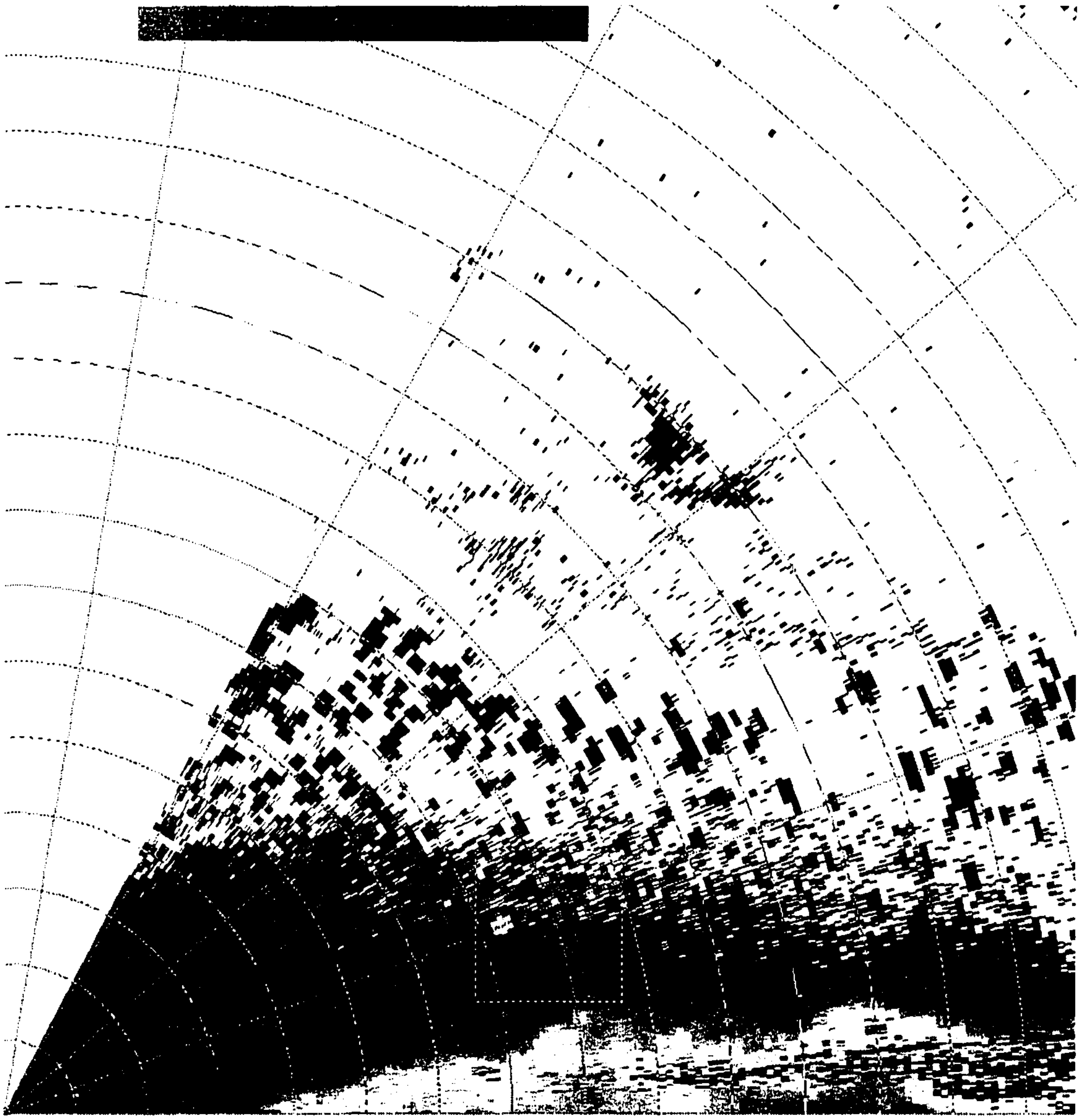

AZM min,max 220.84 221.14 Assumed data range: -16. 8.@ 2 gspace 49.
DATE: 6 1100 Times: 23 4 37 23 4 43 GMT RADS: 24689 25200
DOW3 RHI VEL, m/s RINGS : 0.50km RAYS: 20.deg MAG 2.0

Figure 3.17: As Fig. 3.16 but for radial velocity. Range of radial velocities displayed is from -16 m/s (very light gray) to 8 m/s (black).

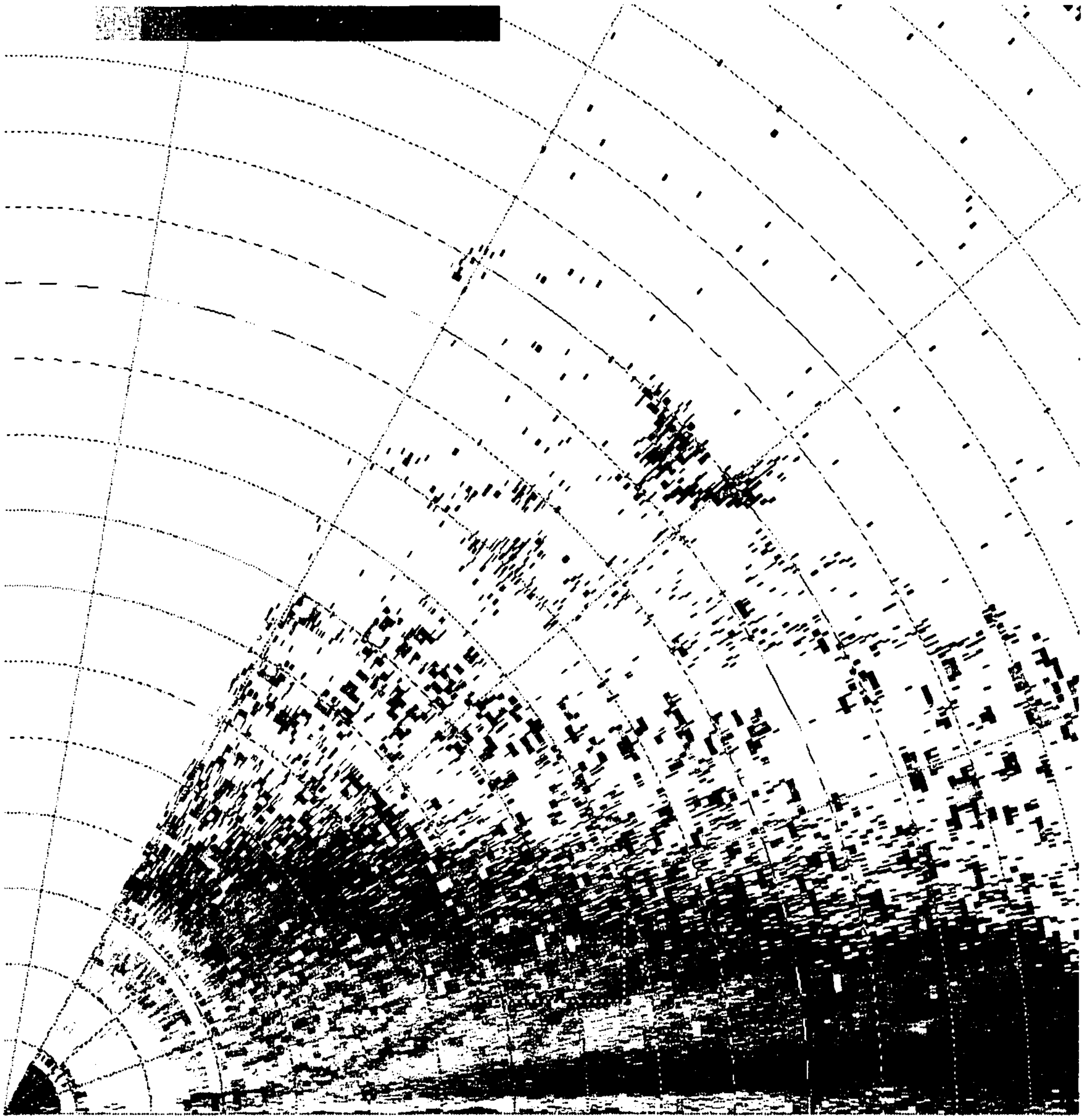

AZM min,max 220.84 221.14 Assumed data range: 0. 10.@ 1 gspace 49.
DATE: 6 1100 Times: 23 4 37 23 4 43 GMT RADS: 24689 25200
DOW3 RHI SPEC, m/s RINGS : 0.50km RAYS: 20.deg MAG 2.0

Figure 3.18: As Fig. 3.16, but for spectral width. Range of values displayed is from 0 m/s (white) to 10 m/s (black).

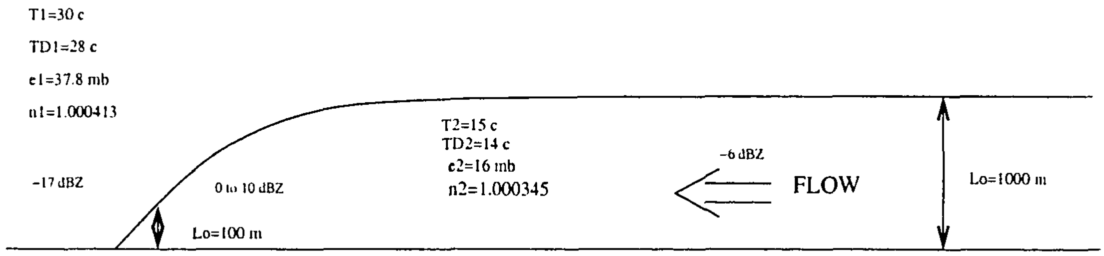

Figure 3.19: Diagram of density current. Thermodynamic properties of temperature, T, dewpoint, TD, water vapor pressure, e, and refractive index, n, are listed at station #1 ahead of the current and station #2 behind the current. Local values of radar reflectivity in dBZ are plotted at a few locations. Lo is the local mixing depth within the current. Based on Fig. 3.16.

about 10 cm^2 and by (3.7) a reflectivity of 15 dBZ at a range of 4 km with this 3 cm radar and a 49 m gate spacing. There is a, however, lot of scatter in radar cross-section data for birds. Vaughn (1985) collects data from numerous studies which have a range of 40 dB in radar cross-section for bird echoes. For a single species of bird, cross-sections can vary by 15 dB depending on the orientation of the bird relative to the radar beam (Vaughn, 1985), so a 15 dBZ echo is generally consistent with a bird explanation. Insects have been reported with radar cross-sections as large as birds. Therefore, the airspeed of the targets alone implies that they are birds. The layer of point targets 3 km above the surface are probably also birds since they are strong reflectors and have a variable Doppler shift.

Of greater interest is the source of reflectivity of the density current itself and the nearby air. DOW3 has received a signal strength sufficient to measure velocities in the entire layer of the atmosphere below about 2 km, with reflectivities of about -17 dBZ outside the density current and 0 to 10 dBZ inside it. The noise level for DOW3 would permit the detection of signals as weak as -24 dBZ at 4 km. Fig. 3.19 is a diagram of the situation with some local reflectivities and hypothetical thermodynamic properties plotted. Data from Vaughn (1985) and Riley (1985) (consistent with Fig. 3.9), which both collect the results of numerous studies on the radar cross-section of birds and insects, combined with the application of (3.7) implies that at a range of 4 km, and with this 49 m gate spacing, DOW3 might expect the dBZ_e levels and radar cross sections listed in Table 3.4 for birds and insects, if only one was present as a point target in a resolution volume. This encompasses objects from the tiniest insects to the largest birds. For multiple targets

TARGET	dBZ_e for DOW3, 49 m gate, 4 km range	σ, cm^2 for 3 cm radar
Birds	-5 to 35 dBZ_e, with 18 dBZ_e typical	10^{-1} to 10^3 with 20 typical
Insects	-25 to 15 dBZ_e with 5 dBZ_e typical	10^{-3} to 10 with 1 typical
Mosquito	-25 dBZ_e	10^{-3}
Sand piper	18 dBZ_e	20
Robin (Eastwood, 1967)	18 dBZ_e	20
Locust	15 dBZ_e	10
Moth	5 dBZ_e	1
Butterfly	-5 dBZ_e	10^{-1}

Table 3.4: Radar cross section and dBZ values for 3 cm radar for some insect and bird targets. From Eastwood (1967), Riley (1985) and Vaughn (1985).

within a resolution volume, the received power would be the sum of that for the individual scatterers, and dBZ values would increase by 10 times the log of the sum. Doubling the power increases dBZ_e by 3 dB, and 10 identical targets in a resolution volume would increase the dBZ_e level by 10 dB, for example. Birds and insects cross-sections overlap so it is often not possible to definitively identify an echo as bird or insect on the basis of the radar cross-section alone, though very weak echoes are probably insects and strong ones may identified as probably birds.

It is possible to explain all of the reflectivity in the density current in terms of insects, since small enough insects exist to give the -17 dBZ reflectivity observed ahead of the current, and large enough ones exists to give the -10 to 10 dBZ reflectivity observed inside the current. Birds are probably not a significant source of reflectivity overall. The -17 dBZ ahead of the current is too weak to be caused by even the smallest birds, and even most birds would be expected to give rise to reflectivities greater than those seen inside the current. However, since the reflectivity is highest near the head of the current, some mechanism for concentrating insects in this region would need to exist in order for insects to explain the observations. That the current head is also a zone of convergence and vertical motion might help to explain a concentration of insects in this region, though this is not clear as the flow is still practically incompressible. Insects would need to move or be moved in a coordinated manner against the air flow in order to concentrate in one location. Though an insect source could be from insects being blown off the ground by the gusty winds. Wilson et al. (1994) explain the hypothetical concentration of insects along convergence lines as being caused by insects actively flying downward to resist being carried upward to colder heights, or in free fall from immobilization caused by cold. Drake and Farrow (1988) discuss this issue and conclude that ground concentrations can be high only if the convergence zone moves slowly.

It is also possible to interpret the observed reflectivities in terms of Bragg scatter. To do this, an estimate of C_n^2 is required so that (3.41) can be used. Recall that C_n^2 is estimated from scaling arguments to be (3.37):

$$C_n^2 = L_o^{\frac{4}{3}}(\vec{\nabla} n)^2$$

For a density current, it is reasonable to expect L_o to be the depth of the current. For the gradient in n, thermodynamic properties are required so that (3.13) can be used to determine n from N=(n-1)X10^6. We do not have synoptic data for this particular case, however typical values for a thunderstorm outflow are plotted in Fig. 3.19 at station #1 ahead of the current and station #2 within the current. From these values, the vapor pressure is found from Teten's formula:

$$e_s = 6.112exp\left(\frac{17.67T_d}{T_d + 243.5}\right)$$

for e_s in mb and dewpoint, T_d, in degrees C. Assuming 1013 mb of atmospheric pressure, the total difference in index of refraction gradient between the two regions of air = (n_1 -n_2)=(1.000413-1.000345)=6.8X10^{-5}. Since the turbulence in the current is generally mixing air from outside the current with that inside the current, it is perhaps reasonable to assume that $\left(\vec{\nabla} n\right)^2 = \left(\frac{\Delta n}{L_0}\right)^2$. It then follows from 3.37:

$$C_n^2 = L_o^{-2/3}(\Delta n)^2 \tag{3.42}$$

Substituting this into (3.41):

$$Z_e(\frac{mm^6}{m^3}) = 1.3X10^{15} L_o^{-2/3}(\Delta n)^2 \lambda^{11/3} \tag{3.43}$$

with Δn an index of refraction difference between two fluid areas being mixed through a depth L_o. Using (3.42) and (3.43) with a Δn of 6.8X10^{-5} and the 3.198 cm wavelength of DOW3 gives the following

Location	C_n^2, $m^{-2/3}$	dBZ_e
within current, L_o = 1000 m	5X10^{-11}	-7
near head, L_o = 100 m	2 X10^{-10}	0

These values are remarkably close to the observed -6 dBZ_e within the current and 0 to 10 dBZ_e near the head. Furthermore, the increase in reflectivity near the head can be explained in terms of Bragg scatter rather simply as being do to the decreased mixing depth. The head is precisely the region with the greatest gradient in thermodynamic properties, and, therefore, also the largest refractive index perturbations caused by turbulence. These results are in excellent agreement with Bragg scatter theory and support the theory that the radar signal could be caused by Bragg scatter. For the air ahead of the current, the reflectivity of -17 dBZ equates to a C_n^2 of 5X10^{-12} $m^{-2/3}$.

Values of C_n^2 high enough to account for the reflectivity reported here of about 10^{-9} to 10^{-12} $m^{-2/3}$ are relatively high compared to those reported in the literature (e.g., Doviak and Zrnic, 1984, p. 386). Common C_n^2 values are 10^{-15} $m^{-2/3}$ with 10^{-13} $m^{-2/3}$ considered strong. However, Knight and Miller (1998) reported reflectivities in 3 cm radar measurements from Bragg scatter of thermals and developing cumuli as high as -10 to 0 dBZ, which correspond to C_n^2 values as high as 10^{-10} $m^{-2/3}$. The wavelength dependence of the signals they observed tended to confirm the Bragg scatter explanation. Gossard (1990) provides a discussion of C_n^2 values needed to account for thin lines in radars and concludes (p. 510) that C_n^2 >10^{-12} are reasonable in density currents, but C_n^2 values sufficient to account for 10 dBZ_e of reflectivity in a 5 cm radar (C_n^2 =5X$10^{-10}$$m^{-2/3}$) are most likely caused by insects. Wilson et al. (1994) analyzed various clear-air echoes with multiple wavelength radars and and examined differential reflectivity values with polarization radar. They concluded that 0 dBZ_e echoes of a thin-line sea-breeze front seen by a 3 cm radar and most other cases of clear-air reflectivity seen in the boundary layer were almost certainly caused by insects since the difference between the reflectivity at 3 cm and 10 cm was only 7 dB (versus an expected 19 dB for Bragg scatter). However, they did admit that a thin line they observed with only one radar (5 cm wavelength) which had reflectivity of 0 dBZ_e could have been caused by Bragg scatter.

The Bragg scatter explanation is supported by the theoretical expectation of C_n^2 values as high as 10^{-10} $m^{-2/3}$, by the remarkable agreement between the calculated reflectivities and the observations, and by the explanation that variations in the mixing depth cause the higher reflectivity in the head region. The small value for L_o is the critical element which gives rise to high C_n^2 values. In small scale phenomena, such as a density current, there is rapid short range mixing of air of very different composition. It should be expected that unusually high refractivity fluctuations (which C_n^2 is a measure of) would occur in such situations. The possibility of small insects, or a combination of insects and Bragg scatter, as the cause of the observed signals, cannot be conclusively ruled-out, however, as a distribution of very small insects could account for the observed reflectivity. The biggest problem with an insect explanation is the difficulty in explaining the concentration of insects in the head region, for which an explanation has not been confirmed, and the need for a high enough concentration of insects in order to account for a spatially continuous signal. However, Drake (1984) notes that entomologists frequently observe concentrations of insects at the head of density currents.

3.8.2 Volumetric Radar Echo Seen by DOW3 and NEXRAD at Goodland, Kansas, May 30, 2000

On May 30, 2000, DOW3 was co-located with the KGLD NEXRAD at the Goodland, Kansas Weather Service Office at approximately 6Z (midnight). Moderately strong clear-air return was seen by KGLD and DOW3 in the lowest 2 km of the atmosphere, as is typical at that time of year. Data were collected for analysis in an attempt to discern the source of echo. Data from two other radars, the UMASS 3 mm radar (also co-located with KGLD) and the McCook, Nebraska 74 cm wind profiler (85 miles away) were also examined. Unfortunately, the UMASS radar was not operating properly at this time and the data were not usable for comparison. Also, the McCook Wind profiler data could not be used. In addition to having no data below 500 m, the reflectivity calibration of this wind profiler (as others of its type) could not be obtained accurately enough for a meaningful comparison.

DOW3 was parked within 100 m of KGLD, just south of the tower, between 5 and 7 Z May 30, 2000. At this time, a squall line had passed off to the north and was far enough away that KGLD was put into clear-air mode about at about 6Z. A strong LLJ had developed with winds to 32 m/s (according to KGLD) with strong clear air reflectivity of 10 dBZ (in KGLD). Analysis of the wind profile obtained with this data set and ground clutter contamination problems are discussed in the Appendix.

Fig. 3.20 is the PPI scan for reflectivity from KGLD for a tilt of 2.5° at 5:56Z, while Fig. 3.21 is the corresponding PPI from DOW3 obtained within one minute of Fig. 3.20. These figures are plotted with height range rings drawn every 200 meters above the surface. The usage of height rings is different from conventional displays in which the rings are usually the horizontal range from the radar. This is done to facilitate analysis of the vertical profile of reflectivity. It is more useful to know how far above the ground the echo is than how far away it is in range. Figs. 3.20 and 3.21 are scans obtained at the same 2.5° tilt for both radars at the same time and plotted on the same scale. The polarization of both radars is also the same (horizontal). The only difference is in the gray scale selected. Because DOW3 had reflectivity about 15 dBZ lower than KGLD, it was necessary to plot on a gray scale 15 dBZ below that of KGLD. Other differences are due to peculiarities of the radars. DOW3 shows some beam blockage to the north (top of figure), probably from the NWS office and KGLD tower. The radial resolution of DOW3 was also superior, with a 137 m gate spacing in this case, versus 1000 m for KGLD. This translates into a finer resolution. Also, while the angular beam size is the same for both radars at .95°, DOW3 was obtaining radials every .2° versus every degree for KGLD. This over-sampling in azimuth adds to the appearance of higher resolution for the DOW3 data.

That DOW3 reported reflectivity factor significantly weaker than that of KGLD is an important clue to the nature of the echo. This rules-out Rayleigh scatterers as the source of

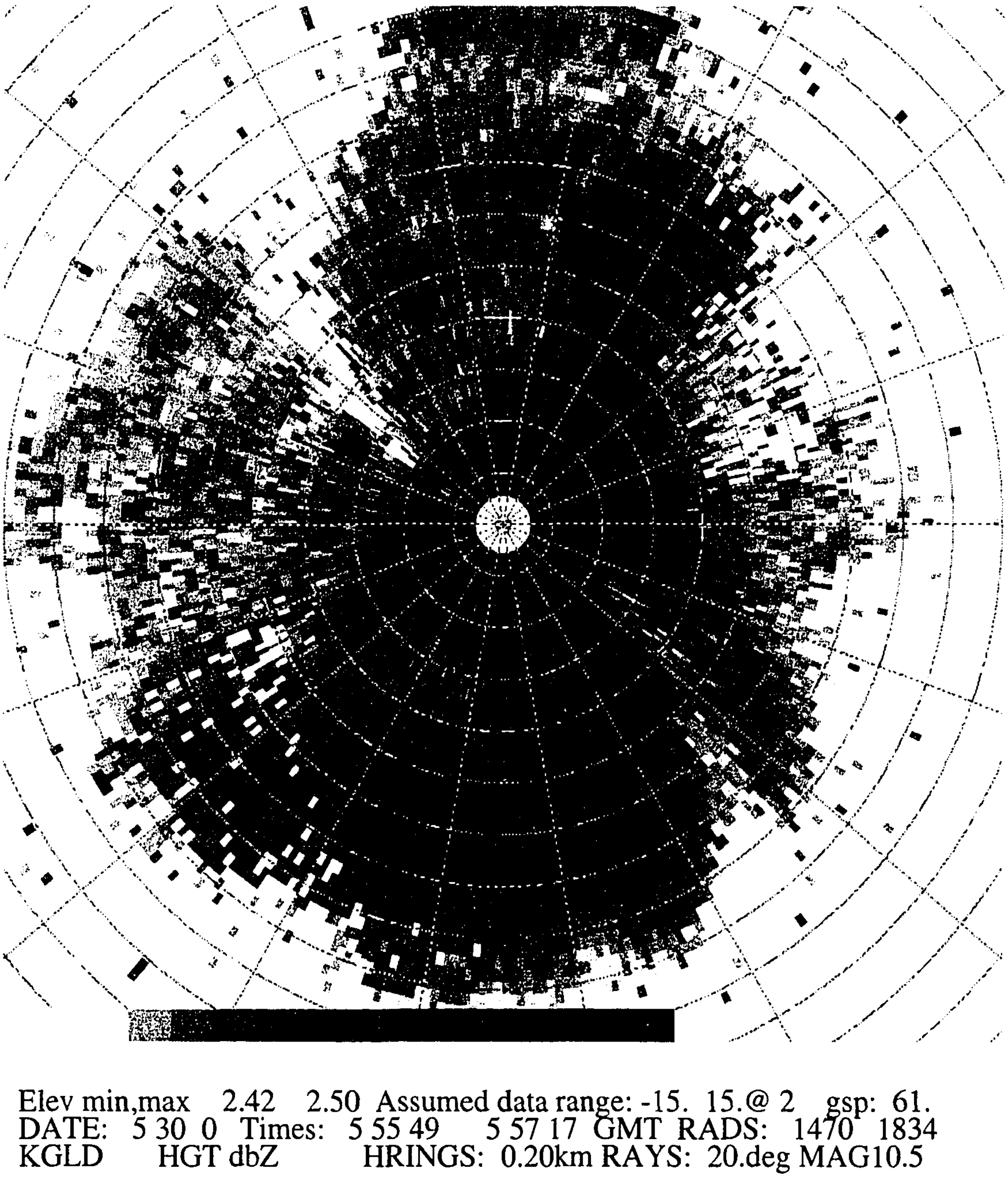

Figure 3.20: PPI scan for KGLD for clear-air return on 5/30/00 at 6Z. Gate spacing was 1 km. Gray scale range is from -15 dBZ (white) to 15 dBZ (black). Rings are height rings drawn every 200 m above the ground. The total horizontal range is about 45 km.

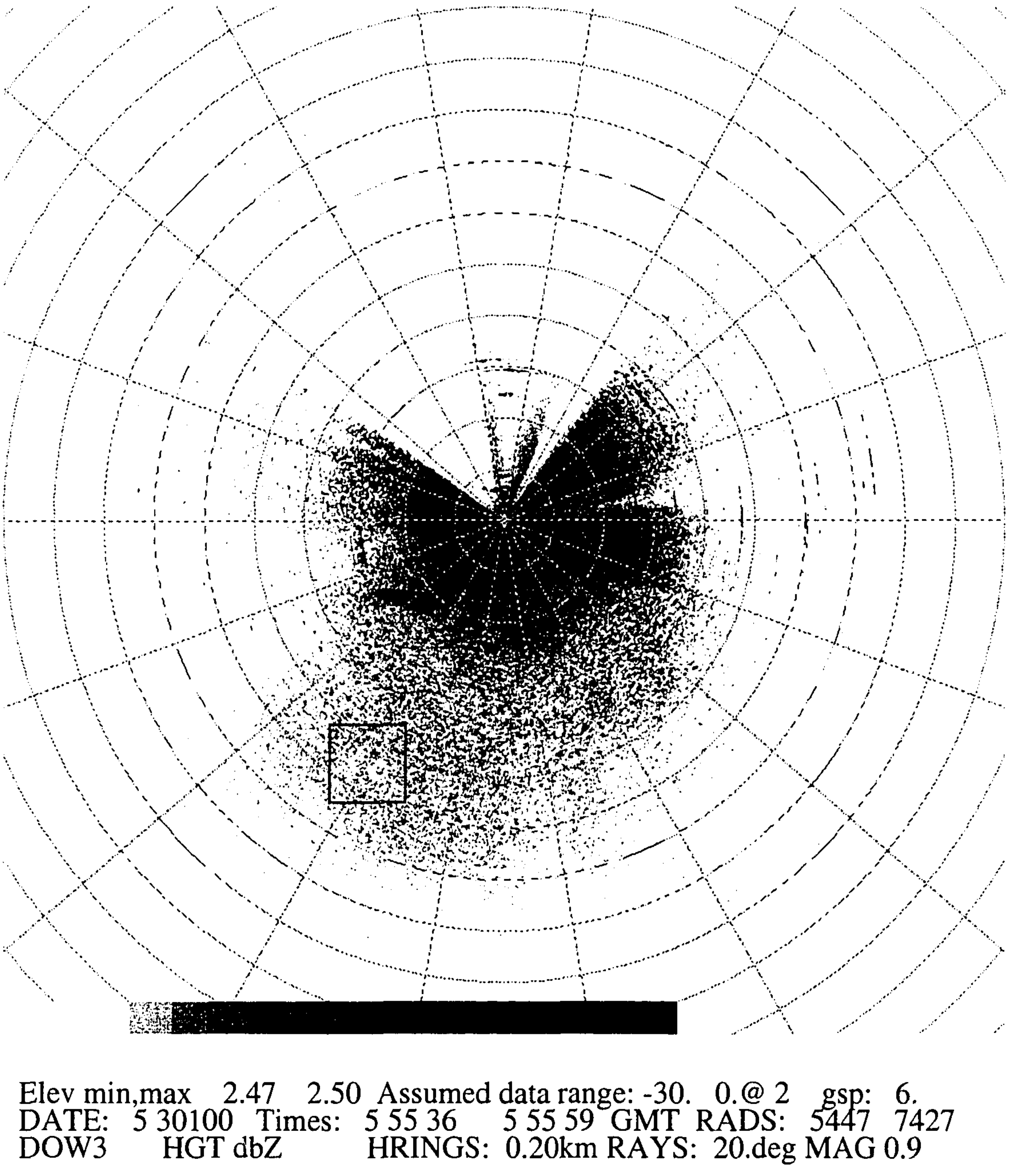

Figure 3.21: PPI scan for DOW3 for clear-air return at 5/30/00 at 6Z. Gate spacing was 137 m. Gray scale range is from -30 dBZ (white) to 0 dBZ (black). Rings are height rings drawn every 200 m above the ground. The total horizontal range is about 45 km.

echo, as these would not show such a dependence on wavelength (Table 3.3). From Table 3.3, it is easily found that the difference in dBZ_e that two different wavelength radars would be expected to have if Bragg scatter were the cause would be:

$$\Delta dBZ_e = \frac{110}{3} log_{10} \frac{\lambda_1}{\lambda_2} \tag{3.44}$$

and the difference for point targets would vary from 0 to:

$$\Delta dBZ_e = 40 log_{10} \frac{\lambda_1}{\lambda_2}$$

Given the 10.0 cm wavelength of KGLD and the 3.198 cm wavelength of DOW3, these equations give:

$$For\ Bragg\ Scatter:\ \ \Delta dBZ_e = 18$$

and

$$For\ Mie\ Scatter:\ \ \Delta dBZ_e = 0\ (very\ small\ insects)\ to\ 20\ (large\ birds)$$

To analyze the difference for this case, a box is drawn to the southwest of the radars in Figs. 3.20 and 3.21. The reflectivity is averaged over this box for comparison. This location is about 1.1 km above the surface (a range of 25 km) and both radars are sampling approximately the same air at approximately the same time. For DOW3, the signal is not continuous and the average is taken only counting those data above the noise level. It is found that DOW3 had an average reflectivity factor within the box of -14 dBZ_e while KGLD had -3 dBZe. Given the 1 dB and 3 dB calibration uncertainties for KGLD and DOW3 respectively, this gives:

$$\Delta dBZ_e\ observed = 11 \pm 4\, dB$$

This value is not consistent with a Bragg scatter or large bird explanation, unless other unaccounted for errors can make-up another 3 dB. It is consistent with insects of large enough size, or possibly small birds and is similar to the 7 dB difference between X and

S-band radars found by Wilson et al. (1994) for similar volume-filling echo. The indicated radar cross section at a range of 25 km for -3 dBZ_e for NEXRAD and -14 dBZ_e for DOW3, from (3.7), are .98 cm^2 and 1.4 cm^2, respectively. The lower NEXRAD value can possibly be attributed to the differing cross-section measured at 10 cm wavelength for some targets (Fig. 3.9) or calibration error. If the DOW3 signals were due to individual targets, then a 1.4 cm^2 is consistent with an typical insect cross-sections, but is low for most birds.

To look at the source of echo further, Fig. 3.22 is a reflectivity PPI scan of higher resolution DOW3 data acquired at a 10° tilt about 10 minutes after Fig. 3.21. These data are of the highest possible resolution attainable with DOW3, with a gate spacing of 12 m. Fig. 3.23 is the corresponding velocity PPI scan (de-aliased). Fig. 3.22 only shows the lowest 500 m of air to a range of 3 km. The numerous point targets evident in this figure implies either an insect or bird explanation. The reflectivity factor of the point targets is about 5 to 12 dBZ_e at a range of 2 km. This corresponds to a radar cross section of from .06 to .32 cm^2, which corresponds with typical insects, but is low for birds (Table 3.4). The increase in dBZ_e for a smaller resolution volume is fairly conclusive in indicating that the targets are dispersed point targets. A volumetric target such as Bragg scattering, would present as the same reflectivity, regardless of resolution volume, as reflectivity measures cross-section per unit volume. The cross section found at this location is about 6 dB below that found at a range of 25 km for 2.5° of tilt and a 137 m gate, discussed above. This is possibly due to the presence of smaller insects at the lower elevation.

The targets are widely distributed enough such that only about one is present in the larger resolution volume at a time. We also note that the velocity scan of Fig. 3.23, after ignoring all the ground clutter and missing data, has smooth velocity (i.e., the point targets are not evident in the velocity information), implying that the point targets are all moving at about the same speed, which further supports an insect over bird explanation as the variance in bird movement is, at least potentially, much higher than that of insects, which would tend to be passive tracers.

That the source of echo was a distribution of point targets might also have been deduced from lower resolution data of Fig. 3.21. This figure has a granularity to it implying that

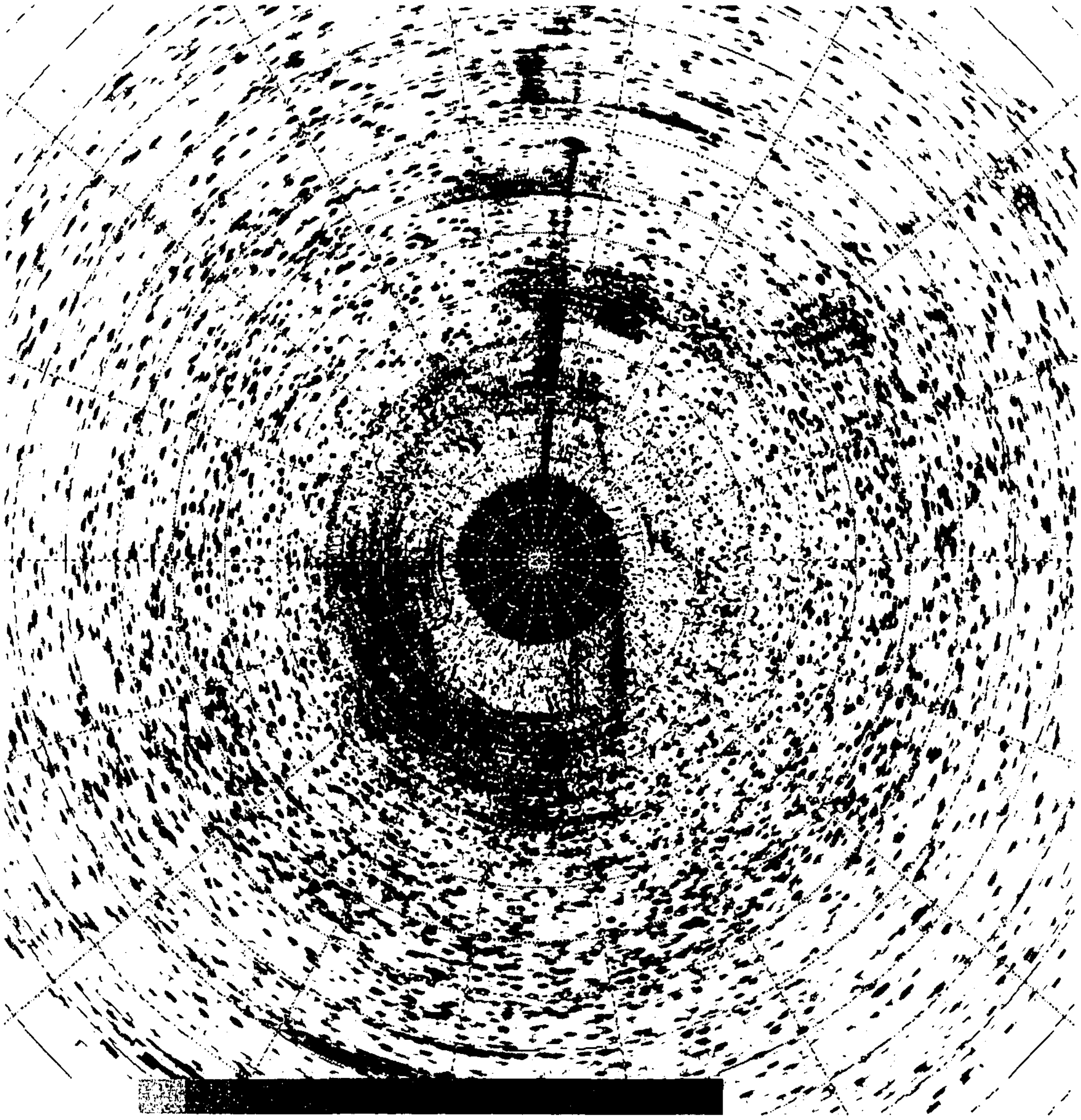

Figure 3.22: PPI reflectivity scan from DOW3 with a 12 m gate spacing, obtained at 6:08 Z, 5/30/00 at a 10 degree elevation. Dark arcs and lines are ground clutter. Reflectivity gray scale is from -20 dBZ (white) to 10 dBZ (black). Range rings are drawn every 50 m in elevation. Total horizontal range is 3 km.

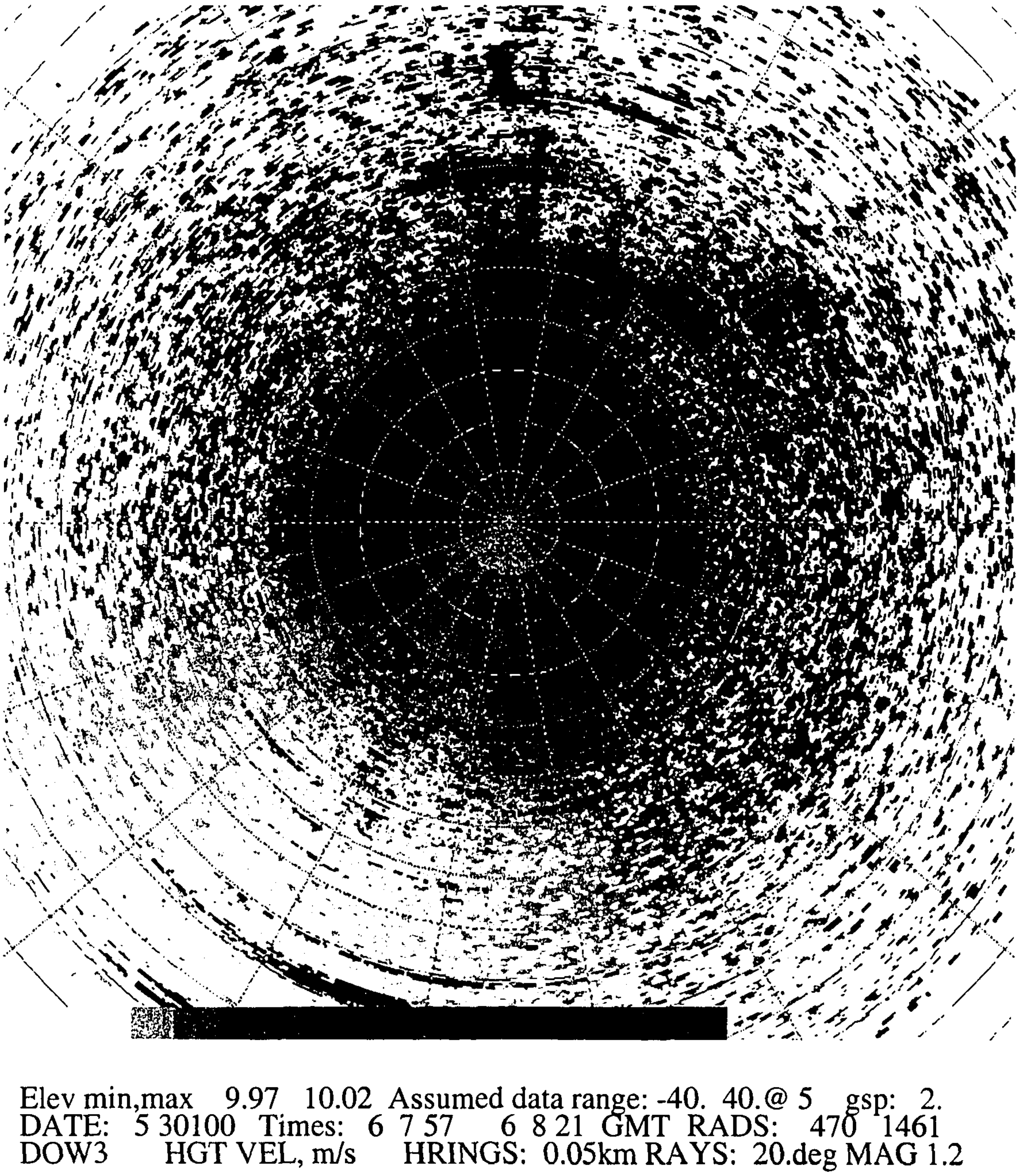

Figure 3.23: As Fig. 3.22, but for radial velocity. Velocity range is from -40 m/s (light gray) to 40 m/s (black). Substantial medium gray shading is from ground clutter.

the target density is insufficient to fili every resolution volume with at least one target. The KGLD PPI of Fig. 3.20 is spatially continuous, and the the target density is sufficient to fill almost every resolution volume for this much larger 1 km gate spacing. NEXRADs can have granular imagery, too, if the density of scatterers is low enough. This is more likely to be seen in the higher resolution (250 m gate) velocity data. Since Bragg scatter is expected to be volume filling at a length scale less than the radar wavelength, it is always expected to give a spatially continuous signal. Granularity is an excellent indication of point targets such as birds or insects. However, a spatially continuous signal does not rule out bird or insects scatterers, as the density of such targets can be quite high.

An RHI scan at the same location as Fig. 3.22 and the same high-resolution 12 m gate spacing at a time about 20 minutes earlier, is shown in Fig. 3.24 for reflectivity and 3.25 for velocity. Here it is seen that the point targets extend up to 2 km in elevation, though they are most numerous below 1 km. Fig. 3.24 also indicates a nearly continuous signal in the shallow layer 200 m above the surface. Point targets are still obvious in this layer, but they are surrounded by much weaker, though detectable, signal. The velocity of the point targets in this layer and the surrounding air is the same, as indicated by Fig. 3.25. The reflectivity at a range of 2.5 km of the weak echo in the layer is about -12 dBZ_e. This corresponds to a radar cross-section of $2X10^{-3}$ cm^2 , consistent with only very small insects. Possibly this layer of air has a very high population of very small insects, or this weak reflectivity could be due to Bragg scatter, since a layer of air near the ground at night might have a strong refractivity gradient caused by radiational cooling.

If birds were present, they must have been few in number since none of the point targets seen in Fig. 3.22 indicate a radar cross section much greater than .2 cm^2.

The number density of point targets in Fig. 3.22 can be estimated and it is instructive to compare this estimate with ornithological bird migration censuses. To estimate the number density, we count the number of targets over a large sector of Fig. 3.22 and divide by the volume of spaced sensed by this sector. To obtain the volume of a sector, the

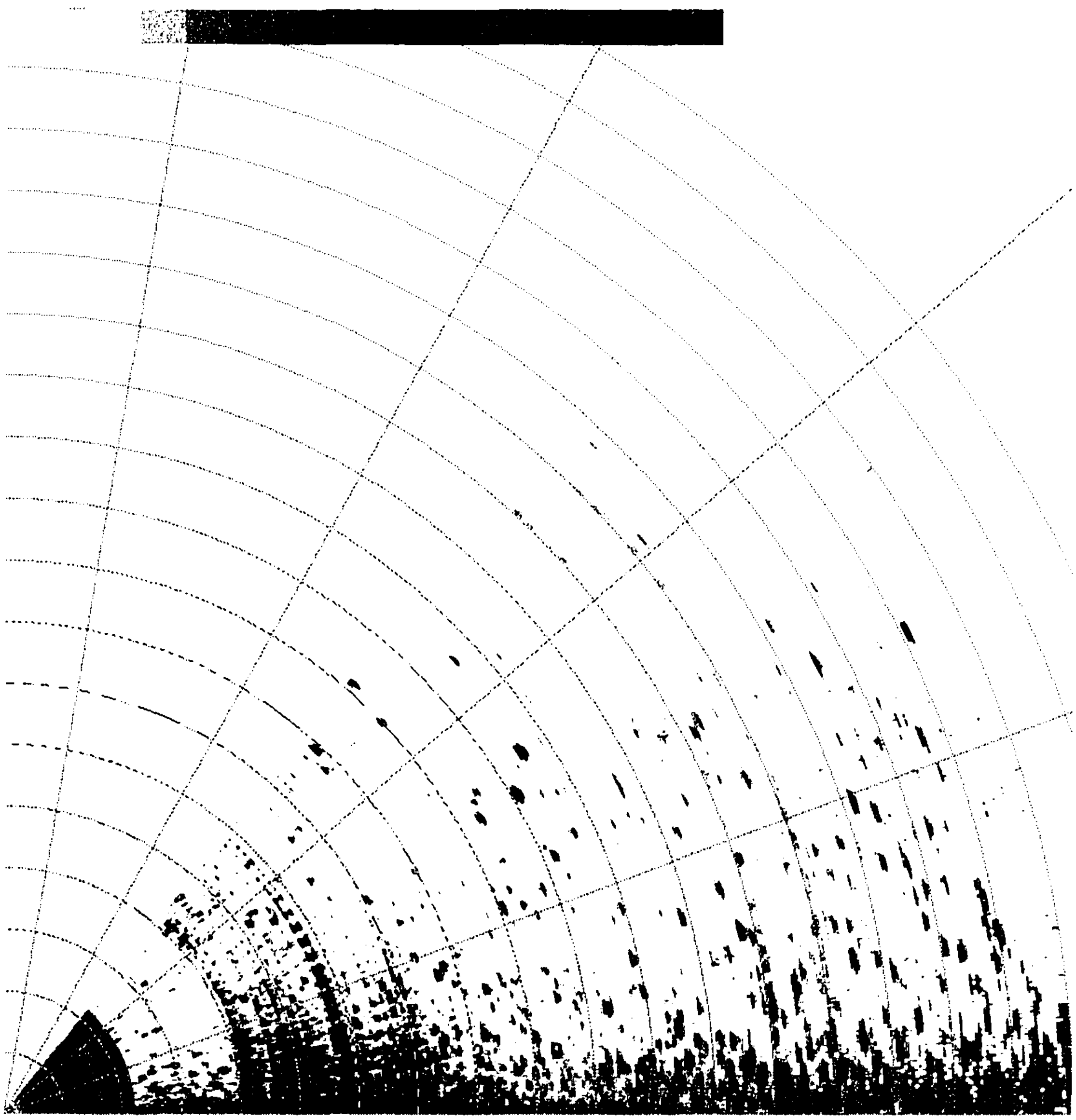

Figure 3.24: Reflectivity RHI scan from DOW3 at Goodland, KS at about 5:48 Z, 5/30/00. Range rings are drawn every 200 m in range. Gray scale is from -20 dBZ (white) to 10 dBZ (gray). Arc echos near radar are from ground clutter.

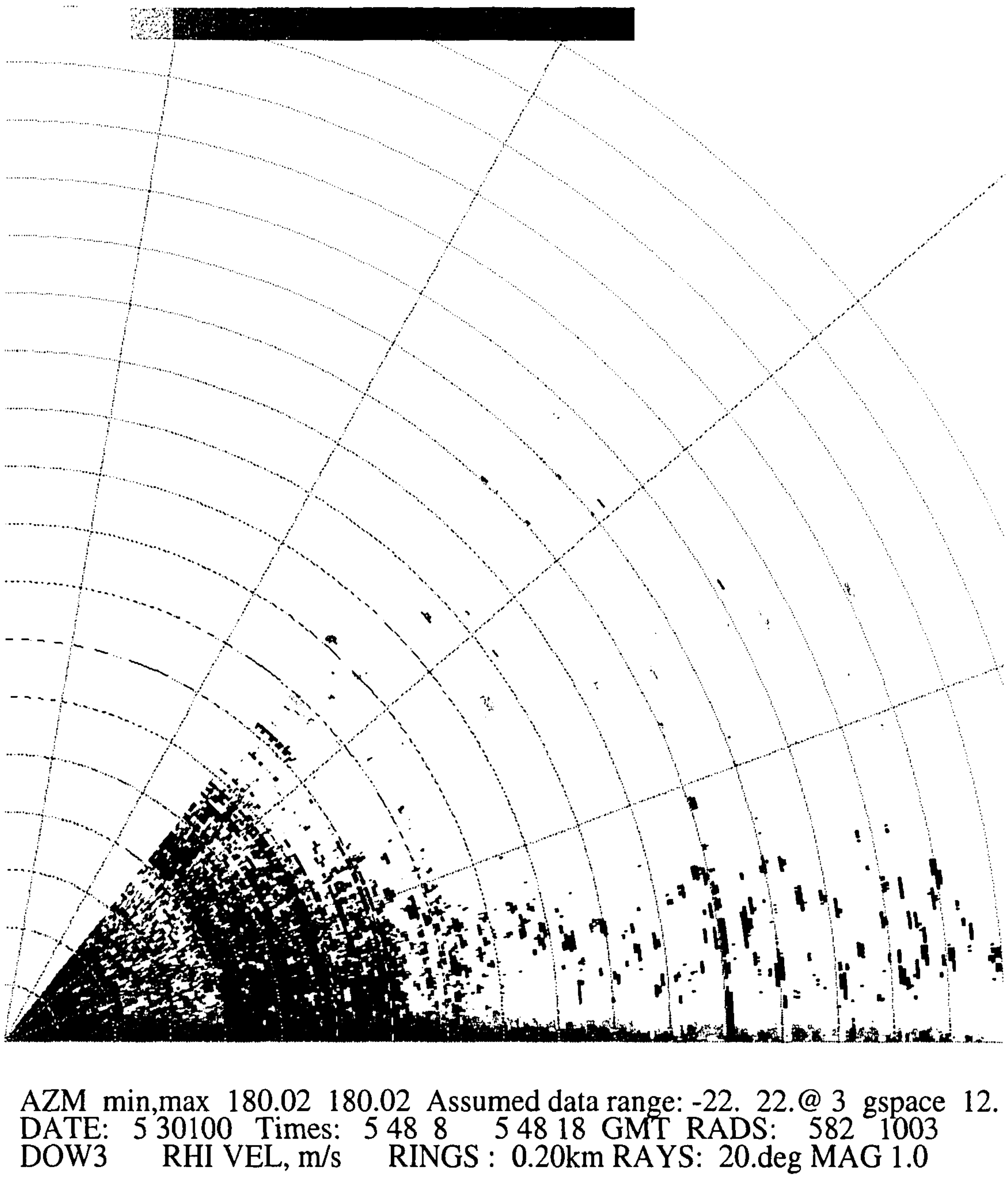

Figure 3.25: As Fig. 3.24, but for radial velocity, not de-aliased.

differential volume in spherical coordinates is integrated over a sector:

$$Vol. = \int_{\phi-\Delta\phi/2}^{\phi+\Delta\phi/2} \int_{0}^{\Delta\theta} \int_{r}^{r+\Delta r} r^2\theta cos\phi dr d\theta d\phi$$

Where r is the radial distance, θ is the azimuthal direction and ϕ is the elevation angle. This integration yields the formula:

$$Vol. of\ sector = \frac{\Delta\theta}{3}[2cos\phi sin\frac{\Delta\phi}{2}][(r+\Delta r)^3 - r^3] \qquad (3.45)$$

Which is correct so long as $|\phi \pm \Delta\phi/2| < \pi/2$. For radar, $\Delta\phi$ is typically small, so 2sin$\frac{\Delta\phi}{2}$ $\approx \Delta\phi$. Converting to degrees, [3.45] simplifies to:

$$Volume\ of\ sector = \frac{4}{3}\pi^2 cos\phi[(r+\Delta r)^3 - r^3]\frac{\Delta\theta\Delta\phi}{360^2}$$

Where r is the inner range of the sector, Δr is the range length of the sector, $\Delta\theta$ is the angular width of the sector in degrees, and $\Delta\phi$ is the beam width in degrees. This leads to an estimate of about 5.0X10^{-6} birds per cubic meter, if the targets were thought to be birds, or an average bird spacing of about 60 meters. To put this number in perspective, if this concentration was the case for all the air below 1 km for the entire state of Kansas, it would imply almost 1 billion birds flying overhead that evening in Kansas. This estimate can also be made from the lower resolution NEXRAD data by simply integrating the total radar cross section seen by the radar over space and dividing by the expected radar cross section. This is much less precise than counting individual point targets in a high-resolution radar since the cross section of birds and insects is highly species dependent, varying by many orders of magnitude, and it is not generally known a priori which are present. Also, for this case, a higher target density occurs near the ground where ground clutter contamination and filtering alter reflectivity values.

Bird density during migration is measured in terms of the number of birds crossing per mile (1610 m) of front per hour, and is referred to in the ornithological literature as "migration traffic rate (MTR)" or "flight density", (Lowery and Newman, 1966). Given the 5.0 X10^{-6} targets per m^3 seen in these data, and the average 25 m/s ground speed of the wind profile below 1 km (Appendix A), the calculated MTR is $7.3X10^5$ birds per 1610 m per hour. In a study utilizing 265 observing stations across the country, Lowery and Newman (1966) measured MTR throughout the country (with the help of 1391 observers) on 4 nights in October of 1952. Bird counts were accomplished by watching the moon through a telescope and applying complex formulas to arrive at MTR values. Lowery and Newman (1966) note various problems with this technique. Their data reduction task was so complex, it took over a decade to accomplish. They found typical migration rates of about 3700, with 4500 being "heavy". This is a factor of 160 less than the traffic rate seen here. Gauthreaux (1998) reports MTR values obtained by moon-watching along the U.S. Gulf Coast, an area which can have particularly intense migratory traffic. The maximum MTR value he reported was about 200 000 (on one occasion, more typical values were 20 000), still 1/3 that observed with these data. Such high MTR values would not be expected to exist over a very wide area for a long time.

The combination of radar cross-section consistent with insects and low for birds, and the number density of scatters vastly exceeding what would be expected from migratory birds, strongly argues against birds being a significant source of radar signal in this case.

3.8.3 UMASS and NEXRAD Clear Air Study, Norman OK, May 19, 2001

To further study the source of clear-air echoes, radar data were acquired on the night of May 19, 2001 at about 4Z at the Max Westheimer Airport in Norman, Oklahoma under clear air conditions. The mobile 3 mm wavelength radar of the University of Massachusetts (UMASS radar, Bluestein and Pazmany, 2000) was used. This radar has exceptional spatial resolution with a beam width of .18° degrees and a pulse length of 60 m. Oversampling in the radial direction is accomplished with a gate spacing of 15 m. Other parameters for this radar are listed in Table 3.1. This night was chosen because strong clear-air reflectivity had been seen at night in NEXRAD radars in the area on previous nights. At the same time, what seemed subjectively to be unusually large numbers of small, brown moths were observed congregating around street lamps and other surface light sources.

3 mm is an unusual wavelength for meteorological applications and use of this radar presents some special problems. One is that the near-field of the radar extends out to 900 m. As the radar is designed with an intended range of less than 10 km, many of the radar targets will be in the near-field. This problem is dealt with by replacing r, the range in standard far-field radar equations, with D/θ, where θ is the $.18°$ beam width, as discussed in Sec. 3.3. Another problem is attenuation. 3 mm radars suffer significant atmospheric attenuation due to absorption by Oxygen (Blake, 1970). As the amount of Oxygen in the atmosphere varies with altitude, the amount of attenuation along a radar radial depends on the tilt of the radial. However, for short ranges, the atmosphere is homogeneous enough to use a single attenuation rate. At 3 mm, two-way attenuation near the earth's surface is about .7 dB/km (Blake, 1970, Fig. 42). This amount is added to reflectivity values to correct for attenuation.

There was no nearby precipitation on this night or the previous day. Fig. 3.26 shows a PPI display of reflectivity at a tilt of 1.5° obtained from KTLX. KTLX is the closest NEXRAD to the location of UMASS, about 25 km away. Fig. 3.27 shows the corresponding PPI for radial velocity.

Fig. 3.26 Indicates a very high reflectivity for clear air, to 25 dBZ in many areas and at least 5 dBZ everywhere below about 2.2 km. This is much stronger than the echo seen in Goodland, KS, discussed in the previous section. The velocity scan shows no evidence of ground clutter contamination, and also has a spatially continuous signal, implying a high target concentration. The velocities are fairly weak, about 6 m/s below 1 km, and reaching 12 m/s at 3 km of elevation. A wind profile derived by VAD analysis of the data in Fig. 3.27 is shown in Fig. 3.28. This high reflectivity suggests the possibility of birds, but the UMASS data to be discussed next strongly argues that it is again insects.

Fig. 3.29 is a time height display of reflectivity obtained by UMASS within 5 minutes of the data of Fig. 3.26. The UMASS radar was parked and the antenna pointed vertically. 2414 radials were obtained in 195 seconds. Fig. 3.29 shows a total depth of 3 km and many targets passing through the beam. Targets are seen below about 2.6 km, in good agreement with the depth of echo seen by KTLX in Fig. 3.26. It should be noted that

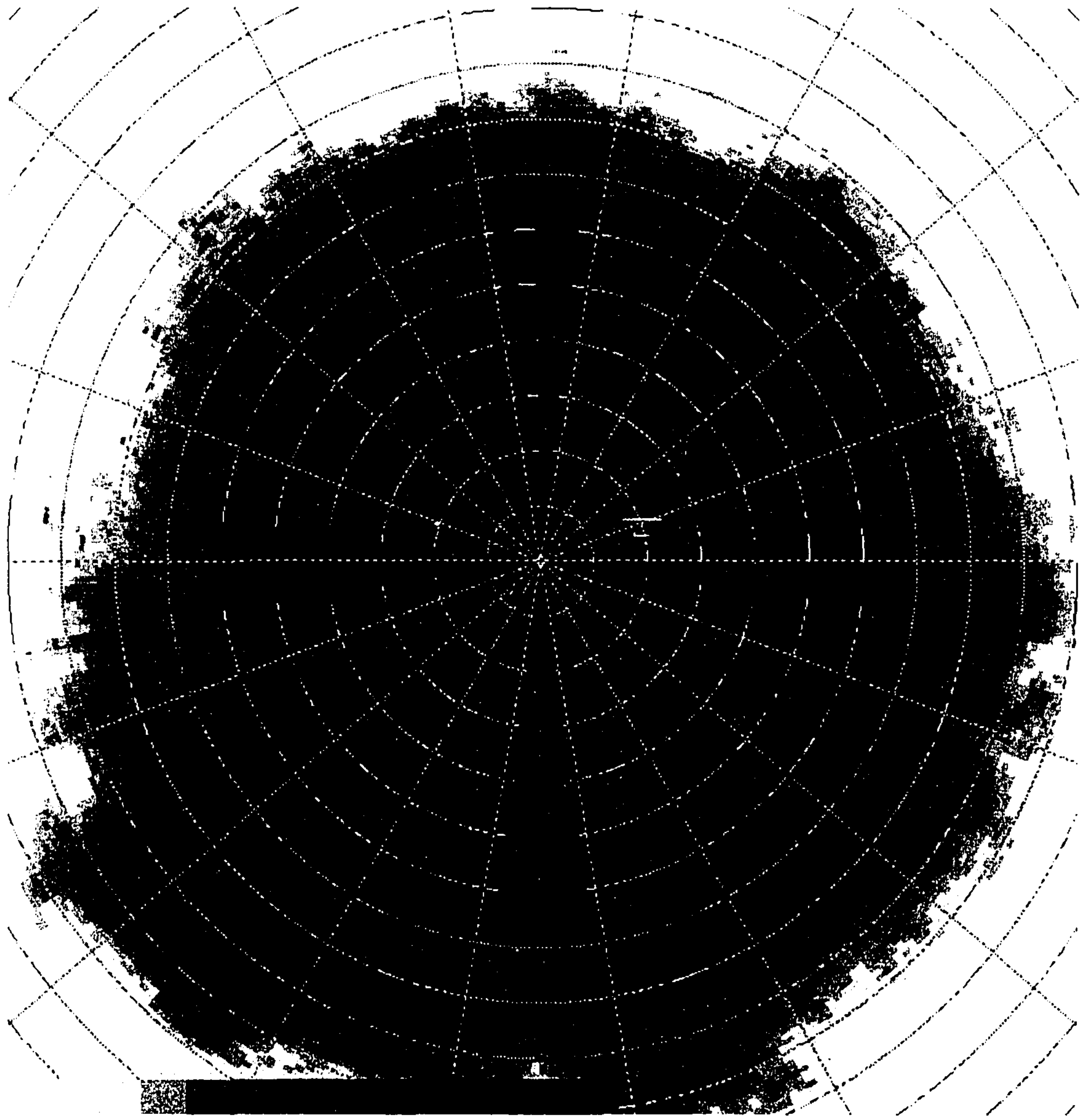

Elev min,max 1.41 1.67 Assumed data range: 0. 25.@ 2 gsp: 25.
DATE: 5 19 1 Times: 3 55 21 3 56 34 GMT RADS: 738 1103
KTLX HGT dbZ HRINGS: 0.25km RAYS: 20.deg MAG 4.1

Figure 3.26: PPI of reflectivity from KTLX. Near 4Z, 5/19/2001, at a tilt of 1.5°. Range rings are drawn every .25 km of height above the ground. Total horizontal range is 95 km. Reflectivity scale is from 0 dBZ (white) to 25 dBZ (black).

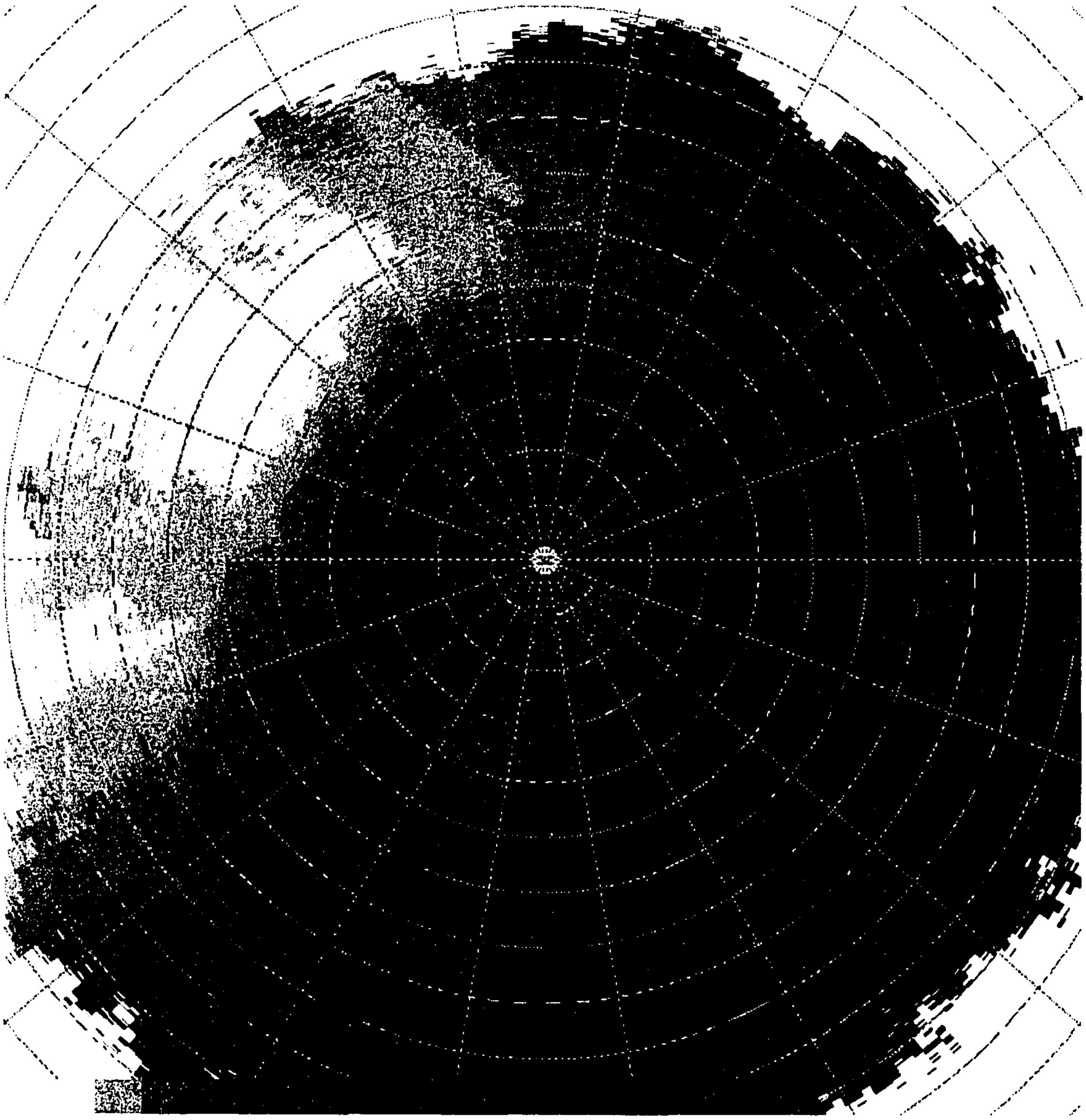

Elev min,max 1.41 1.45 Assumed data range: -15. 15.@ 2 gsp: 6.
DATE: 5 19 1 Times: 3 56 36 3 57 55 GMT RADS: 1105 1470
KTLX HGT VEL, m/s HRINGS: 0.25km RAYS: 20.deg MAG 2.3

Figure 3.27: As Fig. 3.26, but for radial velocity. Scale is from -15 m/s (light gray) to 15 m/s (black).

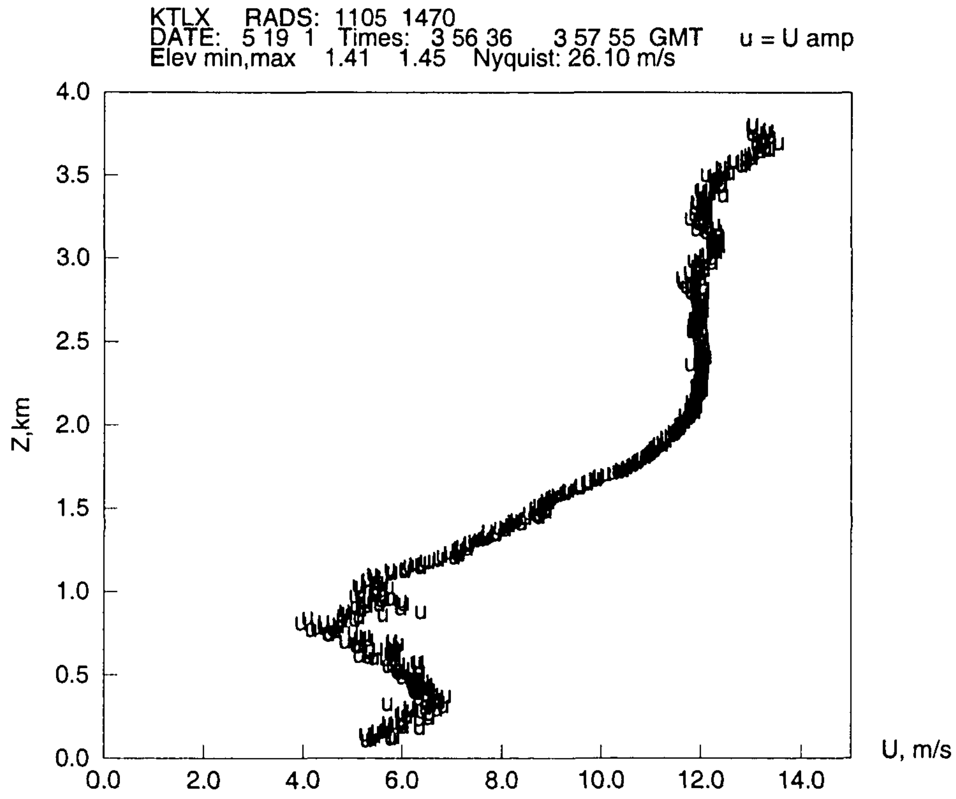

Figure 3.28: Wind profile derived by VAD analysis of Fig. 3.27.

the radar beam is much wider at upper levels, so that if the time-height display shows about the same target density at all levels below 2.2 km, this would imply a lower density of targets aloft. It is also instructive to note that fewer targets are seen in the layer near 1 km altitude in Fig. 3.29 than are seen at other levels. This is most likely due to the weaker winds at this level causing individual insects to spend more time in the radar beam as they drift by, and agrees well with the weak winds in the wind profile at this level seen in Fig. 3.28. The targets in this layer are about the same reflectivity as other layers. Radar cross-sections for the strongest echoes around 1 km elevation (-16 dBZ_e) are about .2 cm^2, calculated from (3.7). The strongest targets around 2 km appear to be larger (-15 dBZ_e) with a cross section of about .5 cm^2. There are no echoes at any level indicating a cross-section larger than 1 cm^2. This small cross-section is consistent with insects, though the species can not be identified. Estimating the target density is straight-forward. The number of targets in the radar beam below 2.2 km is counted by computer for each radial, and this number is divided by the beam volume through a depth of 2.2 km. This count

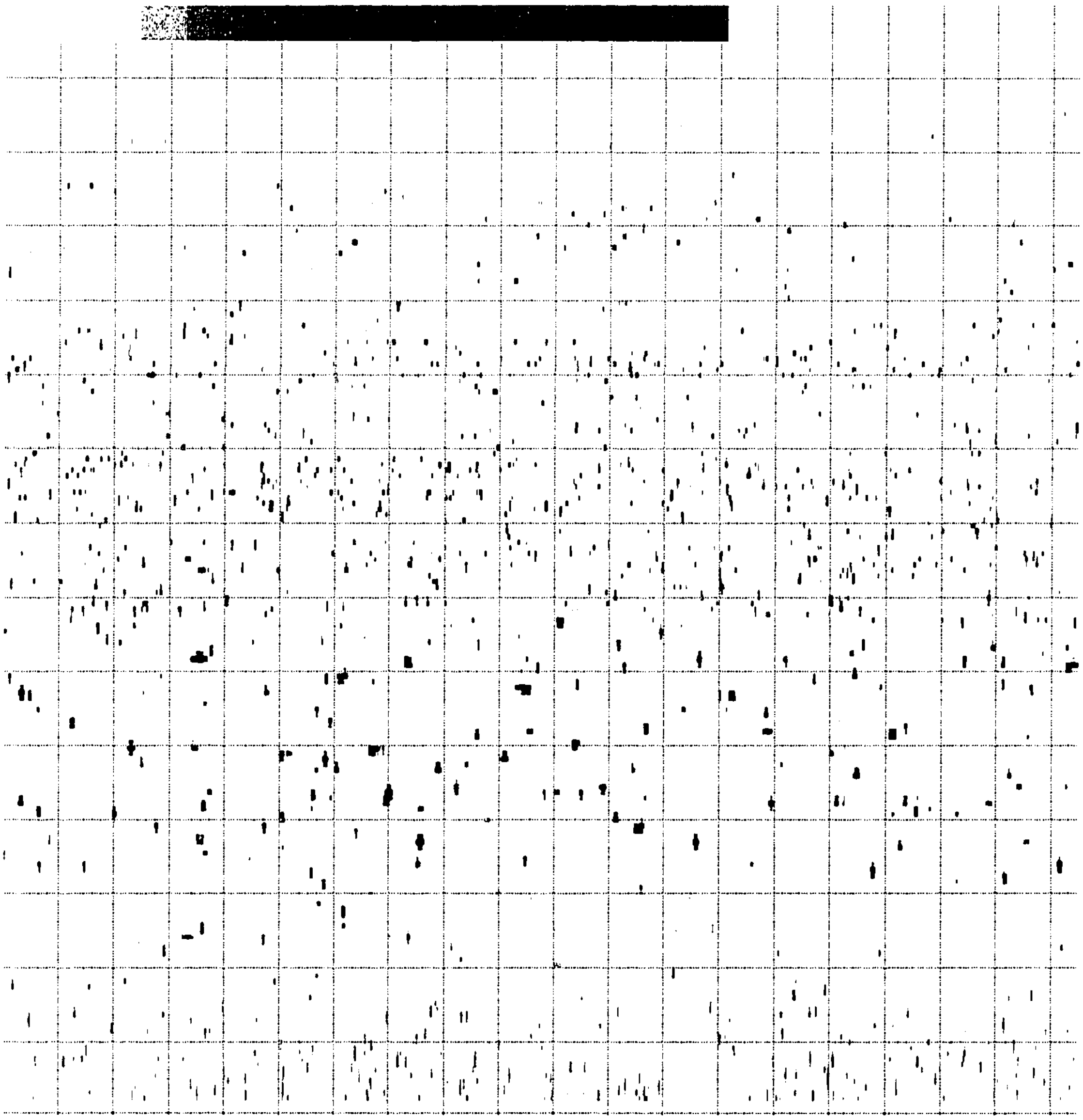

Figure 3.29: Time-height display for reflectivity from UMASS radar at Norman, OK, May 19, 2001 near 4Z. Vertical lines are drawn every 10 seconds and horizontal lines are drawn every 200 m. Total depth displayed is 3 km and total time is 195 s. Reflectivity scale is from -30 dBZ (white) to -15 dBZ (black).

gives about an average of 2.7 targets in the beam at any given time, implying a target density of $1.0X10^{-4}$ per m^3. This is twenty times that seen at Goodland. This number density times a radar cross section of .1 cm^2 implies by (3.5) a KTLX reflectivity of about 25 dBZ_e, in reasonable agreement with that observed.

Near 2 km in elevation, UMASS recorded reflectivities of about -15 dBZ_e, while KTLX values averaged about 10 dBZ_e. This is a difference of 25 dB. The expected difference from Bragg scatter or from birds (3.44) would be 61 dB. This further supports the insect explanation for these echoes. The very high target density and radar cross-section typical of insects, again argue strongly that the targets are mostly, if not entirely, insects.

3.8.4 Summary of Clear-Air Studies

Due to a combination of low radar cross-section and the large number density of targets, the two studies of nocturnal clear-air return conducted here both came to the conclusion that the targets were almost certainly insects, with not a single bird being clearly identified. The difference in reflectivity between the two different radar wavelengths for each study was much smaller than that expected for birds, which further supports this conclusion. This is in agreement with the recent results of Wilson et al. (1994), and older conclusions from entomologists and radar meteorologists that insects are the most common cause of clear-air echoes. The current emphasis on bird-contamination of nocturnal radar wind measurements (Wilczak et al., 1995; Gauthreaux et al., 1998b) may be misplaced. Clearly, such contamination does occur, but the incidence must be low as detailed studies come to the conclusion that insects are the cause. It is possible that some geographic locations such as the U.S. Gulf coast could have a larger problem with bird contamination than others due a higher rate of bird migration.

The usage of high-resolution radars was extremely useful. High resolution permits the resolving of the individual radar targets and the estimation of their number density. This leads to the firm conclusion that the targets were insects. This also leads to the ruling out of Bragg scatter as the cause of echo as this would be expected to give a spatially continuous reflectivity measurement. However, some continuous weak-reflectivity echo was seen below 200 m at Goodland and in the density current. The reflectivity seen in the density current is in close agreement with that theoretically calculated from Bragg scatter equations, with an assumption of a shallow mixing depth. It is possible that some of the weak reflectivity seen in these studies was, in fact, due to Bragg scatter. This is an interesting possibility, especially for the density current. If the reflectivity is due to Bragg scatter, then this information could be used in a data assimilation strategy to retrieve thermodynamic information, due to the dependence of refractivity perturbations on thermodynamics.

It is possible to construct a theory to explain the nocturnal reflectivity entirely in terms of refractivity. Such a theory has never been proposed, but one will be outlined here. At night fall, the turbulence in the atmosphere rapidly declines, and radiative cooling of the surface and atmosphere commences. This decline in turbulence leads to an increase in the inner scale of the turbulence, but the outer scale, which is related to the boundary layer depth, could be unaffected. The decline in turbulence would be expected to lead to a potentially large increase in the refractivity gradient. This could lead to much stronger refractivity perturbations from the residual, large-scale turbulence. These perturbations could be large in size with isolated areas of poorly mixed fluid which could look like point targets. Bragg scatter equations would not apply as they assume the existence of small-scale turbulence. This scenario would account for the rapid increase of reflectivity at sunset. However, the insect explanation is much simpler and is in agreement with most data, and is, in all likelihood, the correct explanation for most cases of nocturnal clear-air return.

It is, of course, possible that Bragg scatter, insects, reflections, and birds may all be present at one time. Which would make bird and insect radar studies particularly difficult.

3.9 Discrimination of Birds and Insects as Radar Targets

Discriminating between birds and insects as the dominant cause of clear-air return is a critical and unresolved issue. Birds on some occasions have been shown to almost certainly significantly bias radar wind estimates, while insects have not been shown to bias such measurements. This is probably because of the significantly higher air speed of birds over insects, and because of the alignment of birds in a single direction due to migratory behavior. If radar targets with an air speed are not systematically aligned, then they would not alter mean wind estimates. The preponderance of evidence implies that most often the return is caused by insects, but clearly sometimes birds are present and sometimes they seriously bias wind estimates. Insects are typically believed to be acceptable tracers of air motion, though it may be possible in some cases of large, energetic insects, for insects to also bias wind estimates.

It is clear that knowledge of bird behavior is of little help in this discrimination. Birds can migrate any time of the day or night, in any direction, against the wind, with the wind, ahead of and behind fronts, and on any day of the year. There are certain patterns of bird behavior, but there are numerous exceptions as well.

One valuable tool for discrimination is the radar cross-section of birds and insects (Vaughn, 1985). Birds can be ruled out in some cases simply if the reflectivity level is too low. How low is easily predicted based on a minimum expected radar cross-section for birds. Vaughn (1985) combines various studies of birds and insects and finds a range of cross-section of from .1 to 1000 cm^2 for birds. However, most of the birds are between 1 and 100 cm^2 and most insects are below 10 cm^2. From Eastwood (1967) passerine birds (the most common nocturnal migrants) have cross-sections of 10 to 30 cm^2. It might, therefore, be reasonable to use 10 cm^2 as a bird threshold. With a minimum cross section of 10 cm^2 in (3.5) for the parameters of a NEXRAD radar, and with one target assumed to be in the beam at a time, the reflectivity must be at least:

$$dBZ_e = 93.6 - 20 log_{10} r \quad (for\ r\ in\ m) \tag{3.46}$$

in order for moderate sized birds to be a possibility. This is alternately recast in terms of height above the ground for a tilt of 1.5° :

$$dBZ_e = 62.0 - 20 log_{10} H$$

Where H is the height above the ground. For example, 1 km above the ground requires at least 2 dBZ_e of reflectivity. If the reflectivity exceeds this level, then birds may or may not be present. As shown here, insects in high concentrations can give rise to reflectivities sufficient to explain any observed reflectivity level. Also, it is worth citing Eastwood (1967) who reported that ornithologists have realized that migrants usually migrate in small groups of several birds, so expected radar cross-sections should be several dB above that expected for a single bird.

If the reflectivity and/or velocity in a PPI display is spatially granular, then this implies a density of targets below the density of resolution volumes. In such cases, it would be expected that each resolution volume would have only a few targets present at one time. In this case, reflectivities above (3.46) would confirm the presence of birds, as insects would be too weak to cause the signal. This technique can be used to confirm the presence of birds in Fig. 1 of Gauthreaux and Belser (1998). In some situations, it might also be possible to exclude birds on the grounds that the number density needed to cause a spatially continuous signal is excessive. Granularity of echo, of course, is resolution dependent. The high-resolution radars used in this work had no trouble resolving the targets of even very high density.

For cases of spatially continuous and strong reflectivity, ambiguity remains. One possibility for discrimination is to use the symmetry of the PPI echo. The radar cross-section of a bird is 15 dB weaker when scanned head or tail on, than when it is scanned broadside. This phenomenon is also true for insects (Vaughn, 1985); however, it might be anticipated that insects do not align them themselves, or at least do so rarely. Alignment is not necessary for insect migration, as migrating insects typically simply use prevailing winds. If insect air speed is small relative to the ground-relative wind, then insect alignment would not be a big improvement in migration efficiency. If migratory birds were present all pointing their bodies in the same direction (which is the only situation in which their presence would add to the mean velocity), then the radar should indicate much lower reflectivities when scanning in the direction of their alignment. A possible example of this phenomenon is shown in Fig. 3.30, which shows a bilaterally symmetric PPI reflectivity factor. The corresponding velocity PPI scan is shown in Fig. 3.31. The only known explanation for such an echo pattern is that the radar targets have some alignment. It seems reasonable that the existence of such a bilateral symmetry could be used to confirm the presence of birds. However, even though it would seem that such a symmetry should always be present when migrating birds were present, it is not known how reliable this indication really is. Such bilateral symmetry is actually rarely seen at night, and is much more common during the day, when migrating birds are thought to be much less common. Fig. 3.30 was obtained in the late morning, for example. The almost universal absence of a bilaterally symmetric echo during nocturnal strong clear-air events is evidence that birds are rarely, if ever, the cause of such reflectivity.

Another possibility is the use of polarization information, as explored by Zrnic and Ryzhkov (1998), and Mueller (1983). Zrnic and Ryzhkov found what they believe to be a characteristic signature of differential reflectivity, Z_{DR}, and phase, δ, which is markedly different for birds and insects. Their technique is a potentially very valuable tool for confirming birds, especially, as they state, since the polarization parameters do not depend on target concentration. It would work just as well for an isolated target as a high density of them. However they only analyzed one case of presumed birds and one of presumed insects. One of the parameters of interest was differential reflectivity, Z_{DR}. Zrnic and Ryzhkov found Z_{DR} higher for presumed insects than for presumed birds. Mueller (1983) found the opposite for the two cases he analyzed. Also, polarization radars are rare and the use of such a discriminator will not be available to the national NEXRAD radar for many years, if ever.

Another possibility for discriminating birds from insect scatters is to use the height of echo above the ground. Strong reflectivity through a deep layer, say 4 km, might indicate the presence of birds as it might be expected that it would be difficult for insects to reach such elevations.

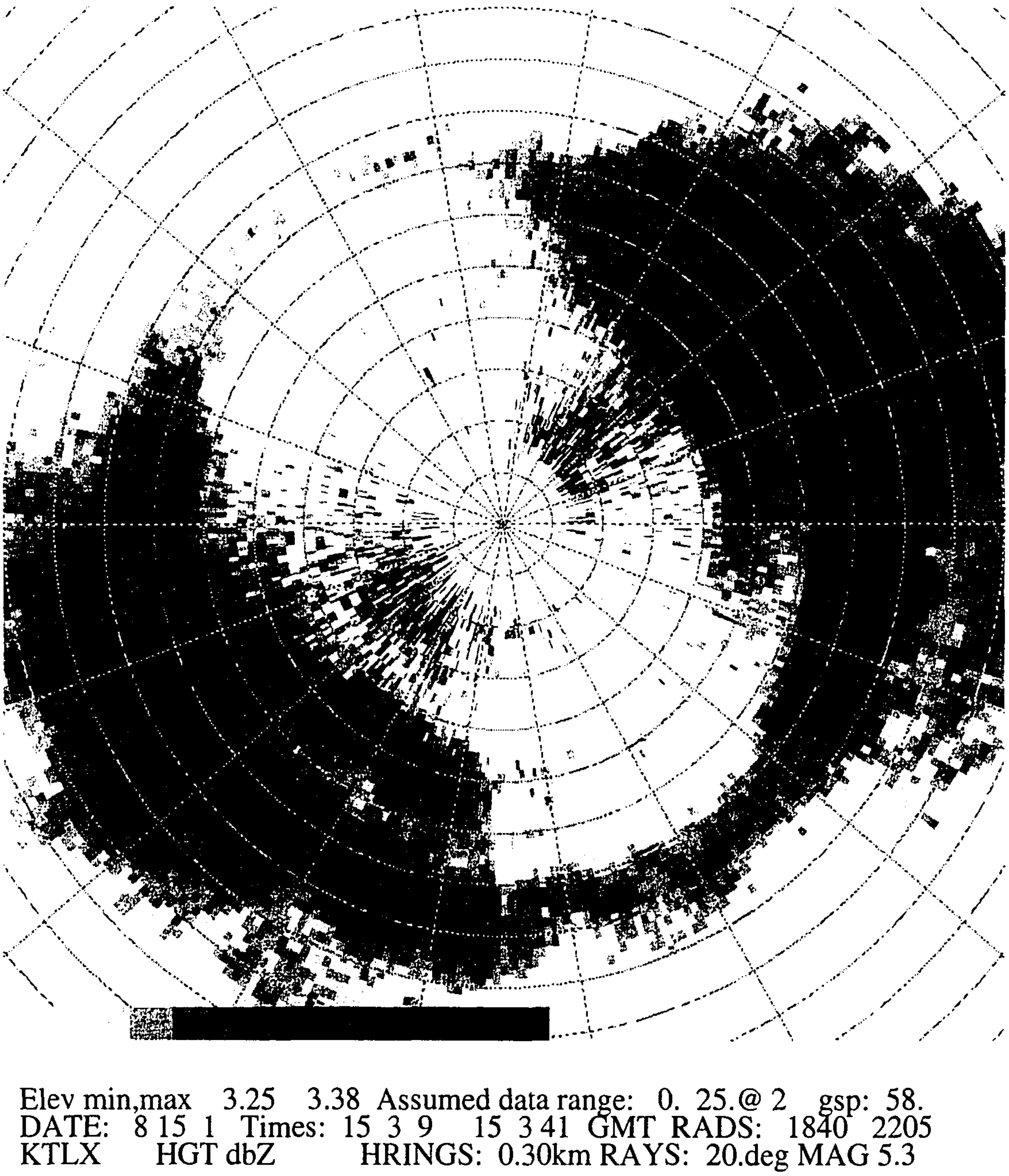

Figure 3.30: PPI reflectivity scan from KTLX at 15Z on 8/15/01 with a tilt angle of 3.3°. Reflectivity range is from 0 dBZ (white) to 25 dBZ (black).

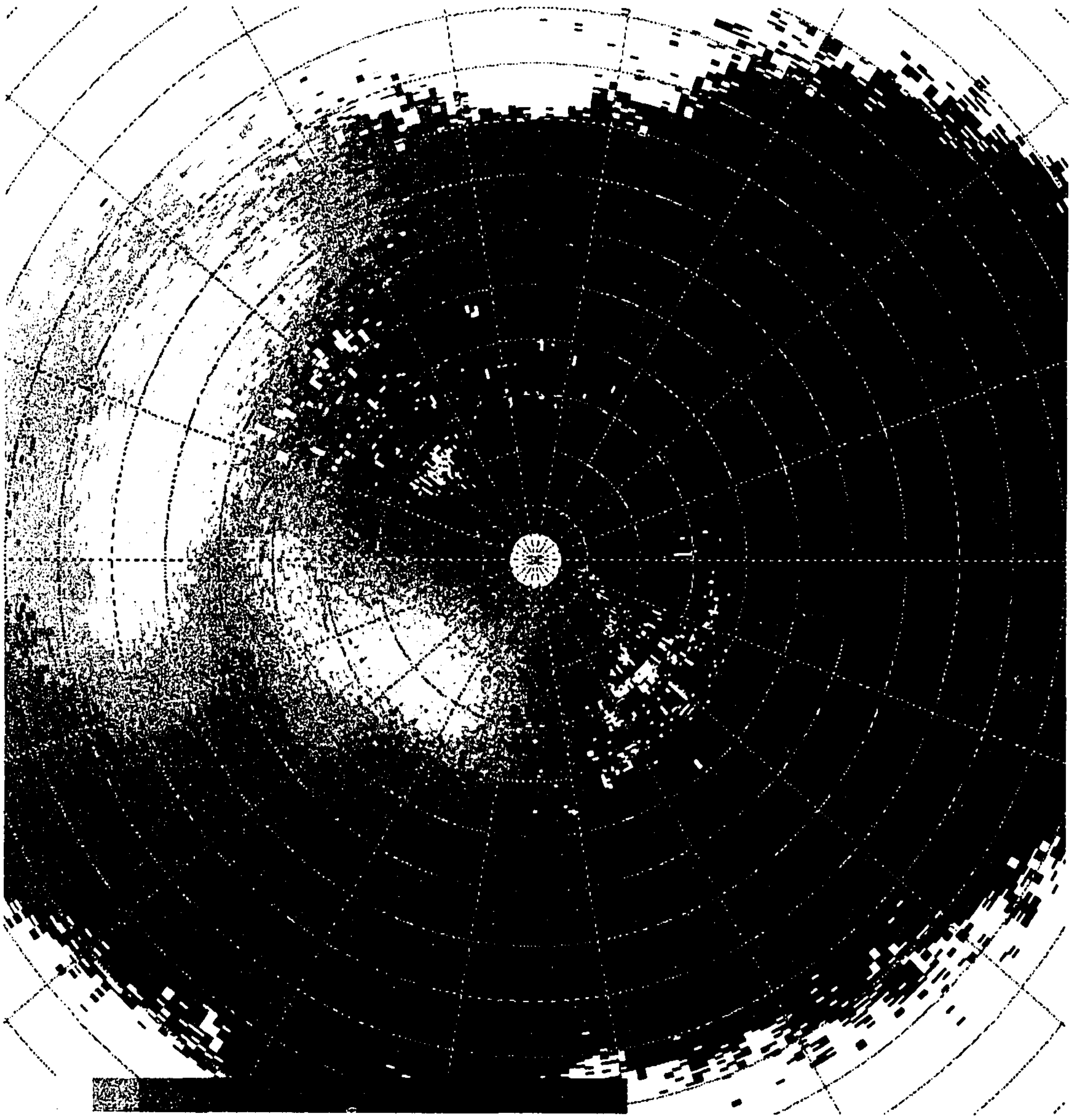

Elev min,max 3.25 3.38 Assumed data range: -20. 20.@ 3 gsp: 15.
DATE: 8 15 1 Times: 15 3 9 15 3 41 GMT RADS: 1840 2205
KTLX HGT VEL, m/s HRINGS: 0.30km RAYS: 20.deg MAG 4.5

Figure 3.31: Velocity scan corresponding to Fig. 3.30.

Chapter 4

Using Radar Data to Measure LLJ Turbulence

For I have dreamt of bloody turbulence, and this whole night
hath nothing been but shapes and forms of slaughter.
-Andromache, Troilus and Cressida, Act V Scene 3

4.1 Dealiasing VAD Data

The minimum pulse repetition time (PRT) of the Cimarron radar is 768.0 μs (see Table 4.1). The maximum speed that can be measured without aliasing, V_{max}, at this PRT is 35.7 m/s, according to

$$V_{max} = \pm \frac{\lambda}{4PRT}$$

V_{max} for NEXRAD radars is about 26 m/s for common scan modes. Since LLJs can have speeds of over 50 m/s, aliasing needs to be dealt with. In this case, the aliasing problem is not too severe as we do not expect more than one fold in velocity. The actual velocity detected from the sampled Doppler shift is either the value determined from the Doppler equation, $V_{indicated}$, or any one of an infinite number of aliases separated by $2V_{max}$:

$$V = V_{indicated} + 2nV_{max}$$

PRT, μs	RANGE, km	Vmax, m/s
768.0	115.2	35.7
921.6	138.2	29.7
1075.2	161.2	25.5
1228.8	184.3	22.3

Table 4.1: Available PRTs, maximum range, and maximum speed without aliasing for Cimarron Doppler Radar

where n is a positive or negative integer. Speeds up to $3V_{max}$ (=107 m/s) will be contained within the first three aliases (n=0 or ±1) and any LLJ is unlikely to exceed this level, so we only need to decide which of these three speed aliases is the correct one. The general way to dealias data (e.g., Doviak and Zrnić, p. 141) is to compare the indicated velocity and all the possible aliases with what one approximately believes the velocity to be. The velocity closest to this approximate velocity is then chosen. Typically, the approximate velocity is obtained by a proximity sounding or by Doppler data of a nearby or analogous region which is not believed to be aliased.

Figure 4.1 shows a VAD (a Velocity-Azimuth Display) which has not been dealiased. Near the minimum and maximum of the data, some points appear to be in error (aliased) by $2V_{max}$. Moving these points by $2V_{max}$ up or down would bring them very close to the best fit curve and the other data points, thus dealiasing the data. To accomplish this by automatic algorithm, we proceed with the following iterative scheme, which was developed as part of this research:

1. We find a point in the data in azimuth that we believe is not aliased. The data (e.g., of Fig. 4.1) are scanned in azimuth to find the first point at which the average of 3 successive data points of speed is less than 4 m/s (2 m/s for DOW and NEXRAD data). These 3 points are also checked to see if adjacent values differ by more than 20 m/s. If they do, then one of the points is probably aliased, and the points are not used as a starting point. As aliasing is a problem near the peaks in speed, speeds near zero are not likely to be aliased, so we have a point at which we are confident the data are not aliased, as long as the actual speeds are below about $2V_{max}$. If speeds greater than about $2V_{max}$ were present, then this method will fail as some

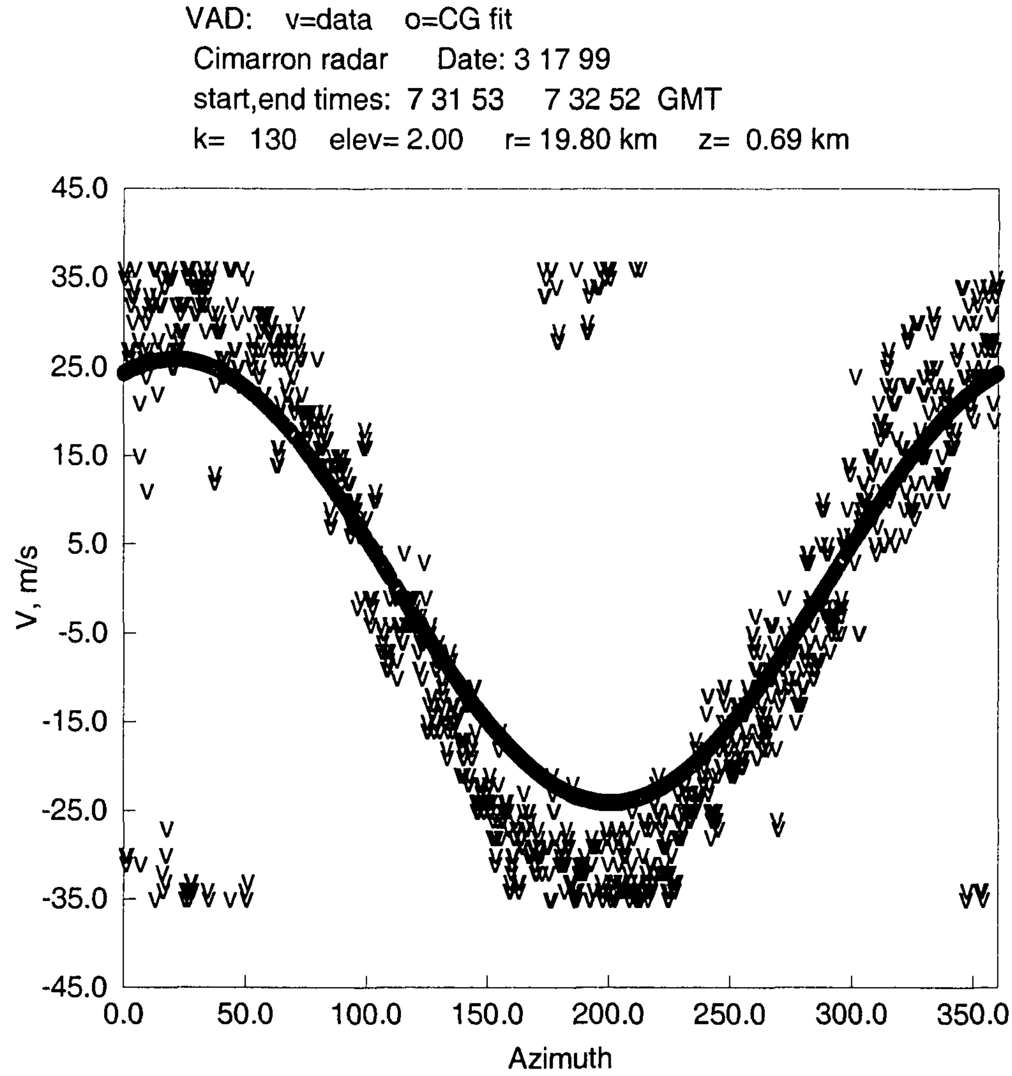

Figure 4.1: VAD plot with some aliased data. V's are data, circles (solid line) is best fit sine wave.

near zero velocities will be aliases. As we proceed through the data in azimuth from this point, the speeds increase or decrease. If aliasing occurs, then it first shows up as a discontinuous jump in speed between adjacent azimuthal points.

2. Proceeding in azimuth through the data from the starting point, an azimuthal running average of 5 data points of speed is calculated and the next point in azimuth is compared with it. We consider this velocity value and the first two aliases (V $\pm 2V_{max}$) This next point is replaced by whichever of these three velocities is closest to the running average. Essentially, the running average in azimuth for data which is assumed to not be aliased is used as an approximate value for comparison to dealias speeds nearby in azimuth. This dealiasing is not done if the point being tested and the running average are more than 25 degrees apart in azimuth, i.e., when the data are too widely spaced.

3. After all the data in the VAD have been dealiased by this first pass through the data, the best fit sine wave is then calculated.

4. This best fit is then used as the approximate velocity for comparison to dealias the data in a second pass. The data are again looped through and the speeds and first aliases are compared with the best fit speeds from step 3. The alias is selected which is closest to the best fit value. This second pass is done because the data are sometimes fairly noisy and the first pass of steps 1-2 occasionally selects the wrong alias. Points which are incorrectly dealiased in step 2 are undealiased back to correct values in step 4.

5. The best fit sine wave is then recalculated. In principle, we could iterate again using this improved best fit to go back and again check for aliasing; but step 4 changes few points in practice, and two passes through the data checking for aliases, once using the noisy data and once using the smooth fit, appears to be sufficient.

Fig 4.2 shows the results of applying this algorithm to the data of Fig. 4.1. This algorithm uses the data near zero speed as a starting point first guess for dealiasing adjacent points in azimuth. The algorithm should work up to the point where high speeds are aliased to close

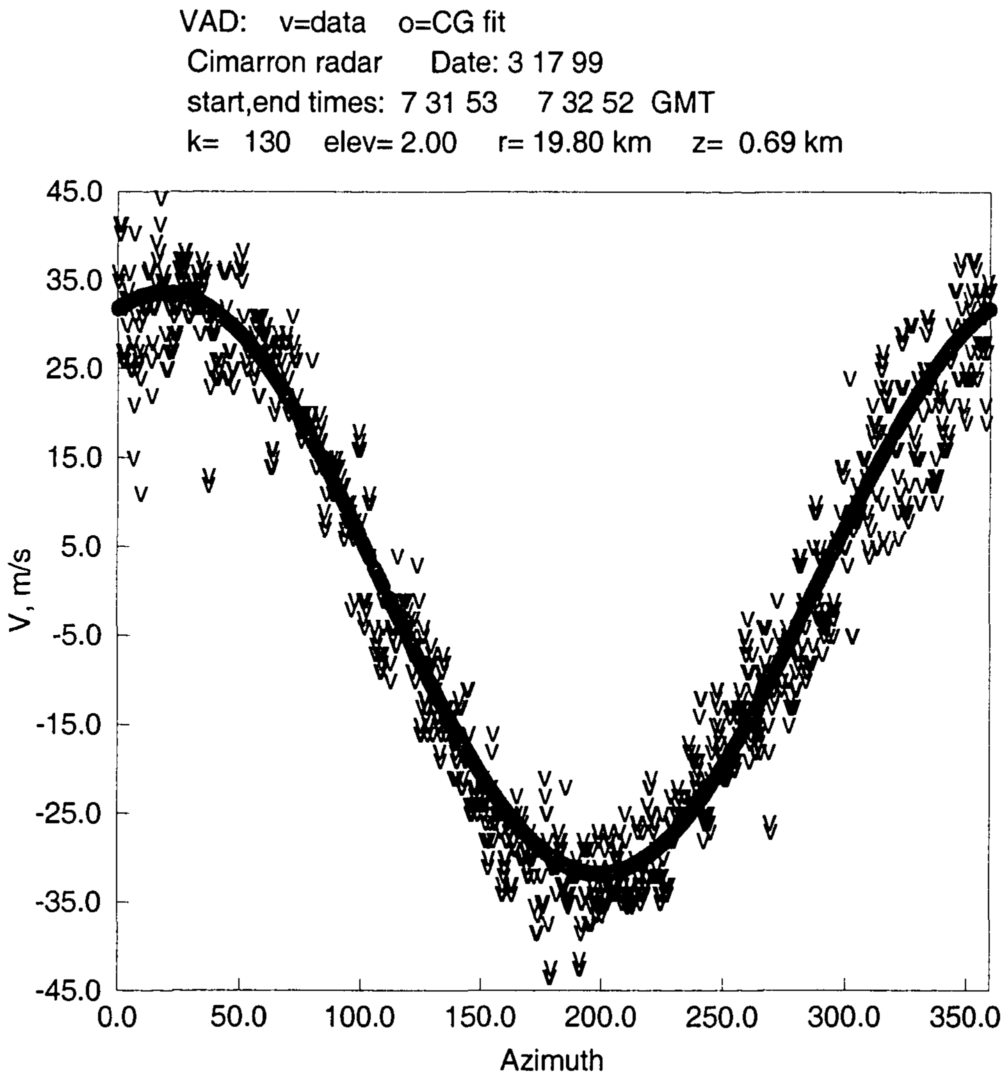

Figure 4.2: VAD data of Fig. 4.1 after dealiasing.

to zero meters per second, since these points then might incorrectly be chosen as unaliased starting points. Consequently, the algorithm may have problems if speeds greater than about 2V$_{max}$ (~70 m/s) were actually present.

4.2 Measurement of turbulence with Doppler radar

Typical measures of turbulence are the variances in the velocity components, $\sigma_u^2 = \overline{u'^2}, \sigma_v^2 = \overline{v'^2}, \sigma_w^2 = \overline{w'^2}$ where the velocity perturbations are u', v', w'; and the covariances of the velocity perturbations, $\overline{u'v'}$, $\overline{u'w'}$, $\overline{v'w'}$, where the overbars refer to time averages. Another measure of turbulence is the turbulent intensities, u'_{rms}/u, v'_{rms}/v, w'_{rms}/w, which involves the root-mean-square velocity perturbations. There is also the turbulent eddy dissipation rate, ϵ. Three techniques to obtain these variables from clear air Doppler radar data have been described in the literature. These methods differ in the length scales of turbulence they are sensitive to. These methods are:

1. Using the Doppler spectrum width, for variances in space based on turbulent length scales smaller than the size of the radar probe volume. (Gossard, 1990). This involves isolating that portion of the spectrum width due to turbulence from that due to other causes.

2. Using the variance of the velocity measurement in azimuth about the VAD wind (Wilson, 1970; Lhermitte, 1968; and Frisch, 1992), for variances based on turbulent length scales larger than the probe volume but smaller than the diameter of the scan circle.

3. Using the variance in time of an ensemble of VAD determined wind values (Kropfli, 1986), for variances based on all turbulent length scales larger than the probe volume size (up to a length scale limited by the ensemble time multiplied by the mean wind speed).

The first two of these will uses spatial variances, while the third uses temporal variances. The difference between spatial and temporal variances will be small provided the speed the probe is scanned through the wind field is large relative to the mean wind speed. This is known as *Taylor's hypothesis* (Tennekes and Lumley, 1972, p. 253). For spectrum width, the sensed radial wind variance is based on a spatial weighted average of the velocity perturbations within the probe volume. These perturbations are sensed simultaneously, implying an infinite scan speed. In a typical VAD scan used here, a scan is acquired in 2 minutes over a circumference of about 20 km. This gives a scan speed of over 150 m/s, compared with LLJ winds of 40 m/s.

For this work, we have applied the first two of these methods, as discussed in the next two sections.

4.3 Deducing Turbulence from Spectrum Width Information

This section describes a technique that is somewhat different from methods published previously. Previous attempts at using spectral width to deduce clear-air turbulence (reviewed by Gossard, 1990) have either neglected the effect of wind shear, or accounted for the effect of wind shear by using measured wind profiles. However, the method discussed here attempts to take advantage of the modulation in amplitude of the spectrum width in azimuth as seen, for example, in Fig. 3.4. The spectrum width is defined to be the standard deviation of the velocity spectrum about the mean, σ_r, and has a modulation in amplitude with azimuth similar to velocity, but with two maxima 180 degrees apart instead of a maximum and a minimum 180 degrees apart. Fig. 3.4 actually plots variance, or σ_r^2. It will now be shown that this modulation is due primarily to vertical wind shear alone, subject to certain assumptions, and that spectrum width information alone can be used to extract both wind shear and turbulence.

Spectrum width information reflects broadening of the velocity spectrum from a variety of sources that are generally additive in terms of variance, or spectrum width squared, namely: turbulence, mean velocity gradients within the probe volume, antenna motion and signal properties, noise, and particulates and precipitation (and possible large objects like birds). To show how these are additive, consider first the variance in the radial velocity spectrum due to wind shear, σ_s^2 . By definition

$$\sigma_r^2 = \sigma_s^2 = \frac{1}{N}\sum_{i=1}^{N}(V'_{r_i})^2$$

where V'_{r_i} is deviation from the mean radial velocity of the ith measurement within the probe volume, and N is the number of velocity measurements considered by the radar system (e.g., the 128 samples typically used for Cimarron). If we now consider the addition of a random turbulent velocity component to V'_{r_i}, T, we have:

$$\sigma_r^2 = \frac{1}{N}\sum_{i=1}^{N}(V'_{r_i} + T_i)^2 = \frac{1}{N}\sum_{i=1}^{N}(V'^2_{r_i} + 2V'_{r_i}T_i + T_i^2)$$

$$= \frac{1}{N}\sum_{i=1}^{N} V_{r_i}'^2 + \frac{1}{N}\sum_{i=1}^{N} 2V_{r_i}' T_i + \frac{1}{N}\sum_{i=1}^{N} T_i^2 \tag{4.1}$$

Since T is a random variable uncorrelated with V_{r_i}', the second summation on the right of (4.1) is zero leaving:

$$\sigma_r^2 = \sigma_s^2 + \sigma_t^2$$

Similar arguments (essentially assuming the sources of spectral broadening are all uncorrelated) can be made for other sources of spectral broadening and Doviak and Zrnić (1984) Eqn. 5.59 states:

$$\sigma_r^2 = \sigma_s^2 + \sigma_\alpha^2 + \sigma_d^2 + \sigma_t^2 \tag{4.2}$$

Where σ_r^2, the velocity spectrum width squared, is the sum respectively of variances from shear, antenna motion (σ_α^2) , droplet fall speeds (σ_d^2) , and turbulence. System noise could also be included for completeness. For the clear-air data considered in this study, we can neglect broadening from variance in droplet fall speeds, σ_d^2. σ_α^2 is also small. Of these sources of spectral broadening, it will be shown here that vertical wind shear is the only one sensitive to radar azimuth (assuming horizontally homogeneous flow and isotropic turbulence). The assumption of isotropic turbulence is perhaps reasonable as the spectrum width is sensitive to turbulence length scales smaller than the size scale of the radar probe volume (based on pulse widths, this is at least 150 m for Cimarron and 250 M for a NEXRAD, though this depends also on range), and small scales of turbulence tend to be more isotropic than large scales. The method of getting the turbulent intensity of scales larger than the probe volume using the variance of the VAD itself, where we allow non-isotropy of turbulence, is discussed in Section 4.4.

To understand how σ_t^2 relates to the turbulent velocity components, we consider a purely turbulent wind field (no shear) within the probe volume. If vertical motions are negligible (true for small tilt angles), then the projection of the horizontal components of the velocity perturbation onto the radar radial at azimuthal angle ϕ gives:

$$V_r' = u' sin\phi + v' cos\phi$$

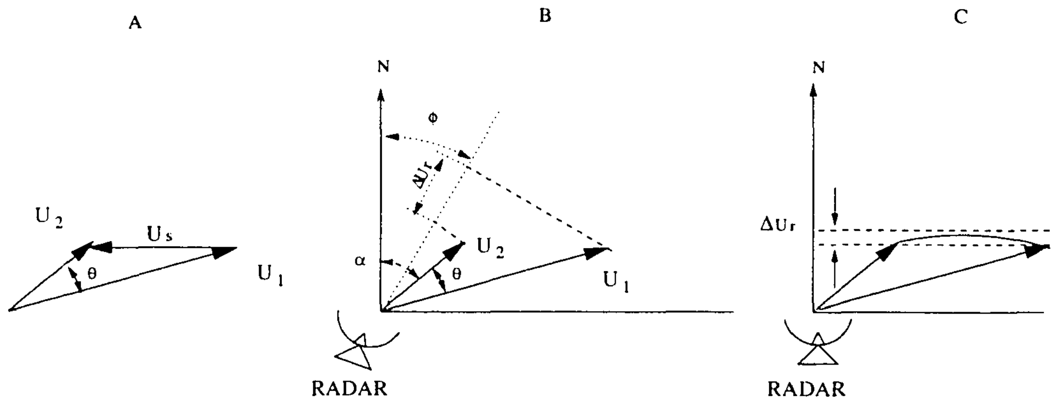

Figure 4.3: Diagram for radar sensing of wind shear within a probe volume. A shows shear vector relative to wind at the bottom and top of the resolution volume. B shows projection of winds onto radar beam direction. C shows error in analysis (see text) due to hodograph curvature.

and

$$\sigma_t^2 = \frac{1}{N}\sum_{i=1}^{N}(u'sin\phi + v'cos\phi)^2 = \frac{1}{N}\sum_{i=1}^{N} u'^2 sin^2\phi + v'^2 cos^2\phi + 2u'v'sin\phi cos\phi \qquad (4.3)$$

If the turbulence is isotropic, u' and v' are uncorrelated and the last term in (4.3) vanishes, leaving:

$$\sigma_t^2 = \sigma_u^2 sin^2\phi + \sigma_v^2 cos^2\phi$$

This has an azimuthal variation; however, isotropy also implies that $\sigma_u = \sigma_v$, so:

$$\sigma_t^2 = \sigma_u^2 = \sigma_v^2 \qquad (4.4)$$

Next, to determine the variance due to wind shear, we first assume that there is no mean vertical wind, which for this clear-air study should be a pretty good assumption. Then, for any given tilt angle, we can project the horizontal wind vectors onto the plane of the radar tilt and consider what happens to these projected winds as azimuth varies. Vertical wind shear results in a range of velocities being present within the resolution volume of the radar of depth ΔZ. As shown in Fig. 4.3a, these velocities range from $\vec{U_1}$ to $\vec{U_2}$ with total shear vector:

$$\vec{U_s} = \vec{U_2} - \vec{U_1} = \frac{d\vec{U}}{dZ}\Delta Z$$

If the probe volume is small, then the radial velocity components of $\overrightarrow{U_1}$ and $\overrightarrow{U_2}$ will be similar (as drawn in Fig. 4.3a) and $\overrightarrow{U_s}$ will be small. The radar beam, at azimuth angle ϕ, will see the projection of all the winds onto the radar radial. Using the convention of Fig. 4.3b, the spread in radial velocities, ΔU_r, will be

$$\Delta U_r = U_2 cos(\alpha - \phi) - U_1 cos(\alpha + \theta - \phi)$$

where $U_1 = \left|\overrightarrow{U_1}\right|$, $U_2 = \left|\overrightarrow{U_2}\right|$, θ is the angle between the wind vectors in the probe volume and α is the azimuthal angle of the wind vector $\overrightarrow{U_2}$. Using trigonometric identities (addition formula for cosines and the law of cosines), we find that this is equivalent to:

$$\Delta U_r = U_s cos(\phi + \psi)$$

where $U_s = \left|\overrightarrow{U_s}\right|$ and

$$\psi = tan^{-1}\left(\frac{U_2 sin\alpha - U_1 sin(\alpha + \theta)}{U_1 cos(\alpha + \theta) - U_2 cos\alpha}\right) = constant$$

That is, the range of velocities seen by the radar is a cosine function of azimuth with an amplitude equal to the amplitude of the shear vector through the depth of the probe volume. As can be seen in Fig. 4.3b, when the radar azimuth is perpendicular to the shear vector (when $\phi = \frac{\pi}{2} - \psi$), both $\overrightarrow{U_1}$ and $\overrightarrow{U_2}$ will have the same projection onto the radar radial and ΔU_r will be zero, whereas when the radar azimuth is in the same direction as the shear vector (when $\phi = -\psi$), the projections of all the mean winds in the probe volume has an amplitude equal to the shear vector. Spectrum width is always a positive quantity, so it is related to the absolute value of ΔU_r. The spectrum width due to wind shear, σ_s, is then equal to an azimuthally varying quantity

$$\sigma_s(\phi) = b\,|U_s cos(\phi + \psi)| \tag{4.5}$$

where the constant b (of order 1) is needed to convert from ΔU_r to standard deviation. The value for b could be calculated from considering the radar beam as a Gaussian shape to weight the velocities and obtain the spectrum width as a function of wind shear. However, the Cimarron radar beam is not perfectly Gaussian, and it might be better to obtain b empirically. In any case, what we originally sought to obtain here is turbulence and not wind shear, though it is possible that wind shear obtained from spectrum width could be more precise than that obtained from differentiating the wind profile determined by VAD analysis, as numerical differentiation is inherently noisy.

Equation 4.5 describes a rectified cosine wave. Retaining only the terms due to wind shear and turbulence in (4.2):

$$\sigma_r^2 = \sigma_s^2 + \sigma_t^2 = b^2 U_s^2 cos^2(\phi + \psi) + \sigma_t^2 \tag{4.6}$$

By trigonometric identity, this is also equal to:

$$\sigma_r^2(\phi) = (\sigma_t^2 + \frac{b^2 U_s^2}{2}) + \frac{b^2 U_s^2}{2} cos 2(\phi + \psi)$$

In other words, the azimuthal display of spectral variance of the radial wind component consists of a cosine wave of frequency 2ϕ entirely due to wind shear, plus a constant, part of which is due to turbulence and part of which is due to wind shear. In principle, this could also be done without the assumption of isotropic turbulence, in which case, (4.6) would include azimuthally varying terms for the different turbulence variances and covariances.

This straight-forward analysis is very useful in interpreting data such as Fig. 3.4, but it has some implicit assumptions which are not always met exactly in practice. In particular, as Fig. 4.3c indicates, if the mean wind vectors within ΔZ follow a curved hodograph rather than all falling along a straight line, then the minimum variance will not be zero and the constant c will have a component due to hodograph curvature. The magnitude of this error would be about U$\sin\Delta\theta$ and should be small as long as ΔZ is small. Also, this approach would not be valid if there are significant deviations from horizontal homogeneity in either the turbulence or mean winds. The cases selected for analysis later in this report appear to be horizontally homogeneous as evidenced by (for example) velocity azimuth display not deviating systematically from a sine wave.

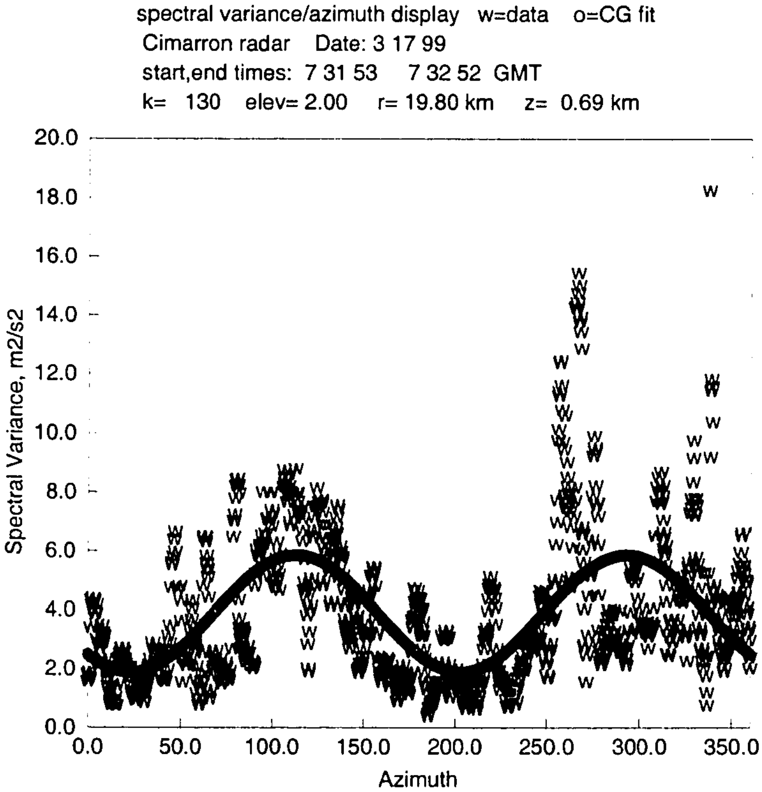

Figure 4.4: Azimuthal display of spectral variance after application of 11 point smoother. Solid line is best fit for (4.6).

What we are interested in determining is the level of turbulence. To determine σ_t^2 from data such as Fig. 3.4, we proceed in a similar way as we do to determine the mean wind profile, except here we are fitting the azimuthal function (4.6) instead of a sinusoid. Figure 4.4 shows an azimuthal display of spectral variance and the best fit to (4.6). Spectrum width measurements have more noise than velocity and to improve the appearance of Fig. 4.4, the data are first passed through an 11 point smoother (which uses a moving average). One possible reason for noisy spectrum width data is that the probe volume size may be small relative to the length scales of the turbulent fluctuations. Despite the noise, Fig. 4.4 does show that the derived function (4.6) is at least qualitatively in agreement with the behavior of the data.

4.4 Deducing Turbulence from the Variance in the VAD

In contrast with Sec. 4.3, which attempts to deduce turbulence by using the spectrum width information and separating it into wind shear and turbulence, previous authors (e.g., Frisch et al., 1992) have used the variance of the wind in azimuth about the best fit function. In this technique the wind is separated into mean and fluctuating components:

$$\begin{aligned} U &= u + u' \\ V &= v + v' \\ W &= w + w' \end{aligned}$$

Where u,v,w are the mean velocity components, u', v', w' are the turbulent perturbations, and U,V,W are the total wind components. The perturbations are generally a function of space and time, $u' = u'(t, x, y, z)$, or from the standpoint of the radar at a certain elevation angle and range, they are functions of time and azimuth, $u' = u'(t, \phi)$. The measured radial wind component sensed by the radar is:

$$V_r = (u + u')sin\phi cos\beta + (v + v')cos\phi cos\beta + (w + w')sin\beta$$

Where β is the elevation angle and ϕ is the azimuth angle. The mean values, u,v, and w (and therefore $\overline{V_r}(\phi)$ which $= usin\phi cos\beta + vcos\phi cos\beta + wsin\beta$), are known from the best-fit analysis of the VAD. This average wind vector is obtained by the least-squares fit of the data to a function around an azimuth circle (over a short period of time) and is a spatial average velocity. The variance of the data about the mean wind in azimuth over an azimuth range from 0 to ϕ' is:

$$var(Vr) = \frac{1}{\phi'} \int_0^{\phi'} (V_r - \overline{V_r})^2 d\phi \tag{4.7}$$

$$= \frac{1}{\phi'} \int_0^{\phi'} (u' sin\phi cos\beta + v' cos\phi cos\beta + w' sin\beta)^2 d\phi$$

$$= \frac{1}{\phi'} \int_0^{\phi'} [(u'^2 sin^2\phi + v'^2 cos^2\phi + 2u'v' sin\phi cos\phi) cos^2\beta$$

$$+ w'^2 sin^2\beta + 2w'u' sin\phi sin\beta cos\beta + 2w'v' cos\phi sin\beta cos\beta] d\phi \qquad (4.8)$$

We now take time averages of both sides of (4.8). If this averaging is done over a short enough period of time such that var(V_r) is constant in time but a long enough period of time for the turbulent length scales to be measured by the variances of u', v', w' to be sensed, (4.8) becomes:

$$var(Vr) = \frac{1}{\phi'} \int_0^{\phi'} [(\overline{u'^2} sin^2\phi + \overline{v'^2} cos^2\phi + 2\overline{u'v'} sin\phi cos\phi) cos^2\beta$$

$$+ \overline{w'^2} sin^2\beta + 2\overline{w'u'} sin\phi sin\beta cos\beta + 2\overline{w'v'} cos\phi sin\beta cos\beta] d\phi \qquad (4.9)$$

This equation can be integrated analytically under the assumption that the turbulence is horizontally homogeneous so that the time averaged quantities are not dependent on azimuth angle, ϕ. The method devised by Wilson (1970) involves evaluating (4.9) by integration over four quadrants of the scan circle. These partial integrals can then be combined to produce the separate covariances and variances. However, if a single integral over 2π is taken, all the covariance terms drop out. With ϕ'=2π, (4.9) yields:

$$var(V_r) = \frac{1}{2}(\overline{u'^2} + \overline{v'^2}) cos^2\beta + \overline{w'^2} sin^2\beta \qquad (4.10)$$

If the turbulence is isotropic, $u' = v' = w'$ and var(V_r)=constant (i.e., no elevation dependence). For small elevation angles (the usual case), (4.10) reduces to:

$$var(V_r) = \frac{1}{2}(\overline{u'^2} + \overline{v'^2}) = horizontal\ TKE = \overline{u'^2} = \sigma_u^2\ if\ isotropic \qquad (4.11)$$

Where TKE is the turbulent kinetic energy. Since TKE=$\frac{1}{2}(u'^2+v'^2+w'^2)$, var($V_r$)=$\frac{2}{3}$TKE. Var($V_r$) is essentially the same variable obtained by the spectral width method, except that the spectral width method is sensitive to TKE at scales below that of the radar probe volume while the variance of the VAD method is sensitive to TKE at scales larger than the probe volume and smaller than the VAD scan circle. Since most of the turbulent energy is in the larger scales, TKE in (4.11) should be larger than that in (4.4). The total TKE would be the sum of these two.

It should also be realized that certain non-turbulent structures could be present in the boundary layer that would increase the variance in the VAD. For example, laminar boundary layer convective or shear rolls would be expected to increase the indicated turbulence, without necessarily being turbulent.

4.5 Best Fit Methodology for VAD Winds and Turbulence

The method used to determine the best fit sine wave through data such as Fig. 4.2 is now discussed. A conjugate gradient routine that minimizes a cost function formulated as a sum of the squared error is used. There are more efficient ways to get the VAD winds than using a conjugate gradient routine, which involves going through the data multiple times to iterate on minimizing a cost function as well as calculating derivatives. For example, Lhermitte (1968) simply gets the first Fourier coefficients, requiring two passes through the data. Fast Fourier transforms would make this method extremely fast. However, using a cost function approach makes it very easy to modify the routine to fit functions more complicated than a sine wave and the conjugate gradient method is still very fast. This method would also allow the incorporation of auxiliary data and constraints. The conjugate gradient routine used here was adapted from *Numerical Recipes* (Press et al.,1986, Sec. 10.6). For determining a VAD wind, the cost function, J, is:

$$J = \sum (V_r - U cos\varphi - V sin\varphi)^2 \tag{4.12}$$

where V_r is the radial velocity component sensed directly by the radar, U and V are the best fit wind components, φ =(90°-azimuth), and the summation is taken over all the data. The data consist of pairs of V_r and φ. That is, J is just the sum over all the data points in a scan of the squared error between the measured radial velocity and the best-fit radial velocity. The derivatives of (4.12) with respect to U and V are needed by the conjugate

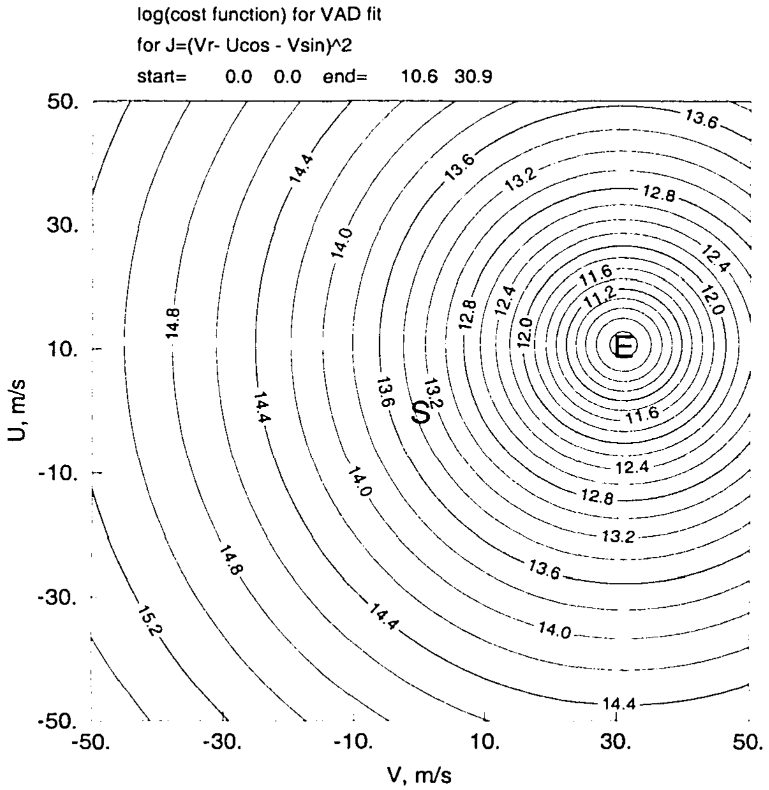

Figure 4.5: Plot of the natural log of the cost function for (4.12) for data of Figure 4.2. S marks the starting point used for the conjugate gradient method and E marks the final minimum found.

gradient routine and are easily calculated as:

$$\begin{aligned}\frac{\partial J}{\partial U} &= \sum -2(V_r - U cos\varphi - V sin\varphi) cos\varphi \\ \frac{\partial J}{\partial V} &= \sum -2(V_r - U cos\varphi - V sin\varphi) sin\varphi\end{aligned}$$

A contour plot of J for the data of Fig. 4.2 is shown as Fig. 4.5. The log of the cost function is plotted as this enhances the number of contours near the optimum. This figure shows that the conjugate gradient routine seems to be working well, with the optimum value marked as "E" in the figure occurring at the visual minimum of the function. It also shows that the cost function is well behaved, so we do not expect problems from multiple minima. In fact, since (4.12) is quadratic in U and V, and since $\frac{\partial^2 J}{\partial U}$ and $\frac{\partial^2 J}{\partial V}$ are both positive definite, there can only be a unique minimum.

The cost function for determining the turbulence from the azimuthally varying spectral

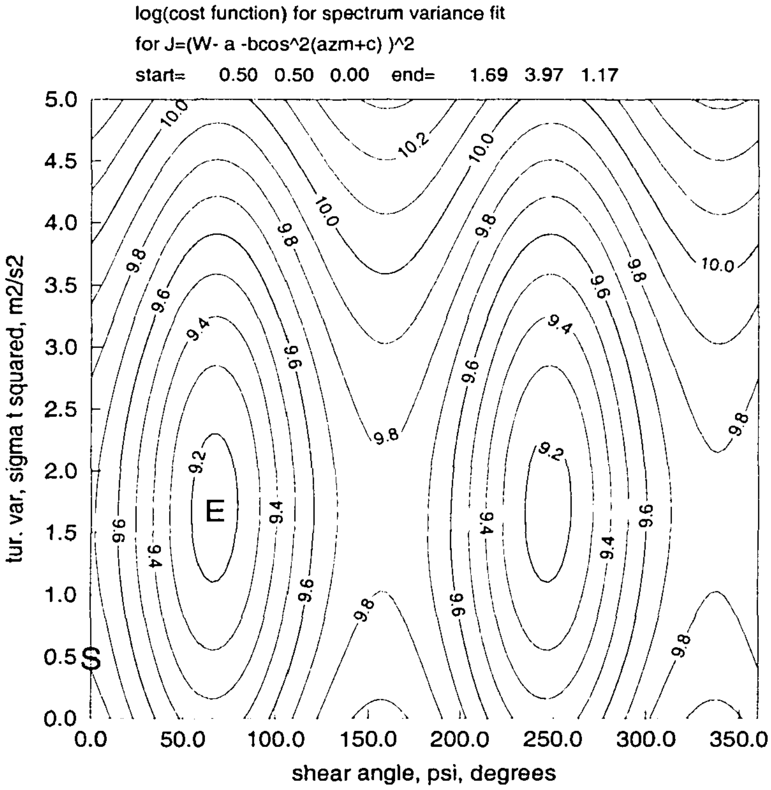

Figure 4.6: Cost function plot (log(J)) for (4.13) using data for Fig. 4.4 with $b^2U_s^2 = 3.97$. S indicates starting point and E the ending point for the minimization routine.

variance is, from (4.6):

$$J = \sum(W^2 - \sigma_t^2 - b^2U_s^2cos^2(\phi + \psi))^2 \tag{4.13}$$

Where W is the radar-measured spectrum width, σ_r. The data consist of pairs of W and ϕ. The derivatives are:

$$\begin{aligned}
\frac{\partial J}{\partial \sigma_t^2} &= \sum -2G \\
\frac{\partial J}{\partial (b^2U_s^2)} &= \sum -2Gcos^2(\phi + \psi) \\
\frac{\partial J}{\partial \psi} &= \sum 2Gb^2U_s^2sin(2\phi + 2\psi)
\end{aligned}$$

Where $G = W^2 - \sigma_t^2 - b^2U_s^2cos^2(\phi+\psi)$. As there are 3 constants to be determined, the cost function is three-dimensional. Figure 4.6 plots the cost function in the plane where $b^2U_s^2 = 3.97$ (the computed optimum for the data of Fig. 4.4). This cost function shows symmetry with two identical minima spaced 180° apart. This is to be expected from the periodicity of (4.13), which gives two possible solutions for ψ since $\cos^2(\phi + \psi) = \cos^2(\phi + \psi + 180)$. Which one of these two solutions the minimization routine finds is determined by the starting point for the iteration (the first guess of the determined parameters), indicated by "S" in Fig. 4.6. This means there will be a 180° ambiguity to the wind shear direction determined with this method.

There is another problem with minimizing the cost function, (4.13). There is a pair of solutions (one real and one spurious) associated with the identity:

$$a + bcos^2\theta = (a+b) - bcos^2(\theta + \frac{2n+1}{2}\pi)$$

or more simply:

$$cos^2\theta = 1 - cos^2(\theta + \frac{2n+1}{2}\pi)$$

for n an integer. This identity means that sometimes the conjugate-gradient routine could potentially find the solution in which the variable $b^2U_s^2$ is reported as a negative number (namely $-b^2U_s^2$) and in which the term σ_t^2 is replaced by $(\sigma_t^2 + b^2U_s^2)$. Both these solutions produce identical fits to the data, but with dramatically different values for the sought variables. Since the square of the shear term cannot physically be negative, this negative shear solution is spurious. Experiments have shown that this spurious solution occurs often enough to be a concern, despite judicious choices of first guess values. This has been dealt with by checking the sign of the returned value for $b^2U_s^2$. If it is negative, $b^2U_s^2$ is replaced by its absolute value, the returned value for the turbulence term is replaced by $(\sigma_t^2)_{replaced} = (\sigma_t^2)_{returned} - b^2U_s^2$, and the angle ψ is shifted by $\frac{\pi}{2}$.

4.6 LLJ Profiles

Profiles are now produced of azimuthal average reflectivity, wind, and turbulence parameters in LLJs. This is generally done by considering a single radar scan at a certain elevation angle (which takes one or two minutes to obtain, depending on scan rate). Reflectivity is averaged around the circle of the scan at each range gate to produce the average reflectivity; and best fit analysis are made for the VAD winds and turbulence for each range gate as well.

A problem with determining azimuthal average reflectivity is that data are not obtained at every radial. As the radar can only measure reflectivities down to about -25 dBZ, averaging together all the reflectivities that were measured above this threshold will produce a high bias as reflectivities below this are not included in the average. Averaging only good data points is incapable of returning an average below the detection threshold. This bias can be quite severe in areas where few good data points are obtained. At scan rates with the Cimarron radar, 600 radials are potentially available per scan to be averaged together. At ranges with weak reflectivity, fewer than 100 good data points may be obtained with 500 or more radials having reflectivities too weak to measure. This bias gets larger with range because the reflectivity needed to be detectable increases with distance from the radar. To reduce this problem, missing data are assigned a value just below the minimum detectable value. This is the largest value the missing data could have had and will still over-estimate the average, but not by nearly as much as ignoring the missing data completely. It should be possible to fit a normal distribution function to the good data points and to deduce the average by the midpoint of the fitted distribution curve. However, the complexity of doing this has not been faced here, and fitting a normal distribution function would be problematic if the data are not normally distributed.

Figure 4.7 shows profiles of azimuthally averaged reflectivity and VAD determined wind speed and direction based on data in the scans shown in Figs. 3.3 and 3.2. In this case, velocities were obtained up to about 3 km while the reflectivity profile was obtained up to 4 km. This difference is caused by the different filtering used in rejecting data for azimuthal analysis. For reflectivity, data are rejected which fall below the system noise level and for which the amplitude of the velocity is less than 1 m/s. This is done to eliminate ground clutter, which has no Doppler shift. For velocity, data are also rejected when the velocity amplitude is less than 1 m/s. It has also been found that velocity data is highly noisy for low reflectivities, and a narrower band of reflectivity values lying between -20 to 50 dBZ are allowed. The 50 dBZ filter is employed since any reflectivities greater than this are

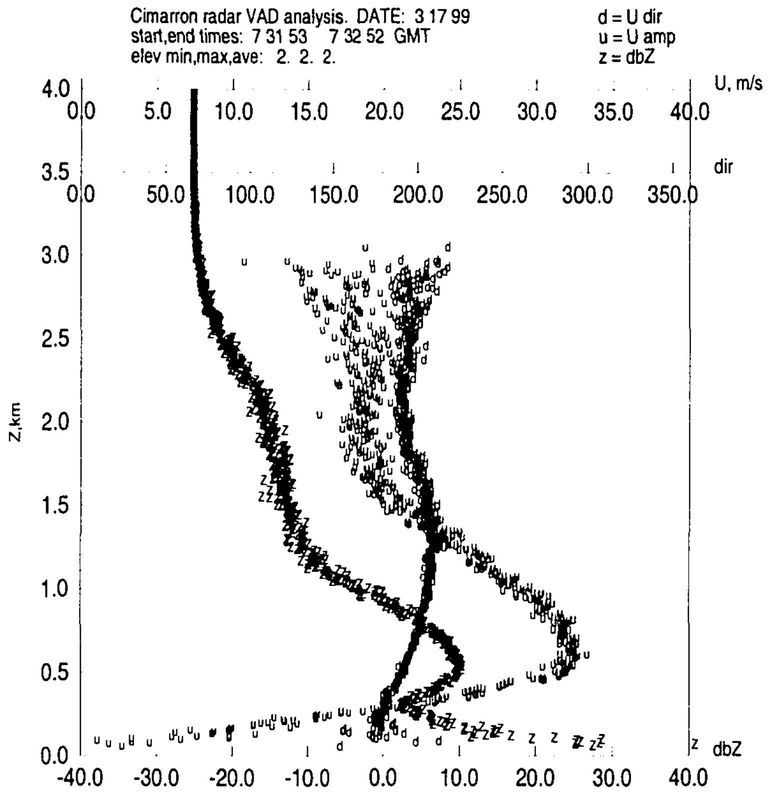

Figure 4.7: Profile of wind speed, direction, and reflectivity for a LLJ from azimuthal analysis of Cimarron radar data. The z's are plotted for reflectivity, u's for wind speed, and d's for wind direction. Data was taken during the night at 7:30 Z, March 17, 1999.

certainly ground clutter. Also, VAD analyses are not performed if there are less than 20 acceptable points in the VAD.

Fig. 4.7 shows a very well defined LLJ with a peak amplitude near 33 m/s at near 700 meters above the ground. This figure also shows a local minimum in reflectivity at about 300 meters in the lower shear layer of the LLJ, and a local maximum at about 600 meters, near the jet core. The hodograph for these data is shown in Figure 4.8. Fig. 4.8B shows the hodograph after the data have been smoothed with a 41 point moving average.

Figure 4.9shows smoothed profiles of wind speed and turbulence. Variances from both methods of deducing turbulence are shown. The two turbulence profiles agree remarkably well qualitatively with regard to the shapes of the profiles, with both having a marked maximum in the lower shear layer and a marked minimum near the jet core. However, the TKE values from the spectral width method have been multiplied by 10 for plotting in Fig. 4.9. This implies that the small scale turbulence measured with this method is an

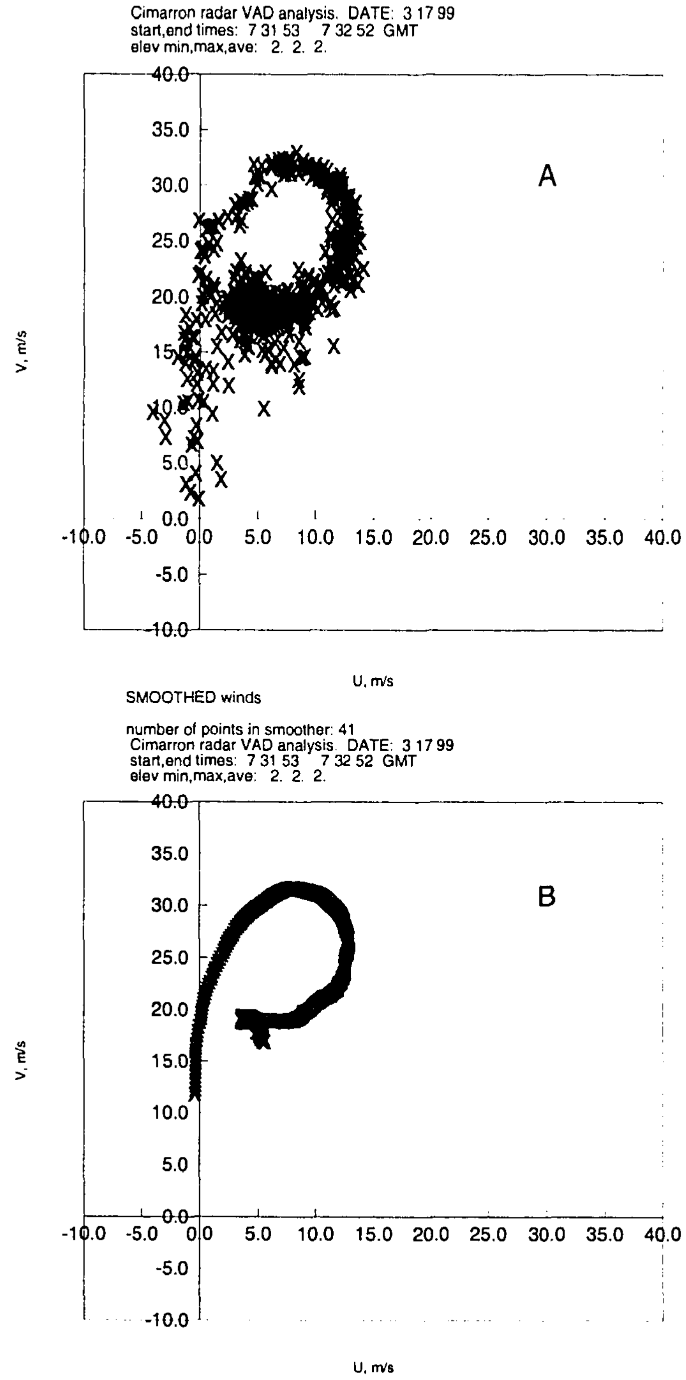

Figure 4.8: Hodograph for wind profile of Fig. 4.7. A is unsmoothed and B is smoothed.

order of magnitude less than the large scale turbulence measured by VAD variance. This may be reasonable as the length scales sensed by the two methods differ by two orders of magnitude.

It is also worth noting how highly correlated the turbulence profiles are with the vertical wind shear, with the peak in turbulence occurring in the vertical center of the lower shear layer. This becomes more apparent when we convert the turbulent variances (with units of $\frac{m^2}{s^2}$) into a quantity having the same units as shear, by taking the square root and dividing by the altitude, Z. This is perhaps a reasonable scaling since at greater heights, the radar probe volume is at a greater distance from the radar and is consequently larger, and the VAD circles are larger; with both these things proportional to Z. So the turbulence measures are sensitive to large length scales at larger altitudes, and might be expected to scale with Z. This scaling is done in Figure 4.10 where we also plot the wind shear calculated from the wind profile.The shear is calculated as a centered difference of the smoothed wind vectors at each vertical triplet of points. Shear calculated in this way is very noisy; consequently, the shear profile is passed through the smoother as well. The shear profile shows that most of the shear is concentrated in the lower shear layer of the jet below 700 meters. Based on the profile of wind speed, one would expect a zero point in shear at the jet peak and an increase in the upper shear layer between 900 and 1500 meters. However, the directional shear is actually strong in the jet core and decreases with height, accounting for the flat shear profile in and above the jet center. Fig. 4.10 shows that most of the scaled turbulence is in the lower shear layer, strongly correlated with the magnitude of the shear.

4.7 LLJ Time-Height Sections

For multiple scans of radar acquired over a long period of time, time-height cross sections can be constructed showing how the profiles of azimuthally averaged quantities evolve over time. Four cases will be considered here using data from the NEXRAD network:

1. May 6-7, 2002, KFWS (Fort Worth, Texas)

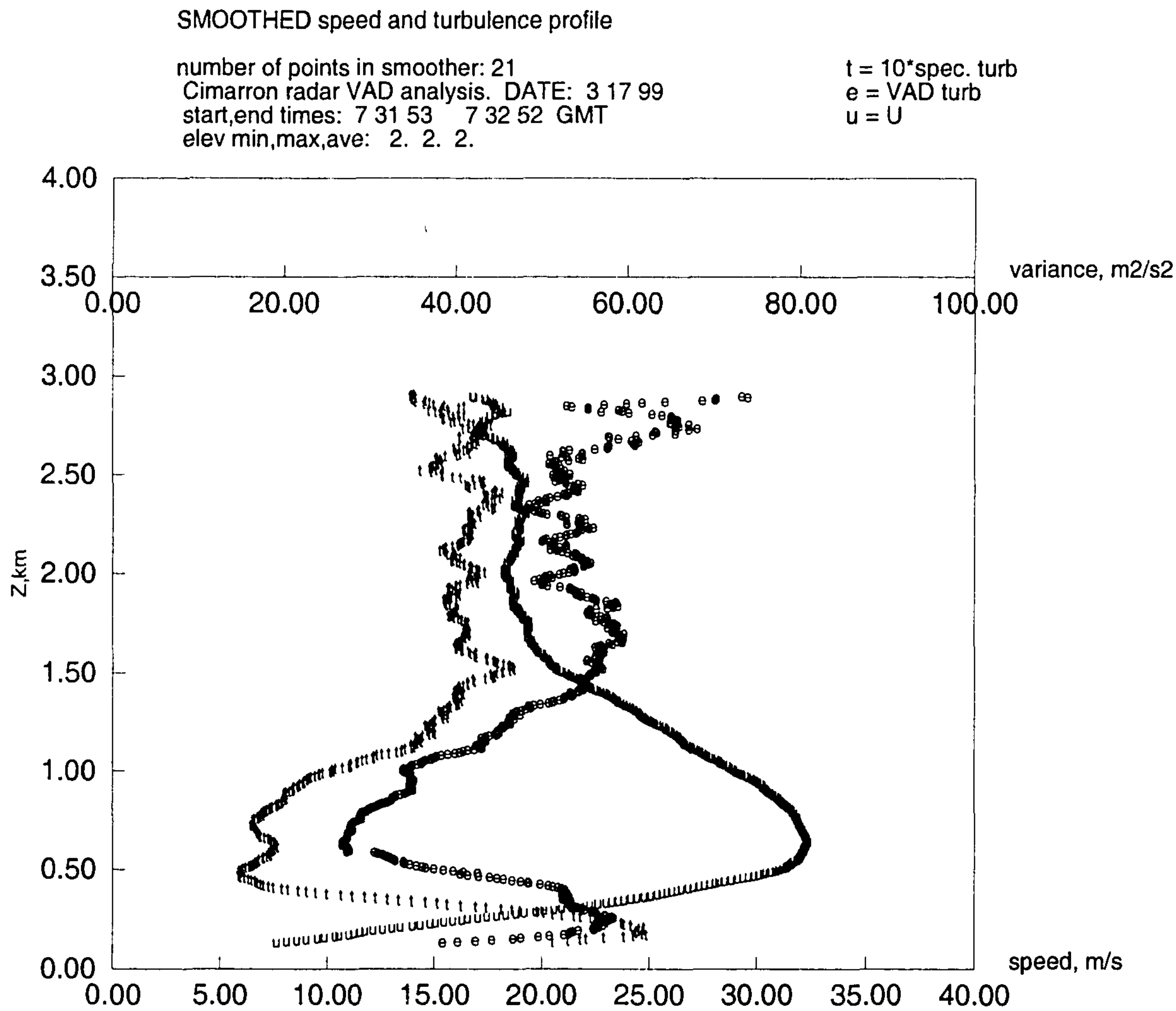

Figure 4.9: Profiles of wind speed and turbulence obtained with Cimarron radar for a LLJ. Plotted u's are LLJ speed. Plotted e's are the variance in the VAD wind as a measure of TKE. Plotted t's are TKE values obtained from separating spectral width data into turbulence and wind shear. The t values have been multiplied by 10. Profiles have been smoothed with a 21 point moving average.

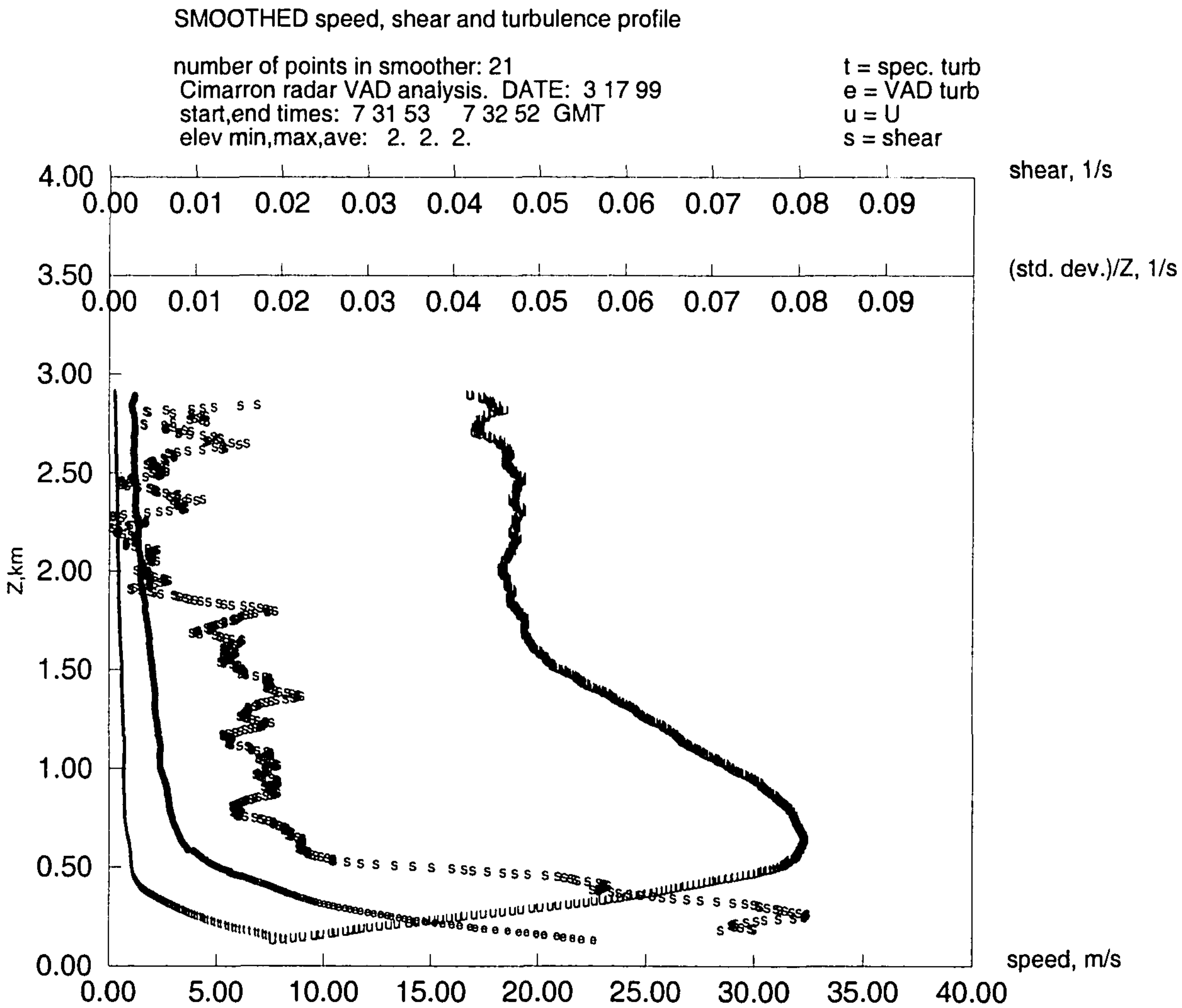

Figure 4.10: Profiles of wind speed, shear, and turbulent standard deviations scaled by height.

2. June 1-2, 2002, KVNX (Enid, Oklahoma)

3. July 15-16, 2000, KFWS (Fort Worth Texas)

4. August 14-15, 2002, KTLX (Twin Lakes, Oklahoma, near Oklahoma City)

These cases are one each month for the warm season. For each case, about 24 hours of data are processed. The data were acquired from the archives of the National Climatic Data Center (NCDC). The recent implementation of internet access to the NEXRAD radar archive at NCDC has made it possible to acquire these data in an efficient manner. Data gaps are common in the archive and it is necessary to search through a considerable quantity of data to find good quality data sets covering the phenomenon of interest. Without rapid access to much of the archive, searching it for usable data would have taken too much time. Once analysis and graphical software has been developed, the time to acquire a data set, check its quality, and produce analytic plots is about an hour. Archived NEXRAD data are superior in quality to the Cimarron radar, at least in terms of signal to noise ratio and ground-clutter suppression. For this reason, and because of the ease of acquiring archived NEXRAD data, NEXRAD date are used instead of Cimarron data for these analyses.

The criteria used to identify cases for analysis are:

1. No precipitation closer than 100 km from the radar during the 24 hour period.

2. The data at night do not have a bilaterally symmetric signature (as in Fig. 3.30). This criterion reduces the probability that the signal is caused by migrating birds.

3. Southerly flow was indicated throughout the period in surface observations.

4. Only data from the 1.5° tilt are used.

The last item follows from Appendix A (q.v.) in which the 1.5° tilt was found to be the best for minimizing the effects of ground clutter.

Most of the time the radars for all of these cases were in clear-air mode. This scan mode gives a volume scan every 10 minutes and, consequently, a wind profile every 10 minutes. Occasionally, a radar will be in precipitation mode. When that happens, scans are obtained every 5 minutes. The data quality is about the same for both scan modes, though the clear-air mode uses more pulses per radial and is a little less noisy. Generally, sufficient signal strength is present in the lower levels of the atmosphere in these cases for high-quality analyses from radars in precipitation or clear-air modes.

Because noisy contours are difficult to interpret, a nine point smoother was applied to much of the data. The smoother is applied multiple times replacing each value in the array by the average of itself and the eight surrounding points. The number of times the smoother is applied is indicated at the top of each figure, and is chosen subjectively so as to achieve a compromise between eliminating too much information and eliminating noise. As is inherent in this smoother, values near the borders of the data are smoothed less than those in the interior, consequently, the contours near the edges of some of the plots presented are still noisy.

To meet the criteria that the reflectivity PPI plots not have a bilateral symmetry, PPI plots are produced at various times for visual examination, especially near the middle of the night (6Z). Reflectivity PPI plots near 6Z are given for each case in Figs. 4.11-4.14, corresponding radial velocity plots are also given in Figs. 4.15-4.18. For these NEXRAD data, velocity range gates are every 250 meters and reflectivity range gates are every 1 km. For a 1.5° tilt, these gates result in a reflectivity measurement every 26 m in the vertical and a velocity measurement every 6.5 m. Fig. 4.13 does show some signs of azimuthal bisymmetry which may imply some alignment of the radar targets and increases the likelihood of birds being present. However, this is not a strong bilateral signature and it is restricted to a layer above 2 km. The LLJ measurements are probably not affected by this potential biasing problem above 2 km.

4.7.1 Reflectivity Time-Height Sections

The first Time-height cross-sections presented are for azimuthally averaged reflectivity. These plots are Figs. 4.19-4.22 for the May, June, July, and August cases respectively. Reflectivity is the least noisy field considered and the fields were not smoothed for these

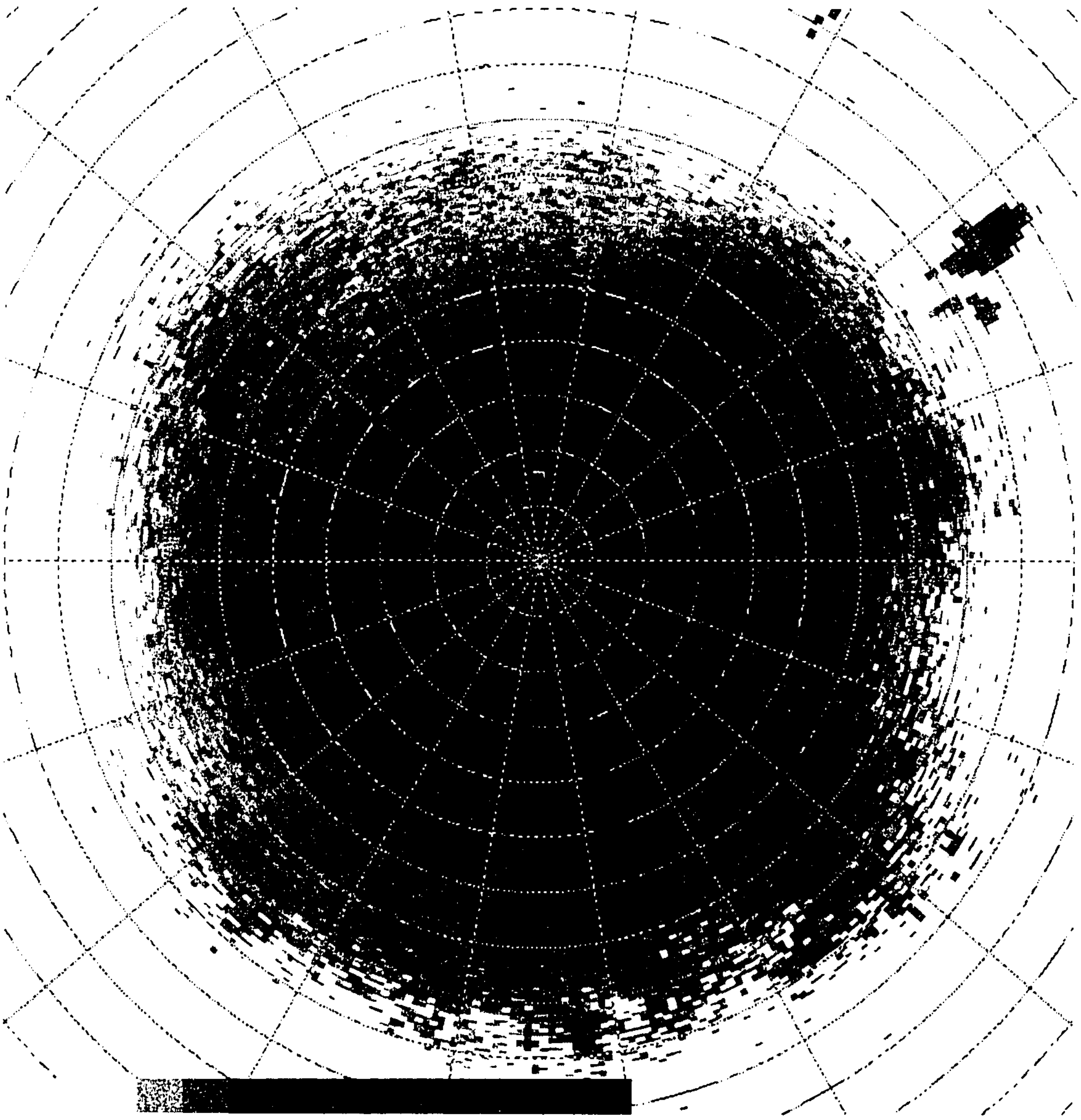

Figure 4.11: PPI of reflectivity near 6 Z on May 7, 2002 at 1.5° tilt from the KFWS NEXRAD radar. Range rings are plotted every 400 meters above the ground. For gray-scale range, minimum displayed reflectivity (white) is -10 dBZ and maximum (black) is 30 dBZ.

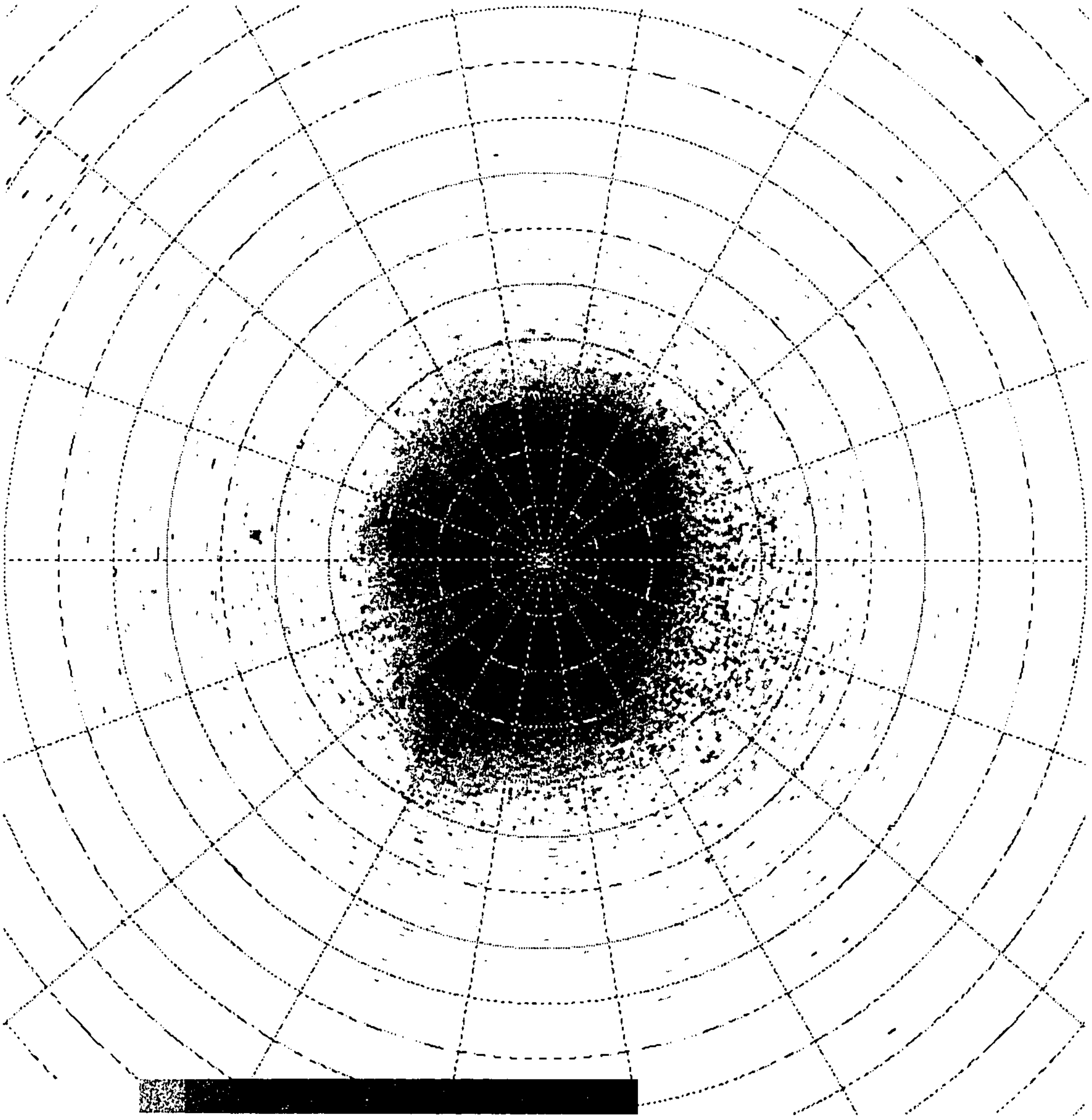

Figure 4.12: PPI of reflectivity near 6 Z on June 2, 2002 at 1.5° tilt from the KVNX NEXRAD radar. Range rings are plotted every 400 meters above the ground. For gray-scale range, minimum displayed reflectivity (white) is -10 dBZ and maximum (black) is 30 dBZ.

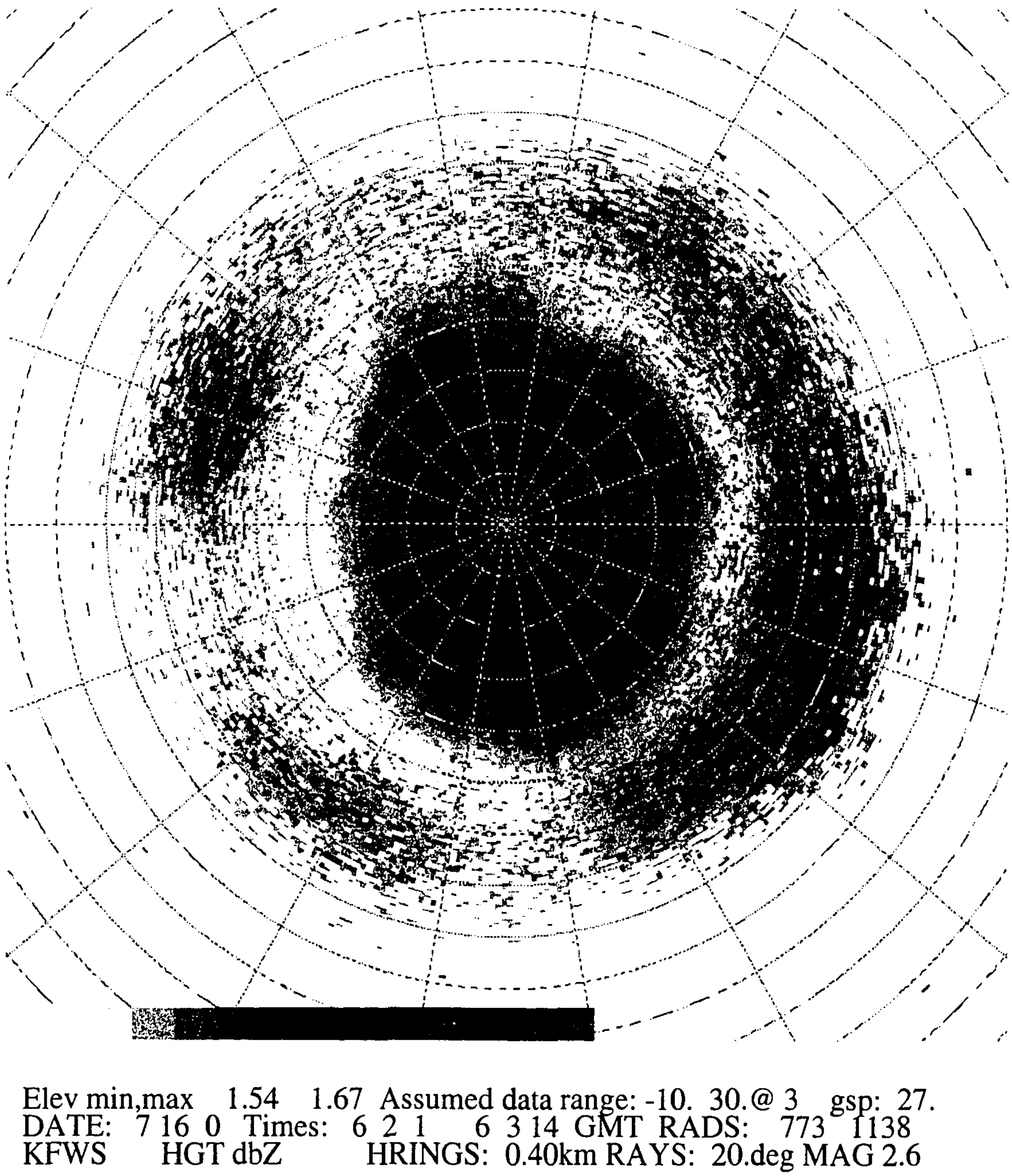

Figure 4.13: PPI of reflectivity near 6 Z on July 16, 2000 at 1.5° tilt from the KFWS NEXRAD radar. Range rings are plotted every 400 meters above the ground. For gray-scale range, minimum displayed reflectivity (white) is -10 dBZ and maximum (black) is 30 dBZ.

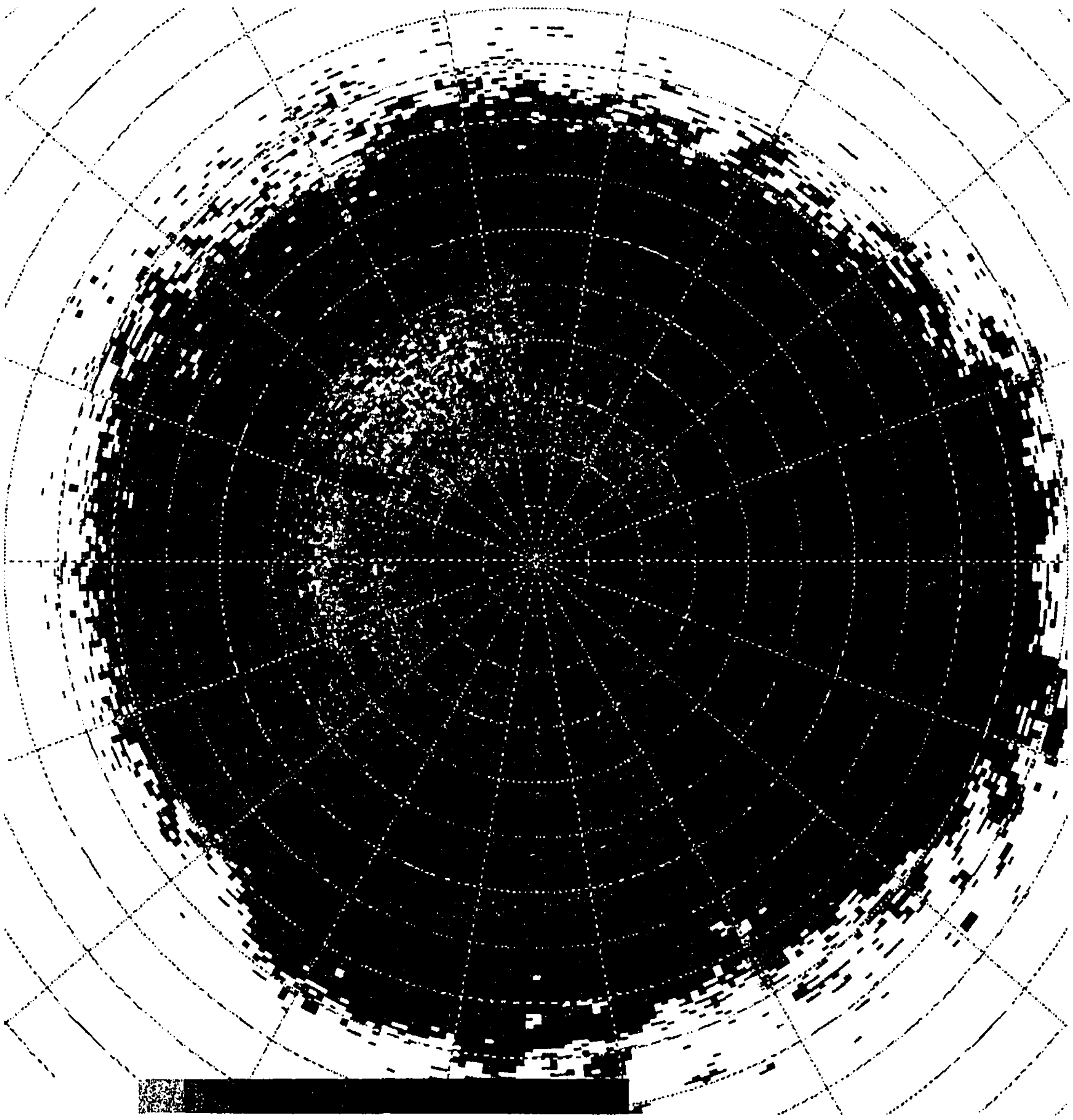

Elev min,max 1.41 1.49 Assumed data range: -10. 30.@ 3 gsp: 26.
DATE: 8 15 2 Times: 6 9 51 6 11 4 GMT RADS: 738 1103
KTLX HGT dbZ HRINGS: 0.40km RAYS: 20.deg MAG 2.3

Figure 4.14: PPI of reflectivity near 6 Z on August 15, 2002 at 1.5° tilt from the KTLX NEXRAD radar. Range rings are plotted every 400 meters above the ground. For gray-scale range, minimum displayed reflectivity (white) is -10 dBZ and maximum (black) is 30 dBZ.

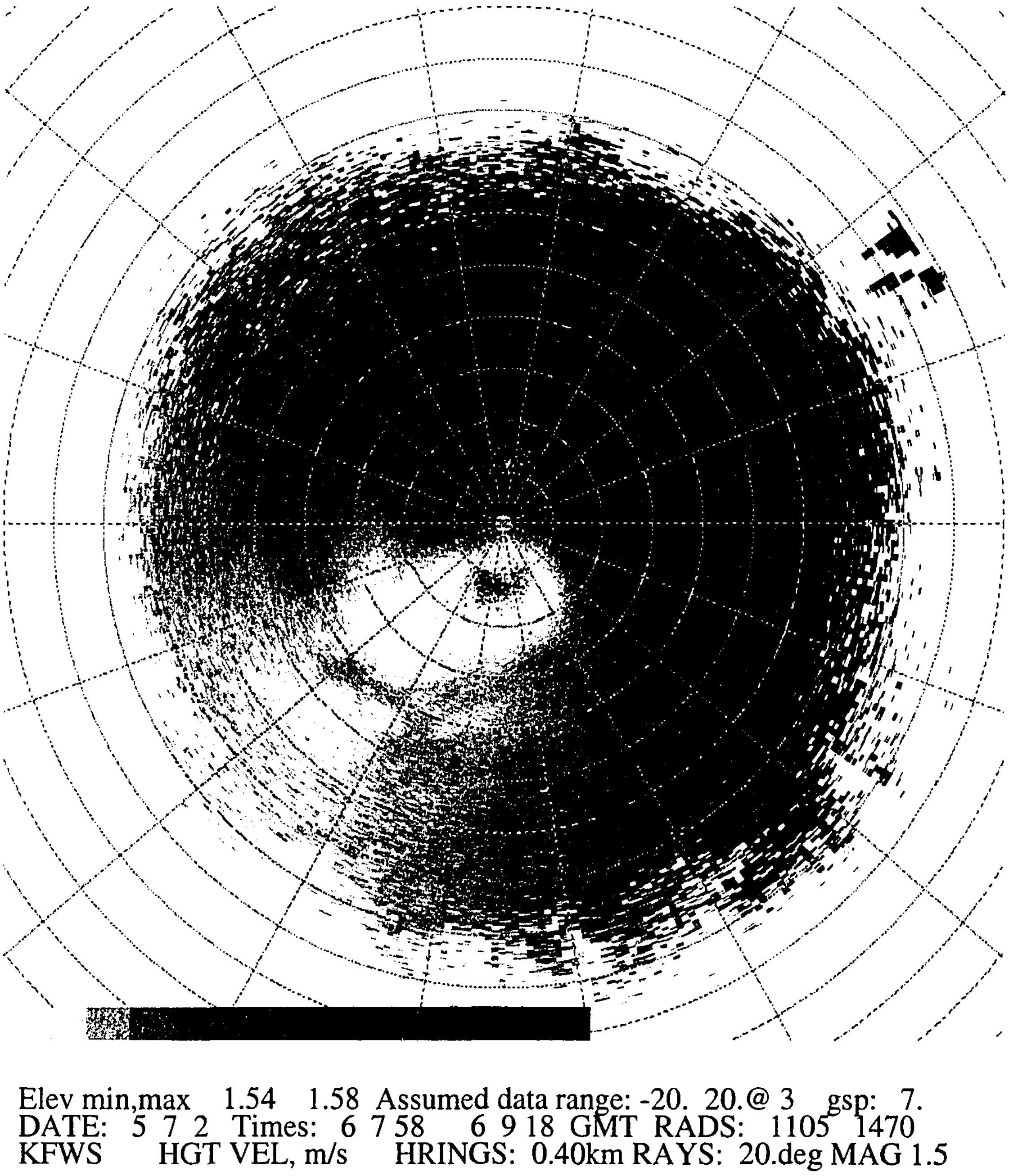

Figure 4.15: PPI of radial velocity near 6 Z on May 7, 2002 at 1.5° tilt from the KFWS NEXRAD radar. Range rings are plotted every 400 meters above the ground. For gray-scale range, minimum displayed velocity (very light gray) is -20 m/s and maximum (black) is 20 m/s.

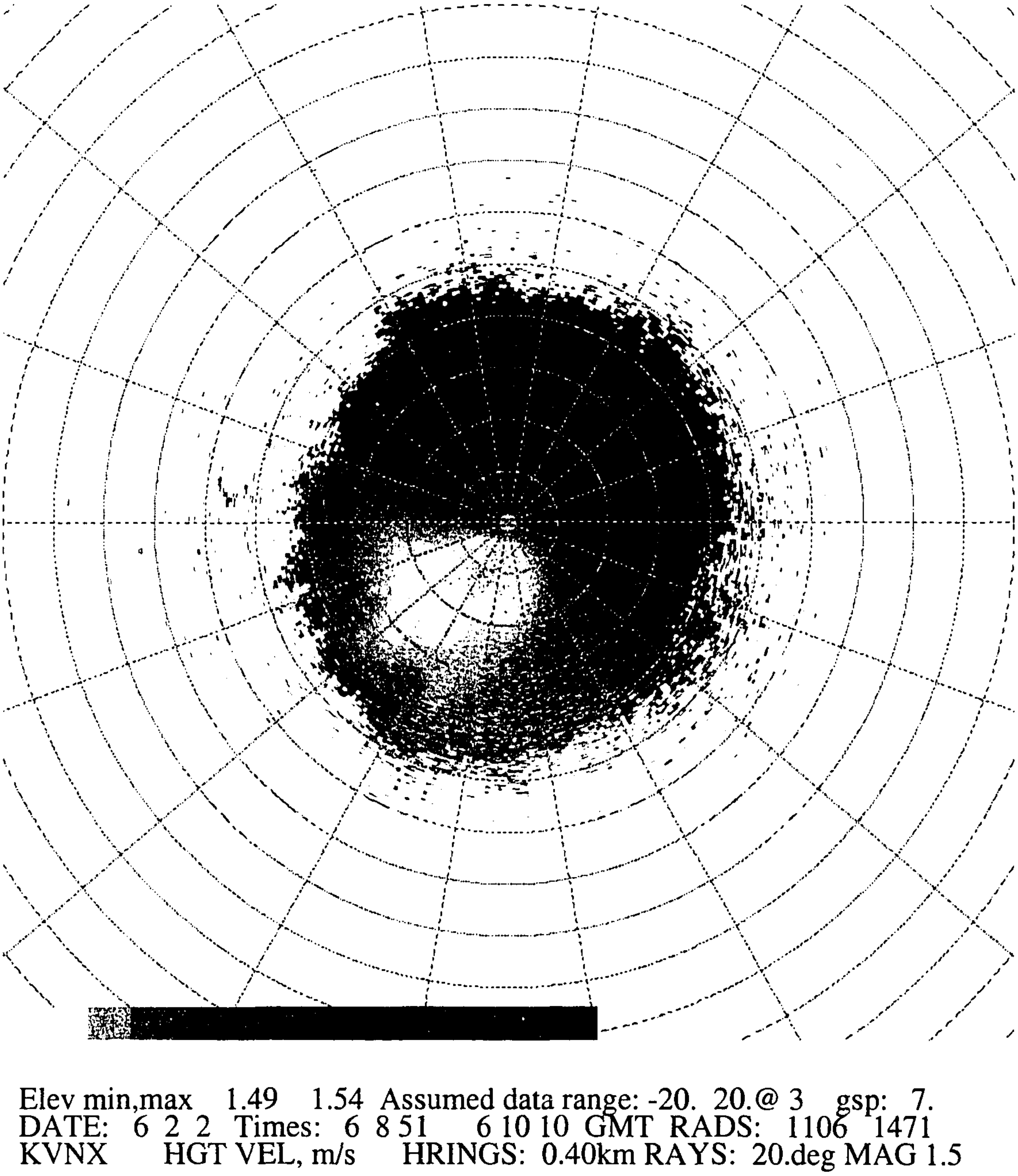

Figure 4.16: PPI of radial velocity near 6 Z on June 2, 2002 at 1.5° tilt from the KVNX NEXRAD radar. Range rings are plotted every 400 meters above the ground. For gray-scale range, minimum displayed velocity (very light gray) is -20 m/s and maximum (black) is 20 m/s.

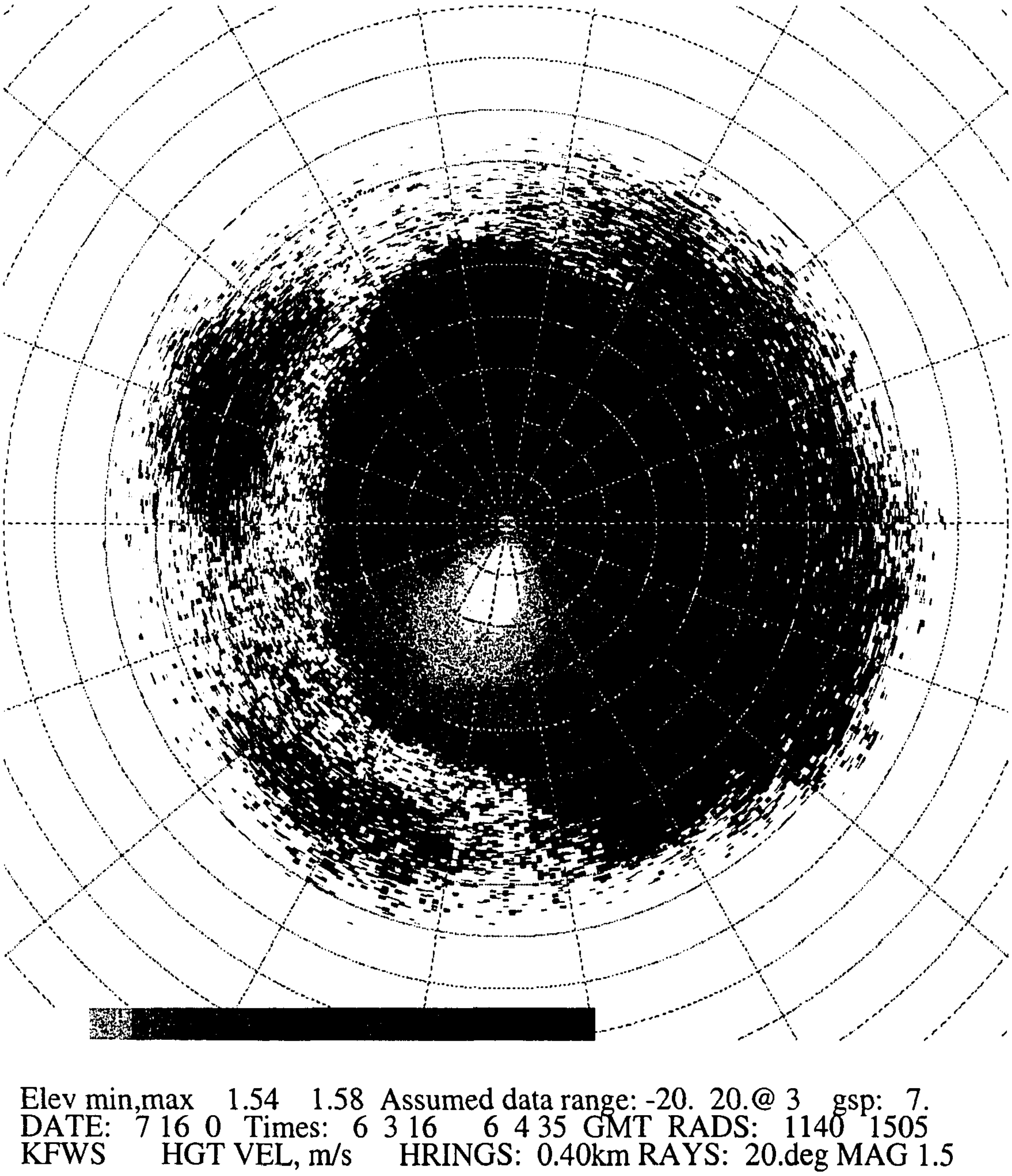

Figure 4.17: PPI of radial velocity near 6 Z on July 16, 2000 at 1.5° tilt from the KFWS NEXRAD radar. Range rings are plotted every 400 meters above the ground. For gray-scale range, minimum displayed velocity (very light gray) is -20 m/s and maximum (black) is 20 m/s.

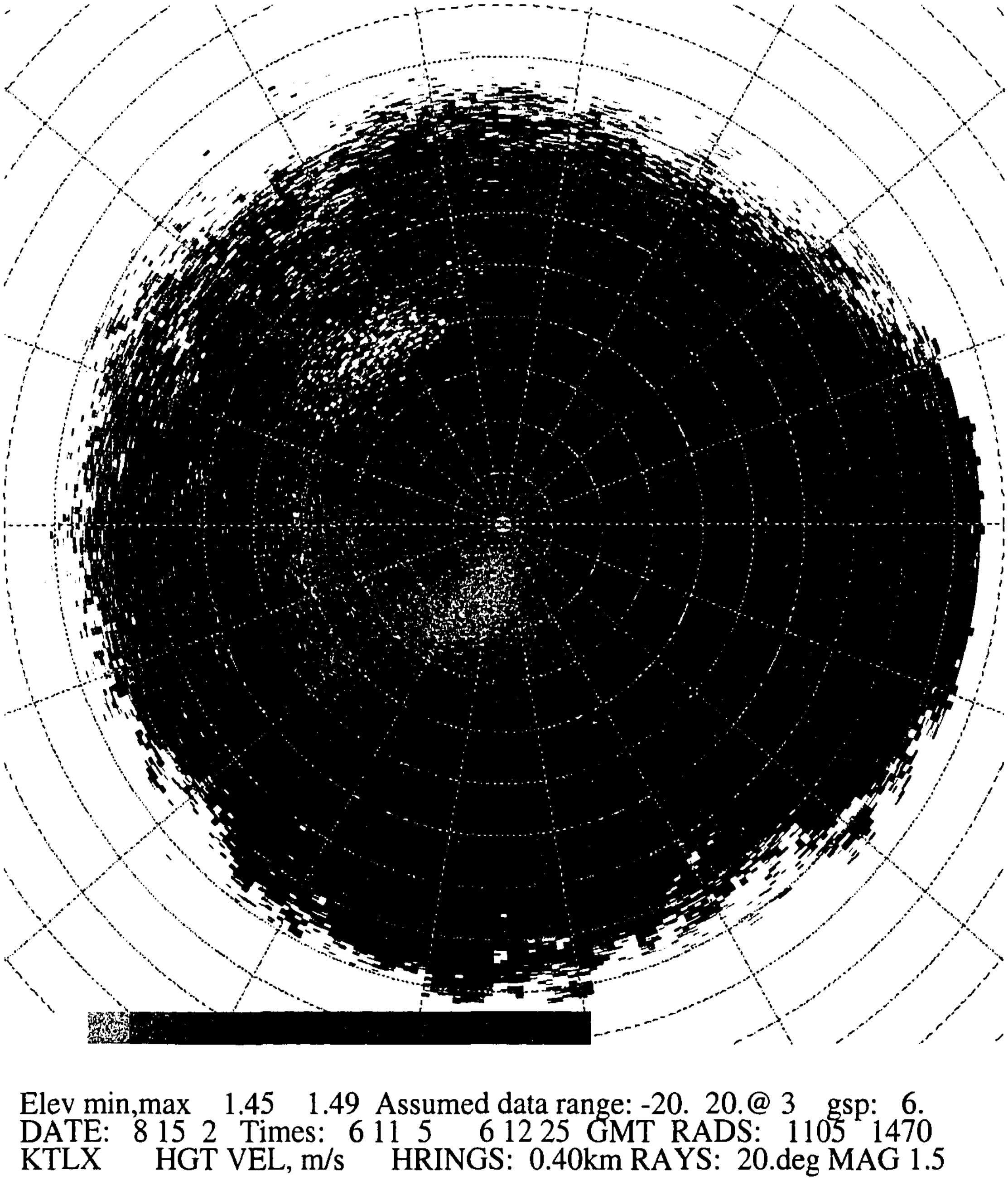

Figure 4.18: PPI of radial velocity near 6 Z on August 15, 2002 at 1.5° tilt from the KTLX NEXRAD radar. Range rings are plotted every 400 meters above the ground. For gray-scale range, minimum displayed velocity (very light gray) is -20 m/s and maximum (black) is 20 m/s.

plots. The Time scale is hours from the beginning of the scanning period, at about 16 UTC. Sunrise is at about 9 hours from the start and sunset is about 19 hours from the start. Vertical lines are drawn at the sunrise and sunset times. Precise values for sunset and sunrise times accurate to one minute (obtained from the NOAA Air Resources Lab calculator) in UTC and hours from the start are given in the following table:

DATE/STATION	LAT./LON.	START UTC	SUNSET UTC/hrs	SUNRISE UTC/hrs
020506/KFWS	32 34N / 97 18W	16:04	1:14/9.17	11:37/19.55
020601/KVNX	36 44N / 98 08W	16:05	1:46/9.68	11:15/19.17
000715/KFWS	32 34N / 97 18W	16:04	1:38/9.57	11:33/19.48
020814/KTLX	35 20N / 97 17W	16:26	1:19/8.88	11:49/19.38

Sunrise and sunset are also indicated directly in the data in some of the plots by short-duration spikes in reflectivity near the top of the domain near 9 and 19 hours from the start, particularly apparent in Fig. 4.19. These are caused by the radar dish being pointed directly at the sun during a scan when the sun elevation above the horizon equals the antenna's tilt, 1.5°. The sun is not a strong source of reflectivity, but it can add significantly to the reflectivity when the reflectivity is otherwise weak, as it often is far above the ground. For NEXRAD data, sun measurements rarely affect velocity measurements as such data are interpreted by the NEXRAD quality control as second-trip echo, and are filtered out of the velocity fields.

All four cases show a rapid change in reflectivity at sunrise and sunset, with a short-duration minimum occurring at sunset and sunrise. The reflectivity transitions from usually relatively weak daytime values, through a short-duration minimum at sunset, to a rapid increase after sunset. Within an hour and a half of sunset, the reflectivity profile, up to heights of 4 km, has reached its strongest level. This level decreases gradually through the night in Figs. 4.20 and 4.22 and remains fairly constant in Figs. 4.19 and 4.21. At sunrise there is another rapid transition through a minimum at sunrise to typically weaker daytime values, though the change is not as rapid as at sunset. This phenomenon is not

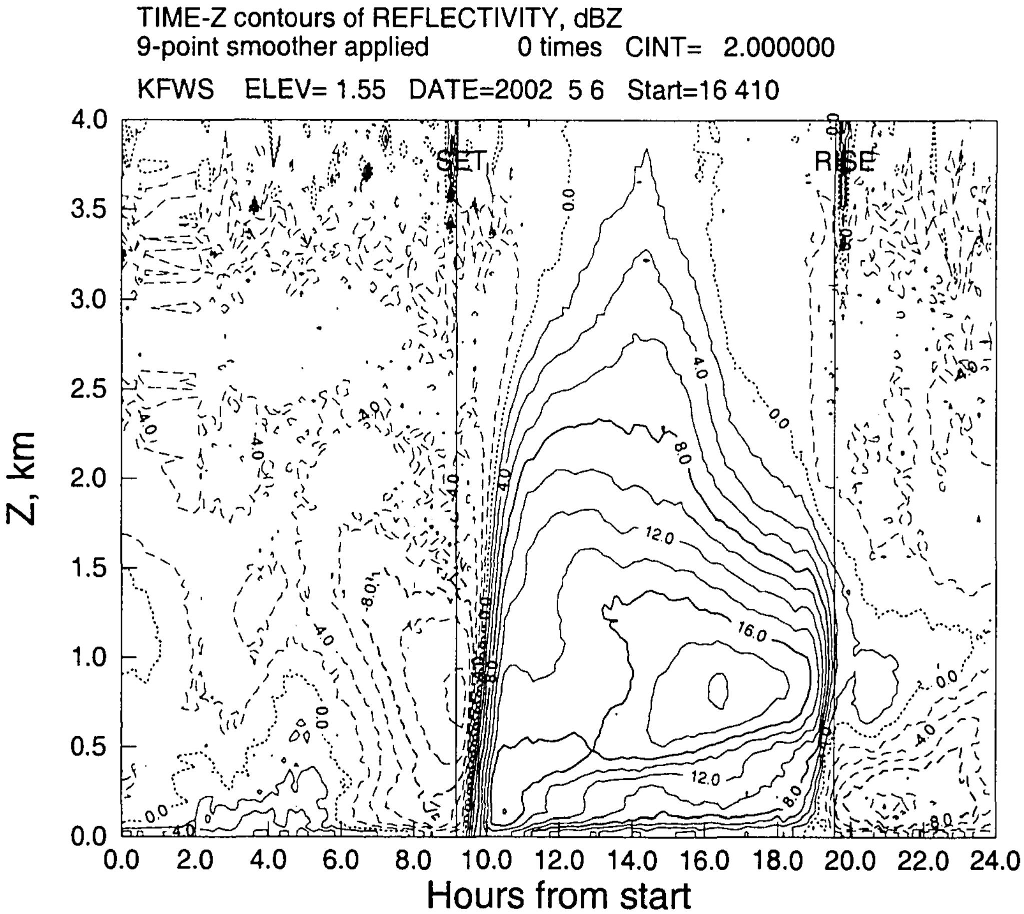

Figure 4.19: Time-height contour plot of reflectivity through a depth of 4 km and for 24 hours from KFWS radar, May 6-7, 2002. 1.5° tilt. Data begins at 16:04Z May 6. Sunrise and sunset times are marked.

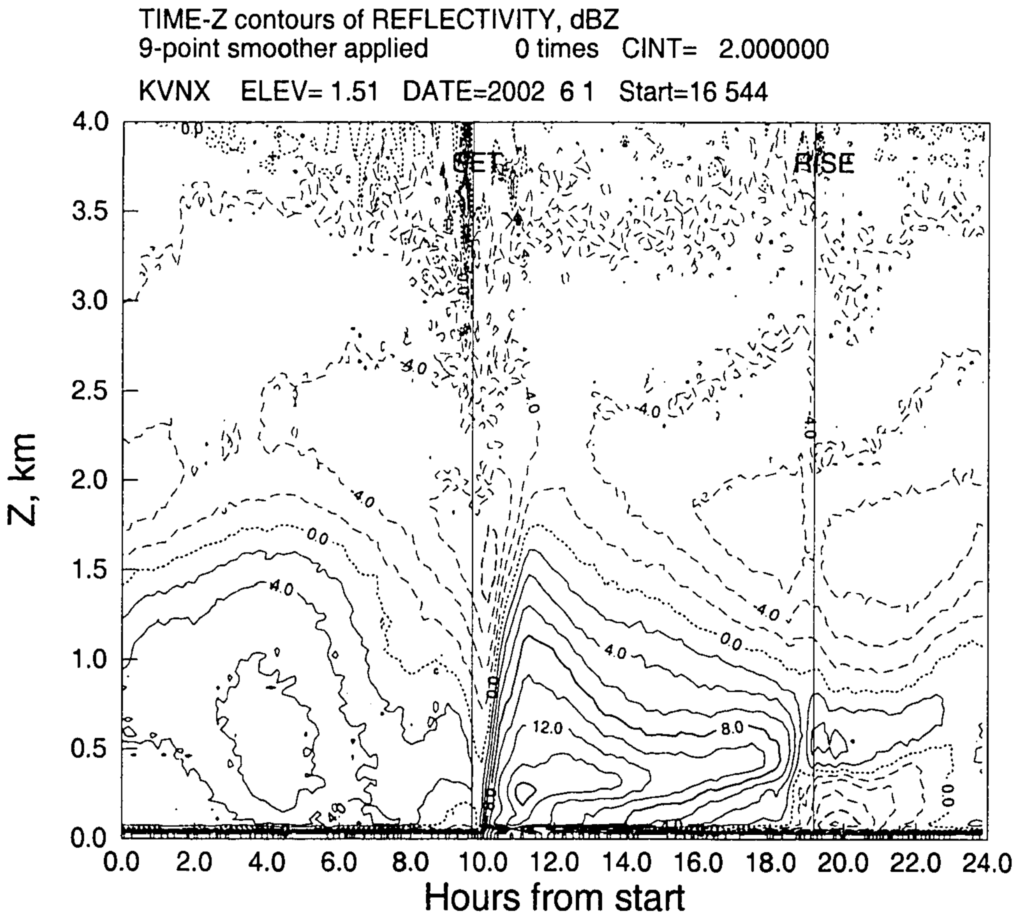

Figure 4.20: Time-height contour plot of reflectivity through a depth of 4 km and for 24 hours from KVNX radar, June 1-2, 2002. 1.5° tilt. Data begins at 16:05Z June 1.

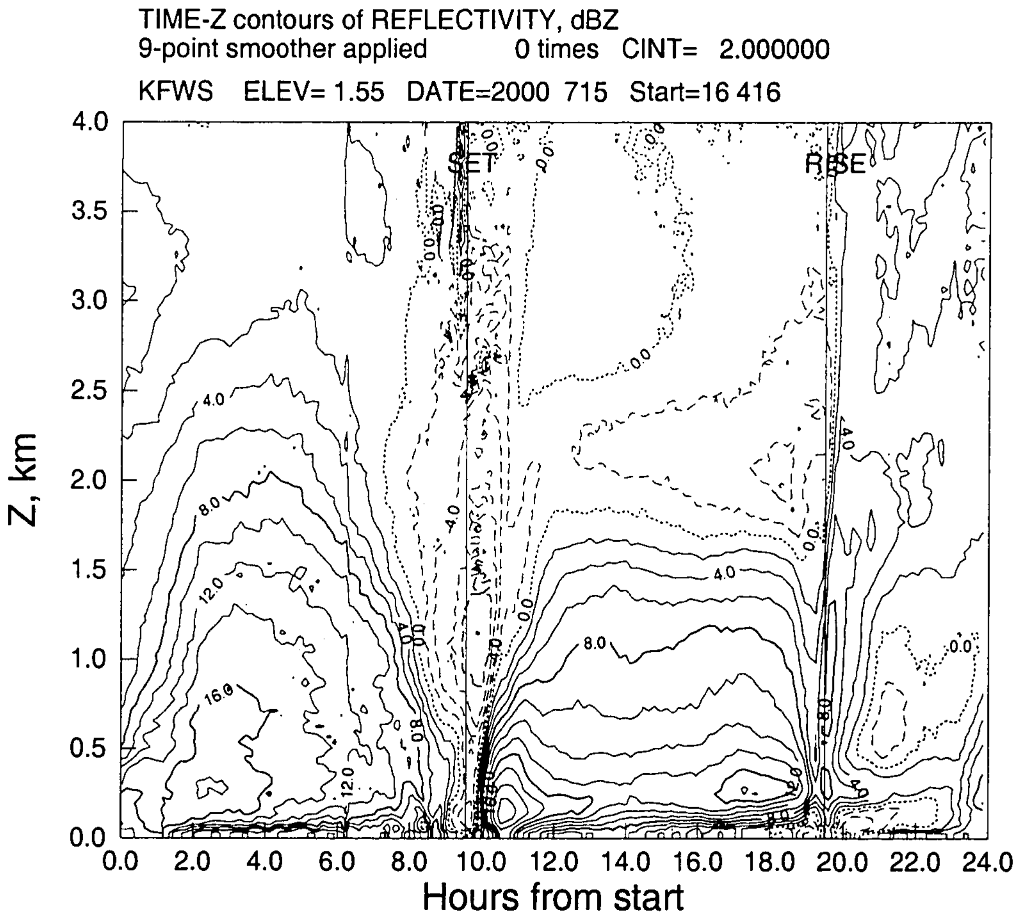

Figure 4.21: Time-height contour plot of reflectivity through a depth of 4 km and for 24 hours from KFWS radar, July 15-16, 2000. 1.5° tilt. Data begins at 16:04Z July 15.

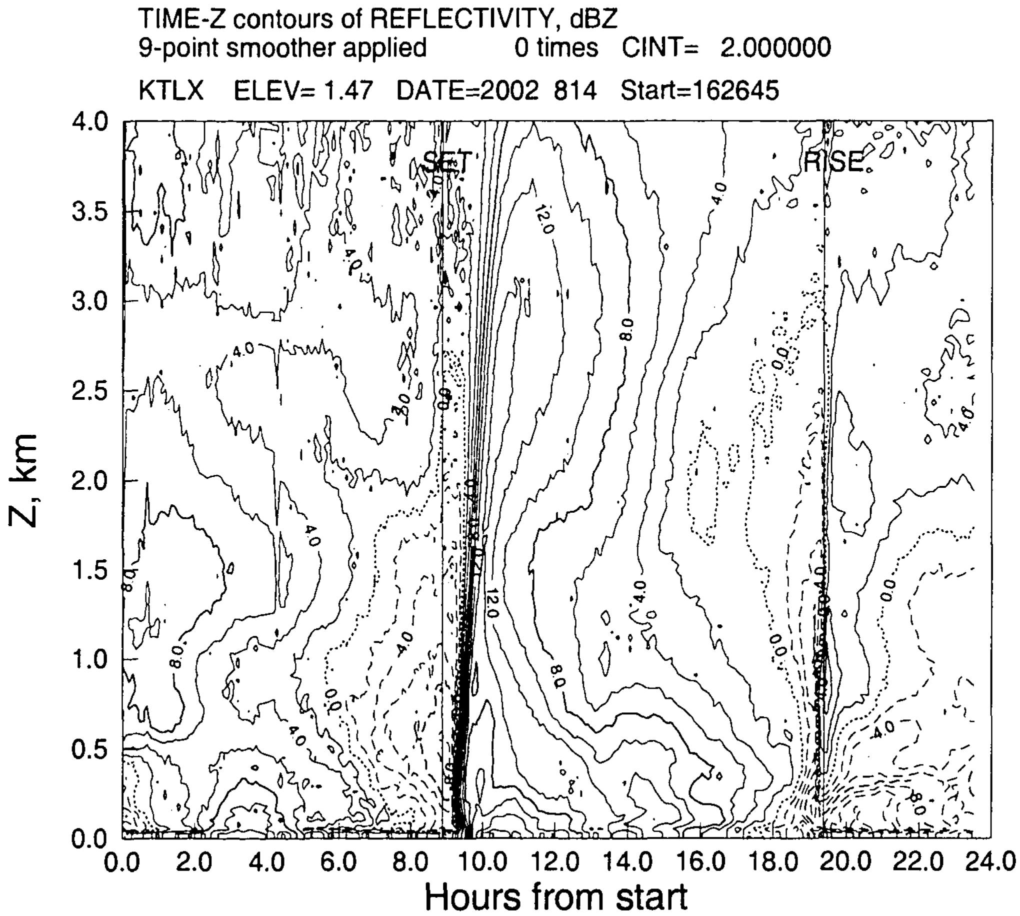

Figure 4.22: Time-height contour plot of reflectivity through a depth of 4 km and for 24 hours from KTLX radar, August 14-15, 2002. 1.5° tilt. Data begins at 16:26Z August 14.

completely understood and was discussed somewhat in Sec. 3.4.1. A possible reason for this phenomenon is that the daytime and nighttime reflectivities are caused by different mechanisms which must switch over at sunrise and sunset, providing a brief period when neither mechanism operates. For example, the daytime reflectivity may be caused by insects carried aloft by vertical mixing. At sunset, vertical motions cease and the insects return to low levels, causing a rapid reduction in reflectivity. At night, there could be a different species of insects, as suggested by Hardy and Glover (1966), which flies at night. A similar theory could be formed for bird species, of course.

4.7.2 Wind Time-Height Sections

Time-height cross-sections of wind speed are given in Figs. 4.23-4.26 for the May, June, July, and August cases, respectively. Each case shows a well-defined LLJ with the peak wind speeds occurring below 1.5 km at about 18 hours after the 16Z start, just before sunrise. The LLJ begins in each case with an increase in wind speed at low levels just after sunset. Wind speed in the jet continues to increase through the night. Winds in the LLJ layer begin to decrease after sunrise.

The peak wind speeds are about 30 m/s for the May case, about 25 m/s for the June case, about 20 m/s for the July case, and about 15 m/s for the August case. The decline in strength of LLJ with month corresponds with the trend towards weaker synoptic systems with weaker synoptic pressure gradients as the warm season progresses. The strongest systems occur in early Spring, and the weakest in mid-Summer. The May and June cases also show an increase in height of the LLJ speed peak as the night progresses. This is quite probably due to the deepening of the nocturnal boundary-layer as the night progresses, though it is interesting that this phenomenon does not occur in the July and August cases. This may be due to the weaker shear leading to less turbulent entrainment from the shear layer for these cases.

An interesting feature of the velocity plots is an increase in wind speed at and above the LLJ near sunrise. This feature is most apparent in the May case, Fig. 4.23. This is feature is not caused by the radar receiving radiation from the sun when the sun shines directly

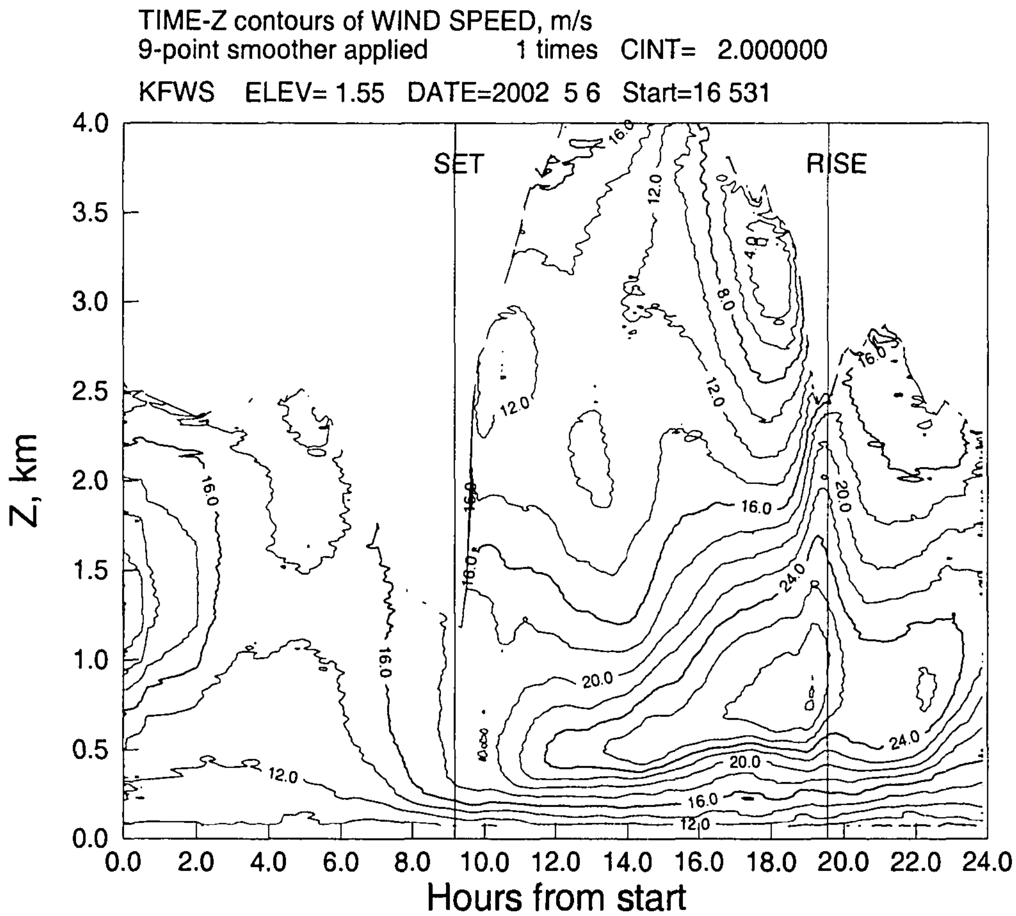

Figure 4.23: Time-height contour plot of wind speed through a depth of 4 km and for 24 hours from KFWS radar, May 6-7, 2002. 1.5° tilt. Data begins at 16:04Z May 6.

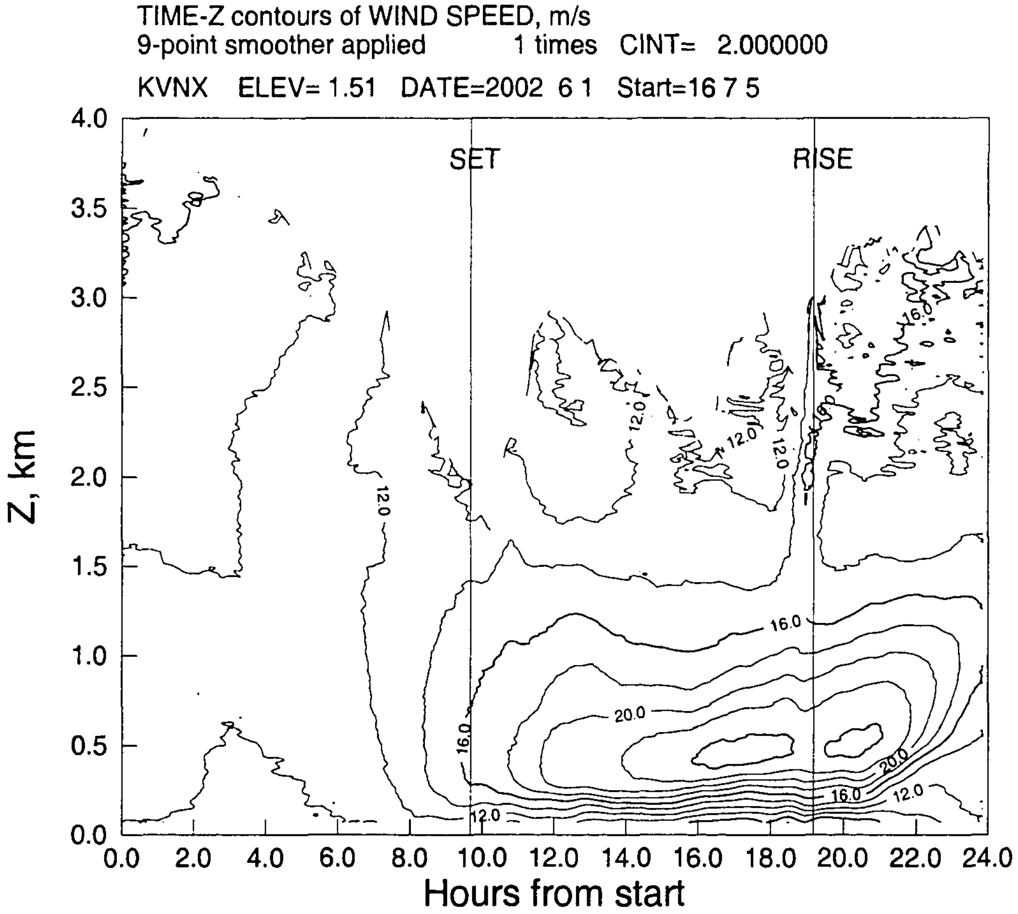

Figure 4.24: Time-height contour plot of wind speed through a depth of 4 km and for 24 hours from KVNX radar, June 1-2, 2002. 1.5° tilt. Data begins at 16:05Z June 1.

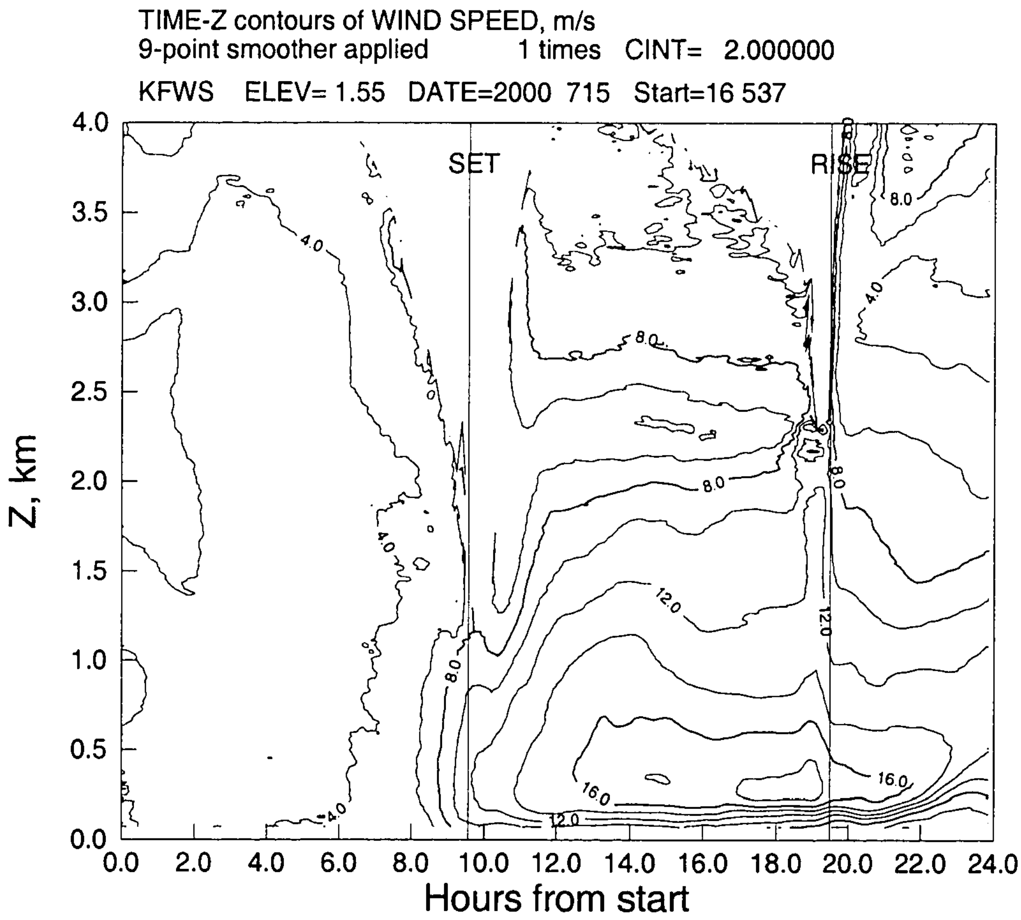

Figure 4.25: Time-height contour plot of wind speed through a depth of 4 km and for 24 hours from KTLX radar, July 15-16, 2000. 1.5° tilt. Data begins at 16:05Z July 15.

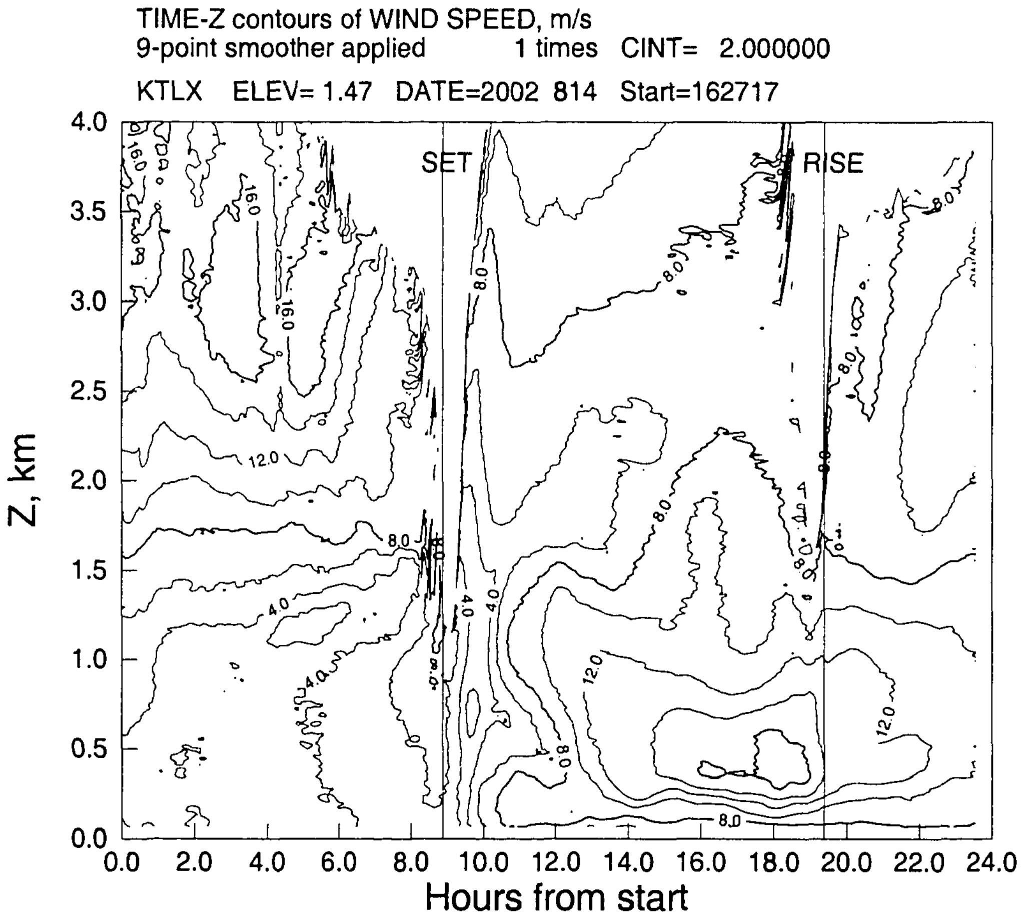

Figure 4.26: Time-height contour plot of wind speed through a depth of 4 km and for 24 hours from KTLX radar, August 14-15, 2002. 1.5° tilt. Data begins at 16:26Z August 14.

into the antenna. Such data are filtered-out as the NEXRAD quality-control algorithm treats them as second-trip echo. Also, time-height contours with the volume scans showing the reflectivity signature of the sun not included, did not show any significant difference. It is not clear what causes this abrupt feature. It is possibly an artifact of unknown origin (such as a greater preponderance of birds near sunset). It appears to be real, however, and could be due to vertical mixing.

Another time history view is obtained by calculating the average wind components in the lower 1 km as a function of time. Figs. 4.27-4.30 plot these average wind components for the 4 cases. These can be compared with the idealized 1-D modeling results from Sec. 2.4 (Figs. 2.11-2.14). The measured time behavior of the LLJ is close to the quasi-sinusoidal behavior seen in the 1-D modeling results. The geostrophic wind (and, hence, the synoptic pressure gradient) could be estimated from these figures as the winds at the time average values for u and v.

Valuable comparable results were obtained by Crawford et al. (1973) who used WKY tall tower measurements to measure wind in the lowest 500 m. They produced annual average wind profiles and time-height sections and saw similar behavior; they particularly noted the rapid change in the wind profiles at sunrise and sunset.

4.7.3 Wind Shear Time-Height Sections

Wind shear is calculated from the u and v component time-height fields. Since calculating wind shear involves differentiation, it tends to be a very noisy calculation. Consequently, the u and v fields are first smoothed using the 9-point smoother 10 times in succession. The u and v component wind shears ($\frac{du}{dz}, \frac{dv}{dz}$) are then calculated by centered differences. The amplitude of the shear vector is then calculated and the results contoured. Figs. 4.31-4.34 present the calculated wind shear amplitudes for the May, June, July, and August cases, respectively. Because this is the amplitude of the wind shear vector, the values are sometimes different than what might be inferred from the wind speed plots in Figs. 4.23-4.26 as the total shear includes the effects of directional shear as well as speed shear.

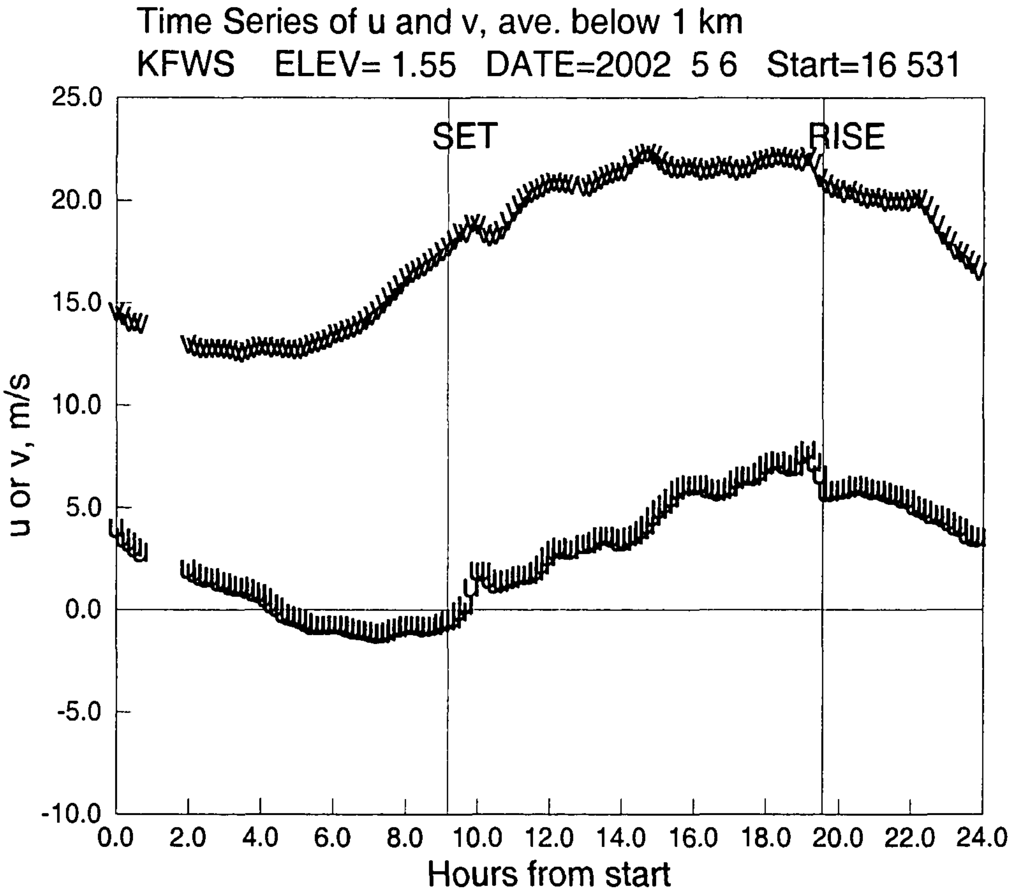

Figure 4.27: Time series of u and v wind components averaged through a depth of 1 km from KFWS radar, May 6-7, 2002. 1.5° tilt. Data begins at 16:04Z May 6.

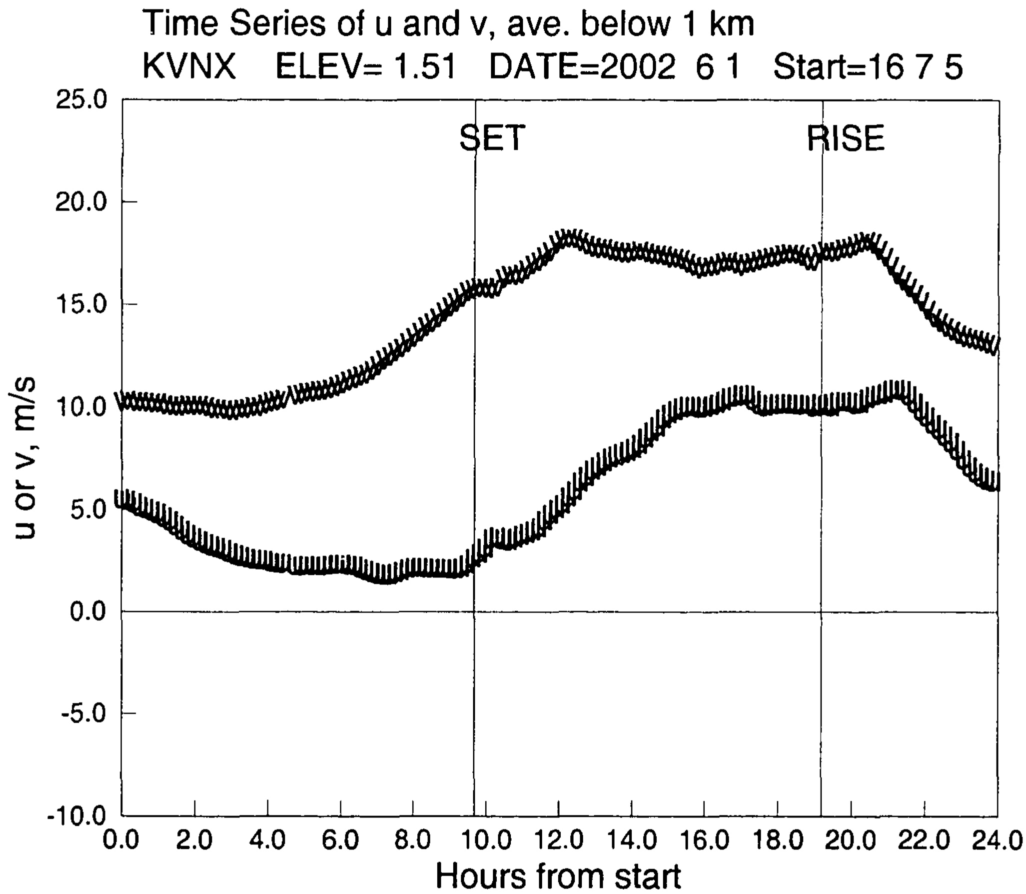

Figure 4.28: Time series of u and v wind components averaged through a depth of 1 km from KVNX radar, June 1-2, 2002. 1.5° tilt. Data begins at 16:07Z June 1.

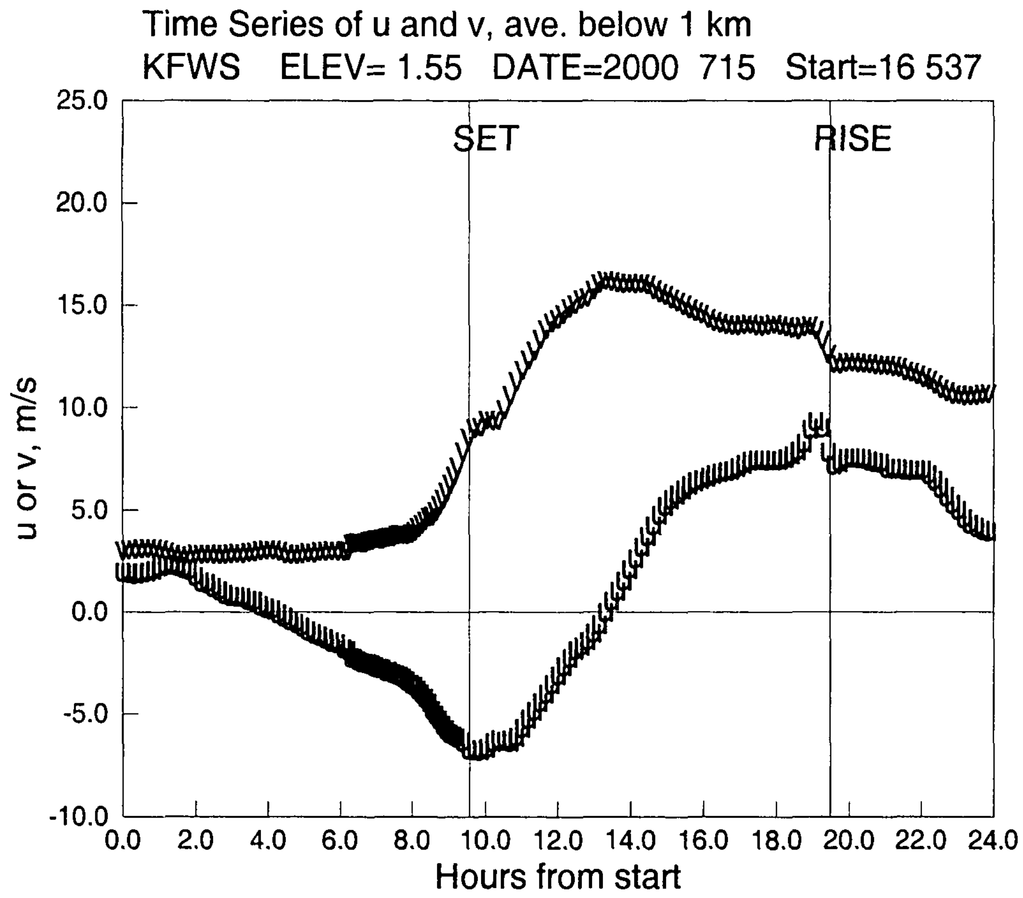

Figure 4.29: Time series of u and v wind components averaged through a depth of 1 km from KFWS radar, July 15-16, 2009. 1.5° tilt. Data begins at 16:05Z May 6.

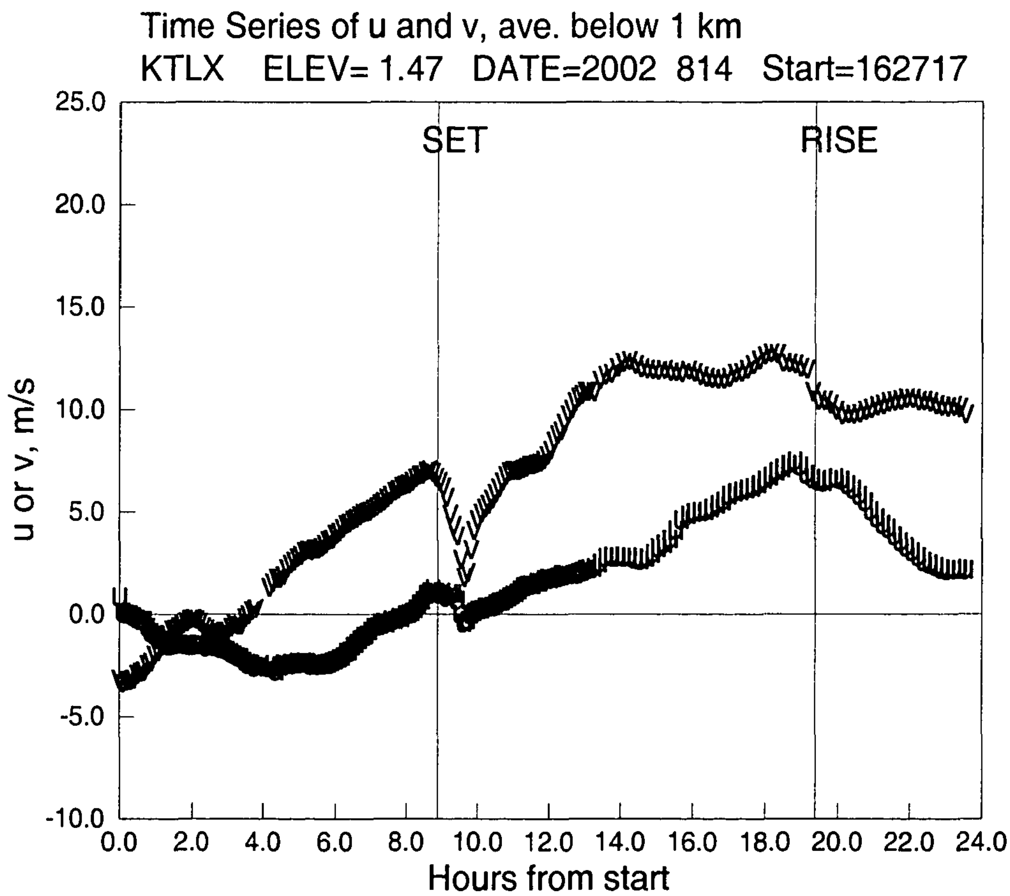

Figure 4.30: Time series of u and v wind components averaged through a depth of 1 km from KFWS radar, August 14-15, 2002. 1.5° tilt. Data begins at 16:27Z August 14.

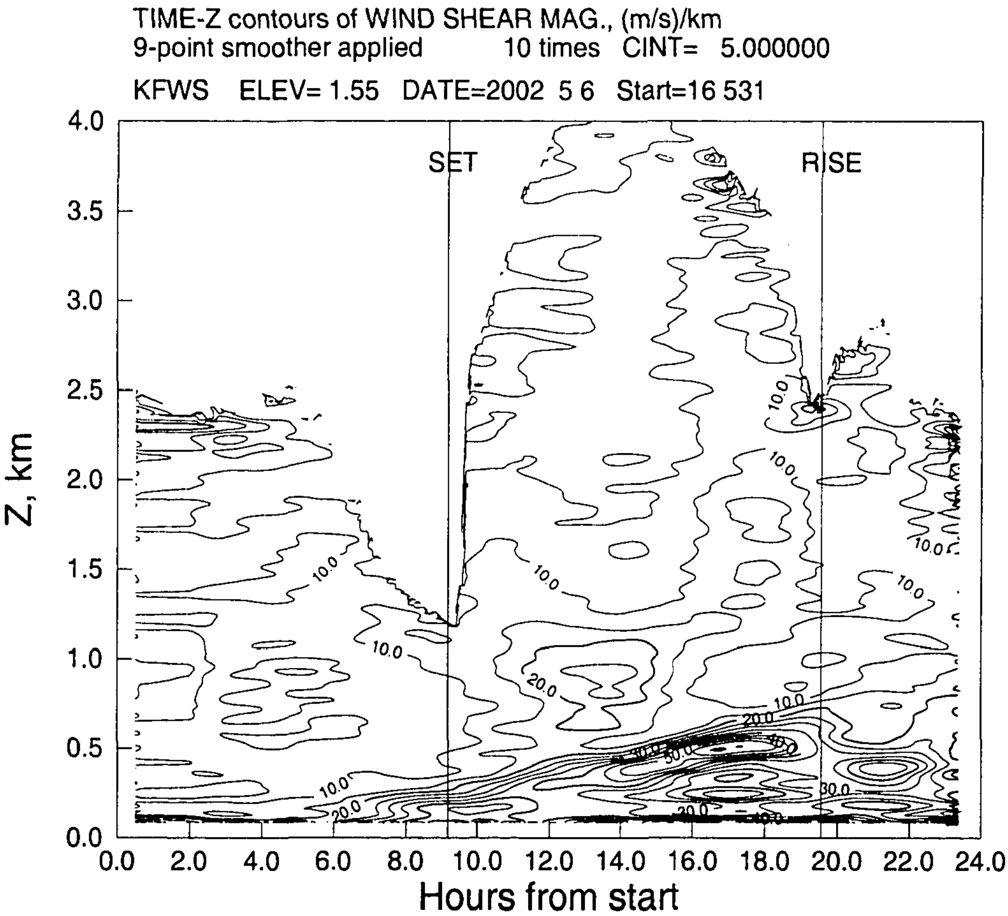

Figure 4.31: Time-height contour plot of wind shear magnitude through a depth of 4 km and for 24 hours from KFWS radar, May 6-7, 2002. 1.5° tilt. Data begins at 16:04Z May 6.

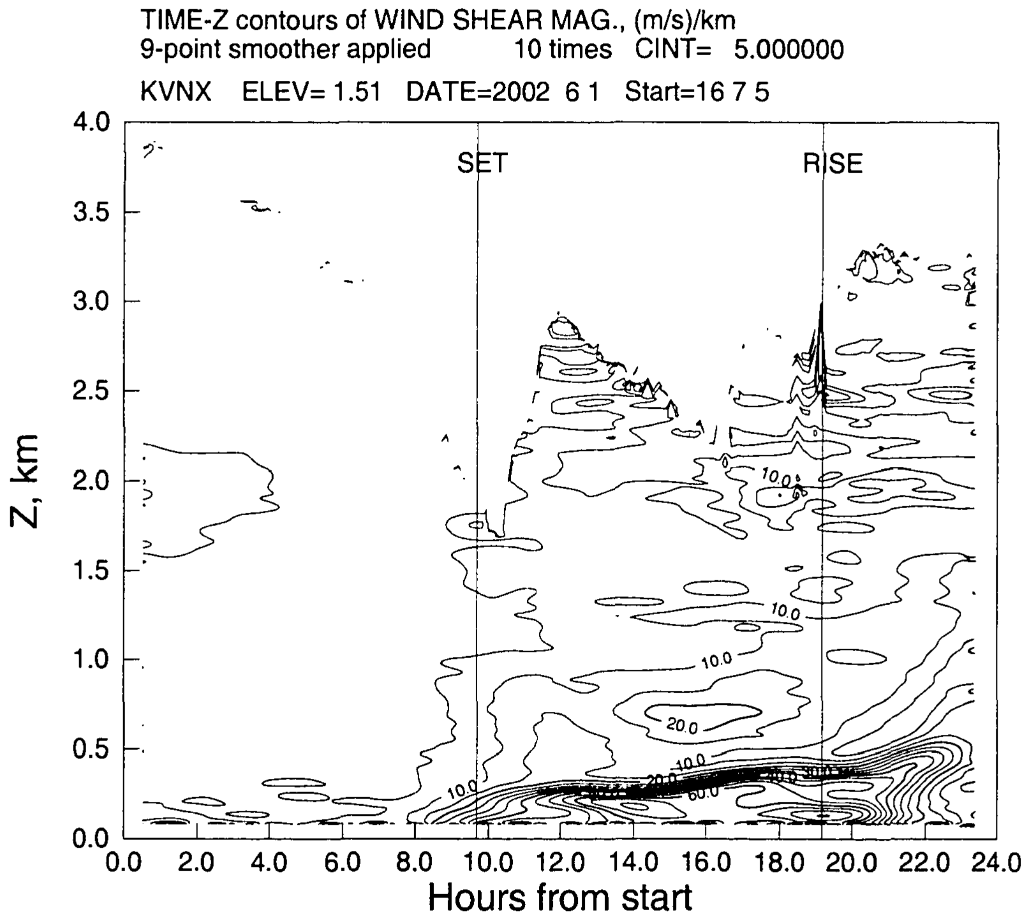

Figure 4.32: Time-height contour plot of wind shear magnitude through a depth of 4 km and for 24 hours from KVNX radar, June 1-2, 2002. 1.5° tilt. Data begins at 16:05Z June 1.

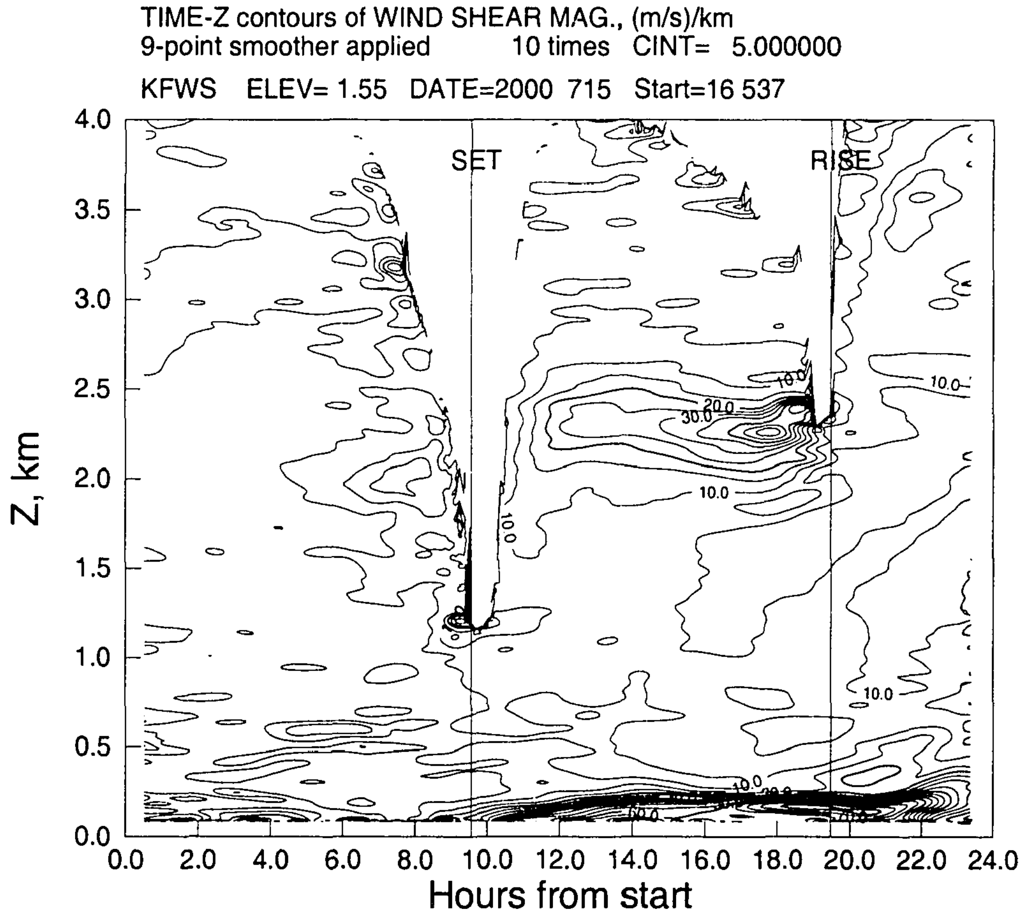

Figure 4.33: Time-height contour plot of wind shear magnitude through a depth of 4 km and for 24 hours from KTLX radar, July 15-16, 2000. 1.5° tilt. Data begins at 16:05Z July 15.

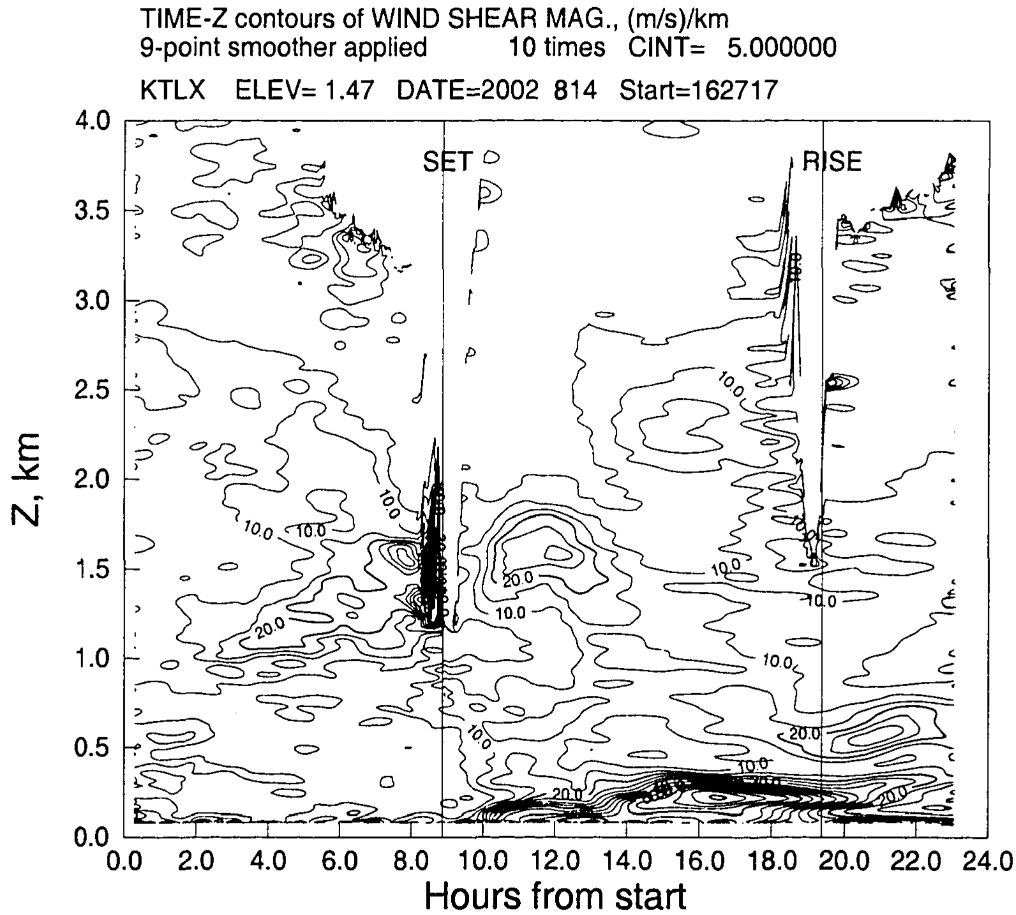

Figure 4.34: Time-height contour plot of wind shear magnitude through a depth of 4 km and for 24 hours from KTLX radar, August 14-15, 2002. 1.5° tilt. Data begins at 16:26Z August 14.

These shear plots show that most of the shear is confined to a lower shear layer below about 500 m. The layer above the core of the jet (the layer of maximum wind speed) shows relatively modest shear. Also, the core of the jet itself, while it does correspond with regions of relatively weak shear, does not correspond to a pronounced minimum in wind shear. The layer below the core, however, does show shear that is much stronger than at any other time or place. This shear layer develops almost immediately after sunset, but remains for 4 to 5 hours after sunrise. Similar to the increase in height of the LLJ core noted in Figs. 4.23 and 4.24, the depth of the shear layer increases throughout the night for the May and June cases of Figs. 4.31 and 4.32.

4.7.4 Turbulence Time-Height Sections

The variance (RMS error) in the VAD winds is related to the TKE by (4.11). Time-height sections of TKE calculated as $\frac{3}{2}$(VAD RMS error) for the four cases are presented in Figs. 4.35-4.38 for the May, June, July, and August cases, respectively. The variance field is somewhat noisy and it was smoothed by applying the 9-point smoother 5 times in succession for these plots.

The May and June cases actually show an increase in turbulence (as measured by TKE) in the region of the LLJ in the shear layer and in the core at night over the daytime values whereas the July and August cases show the more anticipated behavior of a decrease in TKE at night co-located with the LLJ. The increase in TKE at night for any case was not expected since it was anticipated that turbulence would almost always decrease at night as the boundary layer stabilized. Despite the May and June measurements, turbulence is almost certainly higher during the day due to strong vertical mixing. However, if these measurements are correct, then horizontal velocity perturbations measured by radar are larger at night in some cases. A possible reason for this difference between the measurements and expected behavior is that the turbulence may not have been isotropic. The VAD is only sensitive to perturbations in the u and v velocity components. If w' was larger than u' and v' then the variance in the VAD would underestimate the TKE. This might well be the case during the day, as the turbulence is largely the result of strong vertical mixing

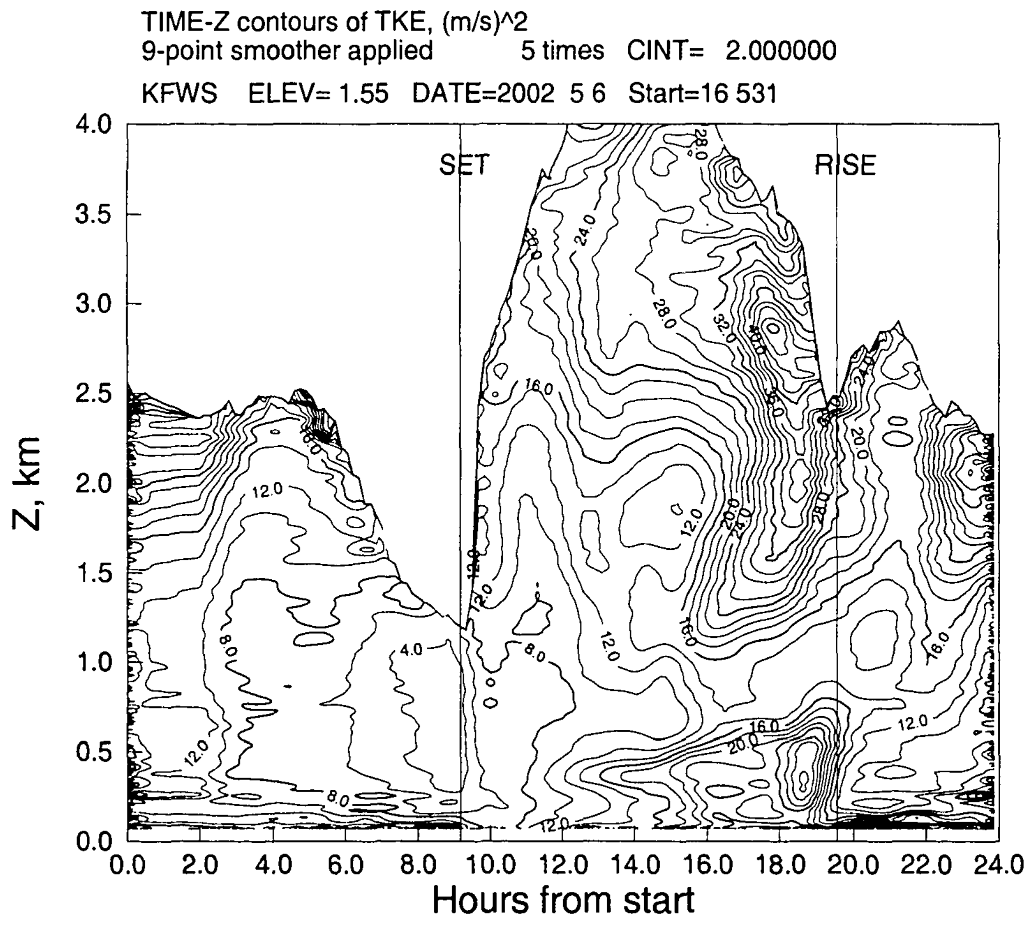

Figure 4.35: Time-height contour plot of TKE through a depth of 4 km and for 24 hours from KFWS radar, May 6-7, 2002. 1.5° tilt. Data begins at 16:04Z May 6.

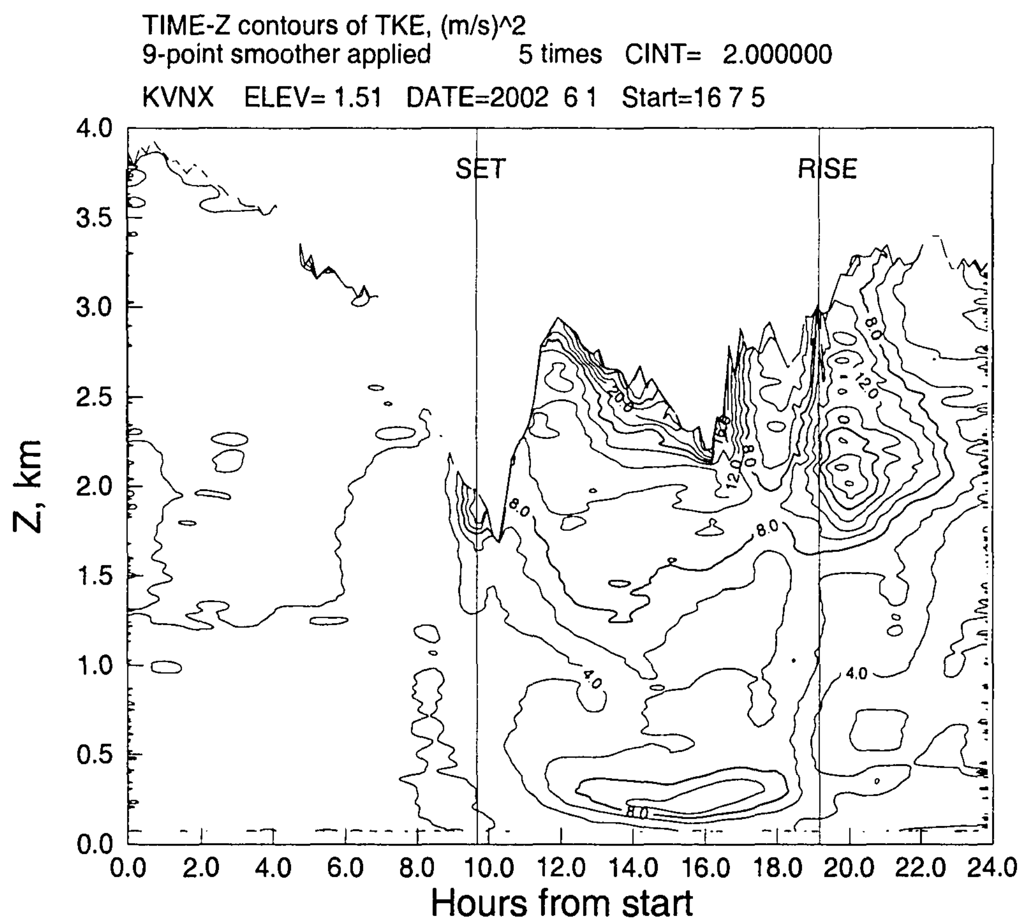

Figure 4.36: Time-height contour plot of TKE through a depth of 4 km and for 24 hours from KVNX radar, June 1-2, 2002. 1.5° tilt. Data begins at 16:05Z June 1.

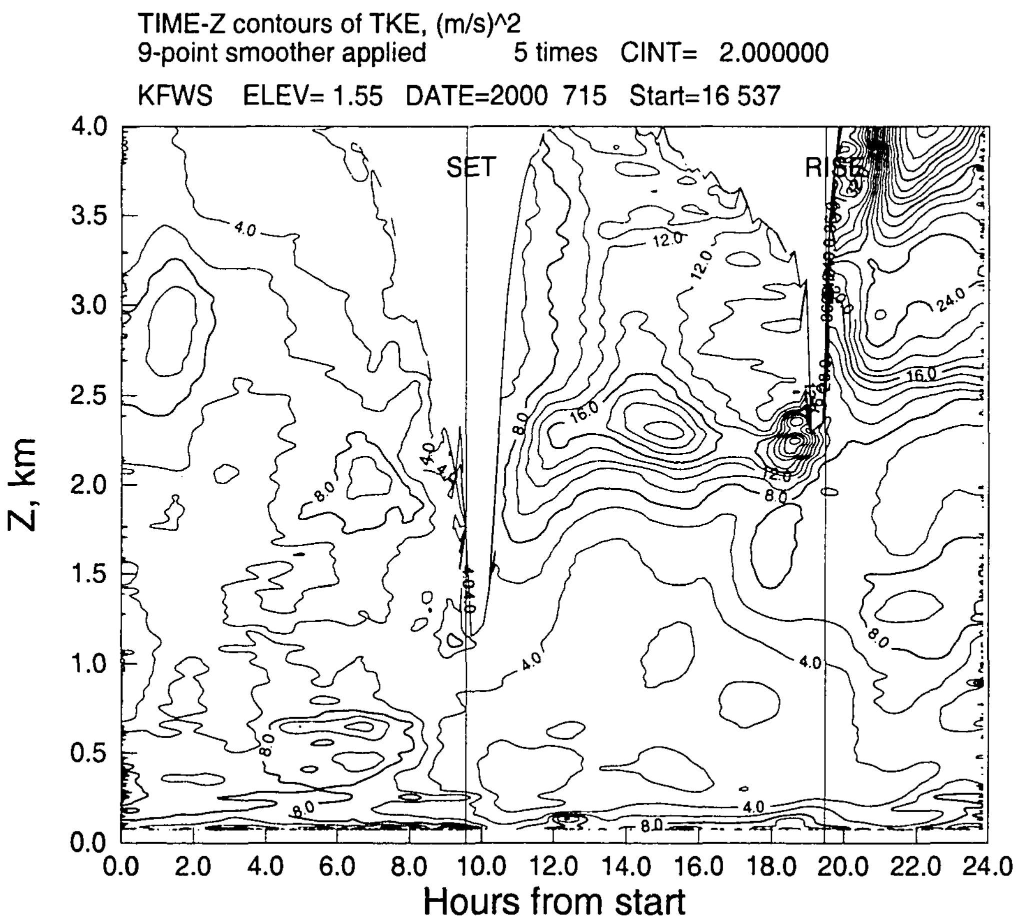

Figure 4.37: Time-height contour plot of TKE through a depth of 4 km and for 24 hours from KTLX radar, July 15-16, 2000. 1.5° tilt. Data begins at 16:05Z July 15.

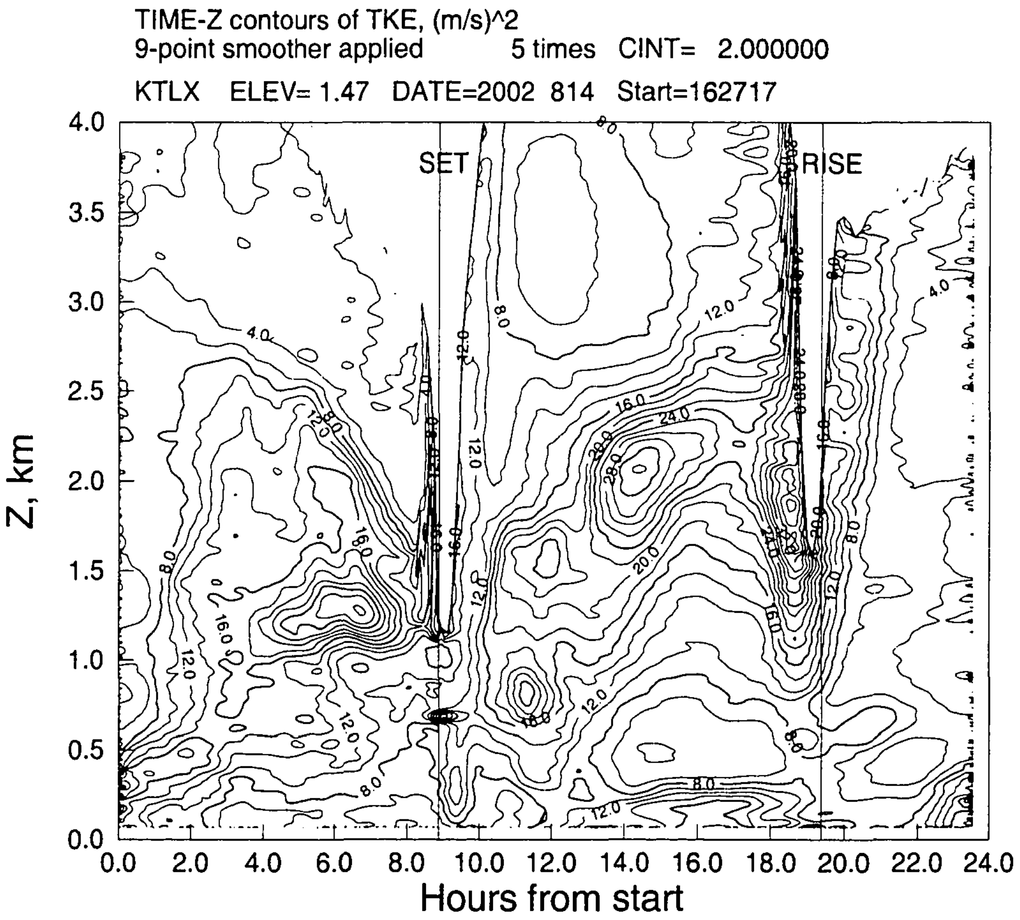

Figure 4.38: Time-height contour plot of TKE through a depth of 4 km and for 24 hours from KTLX radar, August 14-15, 2002. 1.5° tilt. Data begins at 16:26Z August 14.

eddies driven by buoyancy. At night, the turbulence is driven more by vertical wind shear, giving relatively larger u′ and v′ values.

However, TKE is not necessarily the best and most meaningful measure of turbulence. The TKE needs to be compared to the strength of the flow in some way, since a specific amount of TKE is more dynamically significant in a weak flow than a strong one. The turbulent viscosity, K, is more significant from a dynamical standpoint than TKE, and, from (2.7) it can be related to the ratio of TKE to wind shear:

$$K \propto \frac{w'^2}{|\nabla \vec{u}|} = \frac{VAD\,RMS\,error}{wind\,shear\,magnitude} \tag{4.14}$$

Where the isotropy assumption, TKE$=\frac{3}{2}$w$'^2$, is used. K can then be seen to be proportional to the strength of turbulence relative to the wind shear (though K is dimensional). As discussed in Sec. 2.2.1, (4.14) is not entirely valid during daytime conditions, though it might be able to provide some indication of the level of turbulent viscosity. The non-dimensional turbulent intensity, $w'_{rms}/|\vec{u}|=\sqrt{VAD\,RMS\,error}/$(wind speed), might also be considered; however, the strength of the TKE relative to the ground-relative mean-wind is not necessarily meaningful as this is a reference frame-dependent quantity. Time-height cross-sections for K (assuming the proportionality constant to be unity in (4.14)) calculated from the radar data according to (4.14) are presented in Figs. 4.39-4.42; however, what is contoured is 1/K rather than K. This is because the RMS error is a positive definite quantity which always has at least some amplitude due to noise, while the wind shear magnitude is often nearly zero in many areas of the time-height domain, especially in the daytime. Dividing a variable by a number which is sometimes nearly zero leads to an extreme amount of noise in the result. For these 1/K plots, increasing values signify a decrease in turbulence.

To make useful plots involving K rather than 1/K, the average K below 1 km is calculated as a function of time for each case and plotted in Figs. 4.43-4.46 for the 4 cases. The drop in K at sunset is evident in these plots. Also, The K values during the day get strong with each month, while the K values at night are about the same in each month. As each successive month is climatically warmer, this is reasonable as more thermal turbulence

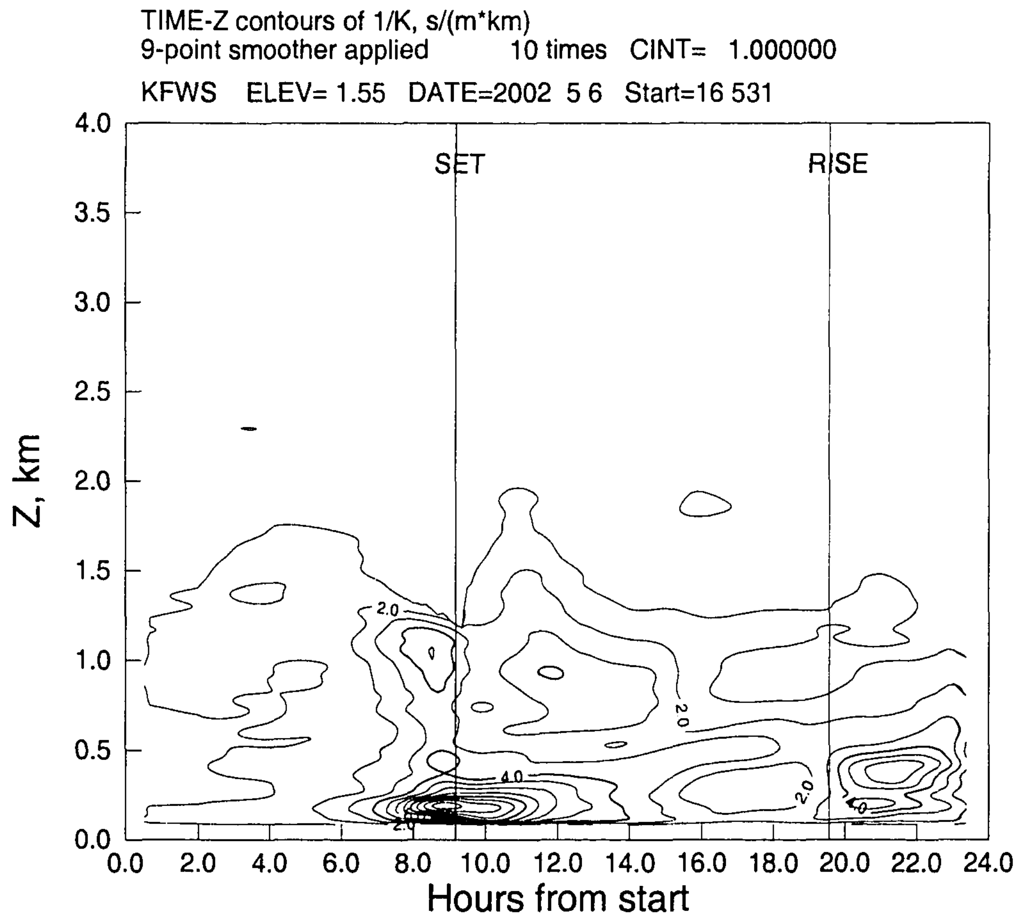

Figure 4.39: Time-height contour plot of 1/K through a depth of 4 km and for 24 hours from KFWS radar, May 6-7, 2002. 1.5° tilt. Data begins at 16:04Z May 6.

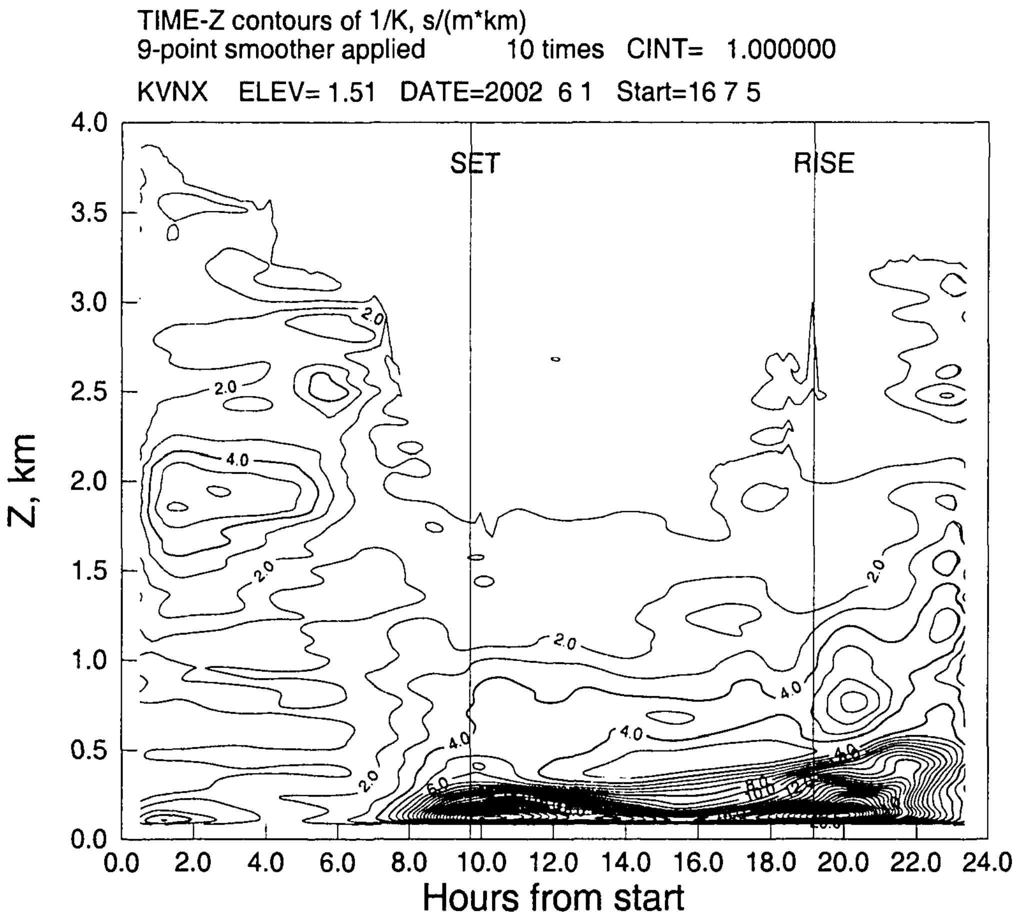

Figure 4.40: Time-height contour plot of 1/K through a depth of 4 km and for 24 hours from KVNX radar, June 1-2, 2002. 1.5° tilt. Data begins at 16:05Z June 1.

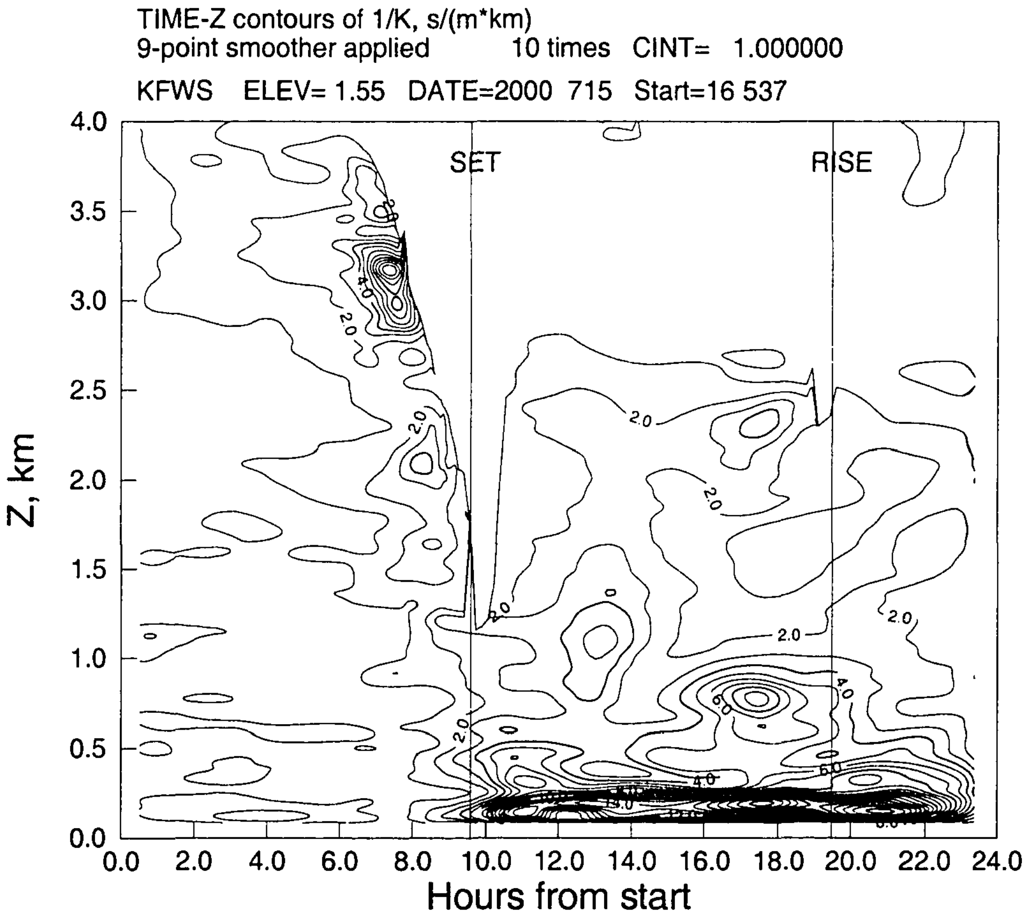

Figure 4.41: Time-height contour plot of 1/K through a depth of 4 km and for 24 hours from KTLX radar, July 15-16, 2000. 1.5° tilt. Data begins at 16:05Z July 15.

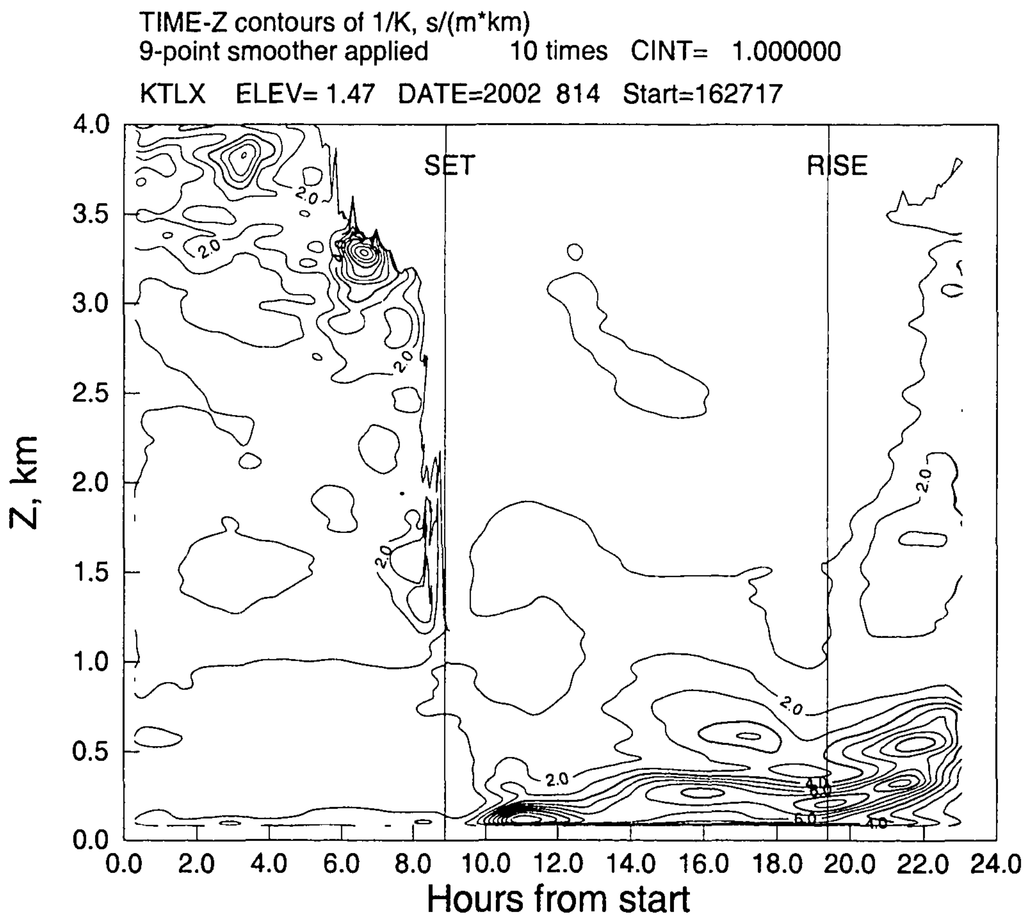

Figure 4.42: Time-height contour plot of 1/K through a depth of 4 km and for 24 hours from KTLX radar, August 14-15, 2002. 1.5° tilt. Data begins at 16:26Z August 14.

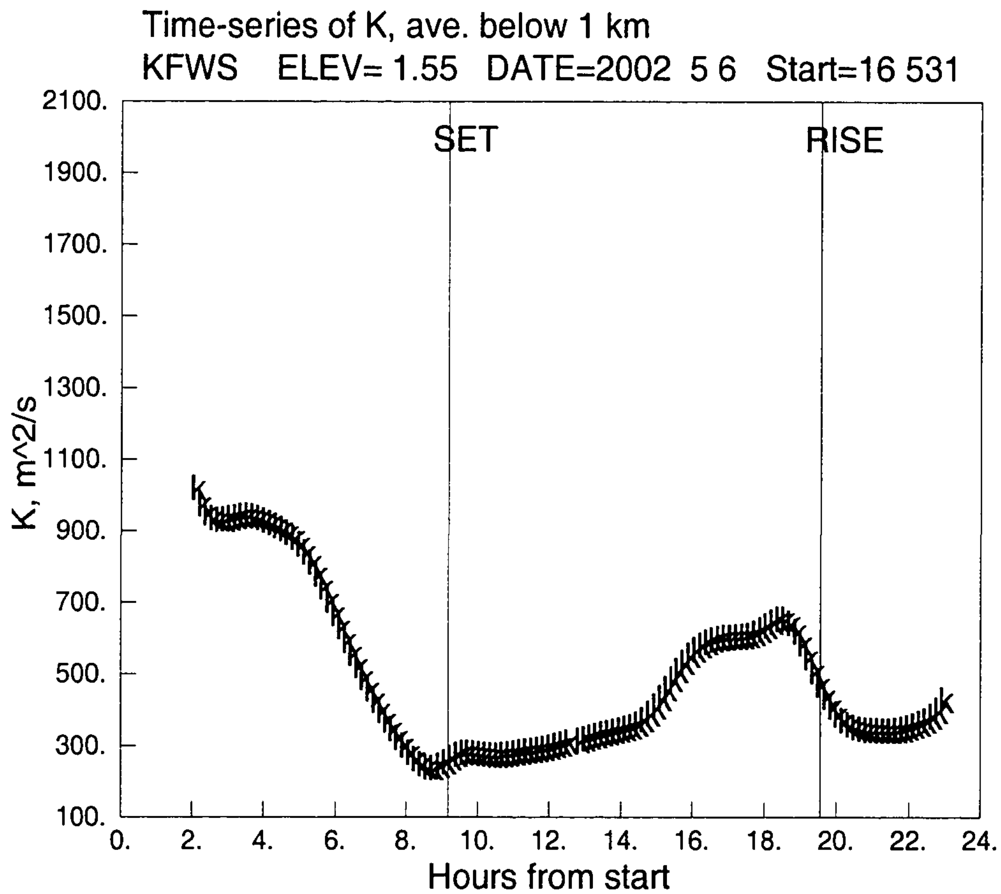

Figure 4.43: Time series of K averaged through a depth of 1 km from KFWS radar, May 6-7, 2002. 1.5° tilt. Data begins at 16:04Z May 6.

ought to be present during the day in warmer months. This leads to a larger contrast between daytime and nighttime conditions under warmer daytime conditions.

For all four cases considered, the turbulent viscosity decreases substantially after sunset in the shear layer below the LLJ core and to a lesser extent in the jet core. This agrees with the expectation of a decline in turbulence in the boundary after dark. Similar to the LLJ wind speed and shear, the low turbulence in the LLJ persists for 3 to 5 hours after sunrise.

An interesting feature of three of the cases (May, June, and August) is that the minimum turbulence (maximum in 1/K) occurs shortly after sunset very close to the ground. Also, for these three cases, another turbulence minimum occurs near the ground after sunrise. This is possibly due to the way the boundary layer transitions from daytime to nighttime regimes. The after-sunset turbulent minimum may be occurring after the day-

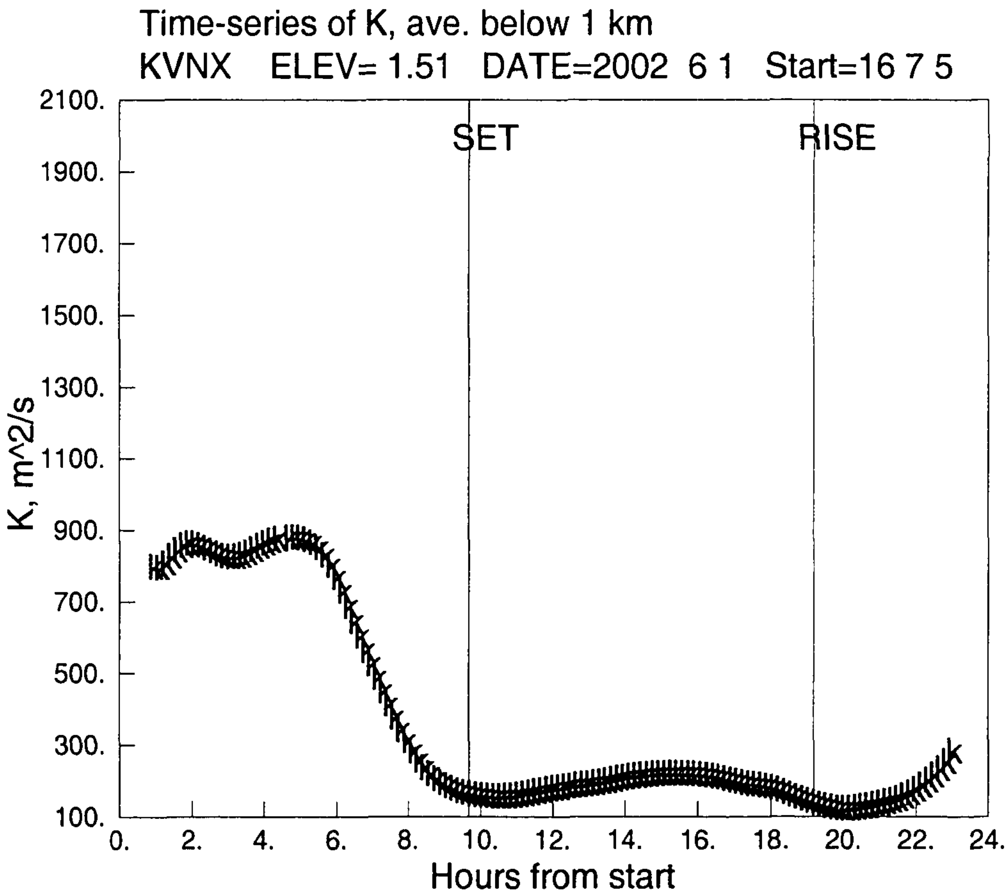

Figure 4.44: Time series of K averaged through a depth of 1 km from KVNX radar, June 1-2, 2002. 1.5° tilt. Data begins at 16:07Z June 1.

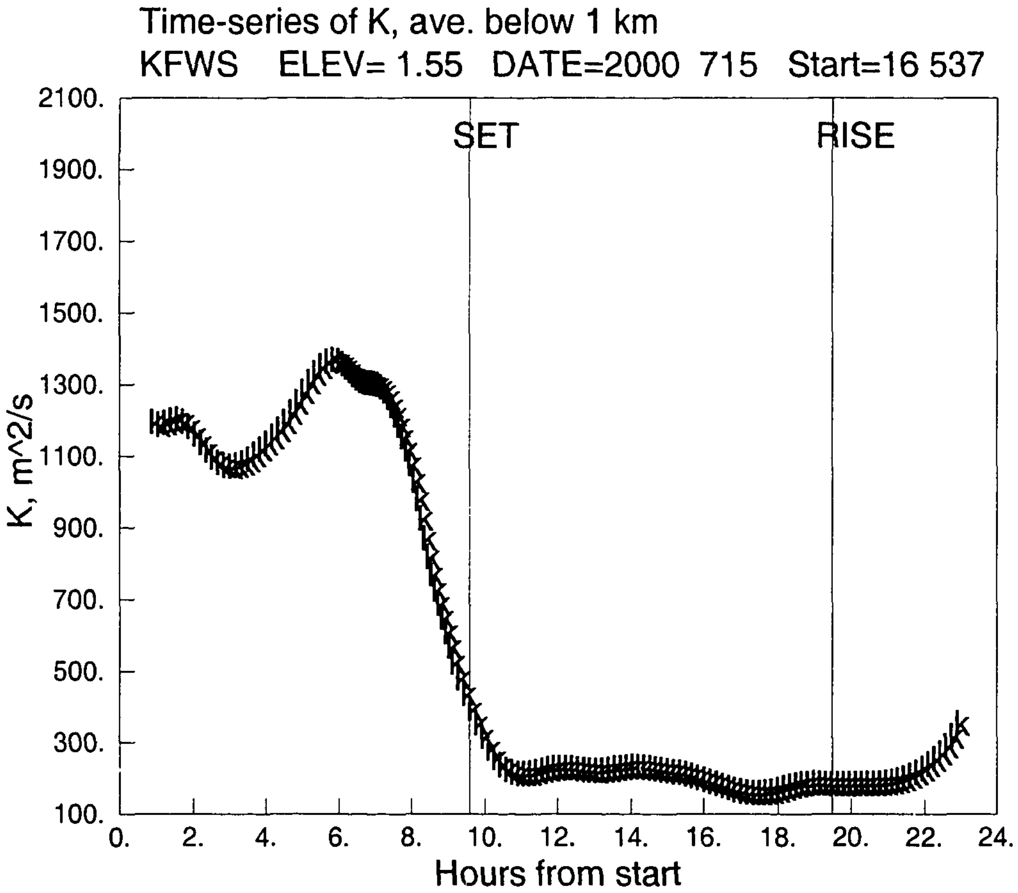

Figure 4.45: Time series of K averaged through a depth of 1 km from KFWS radar, July 15-16, 2009. 1.5° tilt. Data begins at 16:05Z May 6.

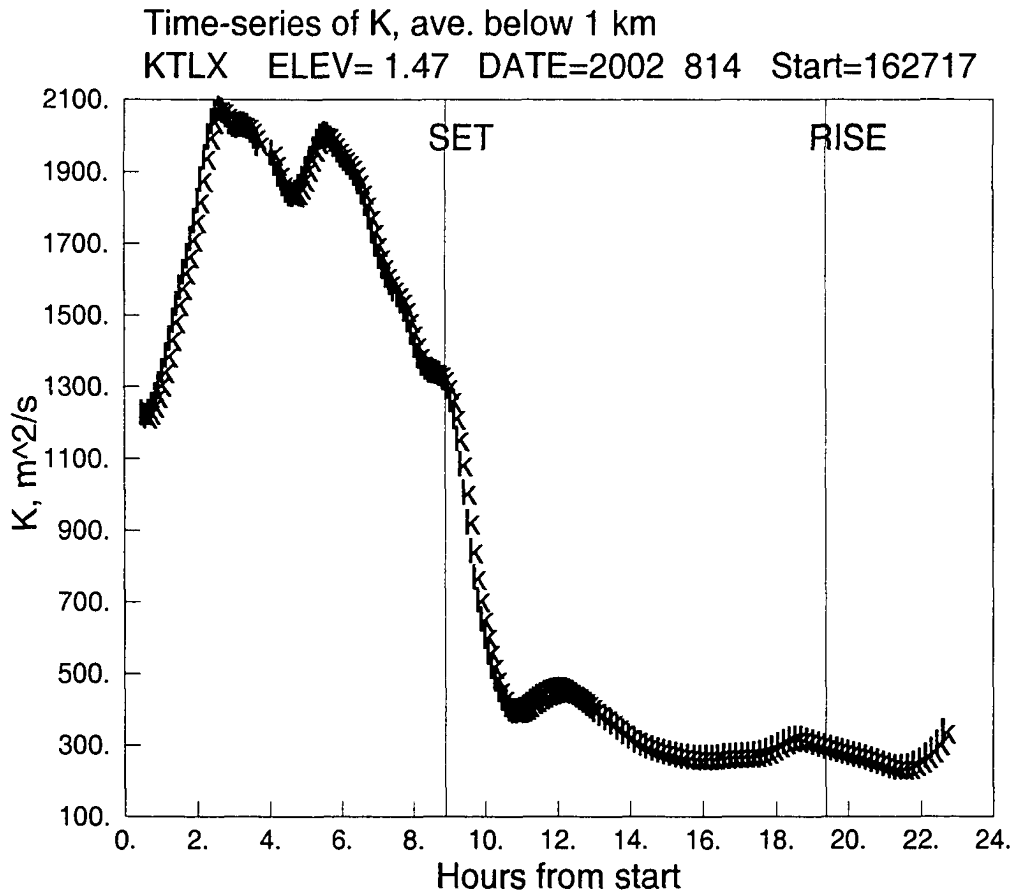

Figure 4.46: Time series K averaged through a depth of 1 km from KFWS radar, August 14-15, 2002. 1.5° tilt. Data begins at 16:27Z August 14.

time, buoyancy-driven turbulence has dissipated and before the nighttime, shear-driven turbulence has had time to develop. Similarly, the morning minimum in turbulence could exist due to the decline in nighttime, shear-driven turbulence prior to the development of substantial daytime, buoyancy-driven turbulence.

4.7.5 Discussion of Time-Height Sections

Lhermitte (1966), Frisch et al. (1992), Jain et al. (1993), and Browning and Atlas (1966) have also obtained time-height cross-sections of velocity from radar data. Each author presents a single time-height cross-section of one LLJ. Browning and Atlas did calculate turbulence profiles, but only for two hours after sunset and only at seven vertical levels. Jain et al. presented a time-height section of reflectivity, and showed the much higher reflectivity at night that has been noted as typical here. Browning and Atlas calculated a time-height plot of the number concentration of angels (related to average reflectivity) and for the few hours of data they obtained, their plot is very similar to the time near sunset in Figs. 4.19-4.22. Lhermitte's measurements of velocity are similar in character to those presented here, with a gradually rising and mostly nocturnal LLJ; while those of Jain et al. and Frisch et al. do not have this rising feature.

It is interesting that the wind shear and the LLJ wind speed remains for 3 to 5 hours after sunrise, while the reflectivity drops quickly right at sunrise. Also, the reflectivity in all the cases increases abruptly at sunset while the profiles of wind speed, shear, and turbulence change more gradually. The source of the velocity measurements in all cases, day or night, is almost certainly either birds or insects (Ch. 3), though it could be different species at different times. So while most of the radar scatters in the atmosphere quickly leave the atmosphere at sunrise for whatever reason and by whatever means, enough remain for radar measurements after sunrise and the LLJ still exists and is still measured. The rapid drop in reflectivity at sunrise and increase at sunset appears to be due to the behavior of biological scatterers responding to the sun and not meteorological factors which evolve more slowly.

That the wind speed for all four cases shows a gradual increase after sunset and a gradual decrease after sunrise, while the reflectivity changes rapidly within an hour at both sunrise and sunset, does not confirm the anomalous nocturnal winds attributed to birds seen with wind profiles (Wilczak et al., 1995; O'Bannon, 1995). Clearly the reported sudden 10 to 15 m/s increase in measured wind speeds due to the injection of birds into the atmosphere are not being seen here. What is seen is a gradual evolution of wind speed that is not closely correlated with reflectivity change. If birds are causing the signal for these cases, then they must be present both day and night, and not just at night. As serious biasing of radar winds due to the motion of biological scatters has not been reported in the literature as a problem during the day, it is reasonably likely that these four cases do not suffer from contamination from birds.

These results are generally consistent with the turbulence budget measurements in the lowest 2 km of the boundary layer during daytime (convective boundary layer) conditions obtain by Lenschow et al. (1980) and at night (stable boundary layer) by Lenschow et al. (1988). Lenschow's 1988 data show that under nocturnal conditions the TKE budget is dominated by shear production and viscous dissipation with some loss in TKE due to the buoyancy term. In the convective boundary layer, Lenschow's 1980 data show that the TKE budget is mostly a balance between buoyant production and viscous dissipation with a small contribution to TKE from shear. Direct radar measurement of the buoyancy term in the TKE budget is not possible due to the lack of temperature information. However, the measurements reported here do show an increase in shear at night which is probably related to shear production of turbulence at night, and a reduction in turbulence (as measured by K) at sunset which is probably related to the elimination of buoyant production.

Despite the highest shear being in the lowest few hundred meters above the ground at night, the turbulence as measured by K is actually a minimum there. However, TKE values are higher in the shear layer so turbulence is probably being produced there. While TKE is higher in the shear layer, it's dynamical importance (as measured by K) is less.

Buoyant suppression of turbulence is the likely reason the LLJ behaves substantially differently from free fluid jets in constant density flow (Tennekes and Lumley, 1974, pp. 127-133). Turbulence in such jets forms at the shear layer around the jet core and rapidly spreads across the entire jet by entrainment. Jets of this nature tend to be uniformly and highly turbulent. The LLJ by contrast is not highly turbulent. While turbulence is probably generated in the shear layer below the jet core, it appears to be suppressed and does not spread by entrainment. The reason for this is probably the effect of thermal stratification, but this can not be definitely confirmed with these data.

The results tend to confirm the Blackadar (1957) theory. Blackadar originally hypothesized that the core of the LLJ would be mostly turbulence-free due to the static stability of the nocturnal boundary layer, while the layer of shear below it would still be somewhat turbulent due to the shear production of turbulence. These data show that, while TKE is higher in the shear layer, there is a strong reduction in K in the shear layer at night, implying that turbulent suppression, probably from thermal stratification, is responsible for the existence of this shear layer, and; therefore, the LLJ.

These data can be used to verify a prediction of the inertial oscillation (Blackadar) theory. A prediction of this theory is that the supergeostrophic amplitude at night increases as the daytime turbulence increases. To try to verify this, the amplitude of the geostrophic wind is calculated as the 24 hour time average of the mean winds below 1 km shown in Figs. 4.27-4.30. This assumes that the mean of these winds does represent the geostrophic wind. This is itself a prediction of the inertial oscillation theory which may not be entirely true. The amplitude of the ageostrophic wind is then calculated as the time average of the difference between the mean wind below 1 km and the geostrophic wind. The daytime K value is obtained as the mean of the daytime peak in K sine in Figs. 4.43-4.46. Table 4.2 lists the results. The last column shows the stronger ageostrophic wind speed relative to the geostrophic wind speed for the warmer months. This correlates well with the higher turbulence (K values) in the July and August. The correlation is not perfect as the turbulence in June is less than that in May for unknown reasons.

These data can not verify the resonance hypothesis discussed and exhibited in the modeling work of Ch. 2. This hypothesis is difficult to verify because of a lack of long time history information. Such information is difficult to obtain because several days in succession with nocturnal jets, no precipitation, stable synoptic conditions, and continuous

Month	Daytime K, m^2/s	$\lvert\vec{u_g}\rvert$, m/s	$\lvert\vec{u_a}\rvert$, m/s	$\frac{\lvert\vec{u_a}\rvert}{\lvert\vec{u_g}\rvert}$
May	900	17.9	4.1	.23
June	825	15.2	4.4	.29
July	1250	8.4	6.8	.81
Aug.	1900	5.6	4.9	.87

Table 4.2: Tabular comparison of turbulence (K) and ageostrophic wind speed relative to geostrophic wind speed for the four LLJ cases considered.

radar data are difficult to find.

Chapter 5

Concluding Remarks

This research has shown that Doppler radar data can be used to accurately measure turbulence and wind profiles in the Great Plains LLJ. To achieve this, considerable attention to quality-control was paid. Quality control is important for minimizing the effect of ground clutter contamination, and for avoiding measurements of migrating birds.

To address the issue of ground clutter contamination, Appendix A was presented in which it was found that tilt angles for NEXRADs of about 1.5° are optimal for minimizing ground clutter. This tilt appears to work well in terms of producing accurate VAD winds, with lower and higher tilts having sometimes significant contamination from ground clutter. The problem of ground clutter at high tilt angles has perhaps been hitherto underappreciated.

To address the issue of contamination from migrating birds, Ch. 3 was presented in which the known possible mechanisms of clear-air radar scatter are reviewed and applied to data obtained with high-resolution radars. These data, along with some of the past and recent literature, supports the position that migratory bird contamination is not a major problem for nocturnal clear-air work in the Great Plains. There is some recent literature which strongly supports the position that migratory birds are a major problem for nocturnal clear-air data from meteorological radars. While it is probable that this problem has been over-emphasized by some, it is no doubt still a problem with some radars in some locations. Because radar measurements are used in operational forecast models, and because of the perceived great value in broadening the assimilation of such information into models, should the data be accurate; the problem of quality-controlling radar data with respect to birds is probably more deserving of more attention than any other topic touched upon in this research.

There is a remarkable symmetry in the daily behavior of birds, insects, and refractivity of the atmosphere. This symmetry makes it particularly difficult to distinguish between them as possible sources of radar signals. Virtually any aspect of clear-air return could be explained in terms of biota or refractivity. Loss of signal at sunset could be due to insects or birds leaving the atmosphere; or it could be due to a reduction in convective mixing from surface heating affecting the refractivity. An increase in signal at night could be caused by the take-off of migratory birds or insects, or by an increase in refractivity gradients caused by stable stratification of the boundary layer due to nocturnal surface cooling. For typical scanning radar wavelengths, the wavelength dependence of scattering is virtually the same for birds as it is for Bragg (refractivity) scatter. Routinely discriminating birds from insects, in particular, will probably require ingenuity, as no simple solutions have suggested themselves.

Having dealt with quality-control issues, what are believed to be accurate time-height profiles of wind and turbulence were produced for four cases spanning the warm season. The most innovative aspect of the data reduction involved the separation of spectral width information into wind shear and turbulence measures. Using this technique provides a measure of small-scale turbulence not obtainable otherwise, and a measure of wind shear which is less noisy than differentiating a profile obtained by conventional VAD. However, most of the energy of turbulence is in the large scales, and wind shear can be obtained with sufficient accuracy by conventional VAD, so it is not clear if the complexity of this method is worth the effort.

The time-height profiles obtained were quite interesting and illustrate what is possible with operational NEXRAD data. High time and space resolution information of wind and turbulence were obtained throughout the boundary layer down to within 100 m of the surface and at all times of the day and night. The profiles obtained here are broadly consistent with the Blackadar theory and with the low-dimensional modeling results of Ch. 2. A key finding is that turbulence, as measured by K, always declines at night in the region of high shear at the lower boundary of the LLJ. This tends to support the Blackadar theory which relies upon this effect. It is also interesting that TKE measures do not always decline at night in this layer, but are always less in the jet core than in the shear layer. It is the TKE that might be sensed as aerodynamic turbulence by an aircraft flying in the jet. The jet core is fairly smooth in an absolute sense, even though turbulence is suppressed more in the shear layer.

While the observations of the relation between turbulence and the LLJ tend to support the Blackadar theory, the observation of oscillating wind by itself can not be used to distinguish between the inertial oscillation theory (Blackadar) and the heating and cooling of terrain theory (Holton, 1967), as both these theories produce oscillating, super-geostrophic LLJs. While the Blackadar theory depends entirely on the diurnal cycle of boundary layer turbulence, turbulence is assumed constant in the Holton theory, which relies on sloping terrain. It is possible that turbulence suppression in the LLJ may occur without being a critical factor in the dynamics.

The resonance concept explored in Ch. 2 was not demonstrated in the data. In fact, had such an effect been present, it would not have been seen in these data as only 24 hours of data were reduced for each case, and resonance requires multiple days of stable conditions to manifest itself. The difficulty in finding cases with a long enough duration of stable conditions for resonance to appear, suggests that this effect, while plausible, may rarely be manifested in practice.

It is interesting to consider differences between the Great Plains LLJ and a free incompressible jet that one might be familiar with from engineering studies. The LLJ shows substantial shear only in the layer near the ground while incompressible jets have high shear completely surrounding the jet core. Also, in the LLJ, the turbulence produced in the shear layer near the ground does not entrain the jet core, which remains smooth (in terms of TKE) most of the night. This contrasts with incompressible jets where turbulence spreads completely across the jet by entrainment. Both of these differences are due, with little doubt, to the suppression of turbulence by the stable stratification of the layer of air below the core of the LLJ. This stratification both reduces the intensity and impact of any turbulence generated in the shear layer and keeps the turbulence confined to this layer. The suppression of turbulence in the shear layer allows a high level of shear to develop, and, consequently, leads to a strong LLJ.

Chapter 6

Suggestions for Further Research

1. Expanding rings of radar echo in the morning are, with little doubt, caused by birds. It is also known unequivocally the direction the birds are aligned in these rings (radially outward). This suggests it would be useful to directly compare the radar signatures of expanding ring echoes with nocturnal return to see if the two are consistent. Rings echoes could also be used for calibrating dual-polarization measurements of birds.

2. Dual-polarization research radars could be used to explore if the polarization information can routinely discriminate between birds and insects.

3. As this research suffered from not having temperature profile information, either high-temporal and vertical-spatial profiles could be obtained by physical soundings, or modeling studies could be done using accurate mesoscale models.

4. One large source of error for measuring rain fall with radar is radar calibration (see Sec. 3.3.1). A re-calibration survey of the entire NEXRAD network ought to be done to reduce this source of error. An elegant way to do this is by intercomparison. Starting with one radar in the network, the calibration of adjacent radars can be checked by examining regions of echo-containing space seen by both radars. It would not be difficult to compile a large volume of suitable data for intercomparing two radars with overlapping scan regions. By such intercomparing, the calibration of the

entire network can be checked (and adjusted) by going from radar to radar doing intercomparisons. Re-calibration can also be done with archived data so that the health of the network over time can be assessed. An automated system can be developed whereby this intercomparison and calibration consistency check could be done as a routine part of operating the system.

5. The geostrophic wind can be theoretically estimated from time series of the u and v wind components such as those in Sec. 4.7.2. These geostrophic values could then be compared with values inferred from synoptic analyses (such as the NCEP reanalysis) as a check on the inertial oscillation theory.

6. A Climatology of LLJ time-height structure could be constructed by using all available NEXRAD radar to produce monthly composites. Perhaps 3-4 days of data could be retrieved per month at a single NEXRAD site over 10 years for a warm season month for compositing. The climatological time-height structure of the LLJ would then be available as a function of month.

7. Higher resolution and more powerful radars than are currently available ought to be developed. Modern improvements in electronics, data management and display and real-time computer processing mean that, with sufficient funding, meteorological radars with resolution and sensitivity at least an order of magnitude superior to any so far constructed could be built. Cryogenically cooled receivers to reduce noise, large phased array antennas to reduce beam width and side lobe energy, arrays of receiving transducers for imaging, FM-CW techniques, antenna arrays, synthetic aperture techniques for airborne or ground-mobile units, and the usage of shorter wave lengths are all avenues that should be pursued for the next generation of research radars. Dual-Doppler measurements of 1 meter resolution of a tornadic supercell are technically feasible. Radars used in meteorology historically are, by some metrics, much more powerful than those used currently. The Wallops Island 10.7 cm radar built in the 1960s (still extant, but used mostly for tracking missile tests) was arguably the most powerful weather radar ever built with 3 MW of power and an 18.4 m diameter antenna (which compares with .75 MW and 8.5 m diameter for a NEXRAD).

Research radars ought to be significantly more powerful than operational ones.

8. A theory does not exist for turbulent radiation scatter for inhomogeneous conditions, such as density stratification and for conditions in which the inner scale of turbulence is large relative to the radar wavelength. It would be of some value to derive such a theory.

Bibliography

[1] Able, K. P., 1999: *Gathering of Angels: Migrating Birds and Their Ecology.* 193 pp. Comstock Books, Ithaca, N.Y.

[2] Anagnostou, E. N., C. A. Morales, and T. Dinku, 2001: The use of TRMM precipitation radar observations in determining ground radar calibration biases. *J. Atmos. Oceanic. Technol.*, **18**, 616-28.

[3] Anderson, D. L. T., 1976: The low-level jet as a western boundary current. *Mon. Wea. Rev.*, **104**, 907-21.

[4] Arrit, R. W., T. D. Rink, M. Segal, D. P. Todey, C. A. Clark, M. J. Mitchell, and K. M. Labas, 1997: The Great Plains low-level jet during the warm season of 1993. *Mon. Wea. Rev.*, **125**, 2176-2192.

[5] Arya, S. Pal, 1988: *Introduction to Micrometeorology.* Academic Press, 307 pp.

[6] Atlas, D., 1960a: Radar detection of the sea breeze. *J. Met.*, **17**, 244-58.

[7] Atlas, D., 1960b: Possible key to the dilemma of meteorological "angel" echoes. *J. Met.*, **17**, 95-103.

[8] Atlas, D., J. H. Richter, and E. E. Gossard, 1969: *Waves, Turbulence, and Insects as Seen By Ultra High Resolution Radar.* Technical Report No. 13, Laboratory for Atmospheric Probing, Department of the Geophysical Sciences, University of Chicago.

[9] Batchelor, G. K., 1955: The scattering of radio waves in the atmosphere by turbulent fluctuations in refractive index. *Research Report EE 262*, School of Electrical Engineering, Cornell University, Ithaca, N.Y.

[10] Battan, L. J., 1973: *Radar Observations of the Atmosphere.* University of Chicago Press, 324 pp.

[11] Bauer, J. R., 1956: *The Suggested Role of Stratified Elevated Layers in Transhorizon Short-Wave Radio Propagation.* Technical Report. No. 124, Lincoln Laboratory, Mass. Inst. of Tech.

[12] Berthold, P., 1993: *Bird Migration: A General Survey.* Oxford University Press, 239 pp.

[13] Berry, R. E. and L. R. Taylor, 1968: High-altitude migration of aphids in maritime and continental climates. *J. Animal Ecol.*, **37**, 713-22.

[14] Blackadar, A. K., 1957: Boundary layer wind maxima and their significance for the growth of nocturnal inversions. *Bull. Amer. Meteor. Soc.*, **38**, 283-390.

[15] Blake, L. V., 1970: Prediction of radar range. In *Radar Handbook*, M. I. Skolnik, ed. McGraw Hill Book Company.

[16] Bluestein, H. B. and A. L. Pazmany, 2000: Observations of tornadoes and other convective phenomena with a mobile, 3-mm wavelength Doppler radar: the spring 1999 field experiment. *Bull. Amer. Meteor. Soc.*, **81**, 2939-51.

[17] Bluestein, H. B. and P. C. Banacos, 2002: The vertical profile of wind and temperature in cyclones and anticyclones over the eastern two-thirds of the United States: A climatology. *Mon. Wea. Rev.*, **130**, 477-506.

[18] Booker and Gordon, 1950: A theory of radio scattering in the troposphere. *Proceedings of the I.R.E*, **38**, 401-12.

[19] Beebe, R. G. and F. C. Bates, 1955: A mechanism for Assisting in the release of convective instability. *Mon. Wea. Rev.*, **83**, 1-10.

[20] Beyrich, F. and B. Klose, 1988: Some aspects of modeling low-level jets. *Bound. Lay. Meteor.*, **43**, 1-14.

[21] Bonner, W. D., 1968: Climatology of the low level jet. *Mon. Wea. Rev.*, **96**, 833-50.

[22] Brekhovskikh, L. M., 1960: *Waves in Layered Media.* Translated from the Russian by David Lieberman. Academic Press, New York.

[23] Browning, K. A. and D. Atlas, 1966: Velocity characteristics of some clear-air dot angels. *J. Atmos. Sci.*, **23**, 592-604.

[24] Buajitti, K. and A. K. Blackadar, 1957: Theoretical studies of diurnal wind-structure variations in the planetary boundary layer. *Quart. J. R. Met. Soc.*, **83**, 486-500.

[25] Burt, P. J. A. and D. E. Pedgley, 1997: Nocturnal insect migration: effects of local winds. *Adv. in Ecol. Res.*, 27, 61-92.

[26] Clark, R. D. and M. L. McDermott, 1997: Measurements of momentum and heat flux divergences associated with the Great Plains low-level jet using an instrumented aircraft. *Proceedings of the 12th Symposium on Boundary Layers and Turbulence.* Vancouver, Canada, 28 July-1 August.

[27] Crawford, A. B., 1949: Radar reflections in the lower atmosphere. *Proceedings of the I.R.E.*, **37**, 404-5.

[28] Crawford, K. C. and H. R. Hudson, 1973: The diurnal wind variation in the lowest 1500 ft in central Oklahoma: June 1966-May 1967. *J. Appl. Meteor.*, **12**, 127-32.

[29] Crum, T.D. and R. L. Alberty, 1993: The WSR-88D and the WSR-88D Operational Support Facility. *Bull. Amer. Meteor. Soc.*, **74**, 1669-87.

[30] Djurić, D., 1981: A numerical model of the formation and evolution of a low-level jet. *Mon. Wea. Rev.*, **109**, 384-90.

[31] Doviak, R. J. and D S. Zrnić, 1984: *Doppler Radar and Weather Observations.* Academic Press, 458 pp.

[32] Doviak, R. J. and D S. Zrnić, 1985: Siting of Doppler weather radars to shield ground targets. *IEEE Trans. on Antennas and Prop.*, **33**, 685-9.

[33] Drake, V. A., 1984: The vertical distribution of macro-insects migrating in the nocturnal boundary layer: a radar study. *Bound. Lay. Meteor.*, **28**, 353-74.

[34] Drake, V. A., 1985: Radar observations of moths migrating in a nocturnal low-level jet. *Ecol. Entomol.*, **10**, 259-65.

[35] Drake, V. A. and R. A. Farrow, 1988: The influence of atmospheric structure and motions on insect migration. *Ann. Rev. Entomol.*, **33**, 183-210.

[36] Eastwood, E., 1967: *Radar Ornithology.* Methuen & Co., Ltd. 278 pp.

[37] Elder, F. C., 1957: Some persistent "ring" angels on high-powered radar. *Proceedings of the Sixth Weather Radar Conference.* Cambridge, Massachusetts, Mar. 26-28.

[38] Fast, J. D. and M. D. McCorcle, 1990: A two-dimensional numerical sensitivity study of the great plains low-level jet. *Mon. Wea. Rev.*, **118**, 151-63.

[39] Fo, A. J. P. and K. C. Crawford, 1999: Mesoscale precipitation fields. Part I: statistical analysis and hydrologic response. *J. Appl. Meteor.*, **38**, 82-101.

[40] Friend, A. W., 1939: Continuous determination of air-mass boundaries by radio. *Bull. Amer. Met. Soc.*, **20**, 202-5.

[41] Friend, A. W., 1940: Developments in meteorological sounding by radio waves. *J. Aero. Sci.*, **7**, 347-52.

[42] Frisch, A. S., B. W. Orr, and B. E. Martner, 1992: Doppler Radar Observations of the Development of a Boundary-Layer Nocturnal Jet. *Mon. Wea. Rev.*, **120**, 3-16.

[43] Gage, K. S., 1990: Radar observations of the free atmosphere: structure and dynamics. In *Radar in Meteorology*, David Atlas, editor. American Meteorological Society, pp 534-74.

[44] Gallet, R. M., 1955: Aerodynamical mechanisms producing electronic density fluctuations in turbulent ionized layers. *Proceedings of the Inst. of Radio Engineers.*, **43**, 1240-52.

[45] Gauthreaux, S. A. and C. G. Belser, 1998: Displays of bird movements on the WSR-88D: patterns and quantification. *Wea. and Fore.*, **13**, 453-64.

[46] Gauthreaux, S. A., D. S. Mizrahi, and C. G. Belser, 1998b: Bird migration and bias of WSR-88D wind estimates. *Wea. and Fore.*, **13**, 465-81.

[47] Gossard, E. E., 1990: Radar research on the atmospheric boundary layer. In *Radar in Meteorology*, David Atlas, editor. American Meteorological Society. pp 477-527.

[48] Gossard, E. E. and J. H. Richter, 1970: Internal waves in the atmosphere from high-resolution radar measurements. *J. Geophys. Res.*, **75**, 3523-36.

[49] Gossard, E. E., and R. B. Chadwick, W. D. Neff, and K. P. Moran, 1982: The use of ground-based Doppler radars to measure gradients, fluxes and structure parameters in elevated layers. *J. Appl. Met.*, **21**, 211-26.

[50] Gossard, E. E. and R. G. Strauch, 1983: *Radar Observations of Clear Air and Clouds.* Elsevier, 280 pp.

[51] Gossard, E. E., D. E. Wolfe,and B. B. Stankov, 1999: Measurement of humidity profiles in the atmosphere by the global positioning system and radar wind profilers. *J. Atmos. Oceanic. Technol.*, **16**, 156-64.

[52] Gunn, K. L. S. and T. W. R. East, 1954: The microwave properties of precipitation particles. *Quart. J. Roy. Meteor. Soc.*, **80**, 522-45.

[53] Hardy, K. R. and K. M. Glover, 1966: 24 hour history of radar angel activity at three wavelengths. *Proceedings: Twelfth Conference on Radar Meteorology,* Norman, Oklahoma.

[54] Hardy, K. R. and I. Katz, 1969: Probing the atmosphere with high power, high resolution radars. *Proceedings of the IEEE*, **57**, 468-80.

[55] Hardy, K. R., K. S. Gage, 1990: The history of radar studies of the clear atmosphere. Ch. 17 in *Radar in Meteorology,* David Atlas ed., American Meteorological Society.

[56] Higgins, R. W., Y. Yao, E. S. Yarosh, J. E. Janowiak, and K. C. Mo, 1997: Influence of the Great Plains low-level jet on summertime precipitation and moisture transport over the Central United States. *J. Clim.*, **10**, 481-507.

[57] Holton, J. R., 1967: The diurnal boundary layer wind oscillation above sloping terrain. *Tellus,* **19**, 199-205.

[58] Jackson, J. D., 1962: *Classical Electrodynamics.* John Wiley & Sons, New York.

[59] Jain, M., M. Eilts, K. Hondl, 1993: Observed differences of the horizontal wind derived from Doppler radar and a balloon-borne atmospheric sounding system. *Preprints: 8th Symposium on Meteorological Observations and Instrumentation.* Anaheim, Calif., 17-22 Jan., 189-94.

[60] Joss, J., and A. Waldvogel, 1970: A method to improve the accuracy of radar measured amounts of precipitation. *Preprints: 14th Radar Meteorology Conference,* 237-8.

[61] Jungbluth, K., J. Belles and M. Schumacher, 1995: Velocity contamination of WSR-88D and wind profiling data due to migrating birds. *Preprints 27th Conference on Radar Meteorology.* Vail, Colorado. Amer. Met. Soc.

[62] Kaimal, J. C., and Y. Izumi, 1965: Vertical velocity fluctuations in a nocturnal low-level jet. *J. Appl. Met.*, **4**, 576-84.

[63] Knight, C. A. and L. J. Miller, 1998: Early radar echoes from small, warm cumulus: Bragg and hydrometeor scattering. *J. Atmos. Sci.*, **55**, 2974-92.

[64] Krasilnikoff, V. A., 1949: On fluctuations of the angle of arrival in the phenomenon of twinkling of stars. *Doklady Akad. Nauk SSSR*, **65**, 291.

[65] Kropfli, R. A., 1986: Single Doppler radar measurements of turbulence profiles in the convective boundary layer. *J. Atmos. Ocean. Tech.*, **3**. 305-14.

[66] Kropfli, R. A., 1990: The Atmospheric Boundary Layer: Panel Report. Ch. 27b in *Radar in Meteorology*, David Atlas, Editor. Amer. Meteor. Soc., Boston.

[67] Kropfli, R. A., I. Katz, T. G. Konrad, and E. B. Dobson, 1968: Simultaneous radar reflectivity measurements and refractive index spectra in the clear atmosphere. *Radio Sci.*, **3**, 991-4.

[68] Kutzbach, G., 1979: *The Thermal Theory of Cyclones.* Amer. Met. Soc., 255 pp.

[69] Lane, J. A. and R. W. Meadows, 1963: Simultaneous radar and refractometer soundings of the troposphere. *Nature*, **197**, 35-6.

[70] Lenschow, D. H., J. C. Wyngaard, and W. T. Pennell, 1980: Mean-field and second-moment budgets in a baroclinic, convective boundary layer. *J. Atmos. Sci.*, **37**, 1313-26.

[71] Lenschow, D. H., X. S. Li, C. Zhu, and B. B. Stankov, 1988: The stably stratified boundary layer over the Great Plains: I. Mean and turbulence structure. *Bound. Lay. Meteor.*, **42**, 95-121.

[72] Lewis, J. M., 1997: The Lettau-Schwerdtfeger Balloon Experiment: Measurement of Turbulence via Austauch Theory. *Bull. Amer. Met. Soc.*, **78**, 2619-35.

[73] Lhermitte, R. M., 1966: Probing air motion by Doppler analysis of radar clear air return. *J. Atmos. Sci.*, **23**, 575-91.

[74] Lhermitte, R. M., 1968: Turbulent air motions as observed by Doppler radars. *Proceedings: 13th Radar Meteorology Conference.* Montreal, Canada, 20-23 Aug., 498-503.

[75] Lhermitte, R., 1990: Attenuation and scattering of millimeter wavelength radiation by clouds and precipitation. *J. Atmos. Ocean. Tech.,* **7**, 464-79.

[76] Lowery, G. H. Jr. and R. J. Newman, 1966: A continentwide view of bird migration on four nights in October. *The Auk*, **83**, 547-86.

[77] Maddox, R. A., 1983: Large-scale meteorological conditions associated with midlatitude, mesoscale convective complexes. *Mon. Wea. Rev.*, **111**, 1475-93.

[78] Mahrt, L., R. C. Heald, D. H. Lenschow, and B. B. Stankov, 1979: An observational study of the structure of the nocturnal boundary layer. *Boundary Layer Meteor.*, **17**, 247-64.

[79] Martin, W. J., and A. Shapiro, 2000: Resonance and low-dimensional modeling of the low-level jet. *Preprints: 15th Conference on Hydrology.* Long Beach, California, 9-14 Jan., 99-102.

[80] McNider, R. T., and R. A. Pielke, 1981: Diurnal boundary-layer development over sloping terrain. *J. Atmos. Sci.*, **38**, 2198-2212.

[81] Miller, P. A., M. F. Barth, J. R. Smart, L. A. Benjamin, 1997: The extent of bird contamination in the hourly winds measured by the NOAA profiler network: results before and after implementation of the new bird contamination quality control check. *Preprints, 1st Symposium on Integrated Observing Systems*, Long Beach, CA. Amer. Meteor. Soc., 138-44.

[82] Moeng, C.-H. and J. C. Wyngaard, 1986: An analysis of closures for pressure-scalar covariances in the convective boundary layer. *J. Atmos. Sci.*, **43**, 2499-513.

[83] Mueller, E. A., 1983: Differential reflectivity of birds and insects. *Preprints, 21st Conference on Radar Meteorology.* Edmonton, Canada. Amer. Meteor. Soc.

[84] O'Bannon, T., 1995: Anomalous WSR-88D wind profiles–migrating birds?. *Preprints 27th Conference on Radar Meteorology.* Vail, CO. Amer. Meteor. Soc.

[85] Obukov, A. M., 1949: Structure of the temperature field in a turbulent flow. *Izv. Akad. Nauk SSSR, Ser. Geograf. Geofiz.*, **13**, 58.

[86] Parish, T. R., A. R. Rodi, and R. D. Clark, 1988: A case study of the summertime Great Plains low level jet. *Mon. Wea. Rev.*, **116**, 94-105.

[87] Prandtl, L., 1925: Uber die ausgebildete turbulenze, *ZAMM*, **5**, 136.

[88] Press, W. H., B. P. Flannery, S. A. Teukolsky, and W. T. Vetterling, 1986: *Numerical Recipes.* Cambridge University Press.

[89] Probert-Jones, J. R., 1962: The radar equation in meteorology. *Quart. J. Roy. Meteor. Soc.* **88**, 485-95.

[90] Riley, J. R., 1975: Collective orientation in night-flying insects. *Nature.* **253**, 113-4.

[91] Riley, J. R., 1985: Radar cross section of insects. *Proceedings of the IEEE*, **73**, 228-32.

[92] Riley, J. R., 1989: Remote sensing in entomology. *Ann. Rev. Entomol.*, **34**, 247-71.

[93] Savijarvi, H., 1991: The United States Great Plains diurnal ABL variation and the nocturnal low-level jet. *Mon. Wea. Rev.*, **119**, 833-40.

[94] Schaefer, G. W., 1976: Radar observations of insect flight. In *Insect Flight*, R. C. Rainey, ed. John Wiley & Sons, New York.

[95] Sherman, J. W., 1970. Aperture-antenna analysis. In *Radar Handbook*, M.I. Skolnik ed., Ch. 9. McGraw-Hill, New York.

[96] Silverman, R. A., 1956: Turbulent mixing theory applied to radio scattering. *J. Appl. Phys.*, **27**, 699-705.

[97] Smagorinsky, J., 1963: General circulation experiments with the primitive equations. I. The basic experiment. *Mon. Wea. Rev.*, **91**, 99-164.

[98] Srygley, R. B. and E. G. Oliveira, 2001: Orientation mechanisms and migration strategies within the flight boundary layer. In *Insect Movement Mechanisms and Consequences. Proceedings of the Royal Entomological Society's 20th Symposium.* I. P. Woiwod et al., eds. CAPI Publishing.

[99] Stensrud, D. J., 1996: Importance of low-level jets to climate. *J. Clim.*, **9**, 1698-711.

[100] Suter, R. B., 1999: An aerial lottery: The physics of ballooning in a chaotic atmosphere. *J. Arachnology*, **27**, 281-93.

[101] Sun and Chang, 1986: Diffusion model for convective layer parameterization. *J. Clim. and Appl. Met.*, **25**, 1445-63.

[102] Sverdrup, H. U., 1942: *The Oceans.* Prentice-Hall.

[103] Swingle, D. M., 1950: *Reflections of Electromagnetic Waves of Continuously Variable Refractive Index.* TR No. 112, Cruft Lab., Harvard Univ.

[104] Tatarski, V. I., 1961: *Wave Propagation in a Turbulent Medium.* Translated from the original Russian by R. A. Silverman. McGraw-Hill Book Company.

[105] Tennekes, H. and J. L. Lumley, 1972: *A First Course in Turbulence.* The MIT Press.

[106] Tipler, P. A., 1978: *Modern Physics*, Worth Publishers, Inc., New York, N.Y.

[107] Turner, J. S., 1973: *Buoyancy Effects in Fluids.* Cambridge University Press.

[108] Uccellini, L. W. and D. R. Johnson, 1979: The coupling of upper and lower tropospheric jet streaks and implications for the development of sever convective storms. *Mon. Wea. Rev.*, **107**, 682-703.

[109] van de Kamp, D. W., and F. M. Ralph, M. F. Barth, P. A. Miller, J. R. Smart, and L. A. Benjamin, 1997: The new bird contamination quality control check applied to hourly winds from NOAA's profiler network. *Preprints, 28th Conference on Radar Meteorology.* Austin, Texas. Amer. Meteor. Soc.

[110] Vaughn, C. R., 1985: Birds and insects as radar targets: a review. *Proceedings of the IEEE*, **73**, 205-227.

[111] Villars, F. and V. F. Weisskopf, 1954: The scattering of electromagnetic waves by turbulent atmospheric fluctuations. *Physical Review*, **94**, 232-40.

[112] Villars, F. and V. F. Weisskopf, 1955: On the scattering of radio waves by turbulent fluctuations of the atmosphere. *Proceedings of the Inst. of Radio Engineerings*, **43**, 1232-39.

[113] Wallin, J. R., and D. V. Loonan, 1971: Low-level jet winds, aphid vectors, local weather, and barley yellow dwarf virus outbreaks. *Phytopathology*, **61**, 1068-70.

[114] Wexler, H., 1961: A boundary layer interpretation of the low-level jet. *Tellus*, **13**, 368-78.

[115] White, F. M., 1974: *Viscous Fluid Flow.* McGraw Hill.

[116] Whiteman, C. D., X. Bian, and S. Zhong, 1997: Low-level jet climatology from enhanced rawinsonde observations at a site in the Southern Great Plains. *J. Appl. Met.*, **36**, 1363-76.

[117] Wilczak, J. M., R. G. Strauch, F. M. Ralph, B. L. Weber, D. A. Merrit, J. R. Jordan, D. E. Wolfe, L. K. Lewis, D. B. Wuertz, J. E. Gaynor, S. A. McLaughlin, R. R. Rogers, and A. C. Riddle, 1995: Contamination of wind profiler data by migrating birds: characteristics of corrupted data and potential solutions. *J. Atmos. Oceanic Technol.*, **12**, 449-67.

[118] Wilson, D. A., 1970: Doppler radar studies of boundary layer wind profile and turbulence in snow conditions. *Proceedings: 14th Conference on Radar Meteorology*, Tucson, 191-6.

[119] Wilson, J. W., T. M. Weckwerth, J. Vivekanandan, R. M. Wakimoto, R. W. Russell, 1994: Boundary layer clear-air radar echoes: origin of echoes and accuracy of derived winds. *J. Atmos. and Ocean. Tech.*, **11**, 1184-1206.

[120] Wiscombe, W. J., 1980: Improved Mie scattering algorithms. *Applied Optics*, **19**, 1505-9.

[121] Wiscombe, W. J., 1979 (revised 1996): Mie scattering calculations: advances in technique and fast, vector-speed computer codes. NCAR Technical Note NCAR/TN-140+STR, 64 pp., National Center for Atmospheric Research.

[122] Wurman, J., 2001: The DOW mobile multiple-Doppler network. *Preprints, 30th International Conference on Radar Meteorology*, Munich, German, Amer. Meteor. Soc.

[123] Wurman, J. and J. Straka, E. Rasmussen, M. Randall, and A. Zahrai, 1997: Design and deployment of a portable, pencil-beam, pulsed 3-cm Doppler radar. *J. Atmos. Ocean. Tech.*, **14**, 1502-12.

[124] Yaglom, A. M., 1949: On the local structure of the temperature field in a turbulent flow. *Doklady Akad. Nauk SSSR*, **69**, 743.

[125] Zahrai, A. and D. S. Zrnić, 1993: The 10-cm-wavelength polarimetric weather radar at NOAA's National Severe Storms Laboratory. *J. Atmos. Oceanic Technol.*, **10**, 649-62.

[126] Zhong, S., J. D. Fast, and X. Bian, 1996: A case study of the Great Plains low-level jet using wind profiler network data and a high-resolution mesoscale model. *Mon. Wea. Rev.*, **124**, 785-806.

[127] Zrnić, D. S. and A. V. Ryzhkov, 1998: Observations of insects and birds with a polarimetric radar. *IEEE Trans. on Geos. and Remote Sensing*, **36**, 661-8.

[128] Zrnić, D. S. and A. V. Ryzhkov, 1999: Polarimetry for weather surveillance radars. *Bull. Amer. Met. Soc.*, **80**, 389-406.

Appendix A

Impact of Radar Tilt and Ground Clutter on Wind Measurements in Clear Air

A.1 Abstract

The VAD technique is a common method of measuring the wind vector from Doppler radar in clear-air conditions. It is very accurate if the assumption of horizontal homogeneity is valid, if the data is uncontaminated by non-meteorological targets such as birds or ground clutter, and if there is not significant anomalous propagation. Under the horizontal-homogeneity assumption, a vertical profile of the horizontal wind can be obtained from a single radar sector scan. The vertical resolution of such a profile depends on the radar elevation (or tilt) angle. An optimum tilt angle at which the best possible vertical resolution is obtained exists theoretically and is derived in this work. This optimum tilt angle is a compromise between the effects of beam divergence and range gate spacing. For typical S-band radar parameters, this optimum tilt angle is found to be about 10 degrees. However, wind analyses at this tilt angle are not accurate in practice because of ground clutter contamination, and sub-optimal angles need to be used.

Ground clutter contamination in clear-air work is a larger problem than it is in precipi-

tation work as the meteorological signal is much weaker (typically 30 dBZ weaker than rain) while the ground signal is the same strength. It is therefore more difficult to discriminate between the meteorological signal in the main radar beam lobe from ground clutter in side lobes. Furthermore, while the first side lobe in a pencil beam radar is typically 30 dBZ weaker than the main lobe, subsequent side lobes only gradually decrease in strength. The result of this is that if any ground clutter is measured from a side lobe, ground clutter can potentially be sensed in any of the side lobes at virtually any tilt angle. For wind profiling in the boundary layer, the impact of ground clutter contamination is greater as the tilt angle is increased since gates closer to the radar need to be used. This is contrary to intuitive expectations.

From experience with 4 radars (KGLD NEXRAD, DOW3, SPOL, and CIMARRON), this research suggests that a fairly narrow range of tilt angles from 1 to 2 degrees is generally acceptable for wind profiling of the boundary layer in clear-air conditions.

A.2 Introduction

The effective vertical resolution that can be achieved in a VAD-determined wind profile depends on the radar elevation (tilt) angle. For example, if the radar has a 100 meter gate spacing at a tilt of .5°, then the VAD technique can give a wind vector measurement at every gate, which is every 100 sin(.5°)= .9 m in the vertical. This resolution is deceptive since the beam width in the vertical is generally larger than .9 m. For a beam width of 1°, the beam width in the vertical at a .5° tilt angle at a range corresponding to 500 m above the surface, would be (Eqn. A.2 below) 2X500tan(.5°)cot(.5°) =1000 m.

The optimal tilt angle for maximizing the effective vertical resolution of a VAD-determined wind profile is achieved as a compromise between these two effects: the gate spacing effect, and the beam width effect. This compromise needs to be further modified to account for the practical problem of ground clutter, a problem which, as will be shown here, gets worse as the elevation angle is increased, contrary to intuitive expectations. It is the purpose of this appendix to analyze in some detail this issue from a theoretical and practical viewpoint.

A.3 Theory

By using the VAD technique, the vertical resolution of the wind profile, ΔZ, obtained with a radar scanning in azimuth at a fixed tilt angle is a function of the radar tilt angle, β, for two reasons with an opposite dependence on β. We wish to determine the tilt angle which makes ΔZ as small as possible.

First, as β is increased, the vertical spacing between data points in the profile, ΔZ_{gate}, increases as the sine of β according to

$$\Delta Z_{gate} = \Delta R sin\beta \tag{A.1}$$

Where ΔR is the spacing between range gates, as shown in Fig. A.1. Strictly speaking, the vertical resolution would be determined by both the gate spacing and the pulse length (whichever was longest); however; these two things are usually closely matched by radar design. The pulse length is selected so as to be twice the gate spacing in most radars, as the receiver simultaneously receives energy reflected from half of the pulse length. From (A.1), arbitrarily fine vertical resolution would appear to be obtainable by using a small β. However, this is not the case for several reasons. One is the impact of ground clutter and beam distortion at low elevation angles (discussed later in this appendix). Another is the that the horizontally-homogeneous assumption for standard VAD work is more likely to be violated if low elevation angles are used as circles of larger radius are needed.

A more fundamental reason (A.1) does not give the actual vertical resolution is that at low tilt angles a specific height above the ground is reached only at large range, and at large ranges, the divergence of the beam degrades the vertical resolution. Consequently, the vertical resolution at some height decreases as β decreases, which gives a ΔZ due to beam broadening, ΔZ_{beam}. For a beam width angle of ϕ (see Fig. A.1),

$$\Delta Z_{beam} = 2Rtan(\frac{\phi}{2})cos\beta$$

where R is the range to a certain gate. At a fixed height above the ground, Z, $R = Z/sin\beta$,

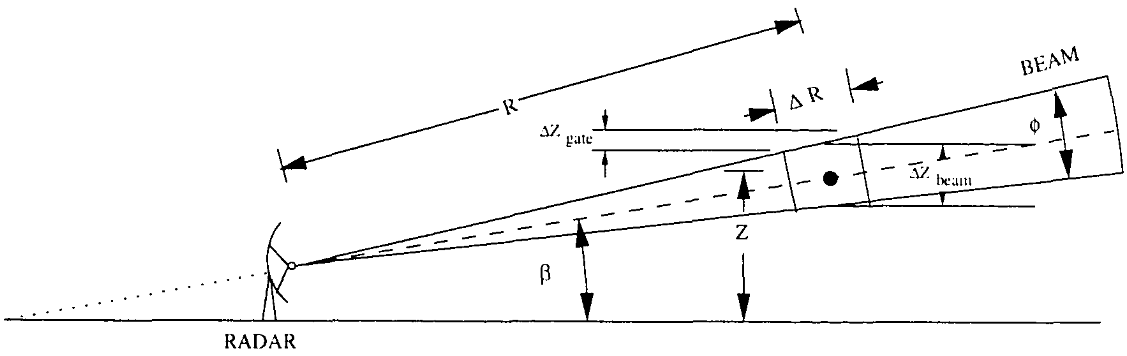

Figure A.1: Diagram for radar resolution

so

$$\Delta Z_{beam} = \frac{2Z tan\frac{\phi}{2} cos\beta}{sin\beta} = 2Z tan\frac{\phi}{2} cot\beta \qquad (A.2)$$

Since the beam actually has a Gaussian shape to it, (A.2) is an upper limit.

The best actual or effective vertical resolution will be, approximately, the largest of these two ΔZs, ΔZ_{gate}, or ΔZ_{beam}. Using the Cimarron beam width of 0.9°, and ΔR of 150m, we plot ΔZ_{gate} and ΔZ_{beam} for several low-level Z values in Fig. A.2

The optimum tilt angle, β_{opt}, for purposes of best (minimum) vertical resolution occurs at the intersection of the two curves plotted in Fig. A.2, where:

$$\Delta Z_{gate} = \Delta Z_{beam}$$

$$or$$

$$\Delta R sin\beta_{opt} = \frac{2Z tan\frac{\phi}{2} cos\beta_{opt}}{sin\beta_{opt}}$$

Which can be written:

$$cos^2\beta_{opt} + \frac{2Z}{\Delta R} tan\frac{\phi}{2} cos\beta_{opt} - 1 = 0$$

This is a quadratic in $cos\beta_{opt}$, since β_{opt} is a positive angle, we use the positive root from

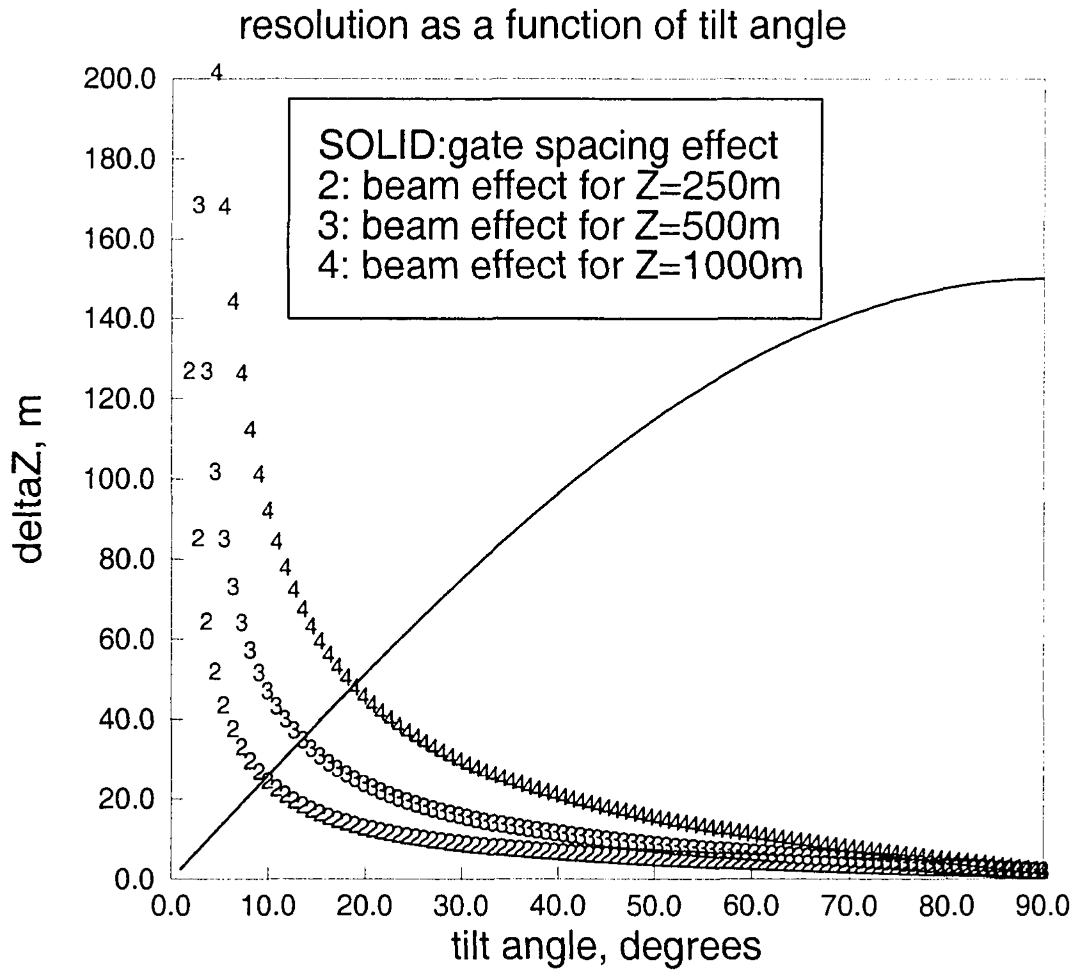

Figure A.2: Vertical resolution versus tilt angle, ΔZ_{gate} (solid line) and ΔZ_{beam} (numbered curves for different elevations). The theoretical vertical resolution at a particular tilt angle and vertical location is the larger of the value obtained from ΔZ_{gate} or ΔZ_{beam}, which is the intersection of a numbered curve and the solid curve.

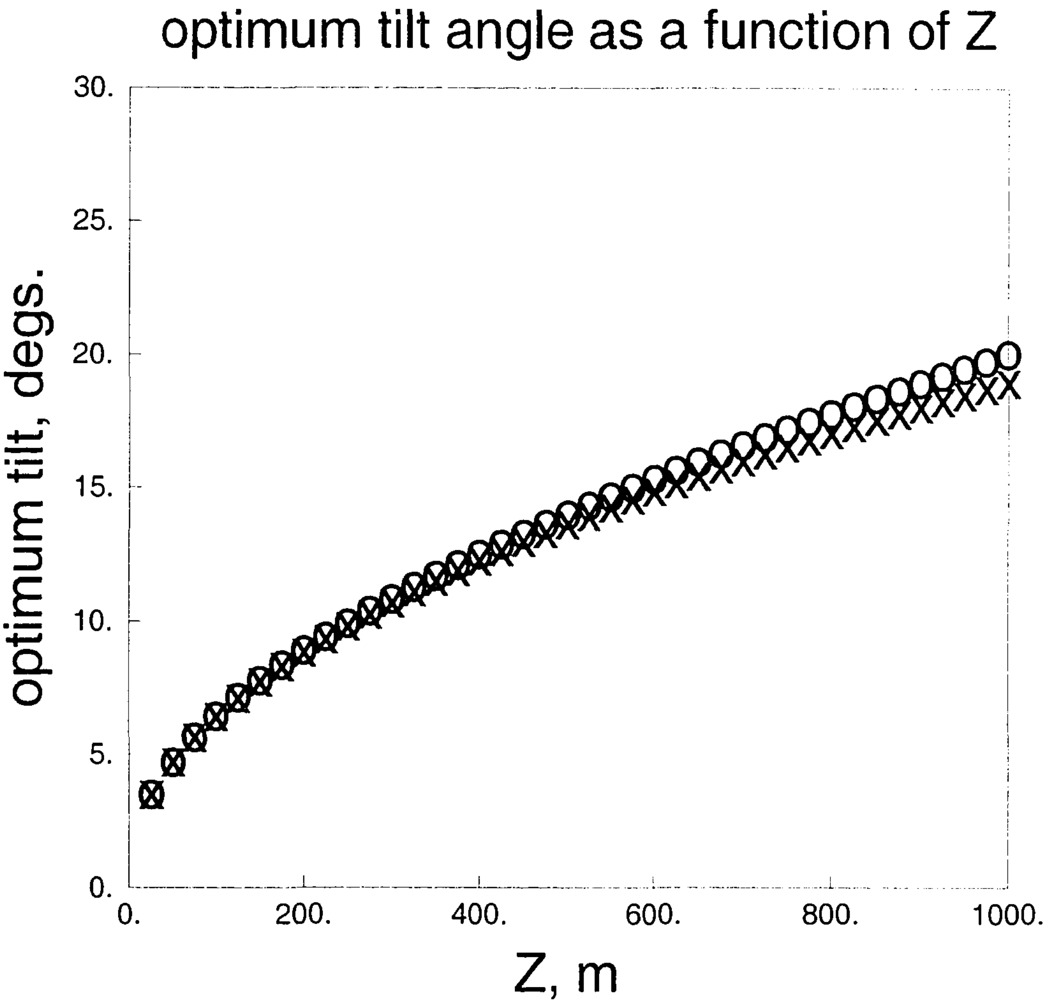

Figure A.3: Optimum tilt angle for best vertical resolution as a function of height above ground using the two methods described in the text. x's indicate first method, based on (A.3) and o's indicate second method, based on (A.6). Plots are for a beam width, ϕ, of .9° and a gate spacing, ΔR, of 150 m.

the quadratic equation, yielding:

$$\beta_{opt} = cos^{-1}\left[\frac{-Z}{\Delta R}tan\frac{\phi}{2} + \sqrt{\frac{Z^2}{(\Delta R)^2}tan^2\frac{\phi}{2} + 1}\right] \tag{A.3}$$

β_{opt} is a function of the height above the ground, Z, as shown in Figure A.3. Since ϕ is typical small (usually a degree or less), (A.3), to a good approximation, is equivalent to:

$$\beta_{opt} = cos^{-1}\left[1 - \frac{Z\phi}{2\Delta R}\right] \tag{A.4}$$

For a ΔR of 250 m, this approximation is good for approximately Z < 3 km. .

An alternate and more accurate way to arrive at the optimal tilt angle is to consider the radar probe volume drawn in Figure A.4. If we wish to consider ΔZ as the distance between the top and bottom points of the probe volume indicated in Fig. A.4, then

$$\Delta Z = (R + \frac{\Delta R}{2})sin(\beta + \frac{\phi}{2}) - (R - \frac{\Delta R}{2})sin(\beta - \frac{\phi}{2})$$

which after some simplification becomes:

$$\Delta Z = 2Rcos\beta sin\frac{\phi}{2} + \Delta R sin\beta cos\frac{\phi}{2} \qquad (A.5)$$

We note that (A.5) reduces approximately to (A.1) or (A.2) as β becomes large or small, respectively. Using R=Z/sinβ and setting $\frac{\partial \Delta Z}{\partial \beta} = 0$ (for constant Z), results in the following relation for β_{opt}:

$$\frac{1}{2}sin2\beta_{opt}sin\beta_{opt} = \frac{2Z}{\Delta R}tan\frac{\phi}{2} \qquad (A.6)$$

Which is equivalent to the cubic equation:

$$cos^3\beta_{opt} - cos\beta_{opt} + \frac{2Z}{\Delta R}tan\frac{\phi}{2} = 0 \qquad (A.7)$$

This equation is most easily solved by iteration for β_{opt}. The results (plotted as circles in Fig. A.3) are very similar to those from (A.3) (plotted as x's), differing by at most 6% for Z<1 km. The method leading to (A.7) is more accurate than that leading to (A.3) because both the beam and width and gate spacing techniques are simultaneously taken into account rather than considering a compromise between the two effects considered separately. However, (A.3) is simpler, has a better intuitive basis, and is almost as accurate.

Since it is not convenient to use a different radar tilt angle for every layer of the wind profile desired (a profile of 20 points would take 20 scans, which at 2 minutes per scan would give us a profile only every 40 minutes, during which time the profile may have been changing), some decision needs to be made as to the level in which the best resolution is desired. The elevation of the LLJ that requires the best resolution is the lower shear layer where the wind profile most rapidly changes with height. This is typically from the surface

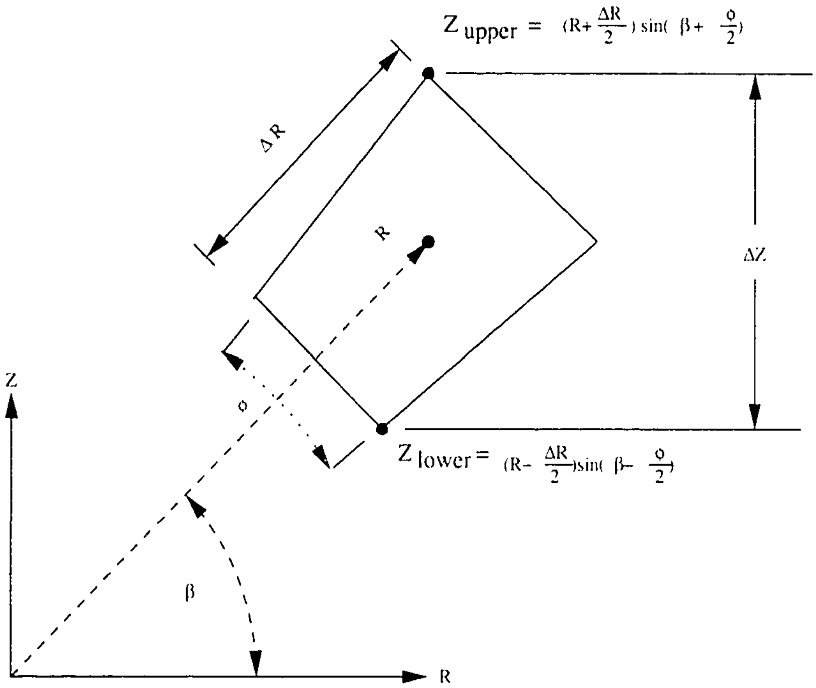

Figure A.4: Radar probe volume schematic for determining ΔZ.

Radar	Beam, Width, °	Gate, Spacing, m	β_{opt} from (A.4, A.3) °	β_{opt} from (A.7), °	ΔZ from (A.1) and (A.7), m
Cimarron	.90	150	9.28, 9.25	9.38	24.4
NEXRAD	.95	250	7.38, 7.37	7.43	32.3
DOW3	.93	137	9.87, 9.84	9.99	23.8
DOW3	.93	12	33.8 , 32.3	42.7	8.1
SPOL	.91	149	9.36, 9.33	9.46	24.5

Table A.1: Optimal tilt angle and resulting vertical resolution at a level 250 m above the surface, for 5 radar configurations.

to 500 m. If we decide to put the best resolution at 250 m, Fig. A.3 then suggests that a tilt angle of about 10 degrees would be desirable for purposes of vertical resolution of that layer when using the Cimarron radar, and Fig. A.2 shows that the vertical resolution would be about 25 m. Table A.1 shows the calculated optimal tilt angles and resulting vertical resolution for 4 radar configurations of interest.

Using a relatively high tilt angle of 10 degrees (relative, for example, to the standard NEXRAD tilts of 0.5, 1.5, 2.5, and 3.5 degrees) has other advantages in addition to improving the vertical resolution. High tilts greatly reduce problems from beam refraction through index of refraction gradients (anomalous propagation), and obtains the VAD wind profile over a much smaller scan radius so the VAD assumption of horizontal homogeneity is more likely to be valid.

A.4 VAD-Determined Wind Profiles as a Function of Radar Elevation Angle

As will be shown in this section, the theoretical results obtained in Section A.3 need substantial modification to deal with the severe practical problem of ground clutter. For this section, wind profiles obtained by the VAD technique using the KGLD NEXRAD radar and DOW radar located in Goodland, KS will be shown, though these results are typical of other locations.

At Goodland Kansas on the night of May 30, 2000, a Doppler on Wheels radar (DOW3) was co-located with the KGLD NEXRAD, and radar scans appropriate for doing VAD analysis were obtained at approximately 6 Z. The low-level jet at this time had an amplitude of about 30 m/s. Since the Nyquist speed for KGLD was 26 m/s and for DOW3 was 16 m/s, significant aliasing of the velocity occurred. All the data were de-aliased using a technique described in Sec. 4.1. The methodology for the VAD analysis is described in Sec. 4.5 and the radar scan display software is described in Sec. 3.2.1. In addition, radar data with a spectral width more than 7 m/s were rejected as it was found that such data are often ground clutter contaminated. Also, the data were corrected for the Earth's curvature by assuming an Earth radius of 4/3 of the actual radius (Battan, 1959, p.24).

Figure A.5 displays VAD-determined profiles of wind speed as a function of radar tilt angle and radar. Each profile has a reference profile plotted on it which was the wind profile obtained by KGLD at 1.5° tilt. The best fit wind vector from the VAD analysis has been divided by the cosine of the elevation angle to account for the tilt effect on the sensed radial velocity. The top row (A, B, C, and D) are profiles from KGLD at elevation angles .5°, 4.5°, 8.5°, and 20°, respectively, with each speed measurement plotted as a 'u' and the reference profile plotted as dots. The bottom row (E, F, G, and H) are profiles from DOW3 at approximately the same tilt angles: .5°, 4.5°, 8.5°, and 20°; with the same 1.5° KGLD reference profile. The KGLD radar was in precipitation mode at the time using

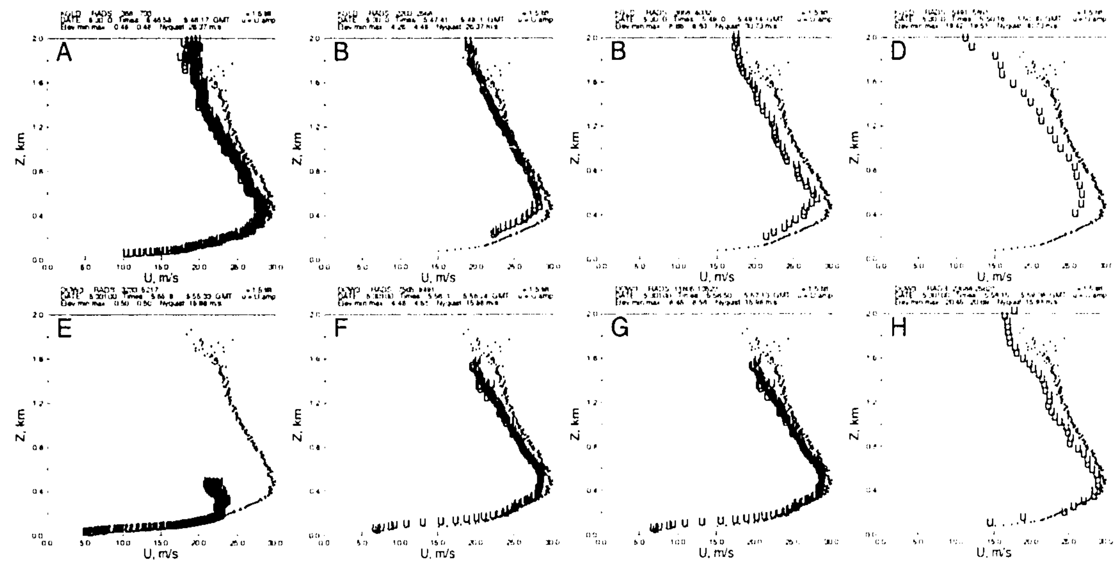

Figure A.5: Wind speed profiles near 6Z at Goodland, Kansas on 5/30/00 versus radar and elevation. A, B, C, and D are profiles from KGLD NEXRAD at .5, 4.5, 8.5, and 20° of tilt. E, F, G, and H are profiles from DOW3 at .5, 4.5, 8.5, and 20° degrees of tilt. Each profile has the same reference profile plotted with it as dots. The reference profile was the 1.5° tilt KGLD profile.

Volume Coverage Pattern 11 (VCP 11). The data required from KGLD for Fig. A.5 was obtained from 5:46 Z to 5:50 Z, and the data from DOW3 was obtained from 5:55 Z to 5:59 Z. Consequently, there is a small 10 minute time difference between the KGLD and DOW3 wind profiles. Also, KGLD had a gate spacing of 250 m and DOW3 had a gate spacing of 137 m, giving the theoretically best tilt angles from Table A.1 of 7° and 10° respectively. If we tentatively consider the reference profile to be accurate, then Fig. A.5 shows a problem at 0.5° tilt for both radars (Figs. A.5 A and E). The profiles have a sharper peak near .4 km in Z and significantly under estimate the wind speed near there. The DOW3 profile at .5° only reaches about .4 km in height since only 300 gates of information were collected, and at 0.5° elevation, the beam does not reach above this level above the ground by the last gate collected. We also note that the .5° tilt profiles have more points in the vertical. These tilts have better resolution according to (A.1), but are really oversampling the profile and smoothing it according to (A.2). At 4.5° tilt, KGLD exhibits good agreement with the reference profile above .6 km, but significant underestimation below .6 km (Fig. A.5 B). At higher tilts, the KGLD profile deteriorates further with significant underestimation of the wind speed and an increasingly noisy profile (Figs. A.5 C and D). DOW3 also exhibits a deterioration of the wind profile as the tilt angle is increased, though to a more limited extent (Figs. A.5 F, G, and H).

Ideally, with a horizontally homogeneous wind field, the wind profiles determined by VAD analysis would be independent of the elevation angle used, with the only difference being the number of points in the vertical where independent measurements were obtained, and the effective resolution of those measurements. It was expected, considering the results from Sec. A.3, that a radar tilt angle of about 10° would be best, but this is not the case. The reason the tilt angle affects the wind profile in unanticipated ways can be appreciated by considering the PPI velocity scans of the same data used to extract the wind profiles shown in Fig. A.5. Fig. A.6 shows PPI velocity scans for the KGLD radar and Fig. A.7 shows the corresponding scans from DOW3. Figs. A.6 and A.7 are plotted on the same scales with the same gray scale table. The figures are directly comparable with the only difference being the radar employed. Also, these figures use height above the ground as the radial distance, rather than distance along the beam (i.e., the range rings drawn are scaled to height above the ground, with a ring drawn every 200m above the ground). This makes the comparison of the PPI velocity plots with the derived profiles of Fig. A.5 much easier, and also makes it easier to compare PPI plots at different tilts.

These figures display data only where the received radar signal was above the noise level (and for KGLD, where second trip contamination has not been detected). The shape of the displayed data is ordinarily expected to be circular if the situation is horizontally homogeneous with an even distribution of scatterers (probably insects for this case). This circular pattern is plainly evident at the higher tilt angles (Fig. A.6 upper right and lower left; and Fig. A.7 lower left and lower right). However, at .5° tilt (Fig. A.6 upper left for KGLD), a non-circular pattern is seen. One probable reason for this distortion is that the beam has been bent by vertical gradients in the index of refraction. This problem is more severe the shallower the tilt angle is (Battan 1973, p. 17-28). Small horizontal gradients in the index of refraction can result in horizontally inhomogeneous beam propagation and non-circular signal patterns at low tilt angles, such as the one seen in Fig. A.6 upper left. Since the index of refraction profile is a thermodynamic property, it is not know what it

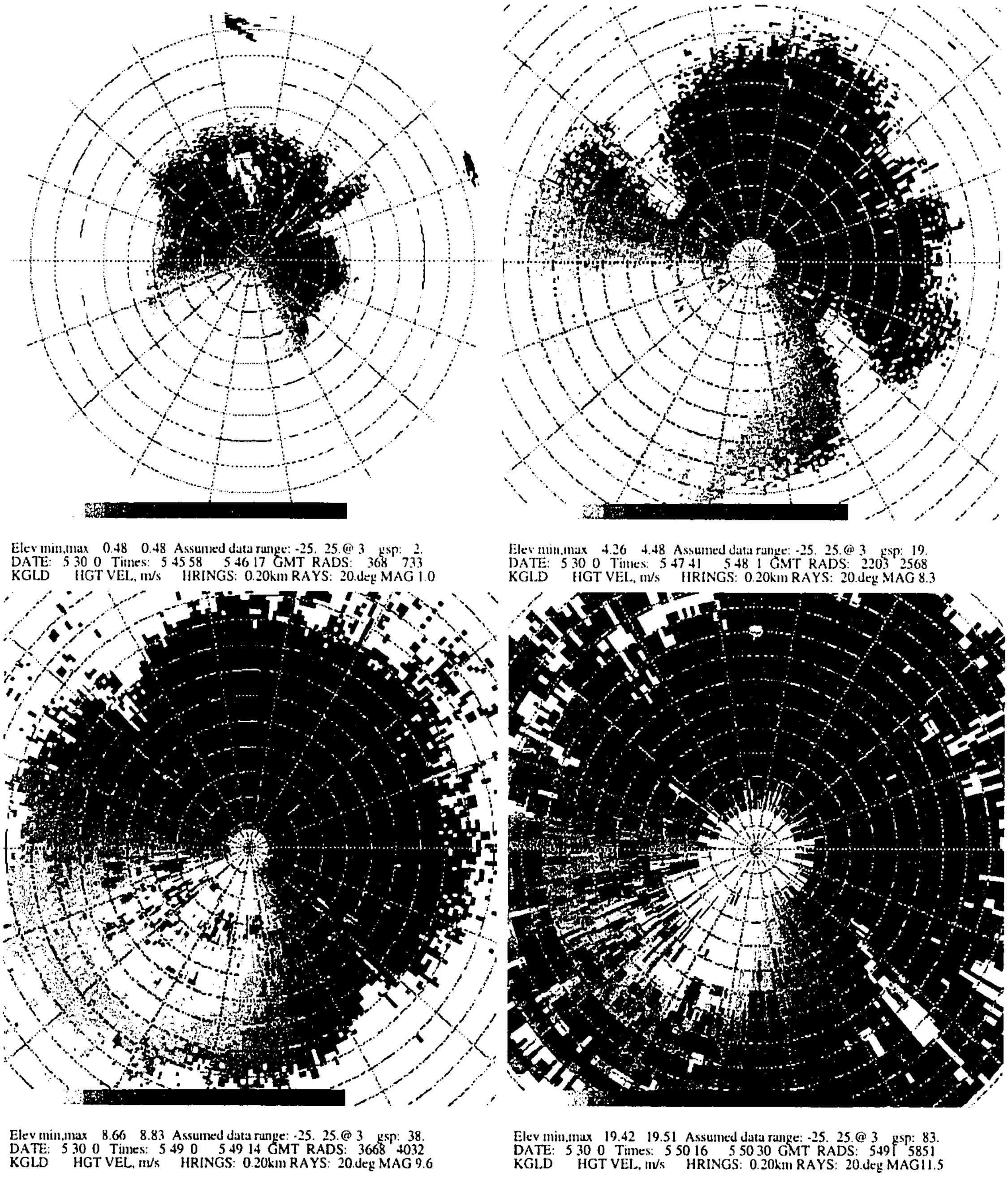

Figure A.6: PPI Velocity scans from KGLD corresponding to profiles obtained in Fig.A.5A, B, C, and D for KGLD. Upper left is for .5° of tilt, upper right is for 4.5°, lower left is for 8.5°, and lower right is for 20° . Rings are drawn every .20 km in height above the ground.

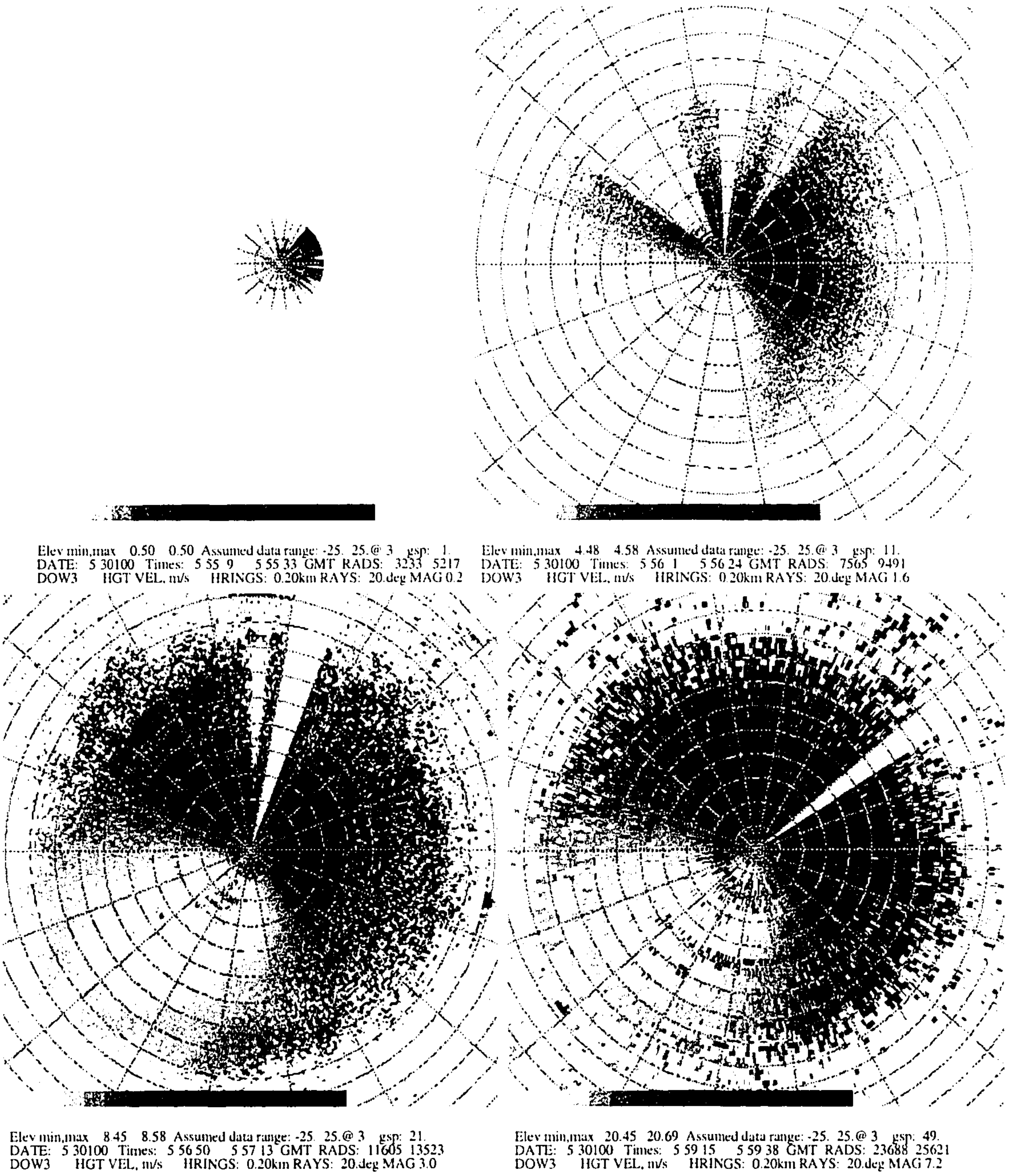

Figure A.7: PPI velocity scans from DOW3 corresponding to profiles shown in Fig. A.5 E, F, G, and H. Upper left is for .5° of tilt, upper right is for 4.5°, lower left is for 8.5°, and lower right is for 20° . Rings are drawn every .20 km above the ground.

was from radar data alone. Knowledge of the index of refraction gradient in the vertical and horizontal sufficient for correcting this problem by beam tracing could only be obtained from numerous thermodynamic soundings around the radar.

The problem with the wind profiles of Fig. A.5 in which the profiles degrade at higher tilt angles can also be explained by examining the PPI velocity scans of Figs. A.6 and A.7. On these plots, can be seen evidence of ground clutter contaminating the winds, a problem which gets worse at higher tilt angles. Since the ground has no velocity, ground clutter directly shows as zero velocity (medium gray in these PPI scans). Ground clutter contamination is obvious in the plots as spots of a few gray pixels in the middle of the high speed regions (black or white). The spiral pattern of missing data (white) in the upper right panel of Fig. A.6 is caused by the clutter filter employed by the KGLD radar. One clutter filter strategy is to remove data with low velocity, presuming it to be due to ground clutter. NEXRADs have a variety of complex clutter filter algorithms available which are selectable by the operator. The clutter filter information is not saved in the level II data format, so it is not possible to discern what clutter filter algorithm was used for these particular data, or any level II data. NEXRAD clutter filter algorithms involve the usage of a known ground clutter map and attempts to correct reflectivity values. Data of zero velocity were not used in the VAD analysis done here, it was filtered-out because of the possibility that it might be due to ground clutter. Indeed, the algorithm used here rejects all data less than or equal to 1 m/s, so data from pixels in Figs. A.6 and A.7 which are obvious ground clutter were not used in determining the wind profiles in Fig. A.5. However, ground clutter can affect the determination of velocity by more subtle means. Radars determine the velocity from a number of pulses which are combined to produce a velocity spectrum, the center of which is output as the radial velocity. Ground clutter affects the spectrum by adding a peak near 0 velocity. For strong ground echoes, most of the signal is ground clutter, and a zero velocity measurement results. However, if the ground clutter is weak enough, its velocity (0) can be weighted with the air velocity producing a velocity measurement which is biased low. An erroneous low measurement of the velocity caused by ground clutter contamination is the most likely explanation for the poor wind profiles at higher radar tilt angles seen in Fig.

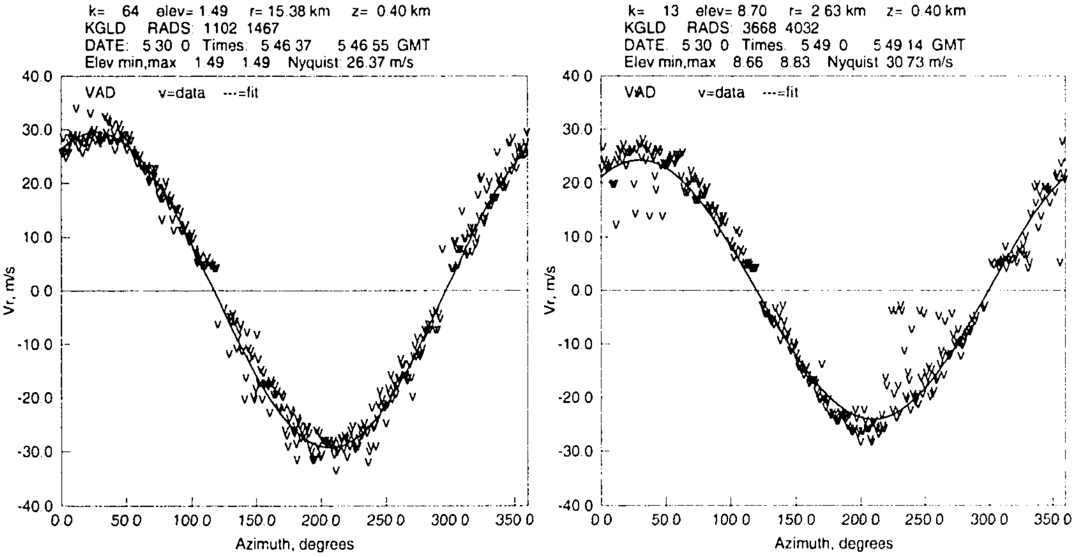

Figure A.8: VAD at a range 400 m above the ground from KGLD radar. LEFT: 1.5° tilt. RIGHT: 8.5° tilt. The v's are the raw (dealiased) radial velocity data, and the solid curve is the best-fit solution.

A.5. This is further supported by Fig. A.8 which shows the data used in the VAD analyses for the vertical location in the wind profile 400 m above the surface, at 1.5° and 8.5° tilts by KGLD, along with the best fit solution curves for the wind. The 8.5° VAD has numerous low speed data below the solution curve which the 1.5° VAD does not have. These low-speed data are very likely erroneous in value due to ground-clutter contamination of the velocity spectrum. Even if these low velocity points could somehow by filtered-out, the envelope of good data still has a smaller amplitude at 8.5° than at 1.5°, and it may well be that most of the data points in the 8.5° VAD have had their velocity spectra contaminated to some extent. A sample of reflectivity PPI scans from KGLD and DOW3 are shown in Figure A.9. Both these reflectivity scans are plotted on identical spatial scales and use the same grey-scale table to display reflectivity intensity. They correspond to the 8.5° velocity PPI scans in Figs. A.6 and A.7. The better spatial resolution of DOW3 relative to KGLD is apparent (137 m gate spacing versus 1 000 m). Also, DOW3 has measured reflectivity in the same air as KGLD. This is because DOW3 has a 3 cm wavelength, versus 10 cm for NEXRAD. The scattering targets in this case were most probably insects (for reasons discussed in Sec. 3.9) and 10 cm radars are more sensitive to targets of this size than 3 cm. Little ground clutter is obvious in Fig. A.9. KGLD, of course, has been ground clutter-filtered, but DOW3 has

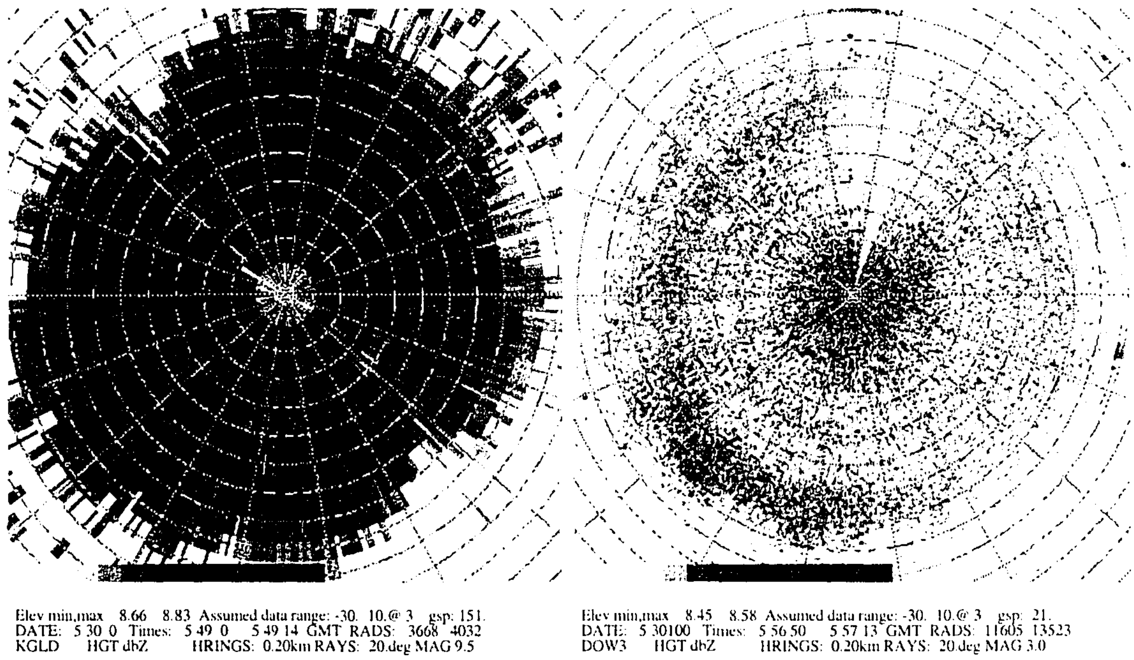

Figure A.9: Reflectivity scans from KGLD (left) and DOW3 (right)

not. Many locations with obvious ground clutter in the velocity scan in the lower left of Fig. A.7 do not correspond to high reflectivities in the dBZ scan of Fig. A.9. Nonetheless, ground clutter contamination is still present, even if the reflectivity of the ground is to weak to stand out in the reflectivity display. Ground clutter is a larger problem for clear-air radar data such as these, due to the very weak clear-air reflectivity (relative to precipitation). Even very weak signals from side lobes can contaminate the signal, if the signal is weak to begin with.

Why ground clutter gets worse at higher tilt angles (which is the reverse of expectations, since it was intuitively expected that ground clutter would be a larger problem when the beam was closer to the ground) can be answered by referring to the RHI scan of Fig. A.10. For this scan, DOW3 was operated at the maximum possible resolution setting of 12 m gates in the same location and at about the same time the PPI scans for doing VAD work were obtained. The point targets evident in the reflectivity scan are believed to be insects and account for most of the received signal and exist up to about 2 km. Ground clutter is also apparent in the reflectivity and velocity scans, especially between .8 and 1.6 km of range from the radar. Clutter appears as arcs of high reflectivity and as arcs of zero radial speed.

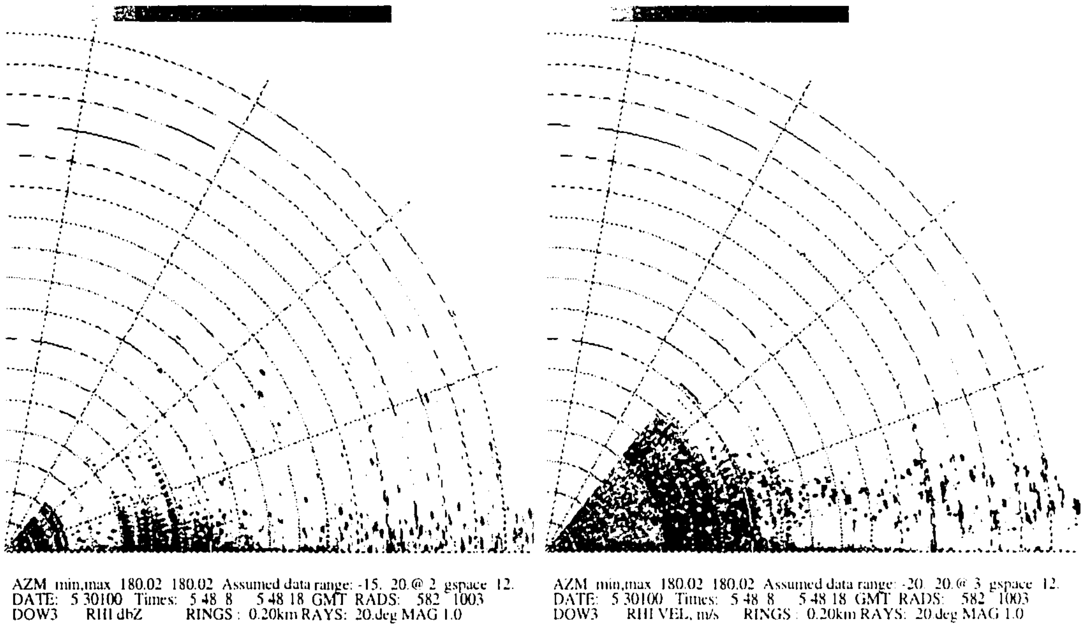

Figure A.10: LEFT: RHI reflectivity scan from DOW radar at Goodland, Kansas on 5/30/00 at 5:48 GMT. The radar was point along azimuth 180° (due south). Range rings are 200 meters apart. Radials are drawn every 20 degrees. Significant ground clutter is seen at a range of .8 km to 1.6 km at all tilt angles. RIGHT: RHI velocity scan at the same time. Ground clutter appears as a medium gray (zero velocity).

Fig. A.11 shows a map of the area with the radar location indicated. An open field existed to the south of the site (180° azimuth) of about a kilometer in length. Beyond this was a network of streets. The ground clutter indicated in Fig. A.10 begins in range (about .8 km) at about the same distance as the street network indicated in Fig. A.11. Beyond about 1.6 km, the side lobes of the radar are apparently screened-out and the problem is greatly reduced. Also, note in the reflectivity scan in Fig. A.10 that the side lobe structure can be inferred from the modulation in signal strength at individual gates. For example, at a range of about 1.2 km, the reflectivity modulates in elevation through about 17 maxima in 40 degrees of elevation. Each maximum corresponds with a particular side lobe intersecting a ground target. In fact, one method of determining a beam power plot is to scan a point target of know reflectivity.

Ground clutter is generally a problem for this site and radar at all tilt angles for any gates less than about 1.6 km from the radar. When a low tilt angle is used for VAD work, most of the gates used for determining the wind profile will be beyond this distance, and

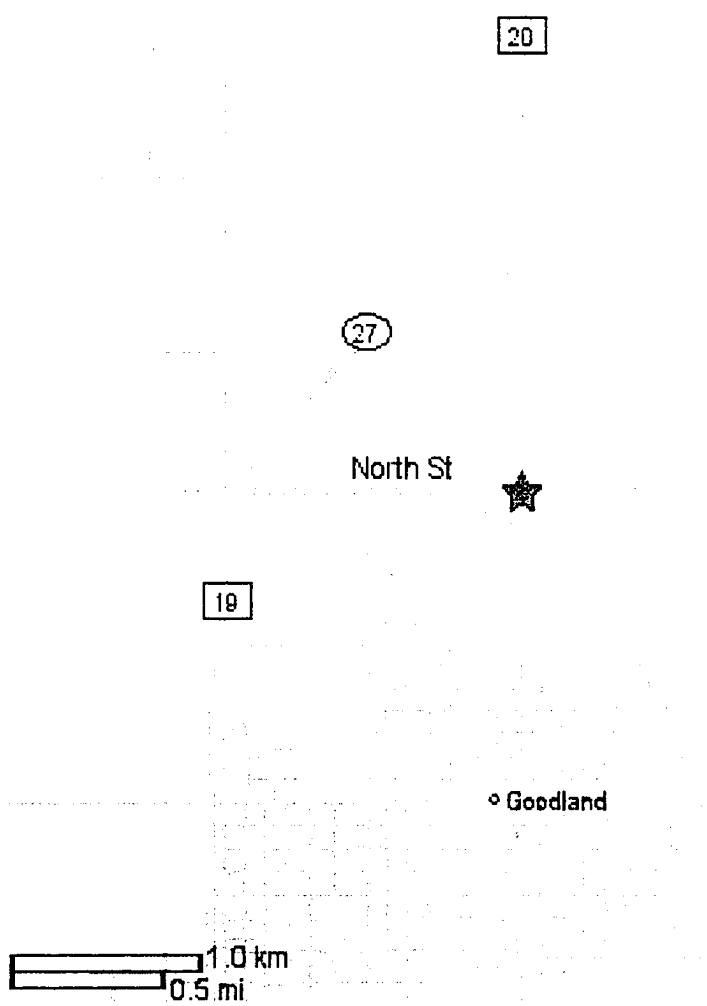

Figure A.11: Road map around the KGLD NEXRAD radar site. Star marks site of the DOW and KGLD radars at 920 Armory Road, Goodland, KS; co-located with the National Weather Service Office. North is toward the top of the figure.

the problem of ground clutter is limited to the lowest levels of the profile. At higher tilt angles, more radar gates that need to be used to measure the low-level winds will be in the ground clutter, and systematically underestimated and noisy winds result. Stated another way, gates closer to the radar need to be used at higher tilt angles; and gates closer to the radar are more likely to be contaminated by ground clutter, regardless of tilt angle.

Assuming that ground clutter contamination falls within a hemisphere centered around the radar of some radius, $R_{clutter}$, a radar tilt angle can be chosen such that wind measurements above a certain minimum height, Z_{min} will be made outside this circle. Approximately, this tilt angle is $\beta_{clutter}$:

$$\beta_{clutter} = tan^{-1}(\frac{Z_{min}}{R_{clutter}}) \tag{A.8}$$

If we desire accurate winds above 200 m and (as Fig. A.10 suggests) ground clutter is limited to 1.6 km from the radar, then (A.8) gives a maximum tilt to use of 7°. However, the problem of ground clutter is worse for KGLD than DOW3. This is possibly because DOW3 has a smaller probe volume, or (more likely) because the antenna for KGLD is atop a tower while DOW3 was near the ground. The screening-out effect of side lobes by the surface does not occur for elevated antennas. Figs. A.5 B and C show degraded wind profiles from KGLD below approximately .7 and 1.4 km for 4.5° and 8.5° tilts. Using these values in (A.8), to solve for $R_{clutter}$ gives $R_{clutter}$ consistently of about 9 km for both tilts. For this $R_{clutter}$, and a Z_{min} of 200 m, (A.8) gives a maximum tilt of about 1.3° to avoid problems from ground clutter. This is consistent with the KGLD wind profile at 1.5° tilt being used as the reference profile in Fig. A.5.

To show that this is a general problem for clear-air VAD work, we present some results from two other radars, SPOL and Cimarron. Fig. A.12 shows wind profiles derived from the deployable S-band Dual Polarization Radar (SPOL) operated by NCAR. Plotted are the 0.5°, 4.5°, 8.5, and 10.5° profiles with the 2.5° profile plotted as dots on each for reference (the 1.5° tilt was not available). These data were obtained with SPOL deployed near Idalia, Colorado near noon (18:40 Z) on July 14, 2000 under clear-air conditions. This radar was sited deliberately in a shallow depression in the terrain in an attempt to minimize ground clutter by way of the screening of side lobes. Nonetheless, these profiles show unmistakable

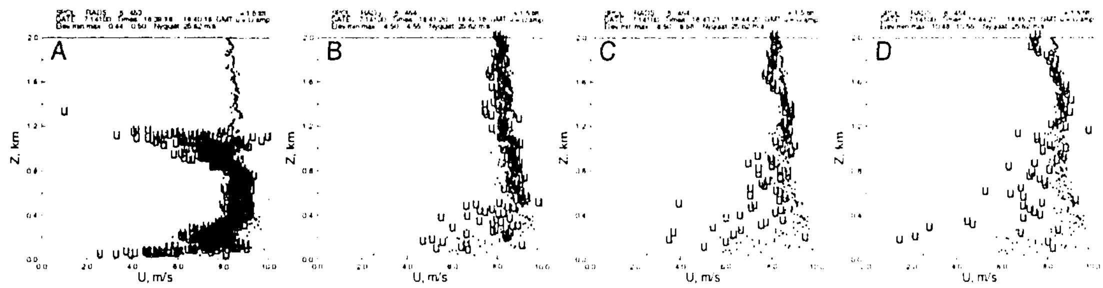

Figure A.12: Daytime VAD wind profiles from SPOL radar on 7/14/00 for tilt angles of 0.5°, 4.5°, 8.5°, and 10.5°. Wind profiles are plotted as 'u's and each has a reference profile plotted as dots which is the 2.5° tilt profile.

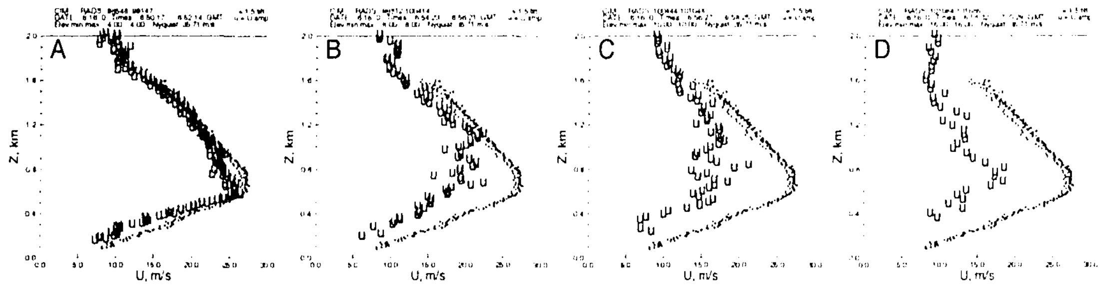

Figure A.13: VAD wind profiles from Cimarron radar near 7 Z on 6/16/00. Plotted dots are the profile obtained at 2° of tilt.

degradation of the wind profiles obtained, due to ground clutter contamination. For Figs. A.12 B, C, and D, respectively, significant noise in the profiles and under estimation of the winds (relative to the plotted 2.5° reference profile) are obvious below .55 km, 1.0 km, and 1.2 km. From (A.8), this leads to a consistent $R_{clutter}$ of about 7 km.

Fig. A.13 shows VAD-derived wind profiles for a LLJ obtained with the Cimarron radar with similar problems. Presented are profiles obtained from tilt angles 4.0°, 8.0°, 10.0°, and 16.0° respectively in Figs. A.13 A, B, C, D. Each figure has the 2.0° profile plotted as the reference profile. The degradation of the wind profile at higher tilt angles in Fig. A.13 implies an $R_{clutter}$ of about 7.5 km.Fig. A.14 shows an RHI scan from Cimarron (from a different date). The range rings are drawn every 2 km and the medium gray shade indicating ground clutter is evident at all tilt angles out to about 8 km in range from the radar. An arc of ground clutter is also present at a range of about 14 km. This is consistent with an $R_{clutter}$ of about 7.5 km found using (A.8) and Fig. A.13.

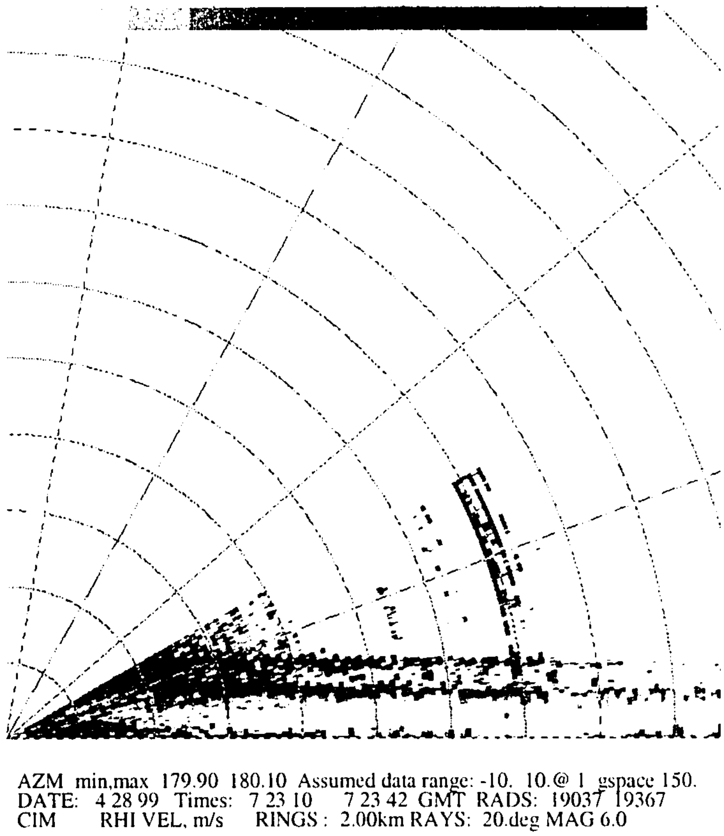

Figure A.14: RHI scan from Cimarron radar at azimuth 180° obtained at about 7 Z on April 28, 1999. Range rings are drawn every 2 km and radial lines are drawn every 20 degrees. Figure indicates southerly velocity component in boundary layer about 2 km deep (light and dark shades) and ground clutter (medium gray shade).

A.5 Summary and Conclusions

This appendix derives theoretically the best radar tilt angle, β_{opt}, to use for maximizing the vertical resolution of VAD-derived wind profiles. This angle is a compromise between gate spacing and beam width effects. Theoretically, we found this value to be given implicitly by:

$$cos^3\beta_{opt} - cos\beta_{opt} + \frac{2Z}{\Delta R}tan\frac{\phi}{2} = 0$$

or approximately and explicitly by:

$$\beta_{opt} = cos^{-1}\left[1 - \frac{Z}{2\Delta R}\phi\right]$$

Where Z is the height above the ground, ΔR is the gate spacing, and ϕ is the beam angular width. This gives a best tilt angle for typical radar configurations of 7 to 10 degrees and a best obtainable vertical resolution of 20 to 30 meters. However, the selection of tilt angle needs to be subject to an over-riding maximum determined by the amount of ground clutter contamination. This leads to the need to have:

$$\beta < tan^{-1}(\frac{Z_{min}}{R_{clutter}})$$

where Z_{min} is the level above which winds are desired and $R_{clutter}$ is the distance from the radar that ground clutter is a problem. Ground clutter is a larger problem for clear-air radar data than for radar data of precipitation targets because the clear-air signal is much weaker, which allows the contamination of the data by ground targets in the radar side lobes. Also, tilt angles below a degree or so should be avoided because of the intersection of the main beam lobe with the ground causes a great deal of ground clutter contamination. So we also need:

$$\beta > 1^\circ$$

The resulting vertical resolution is the maximum of either:

$$\Delta Z_{gate} = \Delta R sin\beta$$

or:

$$\Delta Z_{beam} = 2Z tan\frac{\phi}{2} cot\beta$$

The main limiting factor was found empirically to be $R_{clutter}$. It is shown that, for VAD work with clear-air data, the problem of ground clutter gets worse as the tilt angle is increased. This is because, for higher tilt angles, data closer to the radar must be used to obtain a VAD at a particular height above the ground. Ground clutter contaminates velocity measurements at all tilt angles by way of beam side lobes and tends to be restricted to ranges less than $R_{clutter}$ from the radar. Since the amount of ground clutter depends on the radar and the radar site, $R_{clutter}$ will generally be site specific. For KGLD, it was found that the 1.5° tilt produced the most accurate wind profiles, even though, by (A.2) the vertical resolution at Z=250 m is only about 150 m, rather than the 32 m which could have been obtained at a tilt angle of 7° had clutter not been a problem. With careful radar siting, or possibly more sophisticated ground-clutter filtering, higher tilt angles could be used, with a consequent increase in vertical resolution.